Franz Roters, Philip Eisenlohr, Thomas R. Bieler,
and Dierk Raabe

Crystal Plasticity Finite Element Methods

in Materials Science and Engineering

WILEY-VCH

WILEY-VCH Verlag GmbH & Co. KGaA

The Authors

Dr. Franz Roters
MPI für Eisenforschung GmbH
Abt. Mikrostrukturphysik
Max-Planck-Str. 1
40237 Düsseldorf
Germany

Dr.-Ing. Philip Eisenlohr
MPI für Eisenforschung GmbH
Abt. Mikrostrukturphysik
Max-Planck-Str. 1
40237 Düsseldorf
Germany

Prof. Dr. Thomas R. Bieler
Michigan State University
College of Engineering
Chemical Engineering and Materials Science
East Lansing, MI 48824
USA

Prof. Dr. Dierk Raabe
MPI für Eisenforschung GmbH
Abt. Mikrostrukturphysik
Max-Planck-Str. 1
40237 Düsseldorf
Germany

V

Notation

As a general scheme of notation, vectors are written as boldface lowercase letters (e. g., $\mathbf{a}$, $\mathbf{b}$), second-order tensors as boldface capital letters (e. g., $\mathbf{A}$, $\mathbf{B}$), and fourth-order tensors as blackboard-bold capital letters (e. g., $\mathbb{A}$, $\mathbb{B}$). For vectors and tensors, Cartesian components are denoted as, a_i, A_{ij}, and A_{ijkl} respectively. The action of a second-order tensor upon a vector is denoted as $\mathbf{A}\,\mathbf{b}$ (in components $A_{ij}b_j$, with implicit summation over repeated indices) and the action of a fourth-order tensor upon a second-order tensor is designated as $\mathbb{A}\mathbf{B}$ ($A_{ijkl}B_{kl}$). The composition of two second-order tensors is denoted as $\mathbf{A}\mathbf{B}$ ($A_{ij}B_{jl}$). The tensor (or dyadic) product between two vectors is denoted as $\mathbf{a}\otimes\mathbf{b}$ (a_ib_j). All inner products are indicated by a single dot between the tensorial quantities of the same order, for example, $\mathbf{a}\cdot\mathbf{b}$ (a_ib_i) for vectors and $\mathbf{A}\cdot\mathbf{B}$ ($A_{ij}B_{ij}$) for second-order tensors. The cross-product of a vector $\mathbf{a}$ with a second-order tensor $\mathbf{A}$, denoted by $\mathbf{a}\times\mathbf{A}$, is a second-order tensor defined in components as $(\mathbf{a}\times\mathbf{A})_{ij}=\epsilon_{ikl}a_kA_{lj}$, where ϵ is the Levi–Civita permutation matrix. The transpose, $\mathbf{A}^{\mathrm{T}}$, of a tensor $\mathbf{A}$ is denoted by a superscript "T," and the inverse, $\mathbf{A}^{-1}$, by a superscript "−1." Additional notation will be introduced where required.

Franz Roters, Philip Eisenlohr, Thomas R. Bieler, and Dierk Raabe: Crystal Plasticity Finite Element Methods —
2010/7/23 — page VII — le-tex

VII

Contents

VIII | *Contents*

Franz~Roters, Philip~Eisenlohr, Thomas~R.~Bieler, and~Dierk~Raabe: Crystal Plasticity Finite Element Methods — 2010/7/23 — page IX — le-tex

Contents | **IX**

X | *Contents*

Preface

In the last 20 years, the Crystal Plasticity Finite Element Method (CPFEM) has developed into an extremely versatile tool for describing the mechanical response of crystalline materials on all length scales from single crystals to engineering parts. While this is clearly reflected by an ever increasing number of publications in scientific journals, to date there is no comprehensive monograph on the topic. To change this situation the authors have brought together their experience with CPFEM into the current book. The aim of the book is to give an overview of the wide field of models and applications in CPFEM at both small and large scales, and to give some practical advice to beginners.

The book is organized as follows: The introduction gives a comprehensive overview over the development of the application of CPFEM in the last 20 years. The first part gives an introduction into the fundamentals on which the Crystal Plasticity Finite Element Method is built. As it works in the interface of material physics, continuum mechanics and applied computer science the reader finds one chapter on each of these aspects. In the second part the Crystal Plasticity Finite Element Method is introduced in detail. First, different single crystal constitutive models are presented, including deformation mechanisms such as dislocation slip, twinning, athermal transformations, and damage. Second, in view of large scale applications, different homogenization schemes for the transition from single to polycrystals are introduced. Finally, some numerical aspects of importance for the practical implementation of CP as a material model in FEM codes are discussed. The last and by far most elaborate part of the book is concerned with application examples. Naturally, most of these examples originate from the work of the authors, plus some important examples taken from the work of other groups. The aim of this part of the book is to give an overview on the numerous potential applications of CPFEM in materials simulation and closes with an outlook of the authors on future applications of the Crystal Plasticity Finite Element Method.

Düsseldorf, April 2010

Franz Roters
Philip Eisenlohr
Thomas R. Bieler
Dierk Raabe

1
Introduction to Crystalline Anisotropy
and the Crystal Plasticity Finite Element Method

Crystalline matter is mechanically anisotropic. This means that the instantaneous and time-dependent deformation of crystalline aggregates depends on the direction of the mechanical loads and geometrical constraints imposed. This phenomenon is due to the anisotropy of the elastic tensor, Figure 1.1, and to the orientation dependence of the activation of the crystallographic deformation mechanisms (dislocations, twins, martensitic transformations), Figure 1.2.

An essential consequence of this crystalline anisotropy is that the associated mechanical phenomena such as material strength, shape change, ductility, strain hardening, deformation-induced surface roughening, damage, wear, and abrasion are also orientation-dependent. This is not a trivial statement as it implies that mechanical parameters of crystalline matter are generally tensor-valued quantities. Another major consequence of the single-crystal elastic-plastic anisotropy is that it adds up to produce also macroscopically directional properties when the orientation distribution (crystallographic texture) of the grains in a polycrystal is not random. Figure 1.3a,b shows such an example of a plain carbon steel sheet with a preferred crystal orientation (here high probability for a crystallographic {111} plane being parallel to the sheet surface) after cup drawing. Plastic anisotropy leads to the formation of an uneven rim (referred to as *ears* or *earing*) and a heterogeneous
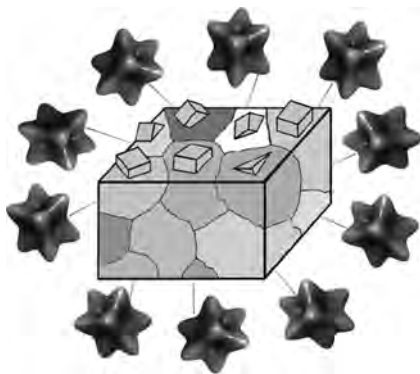
Figure 1.1 Elastic anisotropy in a polycrystal resulting from superposition of single-crystal anisotropy.

Figure 1.2 Plastic anisotropy in a single crystal due to distinct crystallography.

(a) (b)
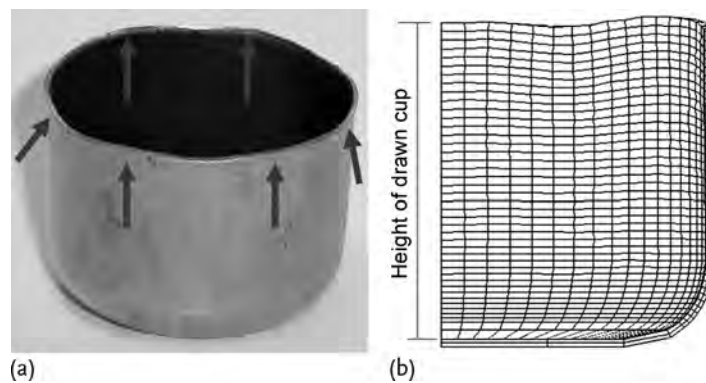
Figure 1.3 Consequence of plastic anisotropy when drawing a textured sheet into a cup. The orientation distribution before deformation exhibits a high volume fraction of grains with a crystallographic [111] axis parallel to the sheet normal. The arrows in (a) mark six ears resulting from preferential material flow. (b) The corresponding crystal plasticity finite element simulation.

distribution of material thinning during forming. It must be emphasized in that context that a random texture is not the rule but a rare exception in real materials. In other words, practically all crystalline materials reveal macroscopic anisotropy.

A typical example of such macroscopic anisotropy is the uniaxial stress–strain curve, which is the most important mechanical measure in the design of structural materials. The introductory statement made above implies that uniaxial stress–strain curves represent an incomplete description of plastic deformation as they reduce a six-dimensional yield surface and its change upon loading to a one-dimensional (scalar) yield curve, see Figure 1.4. Another consequence of this statement is that the crystallographic texture (orientation distribution) and its evolution during forming processes is a quantity that is inherently connected with plasticity theory, more precisely, with the anisotropy of the underlying plasticity mechanisms. Texture can, hence, be used to describe the integral anisotropy of polycrystals in terms of the individual tensorial behavior of each grain and the orientation-dependent boundary conditions among the crystals. Formally, the connection between shear and texture evolution becomes clear from the fact that any deformation gradient can be expressed as the combination of its skew-symmetric portion, which represents a pure rotation leading to texture changes if not matched by the rotation implied by plastic shear, and a symmetric tensor that is a measure of pure stretching. Plastic shear, hence, creates both shape and orientation changes, except for certain highly symmetric shears. Therefore, a theory of the mechanical properties of crystals must include, first, the crystallographic and anisotropic nature of those mechanisms that create shear and, second, the orientation(s) of the crys-
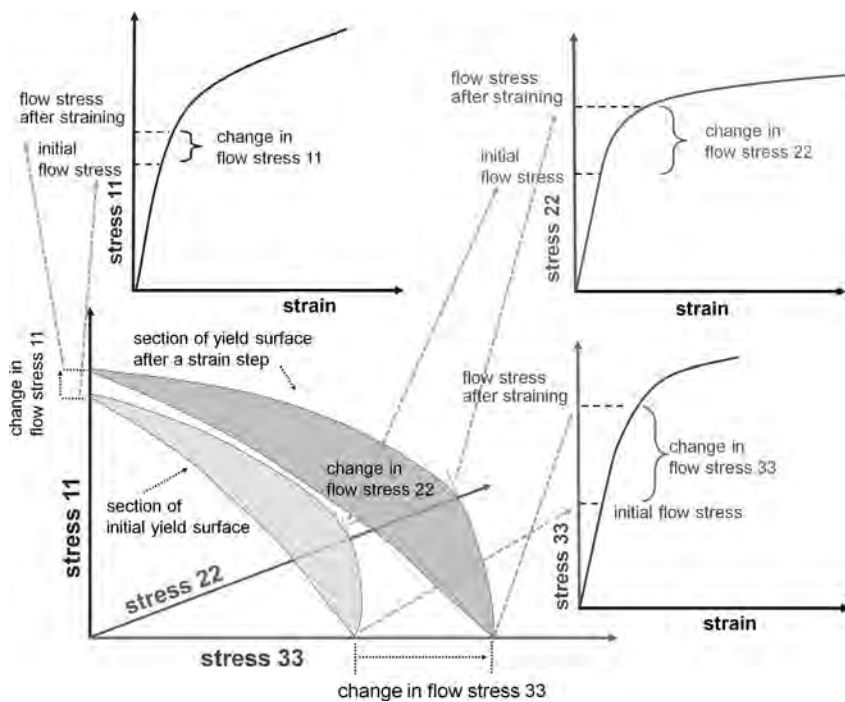
Figure 1.4 Flow stress and strain hardening of anisotropic materials are tensor quantities.

tal(s) studied relative to the boundary conditions applied (e.g., loading axis, rolling plane).

Early approaches to describe anisotropic plasticity under simple boundary conditions considered these aspects, such as the Sachs (1928), Taylor (1938), Bishop–Hill, and Kröner (1961) formulations. However, these approaches were neither designed for considering explicitly the mechanical interactions among the crystals in a polycrystal nor for responding to complex internal or external boundary conditions, see Figure 1.5a–d. Instead, they are built on certain simplifying assumptions of strain or stress homogeneity to cope with the intricate interactions within a polycrystal.

For that reason variational methods in the form of finite element approximations have gained enormous momentum in the field of crystal mechanical modeling. These methods, which are referred to as crystal plasticity finite element (CPFE) models, are based on the variational solution of the equilibrium of the forces and the compatibility of the displacements using a weak form of the principle of virtual work in a given finite-volume element. The entire sample volume under consideration is discretized into such elements. The essential step which renders the deformation kinematics of this approach a crystal plasticity formulation is the fact that the velocity gradient is written in dyadic form. This reflects the tensorial crystallographic nature of the underlying defects that lead to shear and, consequently, to both shape changes (symmetric part) and lattice rotations (skew-symmetric part), see Chapter 3. This means that the CPFE method has evolved as an attempt to employ some of the extensive knowledge gained from experimental and theoretical studies of single-crystal deformation and dislocations to inform the further development of continuum field theories of deformation. The general framework supplied by variational crystal plasticity formulations provides an attractive vehicle for developing a comprehensive theory of plasticity that incorporates existing knowledge of the physics of deformation processes (Arsenlis *et al.*, 2004; Curtin and Miller, 2003; Vitek, Mrovec, and Bassani, 2004a) into the computational tools of continuum mechanics (Zienkiewicz, 1967; Zienkiewicz and Taylor, 2005) with the aim to develop advanced and physically based design methods for engineering applications (Zhao *et al.*, 2004a).

One main advantage of CPFE models lies in their capability to solve crystal mechanical problems under complicated internal and/or external boundary conditions. This aspect is not a mere computational advantage, but it is an inherent part of the physics of crystal mechanics since it enables one to tackle those boundary conditions that are imposed by inter- and intragrain micro-mechanical interactions, Figure 1.6 (Sachtleber, Zhao, and Raabe, 2002). This is not only essential to study in-grain or grain cluster mechanical problems but also to better understand the often quite abrupt mechanical transitions at interfaces (Raabe *et al.*, 2003).

However, the success of CPFE methods is not only built on their efficiency in dealing with complicated boundary conditions. They also offer high flexibility with respect to including various constitutive formulations for plastic flow and hardening at the elementary shear system level. The constitutive flow laws that were
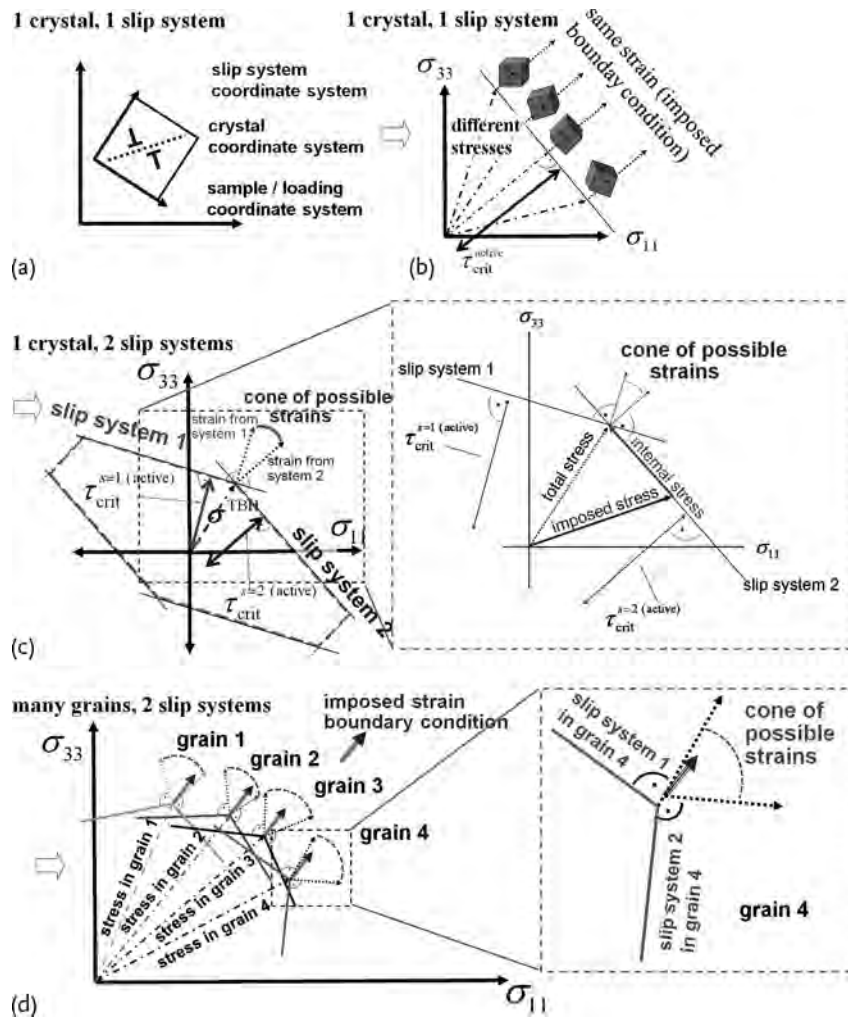
Figure 1.5 The increasing complexity of crystal-scale micromechanics with respect to the equilibrium of the forces and the compatibility of the displacements for different situations: (a, b) Single-slip situation in a single crystal presented in stress space. (c) Portion of a single-crystal yield surface with three slip systems. (d) Multislip situation in a polycrystal where all different crystals have to satisfy an assumed imposed strain in their respective yield corners. If the strain is homogeneous, this situation leads to different stresses in each crystal (Raabe *et al.*, 2002a, 2004a). τ_{crit}: critical shear stress; σ^{TBH}: Taylor–Bishop–Hill stress state (stress required to reach a yield corner).

suggested during the last few decades have gradually developed from empirical viscoplastic formulations (Asaro and Rice, 1977; Rice, 1971) into microstructure-based multiscale models of plasticity including a variety of size-dependent effects and interface mechanisms (Arsenlis and Parks, 1999, 2002; Arsenlis *et al.*, 2004; Cheong and Busso, 2004; Evers, Brekelmans, and Geers, 2004a,b; Evers *et al.*, 2002;
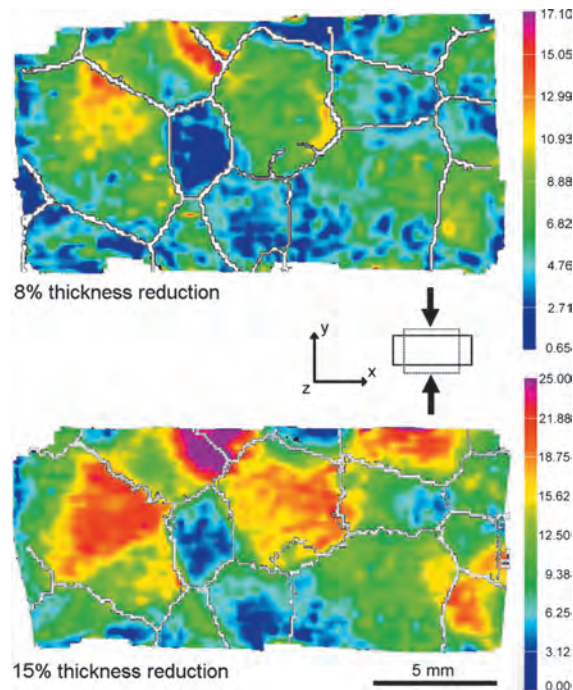
Figure 1.6 Experimental example of the heterogeneity of plastic deformation at the grain and subgrain scale using an aluminum oligocrystal with large columnar grains (Sachtleber, Zhao, and Raabe, 2002). The images show the distribution of the accumulated von Mises equivalent strain in a specimen after $\Delta\gamma/\gamma_0 = 8$ and 15% thickness reduction in plane strain (γ_0 is the initial sample height). The experiment was conducted in a lubricated channel-die setup. White lines indicate high-angle grain boundaries derived from electron backscatter diffraction microtexture measurements. The equivalent strains (determined using digital image correlation) differ across some of the grain boundaries by a factor of 4–5, giving evidence of the enormous orientation-dependent heterogeneity of plasticity even in pure metals.

Ma and Roters, 2004; Ma, Roters, and Raabe, 2006a,b). In this context it should be emphasized that the finite element method itself is not the actual model but the variational solver for the underlying constitutive equations. Since its first introduction by Peirce *et al.* (1982), the CPFE method has matured into a whole family of constitutive and numerical formulations which have been applied to a broad variety of crystal mechanical problems. See Table 1.1 for examples and Roters *et al.* (2010) for a recent review.

In this book we give an overview of this exiting simulation method. In Part One we introduce the fundamentals of the approach by briefly reiterating the basics of the underlying metallurgical mechanisms, of continuum mechanics, and of the finite element method.

Subsequently, in Part Two, we discuss the details of classical and more advanced dislocation-based constitutive models which are currently used in this field. In this

Table 1.1 Some examples for different applications of the crystal plasticity finite element (CPFE) method.

Application of the CPFE method	References
Forming, deep drawing, process modeling, cup drawing, springback, earing, wire drawing, extrusion, anisotropy, design	Beaudoin *et al.* (1993), Beaudoin *et al.* (1994), Neale (1993), Kalidindi and Schoenfeld (2000), Nakamachi, Xie, and Harimoto (2001), Zhao *et al.* (2001), Xie and Nakamachi (2002), Raabe *et al.* (2002a) McGarry *et al.* (2004), Raabe and Roters (2004), Zhao *et al.* (2004a), Tugcu *et al.* (2004), Delannay *et al.* (2005), Li, Kalidindi, and Beyerlein (2005), Raabe, Wang, and Roters (2005), Tikhovskiy, Raabe, and Roters (2006), Delannay, Jacques, and Kalidindi (2006), Chen, Lee, and To (2007), Raabe (2007), Nakamachi, Tam, and Morimoto (2007), Ocenasek *et al.* (2007), Tikhovskiy, Raabe, and Roters (2007), Li, Donohue, and Kalidindi (2008c), Li *et al.* (2008b), Zhuang *et al.* (2008), Delannay *et al.* (2009), Zamiri, Bieler, and Pourboghrat (2009)
Surface roughening, ridging, roping, thin-film mechanics	Becker (1998), Raabe *et al.* (2003), Zhao, Radovitzky, and Cuitino (2004b), Yue (2005), Siska, Forest, and Gumbsch (2007), Zhao *et al.* (2008)
Damage, fatigue, cyclic loading, void growth, fretting	Bruzzi *et al.* (2001), Turkmen, Dawson, and Miller (2002), Goh, Neu, and McDowell (2003), Turkmen *et al.* (2003), Kysar, Gan, and Mendez-Arzuza (2005), Dick and Cailletaud (2006), Sinha and Ghosh (2006), Potirniche *et al.* (2006), Zhang and McDowell (2007), Cheong, Smillie, and Knowles (2007), Dunne, Walker, and Rugg (2007a), Liu *et al.* (2007), Bieler *et al.* (2009), Kumar *et al.* (2008), Mayeur, McDowell, and Neu (2008), Patil *et al.* (2008), Watanabe *et al.* (2008), McDowell (2008), Mayama, Sasaki, and Kuroda (2008), Borg, Niordson, and Kysar (2008)
Creep, high-temperature deformation, diffusion mechanisms	McHugh and Mohrmann (1997) Balasubramanian and Anand (2002), Hasija *et al.* (2003), Bower and Wininger (2004), Venkatramani, Ghosh, and Mills (2007), Agarwal *et al.* (2007), Venkataramani, Kirane, and Ghosh (2008), Xu *et al.* (2009)
Nanoindentation, pillar testing, microbending, microscale deformation, miniaturized mechanical testing	Wang *et al.* (2004), Zaafarani *et al.* (2006), You *et al.* (2006), Raabe, Ma, and Roters (2007a), Casals, Ocenasek, and Alcala (2007), Zaafarani *et al.* (2008), Alcala, Casals, and Ocenasek (2008), Weber *et al.* (2008), Xu *et al.* (2009), Demir *et al.* (2009)

Table 1.1 Some examples . . . (continued).

Application of the CPFE method	References
Grain boundary mechanics, Hall–Petch behavior, grain interaction, grain size effects, strain gradient effects, nonlocal formulations, interface mechanics, superplasticity	Becker and Panchanadeeswaran (1995) Mika and Dawson (1998), Acharya and Beaudoin (2000), Meissonnier, Busso, and O'Dowd (2001) Barbe *et al.* (2001), Raabe *et al.* (2001), Evers *et al.* (2002), Park *et al.* (2002), Clarke, Humphreys, and Bate (2003), Wei and Anand (2004), Fu, Benson, and Meyers (2004), Evers, Brekelmans, and Geers (2004a), Evers, Brekelmans, and Geers (2004b), Diard *et al.* (2005), Bate and Hutchinson (2005), Wei, Su, and Anand (2006), Murphy *et al.* (2006), Deka *et al.* (2006), Ma, Roters, and Raabe (2006a), Ma, Roters, and Raabe (2006b), Counts *et al.* (2008a), Gurtin, Anand, and Lele (2007), Venkatramani, Ghosh, and Mills (2007), Okumura *et al.* (2007), Gerken and Dawson (2008b), Gerken and Dawson (2008a), Kuroda and Tvergaard (2008a), Bitzek *et al.* (2008), Borg, Niordson, and Kysar (2008), Li *et al.* (2009)
In-grain texture formation, grain-scale mechanics, mesoscale, nonuniform deformation, texture evolution, texture stability, anisotropy	Peirce *et al.* (1982), Peirce, Asaro, and Needleman (1983), Asaro and Needleman (1985) Becker (1991), Becker *et al.* (1991), Bronkhorst, Kalidindi, and Anand (1992), Kalidindi, Bronkhorst, and Anand (1992), Beaudoin *et al.* (1995), Becker and Panchanadeeswaran (1995), Beaudoin, Mecking, and Kocks (1996), Beaudoin, Mecking, and Kocks (1996), Sarma and Dawson (1996b), Sarma and Dawson (1996a), Bertram, Böhlke, and Kraska (1997), Mika and Dawson (1998), Sarma, Radhakrishnan, and Zacharia (1998), Forest (1998), Mika and Dawson (1999), Miehe, Schröder, and Schotte (1999), Bhattacharyya *et al.* (2001), Raabe *et al.* (2001), Miller and Turner (2001), Kalidindi (2001), Balasubramanian and Anand (2002), Van Houtte, Delannay, and Kalidindi (2002), Delannay, Kalidindi, and Van Houtte (2002), Raabe, Zhao, and Mao (2002b), Raabe *et al.* (2002c) Sachtleber, Zhao, and Raabe (2002), Kim and Oh (2003), Clarke, Humphreys, and Bate (2003), Choi (2003), Zaefferer *et al.* (2003), Erieau and Rey (2004), Roters *et al.* (2004), Bate and An (2004), Raabe, Zhao, and Roters (2004b), Li, Van Houtte, and Kalidindi (2004), Sarma and Radhakrishnan (2004), Anand (2004), Roters, Jeon-Haurand, and Raabe (2005), Van Houtte *et al.* (2005), Li, Kalidindi, and Beyerlein (2005), Van Houtte *et al.* (2006), Delannay, Jacques, and Kalidindi (2006), Tang *et al.* (2006), Tikhovskiy, Raabe, and Roters (2006), Kim and Oh (2006), Murphy *et al.* (2006), daFonseca *et al.* (2006), You *et al.* (2006), Musienko *et al.* (2007), Han and Dawson (2007), Lee, Wang, and Anderson (2007), Tikhovskiy, Raabe, and Roters (2007), Zhao *et al.* (2008), Mayeur, McDowell, and Neu (2008), Delannay *et al.* (2009) Zhang *et al.* (2009)

Table 1.1 Some examples ... (continued).

Application of the CPFE method	References
Dislocation-based constitutive modeling	Arsenlis and Parks (1999), Arsenlis and Parks (2002), Arsenlis and Tang (2003), Arsenlis *et al.* (2004), Evers *et al.* (2002), Evers, Brekelmans, and Geers (2004b), Cheong and Busso (2004), Ma and Roters (2004), Evers, Brekelmans, and Geers (2004a), Ma, Roters, and Raabe (2006a), Ma, Roters, and Raabe (2006b), McDowell (2008), Li *et al.* (2009)
Deformation twinning	Kalidindi (1998), Staroselsky and Anand (1998), Marketz *et al.* (2002), Staroselskya and Anand (2003), Marketz, Fischer, and Clemens (2003), Salem, Kalidindi, and Semiatin (2005)
Martensite mechanics, phase transformation, shape memory	Marketz and Fischer (1994), Marketz and Fischer (1995), Tomita and Iwamoto (1995), Diani, Sabar, and Berveiller (1995), Diani and Parks (1998), Cherkaoui, Berveiller, and Sabar (1998), Cherkaoui, Berveiller, and Lemoine (2000), Thamburaja and Anand (2001), Tomita and Iwamoto (2001), Govindjee and Miehe (2001), Anand and Gurtin (2003), Turteltaub and Suiker (2005), Thamburaja (2005), Lan *et al.* (2005), Turteltaub and Suiker (2006b), Tjahjanto, Turteltaub, and Suiker (2008), Geers and Kouznetsova (2007),
Multiphase mechanics	Hartig and Mecking (2005), Tjahjanto, Roters, and Eisenlohr (2007), Mayeur, McDowell, and Neu (2008), Inal, Simha, and Mishra (2008), Vogler and Clayton (2008)
Crystal plasticity and recrystallization	Bate (1999), Raabe and Becker (2000), Raabe (2000), Radhakrishnan *et al.* (2000), Raabe (2002), Takaki *et al.* (2007), Raabe (2007), Semiatin *et al.* (2007), Zambaldi *et al.* (2007), Loge *et al.* (2008)
Numerical aspects, finite element shape effects, mesh dependence, accuracy, robust integration methods, texture discretization	Miehe (1996), Bachu and Kalidindi (1998), Harewood and McHugh (2006), Amirkhizi and Nemat-Nasser (2007), Harewood and McHugh (2007), Kuchnicki, Cuitino, and Radovitzky (2006), Melchior and Delannay (2006), Zhao *et al.* (2007), Li, Yang, Sun (2008a), Eisenlohr and Roters (2008), Ritz and Dawson (2009), Barton *et al.* (2004), Gerken and Dawson (2008b)

context we explain the representation of dislocation slip, displacive transformations such as martensite formation and mechanical twinning, and the failure mechanism within such a variational framework. Also, we address homogenization and numerical aspects associated with the finite element solution of crystal plasticity problems.

Finally, Part Three presents a number of microscopic, mesoscopic, and macroscopic applications from the field of CPFE modeling.

Part One   Fundamentals

2
Metallurgical Fundamentals of Plastic Deformation

2.1
Introduction

One of the most essential aspects of microstructures is that although their evolution direction is prescribed by thermodynamic potentials and their gradients, the selection of the actual evolution path is strongly determined by kinetics.

This means that microstructures form on thermodynamic transients and as a rule not in full thermodynamic equilibrium. It is this strong influence of thermodynamic nonequilibrium mechanisms that entails the large variety and complexity of microstructures typically encountered in engineering materials. Frequently, microstructures that correspond to a highly nonequilibrium state provide particularly advantageous material property profiles (see Figure 2.1).
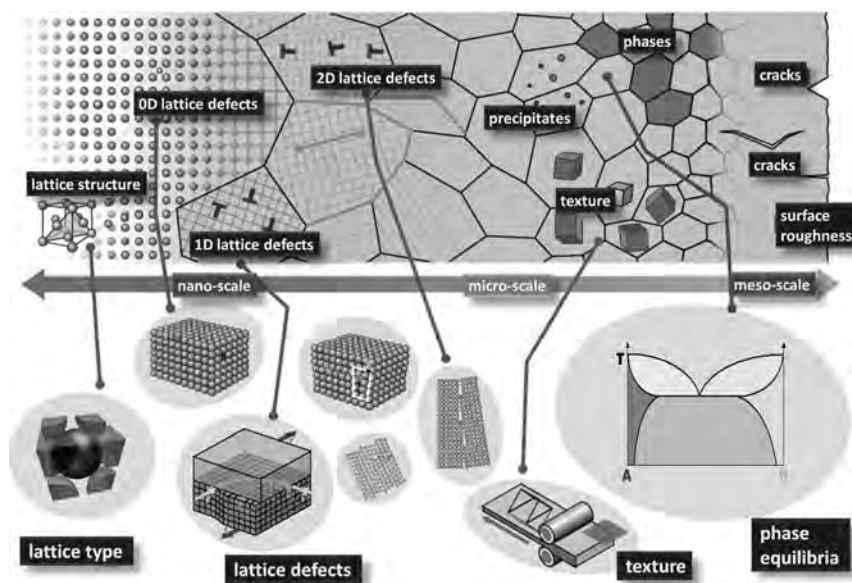
Figure 2.1 Some of the important scales and lattice defects in metallurgical engineering.
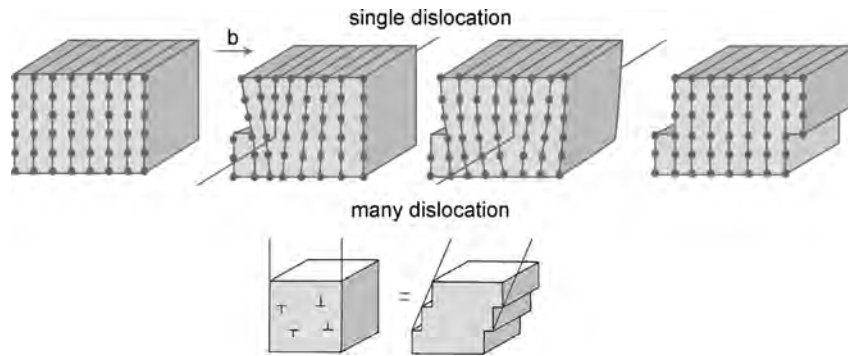
Figure 2.2 Edge dislocation and its effect on crystallographic shear.

This book is concerned with those microstructural defects that contribute to the elastic-plastic deformation of metals. Plastic deformation at ambient temperature occurs in crystalline metals mainly through dislocations, martensite formation, and mechanical twinning. In this context dislocations are the most important lattice defects and they are usually the main carriers of plastic deformation (see Figure 2.2).

Mechanical twinning and martensite formation are referred to as displacive deformation mechanisms and they typically contribute less to the plastic shape changes than do dislocations but have a large impact on hardening and flow stress.

2.2
Lattice Dislocations

Dislocations are linear crystallographic defects within the otherwise regular crystal structure. They are geometrically described by the line tangential vector and the *Burgers vector* (shear vector). There are the two extreme cases of a *screw dislocation*, where the tangential and the Burgers vector coincide, and the *edge dislocation*, where they are perpendicular to each other, see Figure 2.3. Mixed dislocations are intermediate between these. Dislocations found in real materials are typically of mixed kind. Two dislocations of opposite orientation, when brought together, can cancel each other (referred to as *annihilation*), but a single dislocation cannot disappear on its own except when reaching a free surface.

Simple edge dislocations can be described as being caused by the termination of a plane of atoms in the middle of a crystal, as illustrated in Figure 2.4a,b. In such a case, the surrounding planes are not straight, but instead bend around the edge of the terminating plane. When enough force is applied, this extra plane passes through planes of atoms, breaking and joining bonds. This means that the dislocation moves and thereby shears the crystal.

The distortion of the atoms surrounding dislocations lead to characteristic strain and stress fields through which the dislocations interact strongly with each other
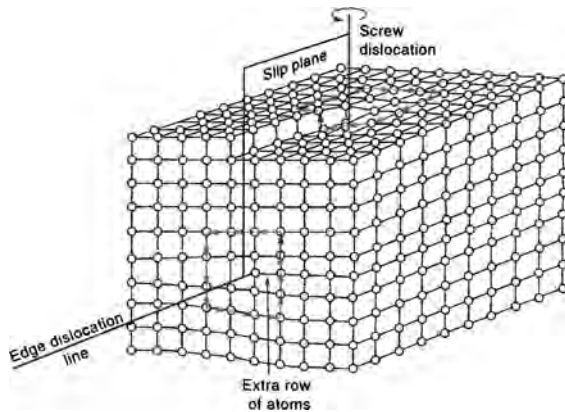
Figure 2.3 The vectors that characterize the geometry of edge and screw dislocations.

(a)

(b)
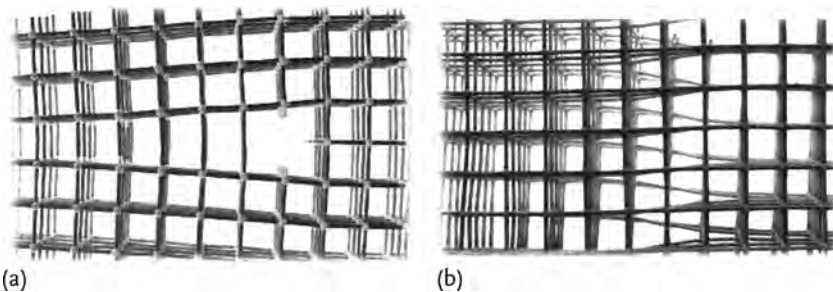
Figure 2.4 Scale images of lattice distortion due to dislocations. (a) View along the line direction of an edge dislocation (i. e., onto the left face in Figure 2.3). (b) View normal to the glide plane of a screw dislocation (i. e., onto the right face in Figure 2.3). The dislocation line runs vertically along the center of the image.

and with other externally or internally imposed elastic fields. The strain and stress fields are different for screw and edge dislocations. Figure 2.5a,b shows two[1] of the three Volterra distortions. The displacement types presented here (shear parallel to the dislocation line: screw dislocation; shear perpendicular to the dislocation line: edge dislocation) indicate the distortions of an initially perfect continuum cylinder. The elastic stresses associated with them describe the elastic fields of ideal edge and screw dislocations, respectively, outside their cores.

The equation for two-dimensional edge dislocations (with an infinite extension of the dislocation line) can be derived by solving the compatibility equations for plane-strain conditions under consideration of force equilibrium according to Volterra (1907). The plane-strain state describes a situation where all particles of a body are displaced parallel to an arbitrary plane, and the displacements are independent of their coordinate parallel to the plane normal. For an infinite edge dislocation with its Burgers vector parallel to the first coordinate axis $\mathbf{e}_1$ and tangent vector parallel

1) $b \parallel x$ and $b \parallel z$
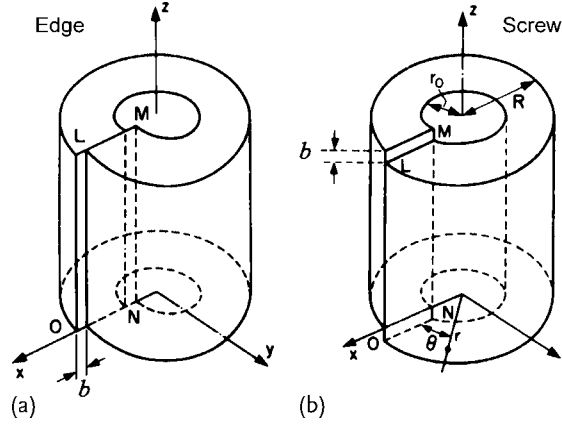
Figure 2.5 Two of the three Volterra distortions. The displacement types of an initially perfect cylinder and the elastic stresses associated with them describe the elastic fields of ideal edge (a) and screw (b) dislocations, respectively, outside their cores.

to the third coordinate axis $\mathbf{e}_3$, the stress field is

$$\sigma_{11} = -\frac{\mu b}{2\pi(1-\nu)} \frac{x_2\left(3x_1^2 + x_2^2\right)}{\left(x_1^2 + x_2^2\right)^2} , \tag{2.1a}$$

$$\sigma_{22} = \frac{\mu b}{2\pi(1-\nu)} \frac{x_2\left(x_1^2 - x_2^2\right)}{\left(x_1^2 + x_2^2\right)^2} , \tag{2.1b}$$

$$\sigma_{12} = \frac{\mu b}{2\pi(1-\nu)} \frac{x_1\left(x_1^2 - x_2^2\right)}{\left(x_1^2 + x_2^2\right)^2} , \tag{2.1c}$$

$$\sigma_{33} = \nu(\sigma_{11} + \sigma_{22}) = -\frac{\mu b\nu}{\pi(1-\nu)} \frac{x_2}{x_1^2 + x_2^2} . \tag{2.1d}$$

The strain field is readily obtained by using *Hooke's law*.

For an infinite screw dislocation with its Burgers vector and tangent vector parallel to $\mathbf{e}_3$ the stress field is given by

$$\sigma_{13} = \sigma_{31} = -\frac{\mu b}{2\pi} \frac{x_2}{x_1^2 + x_2^2} , \tag{2.2a}$$

$$\sigma_{23} = \sigma_{32} = \frac{\mu b}{2\pi} \frac{x_1}{x_1^2 + x_2^2} . \tag{2.2b}$$

In Eqs. (2.1) and (2.2) σ_{ij} denotes the stress field, μ is the shear modulus, and ν is the Poisson ratio. These eigenstress fields introduced by dislocations into the metallic lattice can lead to pronounced interactions among them promoting structure formation (e.g. dislocation cells), see Figure 2.6.

In real crystals dislocations usually slip on densely packed planes containing both the dislocation line and the Burgers vector. The Burgers vector is usually along a densely packed crystallographic direction, as illustrated in Figure 2.7. Using densely packed planes and the shortest possible translational shear vectors minimizes the elastic energy and the Peierls barrier of the defect.
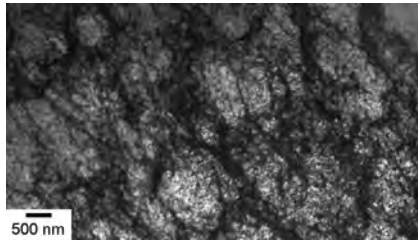
Figure 2.6 Bright-field transmission electron microscope image of dislocations in a face-centered cubic Fe–Mn steel. The image reveals that dislocations tend to self-organize and arrange in cell structures provided that the stacking fault energy and the temperature are not too low.
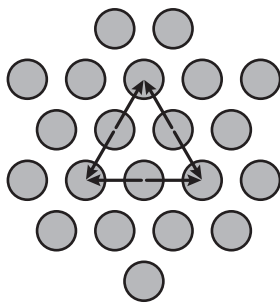
Figure 2.7 Close-packed lattice plane ($\{111\}$ in face-centered cubic, or $\{0\,0\,0\,1\}$ in hexagonal crystals) with arrows indicating the six lattice-invariant displacement (Burgers) vectors (corresponding to $\langle 110 \rangle$ in fcc and $\langle 11\text{-}20 \rangle$ in hex).

For a screw dislocation, the dislocation line direction and the Burgers vector are parallel; hence, the dislocation can slip in any plane containing the dislocation. For an edge dislocation, the dislocation line direction and the Burgers vector are perpendicular, so there is only one plane in which the dislocation can slip. There is an alternative mechanism of dislocation motion, fundamentally different from slip, that allows an edge dislocation to move out of its slip plane, known as dislocation climb. Dislocation climb allows an edge dislocation to move perpendicular to its slip plane. However, this mechanism is nonconservative as it requires the diffusion of point defects through the crystal lattice. If a vacancy moves next to the boundary of the extra half plane of atoms that forms an edge dislocation, the atom in the half plane closest to the vacancy can jump and fill that vacancy. This atom shift moves the vacancy in line with the half plane of atoms, causing a shift, or positive climb, of the dislocation. The process of a vacancy being absorbed at the rim of a half plane of atoms, rather than being created, is referred to as negative climb. A main difference between dislocation slip and climb is the temperature dependence. Climb occurs much more rapidly at high homologous temperatures than at low temperatures owing to an increase in vacancy density and motion. Slip, on the other hand, has a weaker dependence on temperature and prevails for most metals at room temperature.

The dislocation density in a material is increased by plastic deformation through dislocation storage, bow out, and multiplication. Their mutual interaction stress and cutting processes increase the overall flow stress of metallic crystals usual-

ly observed during plastic straining in a regime below about 0.3 of their absolute melting temperature. This effect is referred to as strain hardening. Tangles of dislocations are found at the early stage of deformation and appear as non-well-defined boundaries. The process of dynamic recovery leads eventually to the formation of a cellular structure containing boundaries with misorientations that usually do not exceed a few degrees.

Adding pinning points that inhibit the motion of dislocations, such as solute alloying elements and additional interfaces (from second phases or grain boundaries), can introduce stress fields that ultimately strengthen the material by requiring a higher applied stress to overcome the pinning stress and continue dislocation motion and multiplication. The effects of strain hardening by accumulation of dislocations and the grain structure formed at high strain can be removed by appropriate heat treatment (annealing) which promotes the recovery and subsequent recrystallization of the material. The combined processing techniques of work hardening and annealing allow for control over dislocation density, the degree of dislocation entanglement, and ultimately the yield strength of the material.

2.3
Deformation Martensite and Mechanical Twinning

Martensitic transformations are characterized by a diffusionless change in the crystal lattice structure. This applies not only to thermally induced martensite formation, but also to deformation-induced formation. It is important to note that the shift of the atom positions relative to their former parent phase breaks the translational symmetry (in contrast to dislocation slip), that is, the transformation creates a new crystallographic orientation variant. Hence, the martensitic transformation involves a definite orientation relationship with the parent phase (matrix) because the atoms shift their positions in a coordinated manner. Possible orientation relationships of this kind were described by Kurdjumov and Sachs (1930), Nishiyama (1934), and Wassermann (1935) in the 1930s. In both models the {110} planes of the martensite are parallel to the {111} planes of the parent austenite. In the description of Kurdjumov and Sachs a ⟨111⟩ direction in the martensite coincides with a ⟨110⟩ direction in the austenite. In the description of Nishiyama and Wassermann a ⟨110⟩ direction in the martensite coincides with a ⟨112⟩ direction in the austenite.

There is always a change in shape, which means that there is a strain associated with the transformation. As in mechanical twinning, there is an invariant plane. Different from mechanical twinning the martensitic transformation may also involve volume changes which occur normal to the invariant plane. More specifically, the overall shape change created by the martensitic transformation can be approximated by a simple shear parallel to the habit plane, which is the common and thus coherent plane between the phases, and a uniaxial expansion normal to that habit plane. Deformation-induced martensitic transformations rarely go to completion as it becomes increasingly difficult during deformation to render the residual
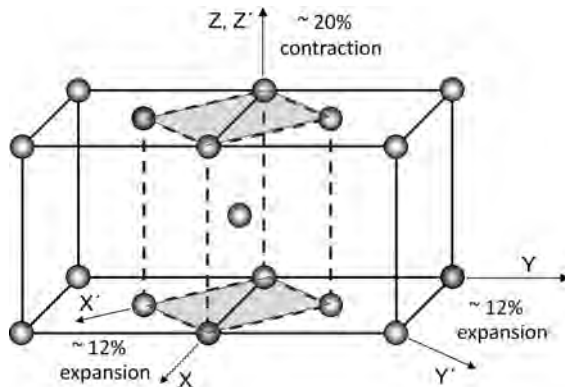
Figure 2.8 Bain model explaining the transformation from the face-centered cubic parent phase (austenite) into the body-centered cubic phase through the compression of the austenitic longitudinal axis and the extension of the two basal axes.

austenite into martensite against the increasing internal stresses that the preceding transformations created.

For the case of face-centered cubic iron transforming to body-centered cubic ferrite (or to tetragonal martensite as in the case of additional interstitial atoms in the iron such as carbon) the *Bain model* provides a simple model for the structural transformation with a minimum of atomic motion, see Figure 2.8. Martensitic transformations cause enormous strains. To minimize the overall mismatch, the martensite and the surrounding matrix often undergo massive dislocation deformation and/or deformation twinning as possible accommodation processes.

Deformation-induced twinning (which is referred to as mechanical twinning) and deformation-induced martensite formation are displacive transformation phenomena. This means that they form through a coordinated motion of atoms without diffusional steps being involved. Mechanical twinning has taken place when two separate crystals share some of the same crystal lattice points in a symmetric manner after straining. The process involves a collective displacement which leads to the reorientation of the sheared material portion relative to the parent material into a mirror configuration. A twin shear system is defined by a twin plane and a twin direction (the shear direction of the process). As deformation-induced twinning is typically constrained by the neighboring material, mechanical twins often form thin zones to reduce the mismatch with the matrix material (see Figure 2.9).

Mechanical twinning occurs preferentially at low temperatures, in coarse-grained polycrystals, and at high strain rates. As the formation of mechanical twins (nucleation phase) is associated with grain boundaries and existing stacking faults, materials with a low stacking fault energy have a higher tendency to form twins. The shear created by a deformation twin can often also be described by the collective motion of partial dislocations on neighboring crystallographic planes. The formation of partial dislocations requires a low stacking fault energy. The latter energy is an important measure in dislocation and twinning plasticity. The
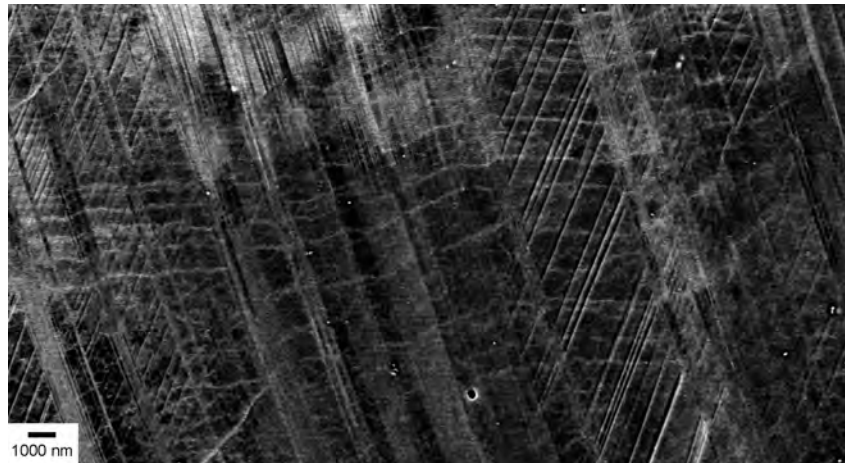
Figure 2.9 Electron channeling contrast image in a scanning electron microscope showing massive mechanical twinning in a face-centered cubic Fe–Mn steel.

face-centered cubic lattice can be built by a stacking sequence of {111} planes. In a perfect lattice three subsequent positions A, B, and C are occupied by the {111} planes. In the case of a stacking fault or twinning process, the stacking sequence is changed, thus rendering the structure locally a hexagonal lattice structure with a stacking sequence A, B of {111} planes. This local transition is associated with a penalty energy, which is referred to as stacking fault energy. Metals with a low stacking fault energy such as austenitic steels or brass have a higher tendency to form partial dislocations and twins than metals with a high stacking fault energy such as aluminum.

Although the total amount of shear that deformation twins contribute during polycrystal straining is not very high compared with dislocation shear, deformation twins play an important role in texture evolution and grain refinement. The first point is obvious since deformation twins discontinuously change the crystallographic orientation. The second point is due to the fact the spontaneous orientation change is larger than 15 degrees, so twin interfaces represent high-angle grain boundaries. Also, it is essential to note that mechanical twinning is an important deformation mode when there are not sufficient slip systems to accommodate an imposed deformation state.

3
Continuum Mechanics

This chapter recalls basic concepts of solid mechanics to the extent necessary for the purpose of this book. The interested reader is referred to more exhaustive treatments of this matter, which can be found, for instance, in Bower (2010); Chadwick (1999); Jirásek and Bazant (2002). Here we restrict ourselves to outlining the essential aspects of kinematics, the static equilibrium, and the thermodynamic dissipation in solid matter.

3.1
Kinematics

The term *kinematics* refers to the study of (typically position-dependent) displacements and, if considering time dependence, motions of a material body without explicitly asking about the forces that are causing them.

3.1.1
Material Points and Configurations

Consider an infinite number of particles, also termed *material points*, aggregated into a deformable body (or *continuum*). This body shall occupy the regions $\mathcal{B}_0$ and $\mathcal{B}$, bound by the surfaces $\mathcal{S}_0$ and $\mathcal{S}$, in three-dimensional space $\mathbb{R}^3$ at two different times t_0 and t, respectively. We term $\mathcal{B}_0$ the *undeformed configuration* and $\mathcal{B}$ the *deformed configuration*.[2] Locations of material points in the undeformed (or *reference*) configuration are given by their position vector $\mathbf{x}$, whereas those in the deformed (or *current*) configuration are denoted by $\mathbf{y}$ (see Figure 3.1). Thus, the displacement occurring between both configurations is given by $\mathbf{u} = \mathbf{y} - \mathbf{x}$ and is required/set to be a smooth function of the position of the material point. Equivalently, one defines

---

[2] This terminology differs from the one proposed by Noll (1972), which used *placement* instead and reserved *configuration* for the *class* of placements that differ only by a rigid-body rotation. However, we follow the main body of literature on the current subject and call each particular placement a configuration.
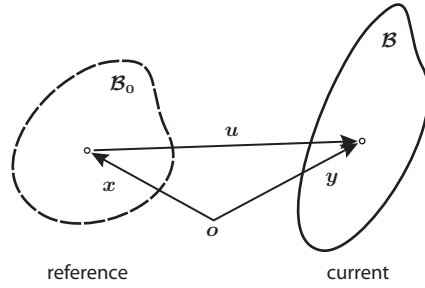
reference   current

Figure 3.1 Deformable body (continuum) occupying region $\mathcal{B}_0$ in the reference configuration and region $\mathcal{B}$ in the current (or deformed) configuration. The positions of material points are, respectively, denoted by **x** and **y**. The spatial heterogeneity of displacement **u** entails a deformation (or just a rotation in special cases).

a mapping

$$\mathbf{y}(\mathbf{x}) : \mathbf{x} \in \mathcal{B}_0 \longmapsto \mathbf{y} \in \mathcal{B} , \tag{3.1}$$

which translates material points from the reference into the current configuration and which is continuously differentiable with respect to position.

3.1.2
Deformation Gradient

Figure 3.2 presents the infinitesimal neighborhood of an arbitrary material point (small circle in Figure 3.1) within the body in both the reference and the current configurations. To establish the deformation experienced by a material line segment d**x** emanating from material point **x** in the reference configuration, we locally expand the mapping given in Eq. (3.1) into a Taylor series and truncate at first order:

$$\mathbf{y} + \mathrm{d}\mathbf{y} = \mathbf{y}(\mathbf{x}) + \frac{\partial \mathbf{y}}{\partial \mathbf{x}} \, \mathrm{d}\mathbf{x} + \mathcal{O}(\mathrm{d}\mathbf{x}^2) ,$$

$$\mathrm{d}\mathbf{y} = \frac{\partial \mathbf{y}}{\partial \mathbf{x}} \, \mathrm{d}\mathbf{x} = \mathbf{F} \, \mathrm{d}\mathbf{x} . \tag{3.2}$$

From Eq. (3.2) we observe that material lines are homogeneously mapped by the second-rank tensor **F**, called *deformation gradient*, which is given by the partial differential of the material point coordinates in the current configuration with respect to the reference configuration:

$$\mathbf{F} = \frac{\partial \mathbf{y}}{\partial \mathbf{x}} = \mathrm{Grad}\,\mathbf{y} \quad \text{or}$$

$$F_{ij} = \partial y_i / \partial x_j \quad \text{in Cartesian components} . \tag{3.3}$$

Note that deformation gradients are a *locally* defined quantity and thus typically vary with position. Hence, **F** is only a valid characterization of the deformation
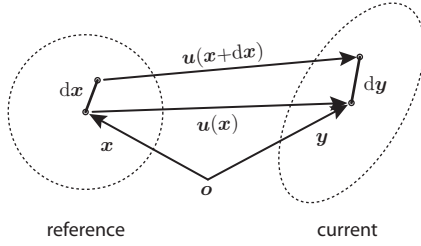
Figure 3.2 Infinitesimal neighborhood around a material point in the reference configuration (at position **x**) and in the current configuration (then at position **y**). The material line segment dx is transformed into dy. A gradient in **y(x)**, which is a consequence of a gradient in the displacement **u(x)**, results in deformation of dx.

outside the infinitesimal neighborhood illustrated in Figure 3.2 in the case of homogeneous (i. e., spatially invariant) deformations.

The inverse of the deformation gradient, denoted by $\mathbf{F}^{-1}$ and defined as $\mathbf{F}^{-1} = \operatorname{grad}\mathbf{x} \iff F_{ij}^{-1} = \partial x_i/\partial y_j$, consequently maps from the current configuration back into the reference configuration.

To map general second-rank tensorial quantities **A** between the reference (subscript "0") and current configurations, the terms *push forward* and *pull back* are employed and refer, respectively, to the operations

$$\mathbf{A} = \mathbf{F}\mathbf{A}_0\mathbf{F}^{-1} , \tag{3.4}$$

$$\mathbf{A}_0 = \mathbf{F}^{-1}\mathbf{A}\,\mathbf{F} . \tag{3.5}$$

The *Jacobian* of a deformation gradient is defined as

$$J = \det\mathbf{F} = \frac{\mathrm{d}V}{\mathrm{d}V_0} = \frac{\rho_0}{\rho} \tag{3.6}$$

and quantifies the ratio in volume (or inverse ratio in mass densities, ρ and ρ_0) between the current and reference configurations. The proof of Eq. (3.6) is skipped, but it can be easily demonstrated by considering the deformation of an arbitrary parallelepiped due to **F**. Since matter cannot be compressed to zero (or even negative) volume, any physically admissible displacement field fulfills $J > 0$. In the special case of incompressibility, which is usually assumed to be satisfied for plastic deformation, the Jacobian is always $J = 1$.

In addition to volumetric changes it is frequently necessary to evaluate changes in length and angles resulting from a deformation characterized by **F**. To this end, consider the segment $\mathrm{d}\mathbf{x} = \mathrm{d}l_0\,\mathbf{a}$ of a material line in the reference configuration which gets mapped to $\mathrm{d}\mathbf{y} = \mathrm{d}l\,\mathbf{b} = \mathrm{d}l_0\,\mathbf{F}\,\mathbf{a}$ in the current configuration, with **a** and **b** of unit length. Invoking the scalar product, we find

$$\mathrm{d}\mathbf{y} \cdot \mathrm{d}\mathbf{y} = \mathbf{F}\,\mathrm{d}\mathbf{x} \cdot \mathbf{F}\,\mathrm{d}\mathbf{x},$$

$$\left(\frac{\mathrm{d}l}{\mathrm{d}l_0}\right)^2 = \mathbf{F}\,\mathbf{a} \cdot \mathbf{F}\,\mathbf{a} = \mathbf{a} \cdot \mathbf{F}^\mathrm{T}\mathbf{F}\,\mathbf{a} = \mathbf{a} \cdot \mathbf{C}\,\mathbf{a} = \lambda^2 . \tag{3.7}$$

Thus, the symmetric tensor

$$\mathbf{C} := \mathbf{F}^{\mathrm{T}}\mathbf{F} = \mathbf{F}^{\mathrm{T}}(\mathbf{F}^{\mathrm{T}})^{\mathrm{T}} = (\mathbf{F}^{\mathrm{T}}\mathbf{F})^{\mathrm{T}} = \mathbf{C}^{\mathrm{T}} \,, \tag{3.8}$$

termed *right Cauchy–Green deformation tensor*, characterizes the stretch λ that a material line along $\mathbf{a}$ experiences. Similarly, knowing the directions $\mathbf{a}_1$ and $\mathbf{a}_2$ and corresponding stretches (from Eq. (3.7)) of two infinitesimal line segments in the reference configuration, we can derive the angle θ between them in the current configuration from

$$\lambda_1 \lambda_2 \cos \theta = \mathbf{a}_1 \cdot \mathbf{C}\,\mathbf{a}_2 \,. \tag{3.9}$$

Since $\mathbf{C}$ is symmetric and positive-definite, all its eigenvalues μ_1, μ_2, and μ_3 are real and positive and the corresponding (unit-length) eigenvectors $\mathbf{n}_1$, $\mathbf{n}_2$, and $\mathbf{n}_3$ form an orthonormal basis. Therefore, we have the spectral decomposition

$$\mathbf{C} = \sum_{i=1}^{3} \mu_i \mathbf{n}_i \otimes \mathbf{n}_i \,. \tag{3.10}$$

Using Eq. (3.7) to calculate the stretches λ_i for material lines aligned with the unit eigenvectors $\mathbf{n}_i$ yields $\mu_i = \lambda_i^{\,2}$, that is, the eigenvalues of $\mathbf{C}$ are the squares of the principal stretches associated with the principal directions $\mathbf{n}_i$. Thus, we can introduce the (symmetric and positive-definite) *right stretch tensor*:

$$\mathbf{U} = \sum_{i=1}^{3} \lambda_i \mathbf{n}_i \otimes \mathbf{n}_i \quad \text{such that} \quad \mathbf{U}\mathbf{U} = \mathbf{U}^2 = \mathbf{C} \,, \tag{3.11}$$

which has the same principal directions as $\mathbf{C}$ but its eigenvalues are the square roots of those of $\mathbf{C}$.

3.1.3
Polar Decomposition

The polar decomposition theorem states that any invertible tensor $\mathbf{F}$ can be uniquely expressed by two alternative (multiplicatively decomposed) forms:

$$\mathbf{F} = \mathbf{R}\mathbf{U} = \mathbf{V}\mathbf{R} \,, \tag{3.12}$$

with $\mathbf{R}$ being a proper orthogonal (i. e., rotation) tensor, and $\mathbf{U}$ and $\mathbf{V}$ being positive-definite symmetric tensors. It is straightforward to demonstrate that $\mathbf{C} = \mathbf{F}^{\mathrm{T}}\mathbf{F} = (\mathbf{R}\mathbf{U})^{\mathrm{T}}(\mathbf{R}\mathbf{U}) = \mathbf{U}^{\mathrm{T}}\mathbf{R}^{\mathrm{T}}\mathbf{R}\mathbf{U} = \mathbf{U}^{\mathrm{T}}\mathbf{U} = \mathbf{U}^2$. Hence, $\mathbf{U}$ resulting from the polar decomposition of the deformation gradient is equivalent to the right stretch tensor defined in Eq. (3.11). A similar argument leads to an equivalent relation between $\mathbf{V}$, termed *left stretch tensor*, and the *left Cauchy–Green deformation tensor* $\mathbf{B} = \mathbf{F}\mathbf{F}^{\mathrm{T}}$. For a more exhaustive treatment of $\mathbf{B}$ the reader is referred to standard treatises on continuum mechanics.

The polar decomposition can, thus, be understood in terms of separating the overall deformation into pure stretching $\mathbf{U}$ along the principal directions $\mathbf{n}_i$ fol-

lowed by rigid-body rotation $\mathbf{R}$. The alternative form $\mathbf{F} = \mathbf{VR}$ now simply exchanges this order of operations such that, first, a rotation $\mathbf{R}$ is performed and, second, pure stretching $\mathbf{V} = \mathbf{R}\mathbf{U}\mathbf{R}^{\mathrm{T}}$ along the now rotated principal directions $\mathbf{R}\,\mathbf{n}_i$ follows.

3.1.4
Strain Measures

The deformation gradient introduced in Eq. (3.3) can be equivalently expressed in terms of the *displacement gradient* $\partial\mathbf{u}/\partial\mathbf{x}$ as follows:

$$
\begin{aligned}
\mathbf{F} = \frac{\partial\mathbf{y}}{\partial\mathbf{x}} &= \frac{\partial(\mathbf{x} + \mathbf{u})}{\partial\mathbf{x}} \\
&= \mathbf{I} + \frac{\partial\mathbf{u}}{\partial\mathbf{x}} \\
&= \mathbf{I} + \frac{1}{2}\left[\frac{\partial\mathbf{u}}{\partial\mathbf{x}} + \left(\frac{\partial\mathbf{u}}{\partial\mathbf{x}}\right)^{\mathrm{T}}\right] + \frac{1}{2}\left[\frac{\partial\mathbf{u}}{\partial\mathbf{x}} - \left(\frac{\partial\mathbf{u}}{\partial\mathbf{x}}\right)^{\mathrm{T}}\right] \\
&= \mathbf{I} + \left(\frac{\partial\mathbf{u}}{\partial\mathbf{x}}\right)_{\mathrm{sym}} + \left(\frac{\partial\mathbf{u}}{\partial\mathbf{x}}\right)_{\mathrm{skew}}
\end{aligned}
\tag{3.13}
$$

$$
= \mathbf{I} + \varepsilon + \omega \;, \tag{3.14}
$$

where the symmetric part, ε, and skew-symmetric part, ω, of the displacement gradient correspond to the (small) strain and (small) rotation derived in the framework of infinitesimal displacements usually known from, for instance, basic courses on material strength. A relation between the infinitesimal and finite strain framework can be seen by substituting Eq. (3.13) into the right Cauchy–Green deformation tensor (Eq. (3.8)) and neglecting terms of quadratic order:

$$
\begin{aligned}
\mathbf{C} = \mathbf{F}^{\mathrm{T}}\mathbf{F} &= \left(\mathbf{I} + \frac{\partial\mathbf{u}}{\partial\mathbf{x}}\right)\left(\mathbf{I} + \frac{\partial\mathbf{u}}{\partial\mathbf{x}}\right)^{\mathrm{T}} \\
&= \mathbf{I} + \left(\frac{\partial\mathbf{u}}{\partial\mathbf{x}}\right)^{\mathrm{T}} + \frac{\partial\mathbf{u}}{\partial\mathbf{x}} + \left(\frac{\partial\mathbf{u}}{\partial\mathbf{x}}\right)\left(\frac{\partial\mathbf{u}}{\partial\mathbf{x}}\right)^{\mathrm{T}} \\
&\approx \mathbf{I} + 2\varepsilon \;.
\end{aligned}
\tag{3.15}
$$

The corresponding relation for the right stretch tensor, using Eq. (3.11), thus reads

$$
\mathbf{U} = \mathbf{C}^{1/2} \approx \mathbf{I} + \varepsilon \;. \tag{3.16}
$$

From Eqs. (3.15) and (3.16) we can infer the following definitions of strain measures based on the right stretch tensor $\mathbf{U}$:

$$
\mathbf{E}^{(1)} = \mathbf{U} - \mathbf{I} \;, \tag{3.17}
$$

$$
\mathbf{E} = \mathbf{E}^{(2)} = \frac{1}{2}(\mathbf{U}^2 - \mathbf{I}) = \frac{1}{2}(\mathbf{C} - \mathbf{I}) = \frac{1}{2}(\mathbf{F}^{\mathrm{T}}\mathbf{F} - \mathbf{I}) \;, \tag{3.18}
$$

$$
\mathbf{E}^{(m)} = \frac{1}{m}(\mathbf{U}^m - \mathbf{I}) \;. \tag{3.19}
$$

The first measure (Eq. (3.17)) is called *Biot strain* and the second one (Eq. (3.18)) *Green's Lagrangian strain*. Both belong to the more general class of *Doyle–Ericksen strain tensors*, for which $m \neq 0$ in Eq. (3.19). All those strain measures are (necessarily) zero for a vanishing displacement gradient and concur with the small-strain tensor in the limit of infinitesimal displacement gradients. Furthermore, they only depend on the stretch, but not on rigid-body rotation (cf. Section 3.1.3).

3.1.5
Velocity Gradient

A time-dependent displacement, or *motion*, of a body entails a nonzero velocity field, given by the time derivative of the corresponding displacement field:

$$\mathbf{v} = \frac{\mathrm{d}}{\mathrm{d}t}\mathbf{u} = \dot{\mathbf{u}} = \dot{\mathbf{y}} \,. \tag{3.20}$$

Its spatial gradient (that is, with respect to the current configuration),

$$\mathbf{L} = \frac{\partial \mathbf{v}}{\partial \mathbf{y}} = \operatorname{grad} \mathbf{v} \,, \tag{3.21}$$

is termed *velocity gradient* and quantifies the relative velocity between two positions in the current configuration. The relation between the velocity gradient and the rate of change, $\dot{\mathbf{F}}$, of the corresponding deformation gradient can be inferred from the equivalence of the relative change in the velocity of two points separated by $\mathrm{d}\mathbf{y}$ and the rate of change of their relative position:

$$\mathbf{L}\,\mathrm{d}\mathbf{y} = \frac{\partial \mathbf{v}}{\partial \mathbf{y}}\,\mathrm{d}\mathbf{y} \equiv \frac{\mathrm{d}}{\mathrm{d}t}\,\mathrm{d}\mathbf{y} = \frac{\mathrm{d}}{\mathrm{d}t}\,\mathbf{F}\,\mathrm{d}\mathbf{x} = \dot{\mathbf{F}}\,\mathrm{d}\mathbf{x} = \dot{\mathbf{F}}\mathbf{F}^{-1}\mathrm{d}\mathbf{y} \,. \tag{3.22}$$

Comparing the leftmost and rightmost expressions in Eq. (3.22), we find that

$$\mathbf{L} = \dot{\mathbf{F}}\mathbf{F}^{-1} \,. \tag{3.23}$$

The velocity gradient can, as any second-rank tensor, be uniquely decomposed in an additive fashion into a symmetric and a skew-symmetric part,

$$\mathbf{L} = \mathbf{L}_{\mathrm{sym}} + \mathbf{L}_{\mathrm{skew}} = \frac{1}{2}(\mathbf{L} + \mathbf{L}^{\mathrm{T}}) + \frac{1}{2}(\mathbf{L} - \mathbf{L}^{\mathrm{T}}) = \mathbf{D} + \mathbf{W} \,, \tag{3.24}$$

which are termed *stretch rate tensor* and *spin tensor*, respectively. We note that $\mathbf{D}$ describes the instantaneous rate of pure stretching of a material point, whereas $\mathbf{W}$ quantifies its rate of rigid-body rotation . To illustrate this, one may look at the rate of change of Green's Lagrangian strain,

$$\dot{\mathbf{E}} = \frac{1}{2}(\dot{\mathbf{F}}^{\mathrm{T}}\mathbf{F} + \mathbf{F}^{\mathrm{T}}\dot{\mathbf{F}}) = (\mathbf{F}^{\mathrm{T}}\dot{\mathbf{F}})_{\mathrm{sym}}$$

$$= \frac{1}{2}(\mathbf{F}^{\mathrm{T}}\mathbf{L}^{\mathrm{T}}\mathbf{F} + \mathbf{F}^{\mathrm{T}}\mathbf{L}\mathbf{F}) = \mathbf{F}^{\mathrm{T}}\mathbf{D}\mathbf{F} \,, \tag{3.25}$$

which, indeed, does depend only on the symmetric (stretching) part of the velocity gradient.

3.1.6
Elastoplastic Decomposition

In all the kinematic treatments above, there has not been any concern regarding the way by which the material accomplishes the shape change (and possibly rotation) from the reference to the deformed configuration. In this section, the influence of the physical nature of the material in question, here particularly metals, is explored.

We recall that for crystalline matter the underlying lattice can deform by (small) displacements from the equilibrium positions (Figure 3.3a) and by permanent alterations of the local atomic neighborhood owing to displacements, which – when the discussion is restricted to perfect dislocation plasticity – are integer multiples of the nearest-neighbor connection along closest-packed planes. An example of elastic lattice shear is shown in Figure 3.3b. The deformation illustrated can, however, be maintained only if forces are acting on the atoms to displace them from their equilibrium locations. Once those forces are relieved, the shape change is undone, that is, the deformation is reversible in nature. Figure 3.3c illustrates the same overall deformation as shown in the elastic case (Figure 3.3b), but this time in the form of a permanent lattice rearrangement due to the motion of one dislocation through the entire observed volume on the lattice plane indicated. Considering an *isolated* volume which has been *fully* traversed by lattice dislocations, two immediate consequences arise: (1) the translation-invariant kinematics of lattice slip entails that the lattice coordinate system after slipping remains unchanged compared with the nonslipped situation and (2) owing to the retained perfect atomic arrangement the lattice is in a stress-free state despite its plastic shape change. Such plastic deformation is a result of stresses acting on the crystal lattice – actually reducing them – but the presence of those is not essential for the *persistence* of plastic strain. Given the fully unloaded state depicted in Figure 3.3c, only further elastic loading of the lattice, as illustrated in Figure 3.3d, introduces a nonzero stress state similar to that observed in Figure 3.3b.

These notions have led to a multiplicative decomposition of the total deformation gradient (Kröner, 1960; Lee, 1969; Lee and Liu, 1967). It is based on the introduction of a configuration, termed *intermediate* (or *relaxed*, or *lattice*), corresponding to a fictitious state of the material in which each material point is individually unloaded, hence being only deformed plastically, and – as the most convenient case[3] – having its particular lattice coordinate system coincide with the fixed laboratory system (see Figure 3.4). The transformation from the reference configuration to this intermediate configuration hence comprises a rotation (to match both coordinate systems) as well as the flow of material expressed in the constant lattice frame, which are jointly characterized by the *plastic deformation gradient* $\mathbf{F}_p$. The subsequent transformation from the intermediate to the current configuration, corresponding to elastic stretching of the lattice (plus potential rotation), is char-

---

3) Keeping the lattice coordinate system aligned with the fixed laboratory system avoids otherwise necessary transformations to rotate the various tensorial material properties into the intermediate configuration.

(a) unstrained reference

(b) elastic shear only

(c) plastic shear from single
dislocation traversal

(d) combined elasto-plastic
deformation
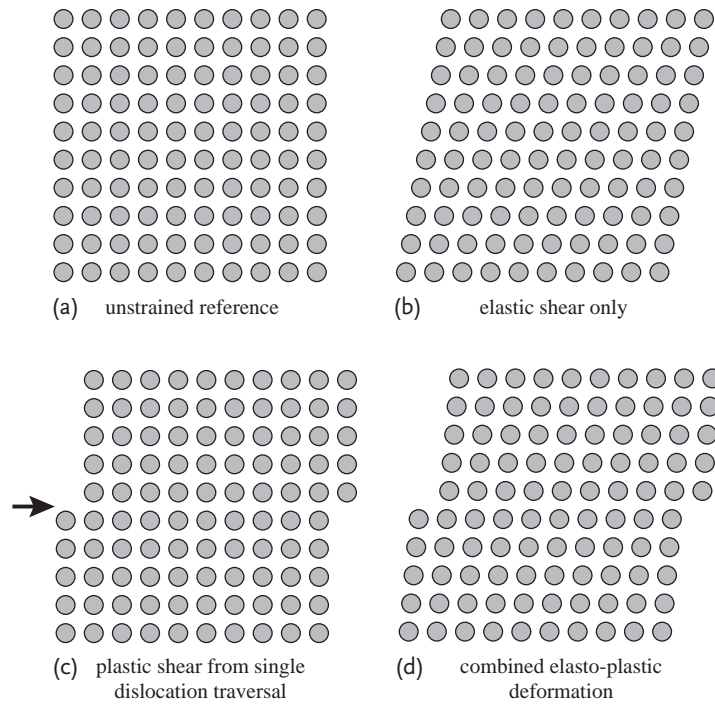
Figure 3.3 Simple cubic lattice structure (a) experiencing a reversible, elastic shear resulting from small displacements away from the equilibrium positions (b), and the same amount of permanent, plastic shear due to motion of a single dislocation on the plane indicated by an arrow, which leaves a step in the surface of the finite volume observed (c). A combined loading situation is illustrated in (d), where the already plastically sheared lattice is elastically strained further, thus putting stress on the configuration depicted in (c).
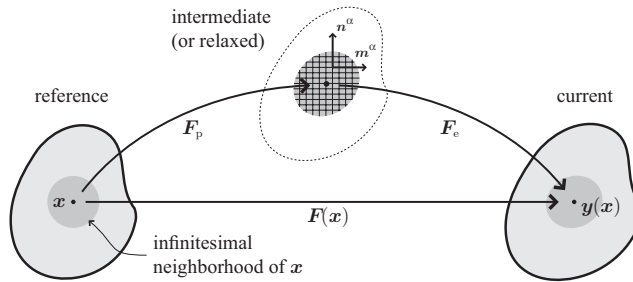
Figure 3.4 Multiplicative decomposition of the total deformation gradient **F** into two parts. The plastic deformation gradient $\mathbf{F}_\mathrm{p}$ relates the reference and intermediate configurations. Next, the transformation from there to the current configuration is characterized by the elastic deformation gradient $\mathbf{F}_\mathrm{e}$. The crystal lattice remains undistorted in the intermediate configuration since dislocation glide rearranges the lattice in a translation-invariant fashion. The slip plane normal $\mathbf{n}^\alpha$ and slip direction $\mathbf{m}^\alpha$ are exemplarily shown for a slip system α.

acterized by the *elastic deformation gradient* $\mathbf{F}_e$. Therefore, the overall deformation gradient relating the reference to the current configuration follows from the sequence of both contributions as

$$\mathbf{F} = \mathbf{F}_e \mathbf{F}_p \ . \tag{3.26}$$

It has to be noted that in general there are no globally defined mappings from which either $\mathbf{F}_p$ or $\mathbf{F}_e$ can be derived as gradients. The reason lies in the spatial heterogeneity of plastic deformation which results in equal and opposite incompatibilities in both, plastic and elastic, deformation maps. Therefore, the approximation of these maps by (first-order) deformation gradients is only valid if the (isolated) material point volume under consideration is either fully traversed by dislocations or uniformly populated by matching dislocations of opposite sign such that the far field of their individual elastic distortions vanishes. This corresponds to the situation depicted in Figure 3.3c. If the total Burgers vector within a material point volume does not vanish, the internal stresses connected to the elastic distortion caused by each dislocation are not equilibrated and result in long-range[4] stress fields. Similarly, even if individual material points are considered to be fully traversed by dislocations or homogeneously populated, there persists a required (geometrically necessary) dislocation content between neighboring material points if both experience different slip system activity (or plastic shape change in a less refined picture). To capture those higher-order effects, the spatial variation of plastic deformation – being equivalent to the respective dislocation activity – has to be taken into account. A substantial body of research regarding this is available, see, for instance Bayley, Brekelmans, and Geers (2006); Evers, Brekelmans, and Geers (2004a,b); Forest, Barbe, and Cailletaud (2000); Gurtin (2002, 2008); Gurtin, Anand, and Lele (2007); Han *et al.* (2005); Kuroda and Tvergaard (2006, 2008b); Levkovitch and Svendsen (2006); Ma and Roters (2004).

Considering the definition of the overall velocity gradient given in Eq. (3.23) together with the above decomposition, we can derive an expression involving the elastic and plastic velocity gradients, $\mathbf{L}_e$ and $\mathbf{L}_p$, which reads

$$\begin{aligned}
\mathbf{L} = \dot{\mathbf{F}}\mathbf{F}^{-1} &= \frac{\partial \left(\mathbf{F}_e \mathbf{F}_p \right)}{\partial t} \mathbf{F}_p^{-1} \mathbf{F}_e^{-1} = \dot{\mathbf{F}}_e \mathbf{F}_p \mathbf{F}_p^{-1} \mathbf{F}_e^{-1} + \mathbf{F}_e \dot{\mathbf{F}}_p \mathbf{F}_p^{-1} \mathbf{F}_e^{-1} \\
&= \dot{\mathbf{F}}_e \mathbf{F}_e^{-1} + \mathbf{F}_e \dot{\mathbf{F}}_p \mathbf{F}_p^{-1} \mathbf{F}_e^{-1} = \mathbf{L}_e + \mathbf{F}_e \mathbf{L}_p \mathbf{F}_e^{-1} \ . \tag{3.27}
\end{aligned}$$

We notice that the total velocity gradient decomposes additively, in contrast to the multiplicative decomposition of the total deformation gradient. Furthermore, as $\mathbf{L}$ is defined with respect to the current configuration (see Eq. (3.21)), so is $\mathbf{L}_e$. The plastic velocity gradient $\mathbf{L}_p$, however, being defined with respect to the intermediate configuration, requires a push forward from there to the current configuration (cf. Eq. (3.4)).

---

4) in comparison with the spatial extent of the material point in question

3.2
Mechanical Equilibrium

After having established useful kinematic relations in Section 3.1, we now turn to
the forces acting on the body of material and causing those kinematic reactions.
For the sake of convenience, we use the *reference* configuration of the body for our
derivations.

The total force, $\mathbf{f}$, experienced by and thus accelerating the body can comprised
body forces per unit mass, $\mathbf{g}$, which result from, for instance, gravitational or mag-
netic fields, and tractions acting on its surface. Since the surface differs between
the reference and the current configuration, two corresponding stress measures are
defined. The *Cauchy stress*, $\boldsymbol{\sigma}$, determines the traction $\mathbf{t}$ per unit deformed area with
normal $\mathbf{n}$ in the current configuration, whereas the *first Piola–Kirchhoff* or *nominal
stress*, $\mathbf{P}$, characterizes the traction $\mathbf{t}_0$ per unit undeformed area with normal $\mathbf{n}_0$ in
the reference configuration. The force $\mathbf{k}$ transmitted via the surface to the body can
thus be alternatively expressed by

$$\mathbf{k} = \int_{\mathcal{S}_0} \mathbf{t}_0 \, dS_0 = \int_{\mathcal{S}} \mathbf{t} \, dS$$

$$= \int_{\mathcal{S}_0} \mathbf{P} \, d\mathbf{n}_0 = \int_{\mathcal{S}} \boldsymbol{\sigma} \, d\mathbf{n} \,. \tag{3.28}$$

Recognizing that infinitesimal, directed areas $d\mathbf{n}_0$ in the reference configuration
transform to $d\mathbf{n} = J\mathbf{F}^{-T} d\mathbf{n}_0$ in the current configuration, with J defined in
Eq. (3.6), one realizes that both stress measures are related by

$$\mathbf{P} = J\boldsymbol{\sigma}\mathbf{F}^{-T} \,. \tag{3.29}$$

Now integrating the body and surface force contributions over the volume and
surface of the material results in

$$\mathbf{f} = \int_{\mathcal{B}_0} \rho_0 \dot{\mathbf{v}} \, dV_0 = \int_{\mathcal{B}_0} \rho_0 \mathbf{g} \, dV_0 + \int_{\mathcal{S}_0} \mathbf{t}_0 \, dS_0 \,, \tag{3.30}$$

where ρ_0 denotes the appropriate density (mass per initial volume) and $\dot{\mathbf{v}} \equiv \ddot{\mathbf{y}}$ the
velocity derivative with respect to time, that is, the acceleration. After substituting
Eq. (3.28) into Eq. (3.30) and invoking the *divergence theorem* to express the surface
integral as a volume integral, the balance of linear momentum (Newton's second
law) reads

$$\mathbf{0} = \int_{\mathcal{B}_0} \left(\rho_0 \mathbf{g} + \frac{\partial \mathbf{P}}{\partial \mathbf{x}} - \rho_0 \dot{\mathbf{v}} \right) dV_0$$

$$= \int_{\mathcal{B}_0} (\rho_0(\mathbf{g} - \dot{\mathbf{v}}) + \mathrm{Div}\,\mathbf{P}) \, dV_0 \,. \tag{3.31}$$

For Eq. (3.31) to hold for arbitrary material volumes, the integrand has to vanish, thus yielding the local form of the linear momentum balance:

$$\text{Div}\,\mathbf{P} = \rho_0\,(\dot{\mathbf{v}} - \mathbf{g}) \ . \tag{3.32}$$

For the case without (significant) body forces and acceleration in the system – which is the case we are concerned with – Eq. (3.32) is identical to zero; hence, *static equilibrium* is then achieved by requiring only a divergence-free stress field, that is, $\text{Div}\,\mathbf{P} = \mathbf{0}$.

Without explicit proof (see Betten (1993) or Gross and Seelig (2001), for instance) it is noted that the balance of angular momentum requires

$$\mathbf{PF}^{\mathrm{T}} = \mathbf{FP}^{\mathrm{T}} \iff \boldsymbol{\sigma} = \boldsymbol{\sigma}^{\mathrm{T}} \ . \tag{3.33}$$

Thus, $\boldsymbol{\sigma}$ is a symmetric tensor characterized by only six independent components, whereas $\mathbf{P}$ in general is nonsymmetric.

3.3
Thermodynamics

To set up a thermodynamic framework for crystal plasticity constitutive laws we make use of u and s, the *internal energy* and *entropy*, both per unit mass, and start by stating the first law of thermodynamics, that is, the *principle of energy conservation*. This can be done by equating the sum of the rate of change in internal and kinetic energy to the sum of external power (based on Eq. (3.32)), heat power from a distributed source with strength r per unit mass, and heat flux connected to the heat flux vector $\mathbf{q}_0$ in the reference configuration:

$$\int_{\mathcal{B}_0} \rho_0(\dot{u} + \dot{\mathbf{v}} \cdot \mathbf{v})\,\mathrm{d}V_0 = \int_{\mathcal{B}_0} \rho_0(\mathbf{g} \cdot \mathbf{v} + r)\,\mathrm{d}V_0 + \int_{\mathcal{S}_0} (\mathbf{t}_0 \cdot \mathbf{v} - \mathbf{q}_0 \cdot \mathbf{n}_0)\,\mathrm{d}S_0$$

$$= \int_{\mathcal{B}_0} (\rho_0(\mathbf{g} \cdot \mathbf{v} + r) +$$

$$\text{Div}\,\mathbf{P} \cdot \mathbf{v} + \mathbf{P} \cdot \text{Grad}\,\mathbf{v} - \text{Div}\,\mathbf{q}_0)\,\mathrm{d}V_0 \ , \tag{3.34}$$

where we have again made use of the divergence theorem to transform the surface integral to a corresponding volume integral. As Eq. (3.34) has to hold for any material volume, the local energy balance in the static case without body force contributions reads

$$\rho_0 \dot{u} - \mathbf{P} \cdot \dot{\mathbf{F}} + \text{Div}\,\mathbf{q}_0 - \rho_0 r = 0 \ , \tag{3.35}$$

which made use of the equality $\text{Grad}\,\mathbf{v} = \partial\dot{\mathbf{y}}/\partial\mathbf{x} = \mathrm{d}(\partial\mathbf{y}/\partial\mathbf{x})/\mathrm{d}t = \dot{\mathbf{F}}$.

The second law of thermodynamics requires the rate of change in entropy to be at least as large as the rate of external entropy supply. The latter is given by summing

the contributions from heat power and heat flux and dividing both of them by the absolute temperature T, thus yielding

$$\int_{\mathcal{B}_0} \rho_0 \dot{s} \, dV_0 \geq \int_{\mathcal{B}_0} \frac{\rho_0 r}{T} \, dV_0 - \int_{\mathcal{S}_0} \frac{\mathbf{q}_0 \cdot \mathbf{n}_0}{T} \, dS_0$$

$$= \int_{\mathcal{B}_0} \left(\frac{\rho_0 r}{T} - \frac{\partial}{\partial \mathbf{x}} \left(\frac{\mathbf{q}_0}{T} \right) \right) dV_0$$

$$= \int_{\mathcal{B}_0} \left(\frac{\rho_0 r}{T} - \frac{1}{T} \operatorname{Div} \mathbf{q}_0 + \frac{\mathbf{q}_0}{T^2} \cdot \operatorname{Grad} T \right) dV_0 \, . \tag{3.36}$$

Invoking the same argument as above (validity in arbitrary material volumes), the local form of the rate, Γ, of internal entropy production follows as the difference between the left-hand-side and right-hand-side integrands of Eq. (3.36) as

$$\Gamma := \rho_0 \dot{s} - \frac{\rho_0 r}{T} + \frac{1}{T} \operatorname{Div} \mathbf{q}_0 - \frac{\mathbf{q}_0}{T^2} \cdot \operatorname{Grad} T \geq 0 \, . \tag{3.37}$$

From this we derive the *dissipation*, defined as the rate of production of internal entropy density multiplied by the absolute temperature (hence, it is also strictly nonnegative), to be

$$\mathcal{D} := \Gamma T = T\rho_0 \dot{s} - \rho_0 r + \operatorname{Div} \mathbf{q}_0 - \frac{\mathbf{q}_0}{T} \cdot \operatorname{Grad} T$$

$$= T\rho_0 \dot{s} - \rho_0 \dot{u} + \mathbf{P} \cdot \dot{\mathbf{F}} - \frac{\mathbf{q}_0}{T} \cdot \operatorname{Grad} T \geq 0 \, , \tag{3.38}$$

in which we substituted the thermal contribution, $\operatorname{Div} \mathbf{q}_0 - \rho_0 r$, from Eq. (3.35).

Now we turn to a constitutive assumption regarding the material behavior. Let the internal energy depend exclusively on the elastic deformation (gradient) and on the entropy, that is,

$$u = u(\mathbf{F}_e, s) \, , \tag{3.39}$$

which entails the rate of change in internal energy reading

$$\dot{u} = \frac{\partial u}{\partial \mathbf{F}_e} \cdot \dot{\mathbf{F}}_e + \frac{\partial u}{\partial s} \dot{s} \, . \tag{3.40}$$

In the simplest case, the mechanical and entropic contributions to the thermodynamic potential are fully decoupled. Furthermore, the mechanical contribution is formulated to depend quadratically on the elastic Green's Lagrangian strain

$$\mathbf{E}_e = \frac{1}{2} \left(\mathbf{F}_e^{\mathrm{T}} \mathbf{F}_e - \mathbf{I} \right) \tag{3.41}$$

only – since rigid-body rotations do not alter the internal energy – and reads

$$u(\mathbf{E}_e(\mathbf{F}_e), s) = \frac{1}{2\rho_0} (\mathbb{C} \mathbf{E}_e) \cdot \mathbf{E}_e + u_{\mathrm{th}}(s) \, , \tag{3.42}$$

with $\mathbb{C}$ being the (fourth-order) elasticity tensor. Then, for the above potential, the stress measure which is work-conjugate to $\mathbf{E}_e$ follows as

$$\rho_0 \frac{\partial u}{\partial \mathbf{E}_e} = \mathbf{S} = \mathbb{C}\mathbf{E}_e \tag{3.43}$$

and is termed *second Piola–Kirchhoff stress*. This stress is a symmetric tensor and is defined in the intermediate configuration. The related stress measure that is work-conjugate to the elastic deformation gradient is connected to the partial derivative of the thermodynamic potential with respect to $\mathbf{F}_e$ and can be derived as

$$\rho_0 \frac{\partial u}{\partial \mathbf{F}_e} = \rho_0 \frac{\partial u}{\partial \mathbf{E}_e} \frac{\partial \mathbf{E}_e}{\partial \mathbf{F}_e} = \mathbf{F}_e \mathbb{C}\mathbf{E}_e = \mathbf{F}_e \mathbf{S} . \tag{3.44}$$

On the basis of these constitutive assumptions, we reformulate the dissipation given in Eq. (3.38) in terms of the elastoplastic decomposition introduced in Section 3.1.6 and substitute the time derivative from Eq. (3.40) to arrive at

$$\mathcal{D} = T\rho_0 \dot{s} - \rho_0 \left(\frac{\partial u}{\partial \mathbf{F}_e} \cdot \dot{\mathbf{F}}_e + \frac{\partial u}{\partial s} \dot{s} \right) + \mathbf{P} \cdot \left(\dot{\mathbf{F}}_e \mathbf{F}_p + \mathbf{F}_e \dot{\mathbf{F}}_p \right) - \frac{\mathbf{q}_0}{T} \cdot \mathrm{Grad}\, T$$

$$= \left(\mathbf{P}\mathbf{F}_p{}^\mathrm{T} - \rho_0 \frac{\partial u}{\partial \mathbf{F}_e} \right) \cdot \dot{\mathbf{F}}_e + \left(T\rho_0 - \rho_0 \frac{\partial u}{\partial s} \right) \dot{s}$$

$$+ \mathbf{F}_e^\mathrm{T}\mathbf{P}\mathbf{F}_p{}^\mathrm{T} \cdot \mathbf{L}_p - \frac{\mathbf{q}_0}{T} \cdot \mathrm{Grad}\, T \geq 0 . \tag{3.45}$$

In Eq. (3.45) we, first, observe that the two bracketed terms have to vanish, since the dissipation cannot depend on the rate of change, $\dot{\mathbf{F}}_e$ and $\dot{s}$, of state variables (otherwise a negative dissipation circle could be constructed). Therefore,

$$\mathbf{P}\mathbf{F}_p{}^\mathrm{T} = \rho_0 \frac{\partial u}{\partial \mathbf{F}_e} \quad \text{and} \quad T = \frac{\partial u}{\partial s} , \tag{3.46}$$

and the only two nonvanishing dissipative terms left in Eq. (3.45) are connected to the plastic strain rate and the heat flux in a temperature gradient. Second, using the equivalence established in Eq. (3.46), one recognizes that the driving force for plastic strain in the intermediate configuration, that is, the stress that is work-conjugate to the plastic velocity gradient, can be expressed in terms of the internal energy and reads

$$\mathbf{F}_e^\mathrm{T}\mathbf{P}\mathbf{F}_p{}^\mathrm{T} = \mathbf{F}_e^\mathrm{T}\rho_0 \frac{\partial u}{\partial \mathbf{F}_e}$$

$$= \mathbf{F}_e^\mathrm{T}\mathbf{F}_e \mathbf{S} \approx \mathbf{S} , \tag{3.47}$$

where the relation found in Eq. (3.44) has been substituted. This measure will reoccur in Chapter 6 on constitutive models; however, since $\mathbf{F}_e^\mathrm{T}\mathbf{F}_e \approx \mathbf{I}$ in metallic materials, it is typically approximated by $\mathbf{S}$ only.

35

4
The Finite Element Method

The finite element method (FEM) is nowadays without doubt the most popular simulation tool in structural mechanics. The first finite element simulation was performed by Courant (1943). The breakthrough of the method came through the publication of "The Finite Element Method in Structural and Continuum Mechanics" by Zienkiewicz (1967). The three succeeding volumes (Zienkiewicz and Taylor, 2005; Zienkiewicz, Taylor, and Nithiarasu, 2005a; Zienkiewicz, Taylor, and Zhu, 2005b) are considered the most important monographs in the field to date.

In the framework of this book, however, it must be emphasized that the FEM is just one of several numerical methods to solve nonlinear partial differential equations. As such, it has to compete with many other methods, such as the finite difference method (Boole, 1872; Richtmyer and Morton, 1967), the boundary element method (Banerjee, 1994; Wrobel and Aliabadi, 2002), and meshless methods such as the discrete element method (Munjiza, 2004; Williams and Mustoe, 1985) and smooth particle hydrodynamics (Hoover, 2006; Monaghan, 1988), to name only the most popular ones. Equally important is to realize that the "M" in FEM is for "method" not "model", that is, the FEM is just the solver; to build a model it has to be combined with some physics. In the case of simulations in the field of solid mechanics a model consists of the geometry of some part (or several parts), mechanical boundary conditions and most important a material model, which in the case of this book is build on crystal plasticity.

Even though the focus of this book is on the material models (crystal plasticity to be precise) and not the FEM as such, it is important to know at least the basics of the FEM as they are in part important for the formulation and coding of material models. In the remainder of the chapter we, therefore, present the fundamentals of the FEM.

4.1
The Principle of Virtual Work

The principle of virtual work is, among others, one way of deriving the fundamental equations of the FEM. We start from the assumption of an arbitrary body with volume V and surface S in static mechanical equilibrium, that is, we set $\dot{\mathbf{v}}$ to zero

in Eq. (3.32) and push it to the current configuration to get

$$\operatorname{div} \boldsymbol{\sigma} + \rho \mathbf{g} = \mathbf{0} \ . \tag{4.1}$$

Equation (4.1) has to be satisfied everywhere in space, that is, at an infinite number of points. As this cannot be handled by a computer, we now invoke the principle of virtual work to finally discretize the equation. First, we introduce an arbitrary vector-valued function, $\delta\mathbf{v}(\mathbf{x})$:

$$(\operatorname{div} \boldsymbol{\sigma}(\mathbf{x}) + \rho \mathbf{g}(\mathbf{x})) \cdot \delta\mathbf{v}(\mathbf{x}) = 0 \ . \tag{4.2}$$

Then we integrate the equation over the volume of the body to find

$$\int_V (\operatorname{div} \boldsymbol{\sigma} + \rho \mathbf{g}) \cdot \delta\mathbf{v} \, dV = 0 \ . \tag{4.3}$$

$\delta\mathbf{v}$ is called a test function, because it tests whether the constraint (4.1) is fulfilled wherever $\delta\mathbf{v}$ is nonzero. As it does this not pointwise but in a volume-averaged (integral) sense, Eq. (4.3) is called the *weak form* of Eq. (4.1).

Using the chain rule and the divergence theorem, we can rewrite Eq. (4.3) as

$$\int_S \mathbf{t} \cdot \delta\mathbf{v} \, dS + \int_V \rho \mathbf{g} \cdot \delta\mathbf{v} \, dV = \int_V \boldsymbol{\sigma} \cdot \operatorname{grad} \delta\mathbf{v} \, dV \ . \tag{4.4}$$

Now it is important to remember that the test function $\delta\mathbf{v}$ is arbitrary. Therefore, if we choose $\delta\mathbf{v}$ to be a displacement, the integrands turn out to be of the nature of mechanical work and this is why the whole procedure is called the *principle of virtual work*. In that case, using $\delta\boldsymbol{\epsilon} = (\operatorname{grad} \delta\mathbf{v})_{\text{sym}}$, we can further rewrite Eq. (4.4) to finally obtain the basic function of the FEM:

$$\int_S \mathbf{t} \cdot \delta\mathbf{v} \, dS + \int_V \rho \mathbf{g} \cdot \delta\mathbf{v} \, dV = \int_V \boldsymbol{\sigma} \cdot \delta\boldsymbol{\epsilon} \, dV \ . \tag{4.5}$$

4.2
Solution Procedure – Discretization

The FEM solves Eq. (4.5) by discretizing the body and introducing a large set of global shape functions M_a (see Figure 4.1). These shape functions are chosen in a way that they have a value of 1 at node a of the finite element mesh and 0 at all other nodes. Any global field, including $\delta\mathbf{v}$, can then be approximated as

$$\delta\mathbf{v}(\mathbf{x}) = \sum_{a=1}^{a=N_n} M_a \delta\mathbf{v}_a \ , \tag{4.6}$$

with N_n being the number of nodes in the mesh and $\delta\mathbf{v}_a$ the value of $\delta\mathbf{v}$ at node a. Equation (4.4) can now be approximated by

$$\sum_{a=1}^{a=N_n} \left[\int_S \mathbf{t} M_a \, dS + \int_V \rho \mathbf{g} M_a \, dV \right] \delta\mathbf{v}_a = \sum_{a=1}^{a=N_n} \left[\int_V \boldsymbol{\sigma} \operatorname{grad} M_a \, dV \right] \delta\mathbf{v}_a \ . \tag{4.7}$$
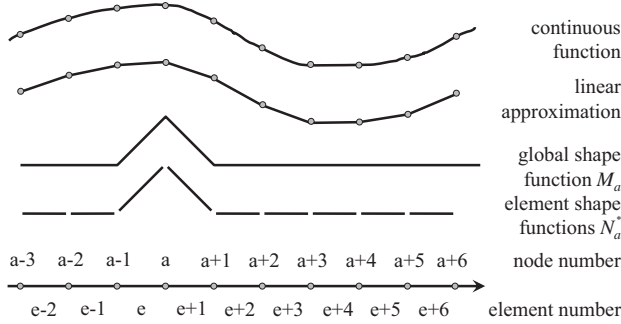
Figure 4.1 The approximation of a continuous function using linear global and element shape functions in one dimension. Function values at nodal positions are marked by the bullets. Element shape functions N_a^* are shown for the running element (upper) index and fixed value of a.

As $\delta\mathbf{v}$ is an arbitrary test function, so are its values $\delta\mathbf{v}_a$. This implies that to fulfill Eq. (4.7) it has to be fulfilled for each individual addend in Eq. (4.7), so the single Eq. (4.7) is transferred into a set of N_n equations of the form

$$\int_S \mathbf{t} M_a \, dS + \int_V \rho \, \mathbf{g} M_a \, dV = \int_V \boldsymbol{\sigma} \, \text{grad} \, M_a \, dV \; . \tag{4.8}$$

The integrals in Eq. (4.8) have to be evaluated over the complete body. To simplify the numerical evaluation of these integrals, we introduce element shape functions N_a^e, which are nonzero only for those elements e that contain node a and are zero for all other elements (see Figure 4.1). Again the value of N_a^e at node a is one. If one now splits the integrals in Eq. (4.8) into sums of integrals over the elements, one gets

$$\sum_{e=1}^{N_e} \left[\int_{S_e} \mathbf{t} N_a^e \, dS_e + \int_{V_e} \rho \, \mathbf{g} N_a^e \, dV_e \right] = \sum_{e=1}^{N_e} \left[\int_{V_e} \boldsymbol{\sigma} \, \text{grad} \, N_a^e \, dV_e \right] , \tag{4.9}$$

where N_e is the number of elements. As the elements used in the FEM have simple regular shapes, the individual element integrals can be easily evaluated numerically using, for example, Gauss quadrature. It is important to notice that owing to the special form of the N_a^e only those elements contribute to the sums that actually contain node a; for all other elements the integrals are zero.

When we finally introduce the short forms

$$R_{ae} = \int_{S_e} \mathbf{t} N_a^e \, dS_e + \int_{V_e} \rho \, \mathbf{g} N_a^e \, dV_e \tag{4.10}$$

and

$$F_{ae} = \int_{V_e} \boldsymbol{\sigma} \, \text{grad} \, N_a^e \, dV_e \tag{4.11}$$

for the outer and inner force contributions, respectively, of element e at node a, then the whole equation system can be written in vector form as

$$
\begin{pmatrix}
F_{11} + F_{12} + \cdots + F_{1N_e} \\
F_{21} + F_{22} + \cdots + F_{2N_e} \\
\vdots \\
F_{N_n1} + F_{N_n2} + \cdots + F_{N_n N_e}
\end{pmatrix}
=
\begin{pmatrix}
R_{11} + R_{12} + \cdots + R_{1N_e} \\
R_{21} + R_{22} + \cdots + R_{2N_e} \\
\vdots \\
R_{N_n1} + R_{N_n2} + \cdots + R_{N_n N_e}
\end{pmatrix}
\tag{4.12}
$$

or simply

$$
\mathbf{F} = \mathbf{R} \tag{4.13}
$$

in the case when $\boldsymbol{\sigma}$ in Eq. (4.11) depends linearly on the strain $\boldsymbol{\epsilon}$; $\mathbf{F}$ can be rewritten as $\mathbf{F} = \mathbf{K}\mathbf{u}$, where $\mathbf{u}$ is the vector of all nodal displacements. $\mathbf{K}$ is called the global stiffness matrix. In this case the finite element solver has to finally solve the linear equation system

$$
\mathbf{R} = \mathbf{K}\mathbf{u} \tag{4.14}
$$

for the nodal displacements $\mathbf{u}$. As stated above, most of the elements do not contribute to the individual sums, which implies that most of the entries of $\mathbf{R}$ and $\mathbf{K}$ are zero, that is, $\mathbf{R}$ and $\mathbf{K}$ are sparse matrices – a fact which is usually exploited in finite element solvers by making use of solution algorithms particularly optimized for sparse matrices.

4.3
Nonlinear FEM

In the framework of FEM two sources of nonlinearity can be distinguished:

Geometrical nonlinearities These are caused by the geometry of the model. Examples are thinning of a tensile sample, buckling, large deformations and/or rotations, and all problems including contact.

Material nonlinearities These are caused by a nonlinear material model. Examples of nonlinear materials are hyperelastic materials, materials such as concrete that show an unsymmetric tension compression behavior, and certainly plastic materials.

As this book deals with crystal plasticity, it becomes immediately clear that we always have to consider nonlinear behavior. In case of nonlinearity, there are two principal ways of solving the problem using linear solvers.

The explicit method uses the results of prior time steps to extrapolate the solution of the current time step. Although this approach guarantees a fast solution, it does not necessarily converge to the correct solution. Therefore, the allowed time step is rather small for explicit solution schemes.

The implicit method uses an iterative scheme to approach the correct solution. In most cases a simple but effective Newton–Raphson scheme is used, but other algorithms are equally possible. Implicit schemes have the advantage of always converging to the correct solution independently of the size of the time step, that is if they converge at all. On the other hand, they are computationally more costly as they require additional calculations of, for example, a stiffness matrix. More aspects of implicit versus explicit integration schemes in the field of crystal plasticity finite element methods can be found in Chapter 8.

5
The Crystal Plasticity Finite Element Method
as a Multiphysics Framework

A main conceptual advantage of the crystal plasticity finite element (CPFE) approach for tackling anisotropic micromechanical problems in materials science and engineering is that it can combine a variety of mechanical effects, which are direction-dependent owing to the underlying crystalline structure. Figure 5.1 shows an example where only elastic anisotropy is considered.

When considering elastoplastic problems, CPFE models may not only include dislocations as the main carriers of plastic deformation in metals but also other mechanisms which follow dyadic kinematics, see Figures 5.2 and 5.3a and b. Some of these mechanisms were implemented in CPFE models in earlier works, such as martensite formation (Lan *et al.*, 2005; Thamburaja and Anand, 2001), shear band formation (e.g., in glassy matter) (Anand and Sun, 2007, 2005), mechanical twinning (Kalidindi, 1998; Marketz *et al.*, 2002; Salem, Kalidindi, and Semiatin, 2005; Staroselsky and Anand, 1998), and even superplastic grain boundary shear (Wei and Anand, 2004; Wei, Su, and Anand, 2006).
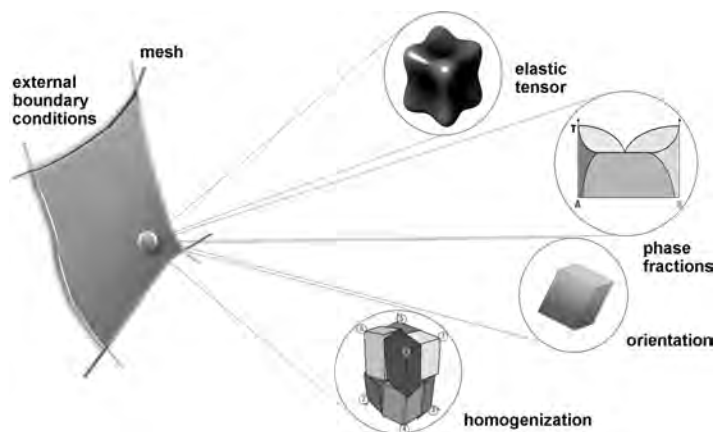
Figure 5.1 Finite element example where only elastic anisotropy is considered. The phase fractions and homogenization approaches are indicated as well for the case when more than one phase and multiple crystals must be considered at one integration point.
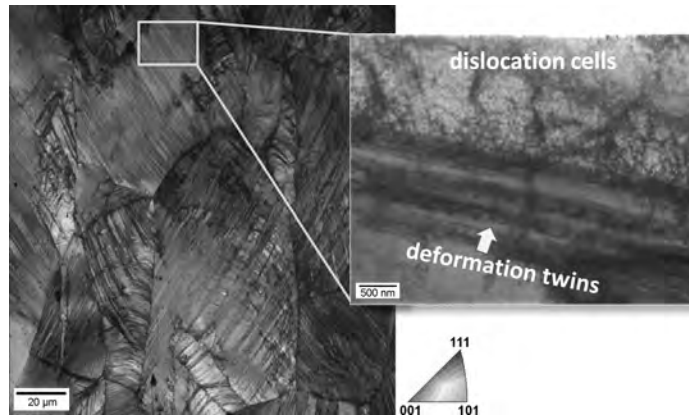
Figure 5.2 Micrograph showing the complexity of deformation microstructures in cases where more than one lattice defect type is involved. The electron backscatter diffraction map shows the orientation contrast of a deformed twinning-induced-plasticity steel. The transmission electron microscopy image in the inset reveals details of the local interaction between dislocation cells and deformation twins.

The CPFE method allows the user to incorporate these mechanisms including their interactions. But it also adds complexity to the model: The use of different competing crystallographic deformation mechanisms within a CPFE model requires the formulation of local homogenization rules (Raabe *et al.*, 2002a; Raabe and Roters, 2004). This means that at some material points only one type of deformation mechanism (e.g., dislocation slip) may occur, whereas at others a mix (e.g., dislocations and twins) must be considered within the same material volume, Figure 5.2. The latter situation requires appropriate submodels that describe the evolving fractions (e.g., of the twinned volume) and the interactions of coexisting and competing deformation mechanisms at the same material point, Figure 5.3. Another aspect that increases complexity in such cases is the possibility that deformation martensite or twins may, after their formation, undergo further plastic deformation or create accommodation strains related to volume changes. Some of these aspects will be discussed in the ensuing sections of this book.

The CPFE approach can and has been used to devise models for size-dependent mechanical behavior. For this, the equivalence between a gradient of the plastic deformation and an excess content of dislocations is exploited. Since excess dislocation content is associated with a lattice orientation change (Kröner, 1958b, 1981; Nye, 1953) (Figure 5.4), the nowadays accessible high-resolution measurements of crystal orientation in two and three dimensions allow for thorough validation of such types of models (Demir *et al.*, 2009; Kuo *et al.*, 2003; Larson *et al.*, 2002; Roters *et al.*, 2004; Zaafarani *et al.*, 2006; Zaefferer *et al.*, 2003; Zaefferer, Wright, and Raabe, 2008).

Typically, the dislocation density in those models is divided into dislocations connected to gradients in plastic strain (then termed *geometrically necessary* (Ashby, 1970)) and ordinary (termed *statistically stored*) dislocation content. It should be
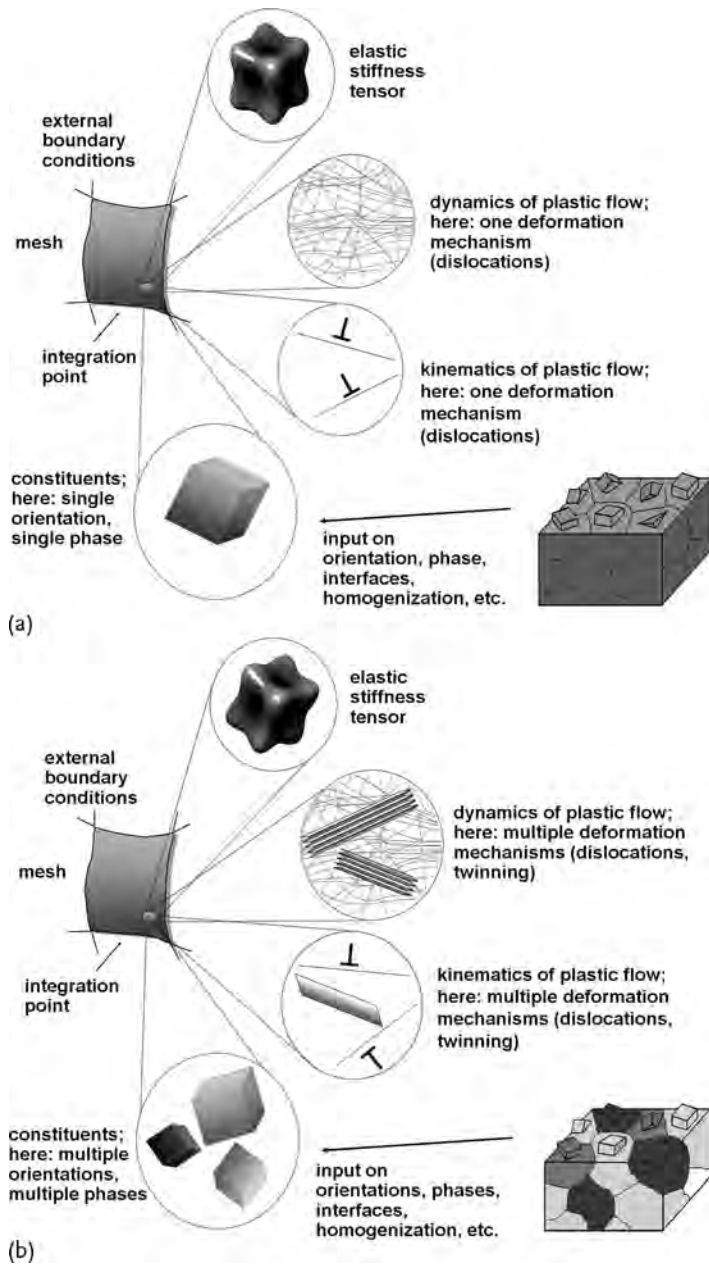
Figure 5.3 The conceptual ingredients in crystal plasticity finite element simulations for elastoplastic micromechanical problems. (a) Example of a case with one type of deformation mechanism (lattice dislocations) and one phase. (b) Example of a case with different deformation mechanisms, phases, orientations, and homogenization schemes at the same integration point.
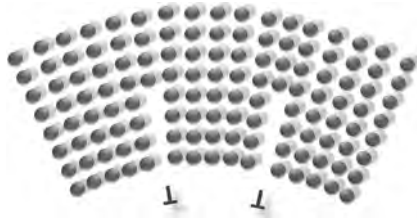
Figure 5.4 Relationship between single dislocations and curvature.

noted, however, that it cannot be distinguished whether an individual dislocation belongs to the geometrically necessary fraction. This distinction follows only as a consequence of excess dislocation *content* within a particular observation volume, determined by the closure failure of a corresponding Burgers circuit. Even then, geometrical necessity does not render those dislocations distinct from statistically stored ones, but both their evolutions must be embedded in a unified kinetic framework, that is, they can assume either state depending on the local lattice defect configuration.

CPFE simulations can be used both at microscopic and at macroscopic scales (Raabe *et al.*, 2002a). Examples of small-scale applications are inter- and intragrain mechanics, damage initiation, mechanics at interfaces, simulation of micromechanical experiments (e.g., indentation, pillar compression, beam bending), and the prediction of local lattice curvatures and mechanical size effects (see Table 5.1). Consequently, the use of CPFE methods is gaining momentum in the field of small-scale material testing, where the experimental boundary conditions are difficult to control and/or monitor. In such cases the experimental results may sometimes be hard to interpret without corresponding CPFE simulations that allow an experimentalist to simulate the effects of details in the contact and boundary conditions. Miniaturization also occurs in engineering design. Many products nowadays have dimensions in the range of the grain scale, such as microelectromechanical systems, bonding wires and pillars, stents, and practically all materials in electronic components. Design of such parts increasingly requires consideration of grain-scale crystalline anisotropy. Some applications along these lines are discussed in Part Three.

Macroscopic applications of the CPFE method occur particularly in the fields of large-scale forming and texture simulations. These problems require appropriate homogenization schemes within a CPFE model since a large number of crystals and/or phases are usually considered in each volume element linked with a finite element integration point. The primary engineering objectives of CPFE applications in macroscopic forming simulations are the prediction of the precise material shape after forming, thickness distribution, material failure, optimization of material flow, elastic springback, forming limits, texture evolution, and the mechanical properties of the part formed (Kraska *et al.*, 2009; Nakamachi, Xie, and Harimoto, 2001; Raabe, Wang, and Roters, 2005; Xie and Nakamachi, 2002; Zhao *et al.*, 2001, 2004a). Further related applications include tool design, press layout, and

Table 5.1 Examples of measurable quantities that can be predicted by crystal plasticity finite element (CPFE) models.

Prediction by CPFE methods	Experimental access
Surface roughening	Speckle interferometry, digital image correlation (photogrammetry), atomic force microscopy, white-light confocal microscopy
Elasticity, interface mechanics, grain size effects, grain interaction, size effects	Indentation testing, tensile and compression testing, mechanical tests with different sample sizes, digital image correlation, electron backscatter diffraction, scanning electron microscopy, ultrasonic testing, X-ray and synchrotron Bragg peak broadening and shifting
Creep, high-temperature deformation, superplasticity	Tensile testing, texture measurement, *in situ* electron microscopy
Dislocation-based constitutive modeling	Flow stress measurement, transmission electron microscopy, lattice orientation measurements, electron channeling contrast imaging in the scanning electron microscope
Martensite mechanics, phase transformation, shape memory	Magnetic measurements, multiphase electron backscatter diffraction, X-ray and synchrotron Bragg diffraction
In-grain texture, grain-scale mechanics, nonuniform deformation, multiphase mechanics	Digital image correlation, indentation hardness testing, orientation determination (Kikuchi diffraction in the transmission or scanning electron microscope; X-ray Bragg diffraction), mechanical testing
Texture evolution, texture stability, in-grain texture formation, anisotropy	Texture measurements using Kikuchi diffraction in the transmission or scanning electron microscope or X-ray Bragg diffraction
Forming, deep drawing, process modeling, cup drawing, springback, earing, wire drawing, extrusion, anisotropy, design, fretting	Shape analysis, cup drawing experiments, springback measurements, ultrasonic measurement of elastic polycrystal constants
Crystal plasticity and recrystallization	Hardness testing, metallography, electrical resistivity, X-ray and synchrotron diffraction, electron backscatter diffraction, transmission electron microscopy, grain size determination, kernel average orientation determination, calorimetry
Deformation twinning	Metallography, X-ray and synchrotron diffraction, electron backscatter diffraction, transmission electron microscopy, electron channeling contrast imaging in the scanning electron microscope
Nanoindentation, microscale deformation, miniaturized mechanical testing	Hardness and stiffness analysis using nanoindenter or nanomanipulator tests, surface shape analysis using atomic force microscopy, electron microscopy

surface properties (see the references in Table 5.1). The latter aspect involves both macroscopic (e.g., wrinkling) as well as microstructural (e.g., roping, ridging, orange peel) mechanisms that influence the surface topography (Becker, 1998; Raabe

et al., 2003; Zhao, Radovitzky, and Cuitino, 2004b). A recent development is the use of the CPFE method as a virtual mechanical laboratory. This approach substitutes crystal plasticity simulations for rather involved mechanical tests required for fitting yield surface coefficients (Kraska *et al.*, 2009).

A further advantage of CPFE predictions is that they can be compared with the finding of experiments in a very detailed fashion probing a variety of quantities. Corresponding studies compared shape changes, forces, strains, strain path and rate effects, texture evolution, interface response, local stresses, and size effects one-to-one at different scales, Table 5.1. Examples of applications and experimental validation procedures are given in Part Three.

Beyond these metallurgical and mechanical considerations, numerical aspects also deserve attention. CPFE formulations can be either fully integrated into finite element codes or implemented as user-defined subroutines into commercially available solvers. The latter point is important because engineering applications are often tackled using commercial platforms. The use of standard solvers also helps to make CPFE methods accessible to a broader community. Since the details of the finite element method, of the mesh, and of the integration procedures also play a significant role in CPFE simulations, some of these aspects are discussed in Chapter 8.

In summary, this book intends to demonstrate that for micro- and macroscale mechanical problems containing dyadic degrees of freedom for shear, the CPFE method is an effective modeling platform as it can deal with the delicate interplay of different effects such as complicated boundary conditions (e.g., imposed by the surrounding microstructure or by external fields), various deformation mechanisms and their interactions (e.g., dislocation mechanics at interfaces or twins and martensite), interface properties (e.g., structural superplasticity or the *Hall–Petch effect*), and details of slip localization (e.g., shear band formation) at reasonable computational cost and by using open-source or commercial solvers.

Part Two   The Crystal Plasticity Finite Element Method

6
Constitutive Models

6.1
Dislocation Slip

6.1.1
Introduction

We use the multiplicative decomposition of the deformation gradient $\mathbf{F}$:

$$\mathbf{F} = \mathbf{F}_e\mathbf{F}_p . \tag{6.1}$$

The plastic deformation evolves as

$$\dot{\mathbf{F}} = \mathbf{L}_p\mathbf{F}_p \tag{6.2}$$

and in the case of dislocation slip as the only deformation process according to Rice (1971) $\mathbf{L}_p$ reads

$$\mathbf{L}_p = \sum_{\alpha=1}^{N} \dot{\gamma}^{\alpha}\mathbf{m}^{\alpha} \otimes \mathbf{n}^{\alpha} , \tag{6.3}$$

where the vectors $\mathbf{m}^{\alpha}$ and $\mathbf{n}^{\alpha}$ are, respectively, unit vectors describing the slip direction and the normal to the slip plane of the slip system α and N is the number of (active) slip systems; $\dot{\gamma}^{\alpha}$ is the shear rate for that same system.

6.1.2
Phenomenological Constitutive Models

Phenomenological constitutive models mostly use the critical resolved shear stresses of the slip systems, τ_c^{α}, as material state variables, S. The resolved shear stress on slip system α, characterized by its slip direction $\mathbf{m}^{\alpha}$ and plane normal $\mathbf{n}^{\alpha}$, is defined as

$$\tau^{\alpha} = \mathbf{F}_e^{\mathrm{T}}\mathbf{F}_e\mathbf{S} \cdot (\mathbf{m}^{\alpha} \otimes \mathbf{n}^{\alpha}) . \tag{6.4}$$

As for metallic materials the elastic deformation is small, Eq. (6.4) is usually approximated as

$$\tau^\alpha = \mathbf{S} \cdot (\mathbf{m}^\alpha \otimes \mathbf{n}^\alpha) . \tag{6.5}$$

The shear rate is then formulated as a function of the resolved shear stress, τ^α, and the critical resolved shear stress,

$$\dot{\gamma}^\alpha = f\left(\tau^\alpha, \tau_c^\alpha\right) , \tag{6.6}$$

and the evolution of the material state is formulated as a function of the total shear, γ, and the shear rate, $\dot{\gamma}$,

$$\tau_c^\alpha = g(\gamma, \dot{\gamma}) . \tag{6.7}$$

One prominent group of examples of such a formulation is the one suggested by Rice, Hutchinson, and Peirce (Rice 1971; Hutchinson 1976; Peirce *et al.* 1982; Peirce, Asaro, and Needleman 1983) for face-centered cubic (fcc) metallic crystals. The kinetic law on a slip system follows

$$\dot{\gamma}^\alpha = \dot{\gamma}_0 \left| \frac{\tau^\alpha}{\tau_c^\alpha} \right|^{\frac{1}{m}} \mathrm{sgn}(\tau^\alpha) , \tag{6.8}$$

where $\dot{\gamma}^\alpha$ is the shear rate for slip system α subjected to the resolved shear stress τ^α at a slip resistance τ_c^α; $\dot{\gamma}_0$ and m are material parameters that quantify the reference shear rate and the rate sensitivity of slip, respectively. The influence of any slip system β on the hardening behavior of slip system α is given by

$$\dot{\tau}_c^\alpha = h_{\alpha\beta} \left| \dot{\gamma}^\beta \right| , \tag{6.9}$$

where $h_{\alpha\beta}$ is referred to as the hardening matrix,

$$h_{\alpha\beta} = q_{\alpha\beta} \left[h_0 \left(1 - \frac{\tau_c^\beta}{\tau_s}, \right)^a \right] \tag{6.10}$$

which empirically captures the micromechanical interaction among different slip systems. In this formulation h_0, a, and τ_s are slip hardening parameters, which are assumed to be identical for all fcc slip systems owing to the underlying characteristic dislocation reactions. The parameter $q_{\alpha\beta}$ is a measure of latent hardening; in most cases its value is taken as 1.0 for coplanar slip systems α and β, and 1.4 otherwise, which renders the hardening model anisotropic.

In the literature a number of variations of Eqs. (6.8) and (6.9) can be found. Some authors use a hyperbolic sine function instead of a power law in Eq. (6.8) (Becker, 1991), whereas others use modified hardening laws such as a generalized Voce equation (Kocks, 1976; Voce, 1948) instead of Eq. (6.9).

These types of kinetic formulations are currently the most frequently used ones although they suffer from the drawback that the material state is only described in terms of the critical resolved shear stress, τ_c^α, and not in terms of lattice defect populations (Kocks, 1966; Mecking and Kocks, 1986). The latter approach, however, is required to render crystal plasticity models path-, history-, and size-dependent as will be discussed in the following.

6.1.2.1 **Extension to Body-Centered Cubic Materials**

In principle, the phenomenological formulation of the constitutive behavior of fcc materials can be also used for body-centered cubic (bcc) materials. There exists, however, an atomic-scale intricacy in bcc metals that leads to the nonplanar spreading of the screw dislocation cores (Duesbery and Vitek, 1998; Hull and Bacon, 2001), with the result that dislocation-mediated plasticity in bcc metals involves more complex mechanisms than in fcc metals. To take these effects into account, the approach of Bassani, Ito, and Vitek (2001) and Vitek *et al.* (2004b) can be adopted, where the effect of nonglide stress is incorporated in the model by modifying the expression for the slip resistance according to

$$\tau_{\mathrm{c,\,bcc}}^{\alpha} = \tau_{\mathrm{c}}^{\alpha} - a^{\alpha}\tau_{\mathrm{ng}}^{\alpha}\,, \tag{6.11}$$

where a^{α} is a coefficient that gives the net effect of the nonglide stress on the effective resistance, and $\tau_{\mathrm{ng}}^{\alpha}$ is the resolved shear stress on the nonglide plane with normal $\tilde{\mathbf{n}}^{\alpha}$, given by[5]

$$\tau_{\mathrm{ng}}^{\alpha} = \mathbf{S} \cdot (\mathbf{m}^{\alpha} \otimes \tilde{\mathbf{n}}^{\alpha})\,. \tag{6.12}$$

The kinetic law is in this case constructed by inserting the modified critical resolved shear stress instead of the classical slip resistance into the power-law expression for the plastic slip rate (Eq. (6.8)). More details on a model for bcc ferrite can be found in Tjahjanto (2007) and Tjahjanto, Turteltaub, and Suiker (2008).

6.1.3
Microstructure-Based Constitutive Models

In contrast to the phenomenological constitutive models, the microstructure-based ones use physical measures, which quantify the microstructure, as material state variables, *S*. In the case of plasticity, the most important internal variable is certainly the dislocation density as the dislocations are the carriers of plastic deformation.[6] Models that treat the evolution of dislocation densities and calculate the flow stress from them have been proposed by various authors (Arsenlis and Parks, 2002; Arsenlis *et al.*, 2004; Cheong and Busso, 2004; Gao and Huang, 2003; Ma, Roters, and Raabe, 2006a,b). We will present the model of Ma and Roters (Ma and Roters, 2004; Ma, Roters, and Raabe, 2006a,b) in more detail in the following subsections. It should be noted that even though the dislocations are the most important internal variable measure, more parameters are required for a full description of the microstructure, for example, grain size and shape, second phase fractions, and precipitate morphology. However, only few of these additional parameters have been introduced into crystal plasticity finite element (CPFE) constitutive models so far.

---

5) Note that the elastic stretch is again neglected, see also Eqs. (6.4) and (6.5).
6) It should be noted that in some models dislocation densities are calculated by using the Taylor equation ($\tau \propto \sqrt{\varrho}$). These approaches must also be regarded as phenomenological models as they do not treat the *evolution* of the dislocations explicitly.

6.1.3.1 **Dislocation-Based Constitutive Laws**
in Crystal Plasticity Finite Element Models

The dislocation-density-based constitutive model introduced by Ma and Roters (Ma and Roters, 2004; Ma, Roters, and Raabe, 2006a,b) uses mobile dislocations, $\varrho_{\mathrm{m}}^{\alpha}$, gliding along slip system α to accommodate a part of the external plastic deformation. For them to do so, they must overcome the stress field of the parallel dislocations, $\varrho_{\mathrm{P}}^{\alpha}$, which causes the passing stress. Also they must cut the forest dislocations, $\varrho_{\mathrm{F}}^{\alpha}$, with the aid of thermal activation. In this framework one can define the parallel dislocation density, $\varrho_{\mathrm{P}}^{\alpha}$, and the forest dislocation density, $\varrho_{\mathrm{F}}^{\alpha}$, for each slip system α in the following way: $\varrho_{\mathrm{P}}^{\alpha}$ are the dislocations parallel to the slip plane, and $\varrho_{\mathrm{F}}^{\alpha}$ are the dislocations perpendicular to the slip plane. Considering the immobile dislocation density density, $\varrho_{\mathrm{SSD}}^{\alpha}$, for fcc crystals, one can use the following projections:

$$\varrho_{\mathrm{F}}^{\alpha} = \sum_{\beta=1}^{N} \chi^{\alpha\beta} \varrho_{\mathrm{SSD}}^{\beta} \left| \cos\left(\mathbf{n}^{\alpha}, \mathbf{t}^{\beta}\right) \right| , \tag{6.13a}$$

$$\varrho_{\mathrm{P}}^{\alpha} = \sum_{\beta=1}^{N} \chi^{\alpha\beta} \varrho_{\mathrm{SSD}}^{\beta} \left| \sin\left(\mathbf{n}^{\alpha}, \mathbf{t}^{\beta}\right) \right| . \tag{6.13b}$$

In these equations we introduce the interaction strength, $\chi^{\alpha\beta}$, between different slip systems, which comprise those of self-interaction, coplanar interaction, cross slip, glissile junction, Hirth lock, and Lomer–Cottrell lock. In this formulation only edge dislocations are considered owing to their limited out-of-plane mobility.

In a dislocation-based model the *Orowan equation* typically replaces Eq. (6.8) as the kinetic equation and reads

$$\dot{\gamma}^{\alpha} = \varrho_{\mathrm{m}}^{\alpha} b v^{\alpha} , \tag{6.14}$$

where $\varrho_{\mathrm{m}}^{\alpha}$ is the density of mobile dislocations, b is the magnitude of the Burgers vector, and v^{α} is the average velocity of the mobile dislocations. According to Ma and Roters (2004), the mobile dislocation density can be calculated from the statistically stored dislocation (SSD) density by a simple scaling law:

$$\varrho_{\mathrm{m}}^{\alpha} = \frac{2 k_{\mathrm{B}} T}{c_1 c_2 c_3 \mu b^3} \sqrt{\varrho_{\mathrm{P}}^{\alpha} \varrho_{\mathrm{F}}^{\alpha}} , \tag{6.15}$$

where T is the absolute temperature, k_{B} is the Boltzmann constant, μ is the shear modulus, and c_1, c_2, c_3 are constants introduced in the dislocation density evolution laws below.

Under the assumption of forest cutting as the rate determining process, the velocity of the mobile dislocations can be calculated as

$$v^{\alpha} = \lambda^{\alpha} v_{\mathrm{attack}} \exp\left(-\frac{Q_{\mathrm{slip}}}{k_{\mathrm{B}} T}\right) \sinh\left(\frac{\tau_{\mathrm{eff}}^{\alpha} V^{\alpha}}{k_{\mathrm{B}} T}\right) \mathrm{sgn}(\tau^{\alpha}) , \tag{6.16}$$

where λ^{α} is the jump width, which is inversely proportional to the forest dislocation spacing, v_{attack} is the attack frequency, Q_{slip} is the effective activation energy for

dislocation glide, and V is the activation volume, which can be calculated as

$$V = c_3 \lambda^\alpha b^2,$$ (6.17)

with c_3 being a fitting constant.

Finally, the effective shear stress τ_{eff}^α can be calculated from the resolved shear stress and the passing stress as

$$\tau_{eff}^\alpha = \begin{cases} |\tau^\alpha| - \tau_{pass}^\alpha = |\tau^\alpha| - c_1 \mu b \sqrt{\varrho_P^\alpha + \varrho_m^\alpha} & \text{for} \quad |\tau^\alpha| > \tau_{pass}^\alpha \\ 0 & \text{for} \quad |\tau^\alpha| \leq \tau_{pass}^\alpha . \end{cases}$$ (6.18)

The phenomenological description of hardening in Eq. (6.9) is substituted by the evolution of the dislocation densities. For this purpose rate equations based on individual dislocation reactions are formulated. In Ma and Roters (2004) four such processes were taken into account, namely, lock and dipole formation as processes increasing the dislocation density and athermal and thermally activated annihilation as recovery processes. A detailed derivations of these rate equations can be found in Ma and Roters (2004). In the following we summarize the results:

- Lock formation

$$\dot{\varrho}_{SSD}^{\alpha+} = \frac{c_4}{b} \sqrt{\varrho_F^\alpha} \dot{\gamma}^\alpha$$ (6.19)

- Dipole formation

$$\dot{\varrho}_{SSD}^{\alpha+} = \frac{c_5}{b} d_{dipole}^\alpha \varrho_m^\alpha \dot{\gamma}^\alpha , \quad \text{with}$$ (6.20)

$$d_{dipole}^\alpha = \frac{\sqrt{3} \mu b}{16\pi(1-\nu)} \left(|\tau^\alpha| - \tau_{pass}^\alpha \right)^{-1}$$ (6.21)

- Athermal annihilation

$$\dot{\varrho}_{SSD}^{\alpha-} = -c_6 \varrho_{SSD}^\alpha \dot{\gamma}^\alpha$$ (6.22)

- Thermal annihilation due to climb of edge dislocations

$$\dot{\varrho}_{SSD}^{\alpha-} = -c_7 \frac{D_0 b^3}{k_B T} \exp\left(-\frac{Q_{bulk}}{k_B T} \right) \varrho_{SSD}^{\alpha}{}^2 |\tau^\alpha| \left(\frac{\dot{\gamma}^\alpha}{\dot{\gamma}_{ref}} \right)^{c_8}$$ (6.23)

The constants $c_4, \dots, c_8$ are used for fitting, d_{dipole} is the critical distance for dipole formation, D_0 is the prefactor of the diffusion coefficient, Q_{bulk} is the corresponding activation energy, and $\dot{\gamma}_{ref}$ denotes a reference shear rate.

6.1.3.2 Introduction of Geometrically Necessary Dislocations

Most of the constitutive laws reported in the literature can be attributed to the group of local models in which the total deformation gradient has been decomposed into

elastic and plastic parts multiplicatively, and from the loading history of one material point the constitutive behavior can be fully described. For stress–strain curves and texture predictions of polycrystals, local models have been shown to be powerful and efficient (Bronkhorst, Kalidindi, and Anand, 1992). However, if the simulation scale gets smaller such as in studies focusing on nanoindentation (Zaafarani *et al.*, 2008, 2006) and micropillar compression (Raabe, Ma, and Roters, 2007a), then local models can be insufficient owing to their inability to describe size effects.

The grain size dependence of the flow stress was first described by Hall and Petch by an empirical equation known as the *Hall–Petch relation* (Hall, 1951; Petch, 1953). Since then, numerous studies have shown that the strengthening effect by a smaller grain size is due to a higher volume fraction of heterogeneous plastic deformation in the vicinity of grain boundaries. There are several explanations in the literature based on dislocation mechanisms such as pileups of mobile dislocations in front of the grain boundaries causing stress concentrations that increase the slip resistance or strain gradients near grain boundaries producing an extra increment of dislocation densities to increase the slip resistance (Evers *et al.*, 2002). Furthermore different kinds of experiments such as microtorsion, microbending, deformation of particle-reinforced metal-matrix composites, and microindentation hardness tests have clearly shown a length-scale dependence of the flow stress (Gao and Huang, 2003).

In these experiments typically nonuniform plastic deformation occurs, which may lead to gradients in orientation and strain near a material point. These gradients can be associated with geometrically necessary dislocations (GNDs) (Ashby, 1970). In phenomenological models it is not straightforward how to integrate GNDs into a constitutive model. In contrast, in dislocation-density-based models GND concepts can be easily integrated as part of the constitutive framework (Nye, 1953).

However, the calculation of strain gradients renders a constitutive model nonlocal, which makes it more difficult to implement. The main reason for this is that in a nonlocal model a material point is strongly coupled with its neighbor points during the evolution of GNDs. This means that strain gradient calculations have to converge for a set of neighboring material points in the same time increment. To achieve this, some authors (Arsenlis *et al.*, 2004; Evers, Brekelmans, and Geers, 2004a) use the divergence theorem to formulate new differential equations using GNDs and SSDs as additional degrees of freedom for every node in an element. These algorithms require additional boundary conditions to be supplied for the dislocation density flux. Although this is not complicated for simple calculations, it is difficult for complex load cases. An alternative and more general integration algorithm was introduced in Ma, Roters, and Raabe (2006a) that can be used to solve any nonlocal constitutive model based on material subroutine access offered by commercial finite element solvers such as MSC.Marc and Abaqus.

In this section we will present how GNDs can be introduced in the dislocation model presented above. Nye's dislocation tensor (Nye, 1953) can be used to trans-

late the strain gradient into GNDs:

$$\mathbf{\Lambda} = \frac{1}{b}\text{Curl}\,\mathbf{F}_\text{p} = -\frac{1}{b}\left(\nabla_\mathbf{x} \times \mathbf{F}_\text{p}^\text{T}\right)^\text{T},\tag{6.24}$$

where the nabla operator $\nabla_\mathbf{x} = \partial/\partial\mathbf{x}$ is defined as the derivative with respect to the reference (material point) coordinate. Using Eq. (6.24), we can calculate the resultant Burgers vector for an arbitrarily oriented surface. In general, the tensor $\mathbf{\Lambda}$ is nonsymmetric with nine independent values. Although there are 12 slip systems for the fcc crystal structure, only six of them are independent (Nemat-Nasser, Ni, and Okinaka, 1998); therefore, it is impossible to calculate the exact GND content for every slip system without using additional assumptions.

When the material time derivative of Eq. (6.24) is used in conjunction with Eq. (6.2), the dislocation tensor in Eq. (6.24) can be decomposed into contributions from the individual slip systems[7] in the following form:

$$\dot{\mathbf{\Lambda}} = -\frac{1}{b}\left(\nabla_\mathbf{x} \times \dot{\mathbf{F}}_\text{p}^\text{T}\right)^\text{T} = -\frac{1}{b}\left(\nabla_\mathbf{x} \times \mathbf{F}_\text{p}^\text{T}\mathbf{L}_\text{p}^\text{T}\right)^\text{T} = \sum_{\alpha=1}^{N}\dot{\mathbf{\Lambda}}^\alpha.\tag{6.25}$$

Substituting the plastic velocity from Eq. (6.3), it follows that

$$\begin{aligned}\dot{\mathbf{\Lambda}}^\alpha &= -\frac{1}{b}\left[\nabla_\mathbf{x} \times \left(\dot{\gamma}^\alpha\mathbf{F}_\text{p}^\text{T}\mathbf{n}^\alpha \otimes \mathbf{m}^\alpha\right)\right]^\text{T}\\ &= -\frac{1}{b}\mathbf{m}^\alpha \otimes \left[\nabla_\mathbf{x} \times \left(\dot{\gamma}^\alpha\mathbf{F}_\text{p}^\text{T}\mathbf{n}^\alpha\right)\right]\end{aligned}\tag{6.26}$$

or, since it is possible that gradients for both $\dot{\gamma}^\alpha$ and $\mathbf{F}_\text{p}$ exist, by expanding the Curl operation, one can rewrite Eq. (6.26) in the form

$$\dot{\mathbf{\Lambda}}^\alpha = -\frac{1}{b}\mathbf{m}^\alpha \otimes \left[\nabla_\mathbf{x}\dot{\gamma}^\alpha \times \mathbf{F}_\text{p}^\text{T}\mathbf{n}^\alpha + \dot{\gamma}^\alpha\left(\nabla_\mathbf{x} \times \mathbf{F}_\text{p}^\text{T}\mathbf{n}^\alpha\right)\right].\tag{6.27}$$

Indeed Eq. (6.26) defines the change of the GND density as

$$\dot{\varrho}_\text{GND}^\alpha = \frac{1}{b}\left\|\nabla_\mathbf{x} \times \left(\dot{\gamma}^\alpha\mathbf{F}_\text{p}^\text{T}\mathbf{n}^\alpha\right)\right\|.\tag{6.28}$$

The integration of the GNDs into the constitutive model is now simply a matter of extending the projection into forest and parallel dislocations (Eqs. (6.13a) and (6.13b)). However, until now it has not been convenient to project $\varrho_\text{GND}^\alpha$ into forest and parallel dislocations as the tangent vectors of GNDs are not constant. Although in the model so far SSDs are assumed to be edge dislocations only, for the GND analysis one has to use edge and screw dislocations to preserve the lattice continuity. Then $\dot{\mathbf{\Lambda}}^\alpha$ can be decomposed into three groups: one group of screw dislocations with a tangent vector parallel to the slip direction $\mathbf{m}^\alpha$, and two groups of edge dislocations with tangent vectors parallel to $\mathbf{n}^\alpha$ and $\mathbf{t}^\alpha = \mathbf{n}^\alpha \times \mathbf{m}^\alpha$, respectively. The decomposition then reads

$$\dot{\mathbf{\Lambda}}^\alpha = \dot{\mathbf{\Lambda}}_\text{s}^\alpha + \dot{\mathbf{\Lambda}}_\text{en}^\alpha + \dot{\mathbf{\Lambda}}_\text{et}^\alpha,\tag{6.29}$$

7) This decomposition is not unique.

with the dislocation tensors

$$\dot{\mathbf{\Lambda}}_{s}^{\alpha} = -\dot{\varrho}_{GNDs}^{\alpha}\mathbf{m}^{\alpha} \otimes \mathbf{m}^{\alpha} , \tag{6.30a}$$

$$\dot{\mathbf{\Lambda}}_{et}^{\alpha} = -\dot{\varrho}_{GNDet}^{\alpha}\mathbf{m}^{\alpha} \otimes \mathbf{t}^{\alpha} , \tag{6.30b}$$

$$\dot{\mathbf{\Lambda}}_{en}^{\alpha} = -\dot{\varrho}_{GNDen}^{\alpha}\mathbf{m}^{\alpha} \otimes \mathbf{n}^{\alpha} \tag{6.30c}$$

and the scalar values

$$\dot{\varrho}_{GNDs}^{\alpha} = \frac{1}{b}\left[\mathbf{\nabla}_{\mathbf{x}} \times \left(\dot{\gamma}^{\alpha}\mathbf{F}_{p}^{T}\mathbf{n}^{\alpha}\right)\right] \cdot \mathbf{m}^{\alpha} , \tag{6.31a}$$

$$\dot{\varrho}_{GNDet}^{\alpha} = \frac{1}{b}\left[\mathbf{\nabla}_{\mathbf{x}} \times \left(\dot{\gamma}^{\alpha}\mathbf{F}_{p}^{T}\mathbf{n}^{\alpha}\right)\right] \cdot \mathbf{t}^{\alpha} , \tag{6.31b}$$

$$\dot{\varrho}_{GNDen}^{\alpha} = \frac{1}{b}\left[\mathbf{\nabla}_{\mathbf{x}} \times \left(\dot{\gamma}^{\alpha}\mathbf{F}_{p}^{T}\mathbf{n}^{\alpha}\right)\right] \cdot \mathbf{n}^{\alpha} , \tag{6.31c}$$

which satisfy

$$\left(\dot{\varrho}_{GND}^{\alpha}\right)^{2} = \left(\dot{\varrho}_{GNDs}^{\alpha}\right)^{2} + \left(\dot{\varrho}_{GNDet}^{\alpha}\right)^{2} + \left(\dot{\varrho}_{GNDen}^{\alpha}\right)^{2} . \tag{6.32}$$

Equations (6.31) are a set of evolution equations for ϱ_{GND}, just like those for ϱ_{SSD} derived in the previous section. Finally, the extended projection reads

$$\varrho_{F}^{\alpha} = \sum_{\beta=1}^{N} \chi^{\alpha\beta}\left[\varrho_{SSD}^{\beta}\left|\cos(\mathbf{n}^{\alpha}, \mathbf{t}^{\beta})\right| + \left|\varrho_{GNDs}^{\beta}\cos(\mathbf{n}^{\alpha}, \mathbf{m}^{\beta})\right|\right.$$
$$\left. + \left|\varrho_{GNDet}^{\beta}\cos(\mathbf{n}^{\alpha}, \mathbf{t}^{\beta})\right| + \left|\varrho_{GNDen}^{\beta}\cos(\mathbf{n}^{\alpha}, \mathbf{n}^{\beta})\right|\right] , \tag{6.33a}$$

$$\varrho_{P}^{\alpha} = \sum_{\beta=1}^{N} \chi^{\alpha\beta}\left[\varrho_{SSD}^{\beta}\left|\sin(\mathbf{n}^{\alpha}, \mathbf{t}^{\beta})\right| + \left|\varrho_{GNDs}^{\beta}\sin(\mathbf{n}^{\alpha}, \mathbf{m}^{\beta})\right|\right.$$
$$\left. + \left|\varrho_{GNDet}^{\beta}\sin(\mathbf{n}^{\alpha}, \mathbf{t}^{\beta})\right| + \left|\varrho_{GNDen}^{\beta}\sin(\mathbf{n}^{\alpha}, \mathbf{n}^{\beta})\right|\right] , \tag{6.33b}$$

where absolute values of GNDs are used, so that polarizations of their Burgers vectors are avoided. A direct result of this treatment is that no kinematic hardening can be predicted, which is acceptable for single-phase material and unidirectional loading.

6.1.3.3 Interface Models

Grain boundaries act as obstacles to the motion of dislocations. At the onset of plastic deformation of polycrystals, mobile dislocations are first created on the slip system with the largest *local* resolved shear stress in the grain with the most favorable orientation. When encountering a grain boundary, these mobile dislocations will accumulate in front of that interface. Such events lead to stress concentrations at a grain boundary that add to the external stress field at this material point. These

microplastic effects, where the local arrangement of dislocations determines the local stress, cannot be treated one-to-one in a crystal plasticity continuum mechanical framework because such models map the underlying dislocation mechanics in a phenomenological statistical or even empirical form. However, homogenization is admissible at larger plastic strains, where most of the slip activation processes can be captured by long-range stresses rather than by local ones (Clark *et al.*, 1992). This means that the dislocation mechanics can, beyond the microplastic regime, be homogenized in the form of statistical dislocation populations, which in turn can be embedded as constitutive rate equations in a crystal plasticity theory (Arsenlis and Parks, 2002; Evers *et al.*, 2002). The applicability of the CPFE approach to a large spectrum of intricate micromechanical problems has been shown by many studies in which both textures and strains were properly predicted when compared with the findings of corresponding experiments (Beaudoin *et al.*, 1995; Kalidindi, Bronkhorst, and Anand, 1992; Raabe *et al.*, 2001; Roters *et al.*, 2004; Sachtleber, Zhao, and Raabe, 2002; Zaefferer *et al.*, 2003; Zhao, Radovitzky, and Cuitino, 2004b).

Dislocation-based models allow explicitly for the incorporation of grain boundaries into the constitutive formulation. Two approaches can be found in the literature. In the first type of models, the grain boundaries are treated as being partially transparent to dislocations (Ma, Roters, and Raabe, 2006b). In the second type of models, interfaces appear as perfect obstacles that do not allow dislocation penetration events (Evers, Brekelmans, and Geers, 2004b). The latter assumption can be implemented in finite element simulations as an additional set of boundary conditions, namely, as a zero-shear condition perpendicular to interfaces. Although the latter approach appears to be relatively straightforward at first view, it can be rather intricate when meshing complicated grain aggregates. As shown in Evers, Brekelmans, and Geers (2004b), these additional boundary conditions result in an increased hardening of the material; however, they do not result in an increase of the initial yield stress, that is, the Hall–Petch effect is not captured. To overcome this drawback, Evers, Brekelmans, and Geers (2004b) suggested grain boundary dislocations (GBDs) as an initial content of GNDs at the position of the grain boundaries. These GBDs are calculated from the crystallographic misorientation across the interface in the following way (Evers, Brekelmans, and Geers, 2004b). Consider two crystals of orientation $\mathbf{Q}_\mathrm{I}$ and $\mathbf{Q}_\mathrm{II}$ with slip systems $(\mathbf{m}^{\alpha,\beta}, \mathbf{t}^{\alpha,\beta}, \mathbf{n}^{\alpha,\beta})$ and $\alpha, \beta = 1, 2, \ldots, 12$,[8)] separated by a grain boundary with normal vector $\mathbf{n}_\mathrm{GB}$ (Figure 6.1). The density of the GBDs is obtained as

$$\varrho^\alpha_\mathrm{GB} = \mathrm{sgn}\left(\mathbf{n}^\alpha \cdot \mathbf{n}_\mathrm{GB}\right) \frac{\left(\left|\mathbf{n}^\alpha \cdot \mathbf{n}_\mathrm{GB}\right| - \left|\mathbf{n}^\beta \cdot \mathbf{n}_\mathrm{GB}\right|\right)^2}{b^2} \, , \tag{6.34}$$

where slip system β has to be chosen such as to minimize the magnitude of $\varrho^\alpha_\mathrm{GB}$.

While a rigid grain boundary was assumed in Evers, Brekelmans, and Geers (2004b), Ma, Roters, and Raabe (2006b) developed a concept to render interfaces partially transparent to dislocations. The transmission of incoming mobile disloca-

---

8) The indices α and β always refer to crystals I and II, respectively.

Figure 6.1 Penetration events for mobile dislocations through a grain boundary. The experimentally obtained micrograph is taken from the work of Shen, Wagoner, and Clark (1986) on steel. Here $\mathbf{t}'^\alpha$, $\mathbf{t}'^\beta$, and $\mathbf{t}_{GB}^{\alpha\beta}$ are the tangent vectors of the dislocation in the grain boundary, and $\mathbf{m}^\alpha$, $\mathbf{m}^\beta$, and $\mathbf{m}_{GB}^{\alpha\beta}$ are the slip direction vectors of the dislocations.

tions through a grain boundary is treated in terms of a thermally activated event. The enthalpy for this activation process is linked to the elastic energy that is required for the formation of misfit dislocations which remain as debris in the interface upon slip penetration. This activation enthalpy enters as an additional contribution into the activation term for the slip of mobile dislocations (Eq. (6.16)). It is likely that each transmission event will occur at the smallest possible energy consumption, which provides a natural selection criterion for the outgoing slip system, when the incoming one is known.

The task now consists in identifying the abutting (outgoing) slip system on the other side of the boundary, which provides the closest geometrical match to the inbound slip system. The smallest misalignment between the active inbound and the expected outbound slip systems leads to the smallest possible energy barrier.[9] For an arbitrary transmission event, it is obvious that some incoming slip system does not, as a rule, match a corresponding one on the outbound side exactly, that is,

---

9) It is not actually checked whether or not this slip system can be activated by the local stress but it is assumed in a somewhat simplifying fashion that this will be possible, as the slip system orientation is close to that of the inbound one.

the shear is usually not coherent on the two sides of a grain boundary. Therefore, to meet the requirement of the conservation of the lattice defect vector sum when crossing an interface, certain misfit dislocations will be created in the grain boundary. The energy required to produce such an extra misfit dislocation is taken as an additional energy barrier measure for this thermally activated slip transmission event.

One should emphasize that this transmission event provides a method to quantify the penalty energy required for such a situation. However, it should be interpreted in a somewhat more statistical manner. This means that it is not required to yield a strict one-to-one correlation between incoming and outgoing dislocations rather than a match in the overall shear on either side. Moreover, it is conceivable that the transmission event only rarely takes place owing to the local stiffening effect that it introduces. Along with this grain boundary hardening effect, the accumulation of GNDs in front of the interfaces increases the local stiffness. A final remark concerns the misfit dislocations. Although they serve as a means to quantify the penalty energy, they will very likely not be stored but be dissolved by some relaxation process in the grain boundary. This implies that there will be no accumulation of misfit dislocations in the boundary, which would alter the process for newly incoming dislocations. The mathematical treatment of this dislocation-based approach to grain boundary effects in the CPFE framework is discussed in the following paragraphs. For the slip transmission to occur, the dislocation line directions have to align with $\mathbf{t}'^\alpha$ and $\mathbf{t}'^\beta$ on the two sides of the boundary, respectively, as illustrated in Figure 6.1. Conservation of the lattice defect, as expressed by the dislocation tensor, requires

$$b_{\mathrm{GB}}^{\alpha\beta} l_{\mathrm{GB}}^{\alpha\beta} \left(\mathbf{m}_{\mathrm{GB}}^{\alpha\beta} \otimes \mathbf{t}_{\mathrm{GB}}^{\alpha\beta} \right) = b^\alpha l^\alpha \left(\mathbf{m}^\alpha \otimes \mathbf{t}'^\alpha \right) - b^\beta l^\beta \left(\mathbf{m}^\beta \otimes \mathbf{t}'^\beta \right) , \qquad (6.35)$$

where b and l denote the length of Burgers vectors and line segments, respectively, and the index "GB" refers to the GBD, that is, to the debris which remains in or at the grain boundary upon slip penetration. The energy of forming this misfit dislocation at the grain boundary fulfills the inequality

$$\mu \left(b_{\mathrm{GB}}^{\alpha\beta} \right)^2 l_{\mathrm{GB}}^{\alpha\beta} \geq \mu (b^\alpha)^2 l^\alpha - \mu (b^\beta)^2 l^\beta . \qquad (6.36)$$

As both mobile dislocations in grains I and II are crystal lattice dislocations, it is assumed that they have equal energies; therefore, the additional energy for the transmission event is the energy stored in the GBD formed during the process. The final task is to identify for every slip system α of crystal I a slip system β in crystal II with the boundary condition that the energy of the GBD is minimized upon the slip transmission:

$$E_{\mathrm{GB}}^{\alpha\beta} = \min_\beta \left\{ \frac{1}{2} \mu \left(b_{\mathrm{GB}}^{\alpha\beta} \right)^2 l_{\mathrm{GB}}^{\alpha\beta} \right\} . \qquad (6.37)$$

One has to determine $b_{\mathrm{GB}}^{\alpha\beta} \mathbf{m}_{\mathrm{GB}}^{\alpha\beta}$ and $l_{\mathrm{GB}}^{\alpha\beta} \mathbf{t}_{\mathrm{GB}}^{\alpha\beta}$ in such a way that Eq. (6.35) is fulfilled. However, as one is interested in the activation energy (Eq. (6.37)) only, it is sufficient to focus on the magnitudes of the left-hand-side and the right-hand-side of

Eq. (6.35), which read

$$b_{\text{GB}}^{\alpha\beta} l_{\text{GB}}^{\alpha\beta} = \| b^\alpha l^\alpha (\mathbf{m}^\alpha \otimes \mathbf{t}'^\alpha) - b^\beta l^\beta (\mathbf{m}^\beta \otimes \mathbf{t}'^\beta) \| . \tag{6.38}$$

This expression does not have a unique solution as discussed by Ma, Roters, and Raabe (2006a,b). Whenever a pair of $b_{\text{GB}}^{\alpha\beta}$ and $l_{\text{GB}}^{\alpha\beta}$ satisfies Eq. (6.38), any scaled pair $b_{\text{GB}}^{\alpha\beta} c'$ and $l_{\text{GB}}^{\alpha\beta}/c'$, with c' being an arbitrary constant, would also be a valid solution. However, when Eq. (6.37) is used to calculate $E_{\text{GB}}^{\alpha\beta}$, the result would change by a factor c'. Certain assumptions can be made to solve this problem. Since dislocation penetration is achieved by rotation and climb inside the grain boundary plane, it is viable to assume that the segments of the incoming and outgoing dislocations have the same length:

$$l = l^\alpha = l^\beta . \tag{6.39}$$

Additionally, it is assumed that the magnitude of the Burgers vector of the GBD debris is a constant fraction of the lattice Burgers vector,

$$b = b^\alpha = b^\beta = b_{\text{GB}}^{\alpha\beta}/c'_9 . \tag{6.40}$$

Putting both Eq. (6.39) and Eq. (6.40) into Eq. (6.38) allows to express the total length of the GBD as

$$l_{\text{GB}}^{\alpha\beta} = \frac{R^{\alpha\beta}}{c'_9} l, \quad \text{with} \tag{6.41}$$

$$R^{\alpha\beta} = \left\| \mathbf{m}^\alpha \otimes (\mathbf{n}_{\text{GB}} \times \mathbf{n}^\alpha) - \mathbf{m}^\beta \otimes \left(\mathbf{n}_{\text{GB}} \times \mathbf{n}^\beta \right) \right\| . \tag{6.42}$$

Furthermore, the energy for the activation event of one segment of an incoming dislocation with length l^α then follows as

$$E_{\text{GB}}^{\alpha\beta} = \min_\beta \left\{ c'_9 \frac{1}{2} \mu b^2 l R^{\alpha\beta} \right\} . \tag{6.43}$$

It is worthwhile mentioning at this point that although the absolute magnitude of $E_{\text{GB}}^{\alpha\beta}$ can be changed by the choice of c'_9, the ratio of the activation energies for different boundaries is not affected by this value.

As an example, the activation energies of an incoming dislocation with segment length b are calculated for twist boundaries which are characterized by rotations about the [111] and [110] crystal directions, respectively, under the additional constraint that the grain boundary plane is perpendicular to the rotation axes. The calculations apply for the fcc crystal structure. The results are shown in Figures 6.2 and 6.3, where the activation energy has been normalized by the factor $\frac{1}{2}\mu b^3$ and the constant c'_9 was set to 1. Both figures also show the average of the energy barrier for better comparison. From these curves it is clear that a grain boundary is a strong obstacle to dislocation motion, as the average activation energies for the formation of the misfit dislocations easily reach the order of magnitude of the activation energy for cutting forest lattice dislocations.
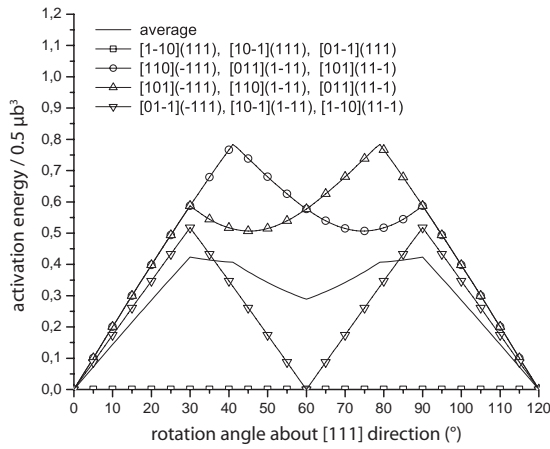
Figure 6.2 Activation energy for the twist grain boundary with rotations about the [111] direction using $c_9' = 1$ in Eq. (6.43).
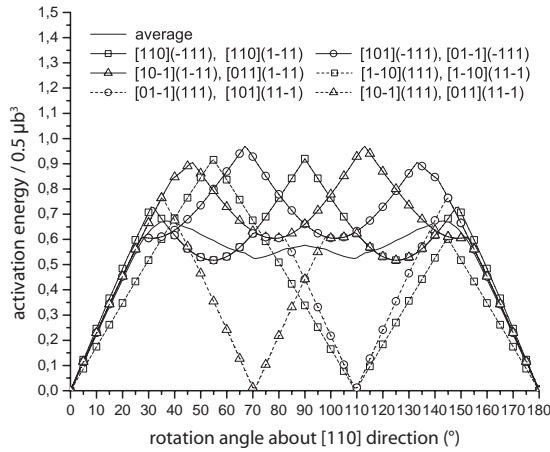
Figure 6.3 Activation energy for the twist grain boundary with rotations about the [110] direction using $c_9' = 1$ in Eq. (6.43).

It is observed that the energies for the slip penetration show a periodic behavior. This periodicity arises from the octahedral symmetry of the slip systems in the crystal. The activation energy for the penetration shows a complicated relationship with the misorientation, especially when the rotation angle is larger than about 20°. One can see that the energy barrier strongly depends on the misorientation of the two crystals. However, the average activation energies show a much more constant behavior, which implies that the strong effects for single slip systems will be averaged out to some extent in macroscopic experiments.

Finally, one has to consider two special situations. First, when the grain boundary plane is parallel to the slip plane of the incoming dislocation, the energy barrier is
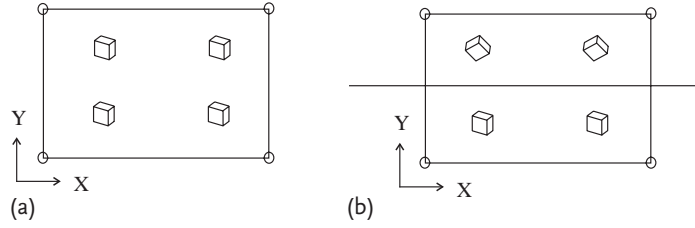
Figure 6.4 Two-dimensional representation of the bulk element (a) and of the grain boundary element (b) for the initial case. During the deformation, for the bulk element grain boundary dislocations should keep the continuity of the lattice in *X* and *Y* directions, whereas for the grain boundary element the lattice continuity is only kept in the *X* direction; in the *Y* direction the penetration energy is introduced.

set to zero, because the mobile dislocation does not penetrate the grain boundary, but it moves parallel to the plane. Second, when the plane of the outgoing dislocation is parallel to the grain boundary, $\mathbf{l}^{\beta'}$ can be set parallel to $\mathbf{l}^{\alpha'}$ as there is no intersection line with the grain boundary.

In summary, the approach provides an obstacle strength imposed by the presence of a grain boundary which does not only depend on the grain boundary misorientation but also depends on the grain boundary plane orientation ($\mathbf{n}_{\mathrm{GB}}$) and on the slip systems involved on either side of the interface.

In most CPFE implementations grain boundaries coincide with element boundaries. In the dislocation-based approach discussed above a special type of element across the grain boundary is introduced. In this element half of the Gauss points belong to one crystal, and the other half belong to the other crystal, see Figure 6.4a and b. In this new type of element one can use a modified version of Eq. (6.16), namely,

$$
v^\alpha = \lambda^\alpha v_{\mathrm{attack}} \exp\left(-\frac{Q_{\mathrm{eff}}^\alpha}{k_{\mathrm{B}} T}\right) \sinh\left(\frac{\tau_{\mathrm{eff}}^\alpha V^\alpha}{k_{\mathrm{B}} T}\right) \mathrm{sgn}\left(\tau^\alpha\right), \tag{6.44}
$$

where Q_{eff}^α is the modified effective activation energy

$$
Q_{\mathrm{eff}}^\alpha = Q_{\mathrm{slip}} + Q_{\mathrm{GB}}^\alpha . \tag{6.45}
$$

When comparing this equation with the one specified in Section 6.1.3.1, the only difference is the use of Q_{eff}^α instead of Q_{slip}. The energy Q_{GB}^α is calculated according to Eq. (6.43) as

$$
Q_{\mathrm{GB}}^\alpha = \min_{\beta} c_9 \frac{1}{2} \mu b^3 R^\alpha , \tag{6.46}
$$

where c_9 is a dimensionless fitting parameter which is a function of c_9' and the grain boundary element thickness L_{GB}.

Modifying the activation energy for an individual dislocation jump in Eq. (6.44) implies that the boundary is overcome in a single jump. The activation area for
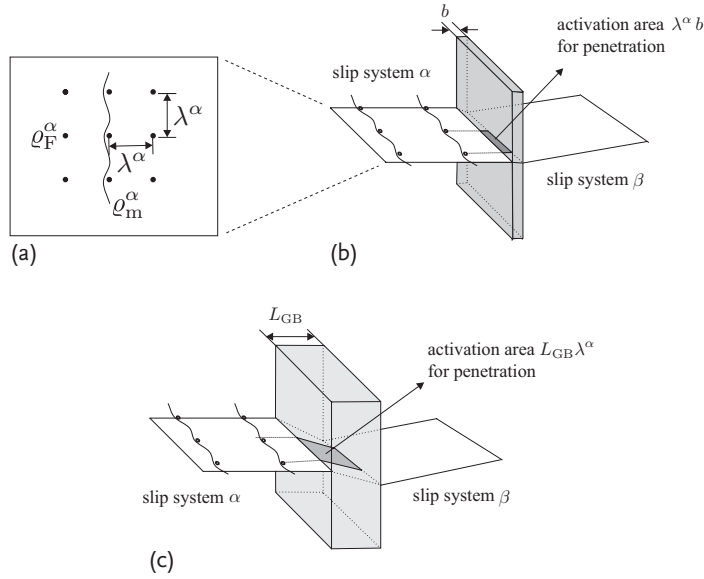
Figure 6.5 The combination of penetration through grain boundaries and forest dislocation cutting: (a) the cutting mechanism, (b) the penetration of a perfect grain boundary, and (c) the finite element method treat-ment of mixing the two processes. $\varrho_{\mathrm{m}}^{\alpha}$ is the mobile dislocation density for slip system α, $\varrho_{\mathrm{F}}^{\alpha}$ is the forest dislocation density, λ^{α} is the average obstacle spacing, and L_{GB} is the thickness of the grain boundary element.

this event is of the order $\lambda^{\alpha} b$. In this expression λ^{α} is the trapping length of the mobile dislocation (see Figure 6.5a) and b is the magnitude of the lattice Burgers vector, which is used as an obstacle width for the piercing dislocation density. However, when simply adding the activation energies, one uses the same activation area for the transmission event. Therefore, if one treats Eq. (6.46) in such way that the length of the transmitted dislocations equals λ^{α}, the element thickness of the boundary element should amount to a value close to b (see Figure 6.5b). If one further starts with a mesh of brick elements, the element volume ($b\lambda^{\alpha}\lambda^{\alpha}$) would be of the order of 1 μm³ or less. Even if one uses small samples in the millimeter size range, this would mean that about one billion elements are required to mesh such a specimen. This number is out of range for practical applications.

The only way to circumvent this problem is to increase the element thickness to L_{GB} (Figure 6.5c). When $L_{\mathrm{GB}} \approx \lambda^{\alpha}$ is used, the dislocation length dependence of Eq. (6.43) can be avoided and the activation energy required for a dislocation penetration event would then have the same order of magnitude as that required for forest dislocation cutting, Figures 6.2 and 6.3. For this case one obtains $c_9 = c_9'$. When a grain boundary element with a thickness different from λ^{α} is used, the fitting parameter is adjusted as follows:

$$c_9 = c_9' \frac{\lambda^{\alpha}}{L_{\mathrm{GB}}} \ . \tag{6.47}$$

It has to be mentioned though that this is a purely empirical calibration adjustment to realize the use of larger finite elements. Another weak point of placing the grain boundary inside an element rather than on the element boundary is that although this works well for the simulation of bicrystals (see Section 9.6), it is rather difficult to mesh more complex grain geometries.

6.2
Displacive Transformations

6.2.1
Introduction

The preceding sections focused on dislocations as carriers of plastic shear. However, materials such as austenitic steels, transformation-induced-plasticity (TRIP) steels, brass, twinning-induced-plasticity (TWIP) steels, and shape-memory alloys deform not only by dislocation slip but also by displacive deformation mechanisms (also referred to as displacive transformations). These mechanisms are characterized by a diffusionless, collective motion of clusters of atoms where each atom is shifted only by a small distance relative to its neighbors. Such transformations create shears with kinematics similar to that of dislocation motions.

Two such mechanisms and their incorporation into the CPFE framework will be discussed here, namely, martensite formation (Lan *et al.*, 2005; Thamburaja and Anand, 2001) and mechanical twinning (Kalidindi, 1998; Marketz *et al.*, 2002; Salem, Kalidindi, and Semiatin, 2005; Staroselsky and Anand, 1998). A martensitic transformation changes the lattice structure of a crystal. The resulting shape change involves, as a rule, also a change in the unit cell volume, that is, a volume dilatation or contraction. Mechanical twinning proceeds by a shear mechanism which reorients the affected volume into a mirror orientation relative to the surrounding matrix. We discuss how the CPFE approach can be modified to include these mechanisms and how the interactions among the competing shear carriers can be considered in the constitutive formulations.

6.2.2
Martensite Formation and Transformation-Induced Plasticity in CPFE Models

As one possible material where the deformation kinetics are supported by martensite formation, we select TRIP-assisted multiphase steels. In these materials, the presence of metastable retained austenite grains is responsible for the strength–ductility characteristics (Jacques, Ladrière, and Delannay, 2001). Under mechanical and/or thermal loading, retained austenite may transform into martensite and generate the TRIP effect. Investigations of the TRIP effect were initiated by Greenwood and Johnson (1965), who observed irreversible plastic deformations at a stress lower than the theoretical yield stress of the material. It has been suggested that the additional plastic deformation of the material is induced by the volume dilata-

tion accompanying the transformation of retained austenite into martensite (see, e.g., Fischer *et al.* (2000)). In the same year, Patel and Cohen (1953) observed that the martensite forming during transformation develops in that preferential orientation which has the maximum transformation driving force.

A crystallographic model for the kinematics of martensitic transformations was proposed by Wechsler, Lieberman, and Read (1953). This concept was refined by Ball and James (1987), who further developed the modeling concept within the energy minimization landscape. During the last few decades, various constitutive models for martensitic transformations have been elaborated, such as the one-dimensional model of Olson and Cohen (1975), which was extended into a three-dimensional model by Stringfellow, Parks, and Olson (1992). Lately, a fair number of more complex micromechanical models were suggested, for example, by Bhattacharyya and Weng (1994); Cherkaoui, Berveiller, and Lemoine (2000); Cherkaoui, Berveiller, and Sabar (1998); Diani and Parks (1998); Diani, Sabar, and Berveiller (1995); Geers and Kouznetsova (2007); Leblond, Mottet, and Devaux (1986a,b); Levitas, Idesman, and Olson (1999a); Levitas, Idesman, and Stein (1999b); Marketz and Fischer (1994, 1995); Tomita and Iwamoto (1995, 2001). These models have been used in particular for the simulation of TRIP steels. However, a major drawback in most of the models mentioned above is that they were derived for a small-strain framework. This can lead to inaccurate predictions as martensite transformations induce locally large elastic and plastic deformations, even if the effective macroscopic deformation is relatively small. Furthermore, an *isotropic* elastoplastic response is often assumed as a simplification. This constraint is quite strong, especially when one is concerned with the single-crystal scale, where the effect of crystallographic anisotropy cannot be neglected.

In the following sections, we elucidate a crystallographically based thermomechanical model for simulating the behavior of multiphase TRIP-assisted steels. The phase transformation model of Suiker and Turteltaub (2005); Turteltaub and Suiker (2005, 2006a) is applied to simulate the transformation of fcc austenite into body-centered tetragonal martensite. This model is developed within a multiscale framework and uses the results from the above-mentioned crystallographic theory of martensitic transformations (Ball and James, 1987; Wechsler, Lieberman, and Read, 1953). The martensitic transformation model is coupled to a single-crystal plasticity model for fcc metals to account for plastic deformation in austenite. The coupling between the transformation and plasticity models is derived using a thermodynamically consistent framework.

6.2.2.1 Decompositions of Deformation Gradient and Entropy Density

The total deformation gradient $\mathbf{F}$ and the total entropy density η can be decomposed into the respective elastic, plastic, and transformation parts:

$$\mathbf{F} = \mathbf{F}_e \mathbf{F}_p \mathbf{F}_{tr} \quad \text{and} \quad \eta = \eta_e + \eta_p + \eta_{tr} . \tag{6.48}$$

Figure 6.6 gives an illustration of the deformation gradient decomposition with two intermediate configurations: the first one characterizes the material point after partly undergoing martensitic transformation, whereas the second intermediate
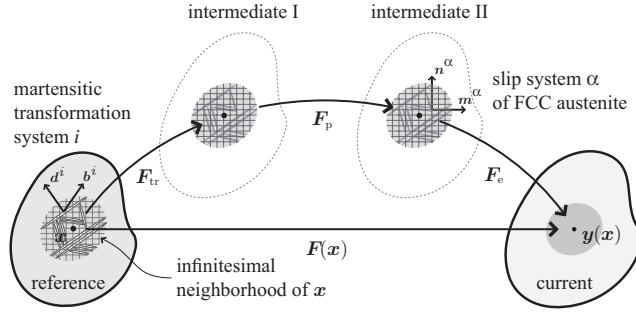
Figure 6.6 The four configurations and the corresponding decomposition of deformation gradient **F** into the elastic, plastic, and transformation parts.

configuration corresponds to the elastically unloaded configuration already introduced in Section 3.1.6.

The transformation part, $\mathbf{F}_{\mathrm{tr}}$, of the deformation gradient and the transformation entropy density, η_{tr}, for a total number of M possible transformation systems are given by

$$\mathbf{F}_{\mathrm{tr}} = \mathbf{I} + \sum_{i=1}^{M} \xi^i \mathbf{b}^i \otimes \mathbf{d}^i \quad \text{and} \quad \eta_{\mathrm{tr}} = \sum_{i=1}^{M} \xi^i \frac{\lambda_{\mathrm{tr}}^i}{\theta_{\mathrm{tr}}} . \tag{6.49}$$

Vectors $\mathbf{b}^i$ and $\mathbf{d}^i$ denote, respectively, the transformation shape strain vector and the unit normal to the habit plane of transformation system i (measured in the reference configuration). $\mathbf{I}$ is the second-order identity tensor and θ_{tr} is the (theoretical) transformation temperature at which transformation occurs instantaneously without any stress (no energy barrier, no dissipation). The latent heat, λ_{tr}^i, quantifies the heat per unit mass required to transform at θ_{tr}. In Eq. (6.49), ξ^i represents the fraction of the crystal volume which underwent transformation in system i, measured in the reference configuration and satisfying the following requirements:

$$0 \leq \xi^i \leq 1 , \quad 0 \leq \sum_{i=1}^{M} \xi^i \leq 1 \quad \text{and} \quad \xi_{\mathrm{A}} = 1 - \sum_{i=1}^{M} \xi^i , \tag{6.50}$$

with ξ_{A} the (remaining) volume fraction of austenite, again measured in the reference configuration. In the case of the transformation from fcc austenite to body-centered tetragonal martensite, the total number of possible transformation systems is $M = 24$.

As a simplification, it is assumed that dislocation plasticity occurs exclusively in austenite but not in martensite owing to its high yield resistance. Furthermore, plastic deformations that occurred within austenite prior to its transformation to martensite are assumed to be inherited by the resulting martensitic phase from the austenitic parent phase. Accordingly, the evolution of the plastic deformation gradient $\mathbf{F}_{\mathrm{p}}$ (given in terms of the plastic velocity gradient $\mathbf{L}_{\mathrm{p}}$) and that of the plastic

entropy density η_{p} are described, in rate forms, by

$$\mathbf{L}_{\mathrm{p}} = \dot{\mathbf{F}}_{\mathrm{p}} \mathbf{F}_{\mathrm{p}}^{-1} = \sum_{\alpha=1}^{N_{\mathrm{A}}} \dot{\gamma}^{\alpha} \mathbf{m}_{\mathrm{A}}^{\alpha} \otimes \mathbf{n}_{\mathrm{A}}^{\alpha} \quad \text{and} \quad \dot{\eta}_{\mathrm{p}} = \sum_{\alpha=1}^{N_{\mathrm{A}}} \dot{\gamma}^{\alpha} \phi_{\mathrm{A}}^{\alpha}, \tag{6.51}$$

where the vectors $\mathbf{m}_{\mathrm{A}}^{\alpha}$ and $\mathbf{n}_{\mathrm{A}}^{\alpha}$ are, respectively, unit vectors describing the slip direction and the normal to the slip plane of the corresponding system in fcc austenite (measured in the second intermediate configuration) and $\phi_{\mathrm{A}}^{\alpha}$ is interpreted as the entropy density related to plastic deformation per unit slip in system α. The number of slip systems in the austenitic phase is denoted by $N_{\mathrm{A}} = 12$. In the above expressions, $\dot{\gamma}^{\alpha}$ can be interpreted as the "effective" plastic slip rate of austenitic slip system α, which is given by $\dot{\gamma}^{\alpha} = \xi_{\mathrm{A}} \dot{\gamma}_{\mathrm{A}}^{\alpha} / J_{\mathrm{tr}}$, with $\dot{\gamma}_{\mathrm{A}}^{\alpha}$ the rate of slip for system α in austenite and $J_{\mathrm{tr}} = \det \mathbf{F}_{\mathrm{tr}}$.

6.2.2.2 Constitutive Relations of Stress–Elastic Strain and Temperature–Reversible Entropy

The constitutive relations between conjugated variables, that is, stress and elastic strain as well as temperature and reversible entropy, are defined by

$$\mathbf{S} = \mathbb{C} \mathbf{E}_{\mathrm{e}} \quad \text{and} \quad \eta_{\mathrm{e}} = h \ln \left(\frac{\theta}{\theta_{\mathrm{tr}}} \right) + \eta_{\mathrm{rev}}, \tag{6.52}$$

where $\mathbf{S}$ is the second Piola–Kirchhoff stress in the second intermediate configuration, which is conjugated to the elastic Green's Lagrangian strain $\mathbf{E}_{\mathrm{e}}$. Temperature is denoted by θ and η_{rev} is the reversible entropy measured at the transformation temperature, that is, at $\theta = \theta_{\mathrm{tr}}$. The effective elasticity tensor $\mathbb{C}$ and the effective specific heat h comprise volumetrically averaged contributions of the individual austenitic and martensitic phases:

$$\mathbb{C} = \frac{1}{J_{\mathrm{tr}}} \left(\xi_{\mathrm{A}} \mathbb{C}_{\mathrm{A}} + (1 + \delta_{\mathrm{tr}}) \sum_{i=1}^{M} \xi^{i} \mathbb{C}^{i} \right) \quad \text{and} \quad h = \xi_{\mathrm{A}} h_{\mathrm{A}} + \sum_{i=1}^{M} \xi^{i} h^{i}, \tag{6.53}$$

where $\delta_{\mathrm{tr}} = \mathbf{b}^{i} \cdot \mathbf{d}^{i}$ gives the (system-independent) volume dilatation associated with each transformation system. Note that the effective elasticity tensor $\mathbb{C}$ and the effective specific heat h evolve with the martensitic volume fractions ξ^{i} during transformation.

6.2.2.3 Driving Forces and Kinetic Relations for Transformation and Plasticity

The driving force for the phase transformation, denoted as f^{i}, can be written as

$$f^{i} = f_{\mathrm{m}}^{i} + f_{\mathrm{th}}^{i} + f_{\mathrm{d}}^{i} + f_{\mathrm{s}}^{i}, \tag{6.54}$$

where f_{m}^{i}, f_{th}^{i}, f_{d}^{i}, and f_{s}^{i} summarize, respectively, the mechanical, thermal, defect, and surface energy contributions to the transformation driving force. The me-

chanical part of the transformation driving force, f_{m}^i, is computed as

$$
\begin{aligned}
f_{\mathrm{m}}^i = {} & J_{\mathrm{tr}} \mathbf{F}_{\mathrm{p}}^{\mathrm{T}} \mathbf{F}_{\mathrm{e}}^{\mathrm{T}} \mathbf{F}_{\mathrm{e}} \mathbf{S} \mathbf{F}_{\mathrm{p}}^{-\mathrm{T}} \mathbf{F}_{\mathrm{tr}}^{\mathrm{T}} \cdot (\mathbf{b}^i \otimes \mathbf{d}^i) \\
& + \frac{1}{2} \left(\mathbb{C}_{\mathrm{A}} - (1 + \delta_{\mathrm{tr}}) \, \mathbb{C}^i \right) \mathbf{E}_{\mathrm{e}} \cdot \mathbf{E}_{\mathrm{e}} \,,
\end{aligned}
\tag{6.55}
$$

which comprises the contribution of the resolved stress and the elastic stiffness mismatch between the martensite product phase and the austenite parent phase with stiffness $\mathbb{C}_{\mathrm{A}}$. The thermal part of the transformation driving force, f_{th}^i, describes the contribution of the mismatch of the specific heat between martensite and austenite as well as the transformation latent heat, that is,

$$
f_{\mathrm{th}}^i = \rho_0 \left(h_{\mathrm{A}} - h^i \right) \left(\theta - \theta_{\mathrm{tr}} - \theta \ln \left(\frac{\theta}{\theta_{\mathrm{tr}}} \right) \right) + \rho_0 \frac{\lambda_{\mathrm{tr}}^i}{\theta_{\mathrm{tr}}} (\theta - \theta_{\mathrm{tr}}) \,,
\tag{6.56}
$$

with ρ_0 being the mass density in the reference configuration. The defect and surface energy contributions are, respectively, given by

$$
f_{\mathrm{d}}^i = \frac{\omega_{\mathrm{A}}}{2} \left(\mu_{\mathrm{A}} - (1 + \delta_{\mathrm{tr}}) \mu^i \right) \beta^2 \quad \text{and} \quad f_{\mathrm{s}}^i = \frac{\chi}{\ell_0} \left(2\xi^i - 1 \right) \,,
\tag{6.57}
$$

with ω_{A} a scaling factor for the defect energy, β the microstrain parameter related to the density of dislocations in the austenitic/martensitic region, χ an interfacial energy per unit area, and ℓ_0 a length-scale parameter representing the volume-to-surface ratio of a circular platelet of martensite within a spherical grain of austenite. In Eq. (6.57), μ_{A} and μ^i represent the (equivalent) shear moduli of austenite and of martensite variant i, respectively. The evolution of the martensite fraction during transformation follows the rate-dependent kinetic formulation:

$$
\dot{\xi}^i =
\begin{cases}
\dot{\xi}_0 \tanh \left(\dfrac{f^i - f_{\mathrm{cr}}^i}{\nu f_{\mathrm{cr}}^i} \right) & \text{if} \quad f^i > f_{\mathrm{cr}}^i \,, \\
0 & \text{otherwise} \,,
\end{cases}
\tag{6.58}
$$

where f_{cr}^i stands for the critical value of the transformation driving force. The parameters $\dot{\xi}_0$ (maximum transformation rate) and ν (viscosity-like parameter) determine the rate dependence of the transformation kinetic law.

The driving force, g_{A}^α, for plastic slip in the austenitic phase is obtained from the thermodynamic formulation as

$$
g_{\mathrm{A}}^\alpha = \mathbf{F}_{\mathrm{e}}^{\mathrm{T}} \mathbf{F}_{\mathrm{e}} \mathbf{S} \cdot \left(\mathbf{m}_{\mathrm{A}}^\alpha \otimes \mathbf{n}_{\mathrm{A}}^\alpha \right) + \rho_0 \theta \, \phi_{\mathrm{A}}^\alpha - \omega_{\mathrm{A}} \mu \beta w^\alpha \,,
\tag{6.59}
$$

where μ is the effective shear modulus, which is computed using a technique similar to that used for the effective elasticity tensor, that is,

$$
\mu = \frac{1}{J_{\mathrm{tr}}} \left(\xi_{\mathrm{A}} \mu_{\mathrm{A}} + (1 + \delta_{\mathrm{tr}}) \sum_{i=1}^{M} \xi^i \mu^i \right) \,.
\tag{6.60}
$$

Furthermore, w^α is a function that relates the rate of microstrain $\dot\beta$ to the plastic slip rates $\dot\gamma^\alpha$ as $\dot\beta = \sum_{\alpha=1}^{N_A} w^\alpha \dot\gamma^\alpha$. Finally, the evolution of plastic slip in the austenitic phase is described using a power-law kinetic relation of the form

$$\dot\gamma_A^\alpha = \begin{cases} \dot\gamma_{A,0}\left(\left(\dfrac{g_A^\alpha}{s_A^\alpha}\right)^{n_A} - 1\right) & \text{if} \quad g_A^\alpha > s_A^\alpha \, , \\ 0 & \text{otherwise} \, , \end{cases} \tag{6.61}$$

where s_A^α is the resistance against plastic slip on system α. The evolution of the slip resistance is described through a hardening law where $\dot\gamma_{A,0}$ and n_A are the reference slip rate and the stress exponent, respectively. More details on the austenite elastoplastic-transformation model are reported in Tjahjanto, Turteltaub, and Suiker (2008).

6.2.3
Mechanical Twinning in CPFE Models

Arbitrary permanent changes of shape of a single crystal require the operation of any five linearly independent shear systems (Taylor, 1938). However, the number of *easily* activated slip systems of a given crystal structure may be insufficient to fulfill this requirement. Thus, alternative displacive modes, for instance, mechanical twinning, can also participate in the overall plastic deformation. Low-symmetry crystal structures, for example, hexagonal crystals with large c/a ratio, are typical examples for this situation. Also, cubic metals may exhibit mechanical twinning owing to a relatively strong increase in the critical shear stress at low temperatures and the rate dependence of slip in the case of bcc materials and owing to a low value of the stacking fault energy in the case of fcc materials (Hirth and Lothe, 1982).

A mechanical twin formally corresponds to a sheared volume for which the lattice orientation is transformed into its mirror image across a so-called *twin* or *composition* or *habitus plane* (central dividing plane in Figure 6.7 between parent and twin). A vector of the initial lattice is moved into its new position in the twin through a transformation/rotation matrix **Q**. The same expression for **Q** was derived for bcc and fcc twins (Hirth and Lothe, 1982; Van Houtte, 1978), exploiting the equivalence of rotating half of the crystal by an angle π either around the twin direction or around the twin normal:

$$\mathbf{Q} = 2\mathbf{n} \otimes \mathbf{n} - \delta_{ij} \, , \tag{6.62}$$
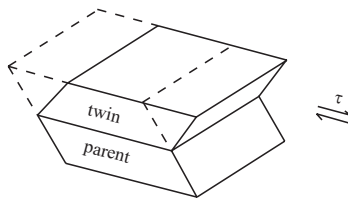

Figure 6.7 Under an applied stress, half of the initial volume (dashed lines) shears to form a twin (solid lines) (after Hirth and Lothe (1982)).

where **n** is the twin plane unit normal and δ_{ij} is Kronecker's symbol. Alternatively, twinning can be viewed as unidirectional shear on the habitus plane, that is, formally similar to bidirectional dislocation slip. In this framework, fcc twins are of type $\{111\}\langle112\rangle$, bcc twins are of type $\{112\}\langle111\rangle$, and hexagonal twins are of type $\{10\bar{1}2\}\langle10\bar{1}1\rangle$. Although strain-induced twinning has been investigated for years (Christian and Mahajan, 1995), most of its governing physical mechanisms still remain unclear. Numerous studies aimed at identifying the influence of the boundary conditions on mechanical twinning have placed attention on temperature, grain size, and stacking fault energy and their respective influence on twin nucleation and growth. Some of the results which are required to derive corresponding micromechanical models are summarized in the following.

- *Temperature and strain rate* In most crystal structures twinning gains relevance as the temperature is lowered and/or the strain rate is increased. The temperature dependence is often explained by the fact that the flow stress increases steeply with decreasing temperature (in bcc metals), so finally the twin stress is reached (Hirth and Lothe, 1982). The temperature dependence of the twin stress is under debate in the literature. Bolling and Richman (1965) and Köster and Speidel (1965) found a negative temperature dependence of the twinning stress in fcc crystals, whereas Mahajan and Williams (1973) suggested for the same structure the opposite trend. Contradictory observations have also been reported for other crystal structures, so the current state of knowledge seems insufficient to reach a definitive conclusion, as pointed out by Venables (1964). Only a few investigations have addressed the strain rate dependence on the twinning stress (Harding, 1967, 1968; Hokka *et al.*, 2006).
- *Grain size* Armstrong and Worthington (1973) were the first to propose a link between the increase in the twinning stress and the decrease of the grain size by means of a Hall–Petch-type relation. Later experimental studies on different materials and structures (El-Dana, Kalidindi, and Doherty, 1998; Meyers, Andrade, and Chokshi, 1995; Song and Gray, 1995; Vöhringer, 1976) supported this suggestion. It is worth noting that the so-called twin slope, that is, the dependence of twin activation on the grain size, is often found to be much higher than the corresponding slope for dislocation slip (Armstrong and Worthington, 1973).
- *Stacking fault energy* It is well established that twinning occurs preferentially in materials with low stacking fault energy. With decreasing stacking fault energy it is easier to separate partial dislocations from each other. This leads to a wider stacking fault, which may eventually trigger a deformation twin. Concerning the effect of other parameters, it was proposed that the stacking fault energy increases with increasing temperature (Rémy, 1975). This might explain the apparent temperature dependence of mechanical twinning. Alternatively, the notion of an effective stacking fault energy was introduced to consider the effect of the orientation on the splitting length between partial dislocations (Karaman *et al.*, 2000b, 1998).

The preceding list of relevant parameters affecting mechanical twinning is not exhaustive since other factors, such as chemical composition, strain and stress state, and precipitates, also influence strain-induced twinning (Christian and Mahajan, 1995).

The motivation for modeling mechanical twinning in a CPFE framework echoes practical as well as fundamental demands. Interest in TWIP steels has grown rapidly over the last few years as these grades simultaneously provide high strength and good ductility. Similar aspects hold for stainless steels, magnesium alloys, and some intermetallic compounds where deformation twinning plays a role. In each of these cases an interest exists to predict the mechanical response, the microstructure evolution, and the texture by using advanced CPFE models.

To our knowledge, the first phenomenological introduction of mechanical twinning into the CPFE framework was accomplished by Doquet (1993), followed by Mecking, Hartig, and Kocks (1996) and Schlögl and Fischer (1997). The corresponding implementation into a finite element scheme was proposed by Kalidindi (1998, 2001) and was further developed in Kalidindi (2004).

6.2.3.1 A Modified CPFE Framework Including Deformation Twinning

The CPFE framework discussed in this section follows the outline introduced above. However, adding mechanical twinning as a possible plastic shear mode requires the introduction of some additional model ingredients. The activation of a twin system β implies that a fraction $\mathrm{d} f^{\beta}$ of the single crystalline parent volume (matrix) reorients by $\mathbf{Q}^{\beta}$. Figure 6.8 illustrates the decomposition of the global deformation gradient $\mathbf{F}$ when a twin system operates. Considering the formal similarity between slip and mechanical twinning, the velocity gradient $\mathbf{L}_{\mathrm{p}}$ is extended by the contribution due to the characteristic twin shear[10] γ_{twin} to read

$$\mathbf{L}_{\mathrm{p}} = \left(1 - \sum_{\beta=1}^{N_{\mathrm{twin}}} f^{\beta}\right) \sum_{\alpha=1}^{N_{\mathrm{slip}}} \dot{\gamma}^{\alpha} \mathbf{m}^{\alpha} \otimes \mathbf{n}^{\alpha} + \sum_{\beta=1}^{N_{\mathrm{twin}}} \gamma_{\mathrm{twin}} \dot{f}^{\beta} \mathbf{m}_{\mathrm{twin}}^{\beta} \otimes \mathbf{n}_{\mathrm{twin}}^{\beta} , \quad (6.63)$$

where N_{slip} is the number of slip systems and N_{twin} is the number of twin systems. It should be noted that the present description does not explicitly account for the morphology and topology of the deformation twins. Instead, a twinned region is specified by its volume fraction and by the boundary condition that no explicit plastic deformation gradient is prescribed within twinned regions. The Cauchy stress $\bar{\boldsymbol{\sigma}}$ of the composite (matrix plus twins) is related to the volume average of the stress over all constituents:

$$\bar{\boldsymbol{\sigma}} = \frac{\mathbf{F}_{\mathrm{e}}}{J_{\mathrm{e}}} \left[\left(1 - \sum_{\beta=1}^{N_{\mathrm{twin}}} f^{\beta}\right) \mathbb{C} + \sum_{\beta=1}^{N_{\mathrm{twin}}} f^{\beta} \mathbb{C}^{\beta} \right] \mathbf{E}_{\mathrm{e}} \mathbf{F}_{\mathrm{e}}^{\mathrm{T}} , \quad (6.64)$$

where $\mathbb{C}_{ijkl}^{\beta} = Q_{im}^{\beta} Q_{jn}^{\beta} Q_{ko}^{\beta} Q_{lp}^{\beta} \mathbb{C}_{mnop}$ is the elasticity tensor of the matrix rotated into the respective twin orientation and $\mathbf{E}_{\mathrm{e}}$ is Green's Lagrangian strain derived
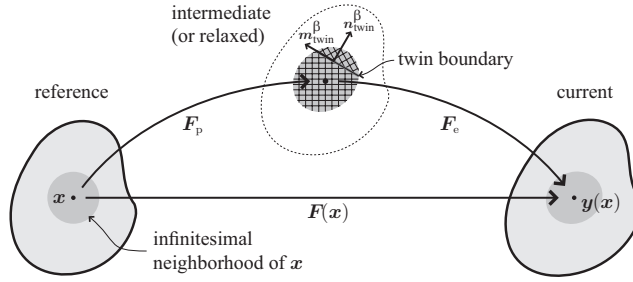
10) $\sqrt{2}/2$ for fcc and bcc crystal structures

Figure 6.8 The three configurations and the corresponding decomposition of the deformation gradient **F** into elastic and plastic contributions, modified by Kalidindi (1998, 2001) to account for mechanical twinning.

from the nonplastic deformation gradient $\mathbf{F}_e$. It is worth noting that a small homogenization error may occur when this procedure is followed, which is due to the generation of an orientation dispersion in the twinned fraction. This deviation occurs whenever the plastic spin of a twin variant is not equal to the plastic spin of the matrix. In the current case this effect does indeed take place because no plastic velocity gradient is given in the twinned regions.

The present expression for $\mathbf{L}_p$ does not consider subsequent dislocation slip within twins. This approximation is often suitable for extremely thin fcc and bcc twins. However, experimental evidence for dislocation activity in mechanical twins has been reported when twins are larger, for example in high-manganese TWIP steels (Meng *et al.*, 2007) (due to large strains) and in hexagonal metals (Mg, Zr due to small twin shear). It may, therefore, be useful to allow for dislocation slip in twinned regions. In that case, Kalidindi (2001) proposed modifying the plastic velocity gradient as follows:

$$
\mathbf{L}_p = \left(1 - \sum_{\beta=1}^{N_{\text{twin}}} f^\beta \right) \sum_{\alpha=1}^{N_{\text{slip}}} \dot{\gamma}^\alpha \mathbf{m}^\alpha \otimes \mathbf{n}^\alpha + \sum_{\beta=1}^{N_{\text{twin}}} \gamma_{\text{twin}} \dot{f}^\beta \mathbf{m}_{\text{twin}}^\beta \otimes \mathbf{n}_{\text{twin}}^\beta
$$

$$
+ \sum_{\beta=1}^{N_{\text{twin}}} \sum_{\alpha=1}^{N_{\text{slip}}} f^\beta \dot{\gamma}^\alpha \mathbf{Q}^\beta \mathbf{m}^\alpha \otimes \mathbf{n}^\alpha \mathbf{Q}^{\beta^{\mathrm{T}}} . \tag{6.65}
$$

Furthermore, the twinning of primary twins (secondary twinning) might be considered as well. At first view the modification of $\mathbf{L}_p$ appears rather straightforward. However, difficulties arise from the increase in the number of shear rates or twin volume fractions that have to be tracked in this approach, rendering such a model highly impractical. The time-integration scheme, presented in Chapter 8, remains essentially unchanged. The nonlinear equation is still expressed in terms of the second Piola–Kirchhoff stress tensor, written in the intermediate configuration, for a given microstructure, that is, for state variables that refer to both slip and twinning. Details on the numerical implementation can be found elsewhere (Kalidindi, Bronkhorst, and Anand, 1992).

6.2.3.2 Phenomenological Approach to Mechanical Twinning

The plastic velocity gradient is defined in terms of all shear rates $\dot{\gamma}^{\alpha}$ and all volume fractions created by the twinning rates $\dot{f}^{\beta}$. Phenomenological expressions of the shear rate for a slip system were introduced above. However, no theory is currently available to provide a clear function for the evolution of the twinned volume fraction for an active twin system. For this reason Kalidindi (1998) proposed using the analogy between slip and twin systems while preserving the unidirectionality of the twinning mechanism. The twin volume fraction of a system β then evolves according to a phenomenological power-law equation:

$$
\dot{f}^{\beta} = \begin{cases} \dot{f}_0 \left(\dfrac{\tau^{\beta}}{\tau_c^{\beta}} \right)^{1/m_t} & \text{if} \quad \tau^{\beta} > 0 \\[2ex] 0 & \text{otherwise .} \end{cases}
\tag{6.66}
$$

The computation of this flow rule requires the specification of a critical twinning shear stress (shear resistance) τ_c^{β} for each twin system. This is a critical point since experimental observations support the idea that mechanical twins have a "double" impact on the global strain hardening of the material. First, an increasing number of twins leads to an increasing hardening effect on slip systems since twin–matrix interfaces act as obstacles to moving dislocations. This concept is illustrated in Figure 6.9 for the fcc case. A moving matrix dislocation will most likely encounter twins that lie on planes that are noncoplanar with its glide plane, that is, only noncoplanar twin systems act as obstacles for dislocation motion. Second, the expansion of new twins is impeded by already existing twins, particularly by those which are noncoplanar with the respective twin system. Following the first idea, we can modify the phenomenological slip hardening rule:

$$
\dot{\tau}_c^{\alpha} = h_{a\tilde{a}} |\dot{\gamma}^{\tilde{a}}|,
\tag{6.67}
$$

where the hardening matrix $h_{a\tilde{a}}$ now depends on the twin volume fractions through the saturation value $\tau_s^{\tilde{a}}$,

$$
h_{a\tilde{a}} = q_{a\tilde{a}} \left[h_0 \left(1 - \frac{\tau_c^{\tilde{a}}}{\tau_s^{\tilde{a}}} \right)^a \right], \quad \text{with}
$$

$$
\tau_s^{\tilde{a}} = \tau_0 + \tau_t \left(\sum_{\beta \text{ noncoplanar with } \tilde{a}} f^{\beta} \right)^{\frac{1}{2}}.
\tag{6.68}
$$

Dislocations tend to accumulate before twin boundaries, which justifies the changes in the saturation value for the slip resistances. The Hall–Petch-like formulation that quantifies the contribution due to deformation twinning in the saturation value is derived naturally from the analogy with grain boundary hardening. It is worth noting that some later works (Salem, Kalidindi, and Semiatin, 2005) suggest not only modifying the saturation values but also modifying h_0 to account for the Basinski effect (Salem *et al.*, 2006; Salem, Kalidindi, and Semiatin,
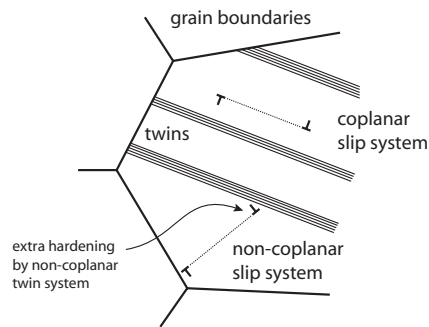
Figure 6.9 The selective hardening role of twin boundaries during dislocation motion for face-centered cubic (fcc) structures.
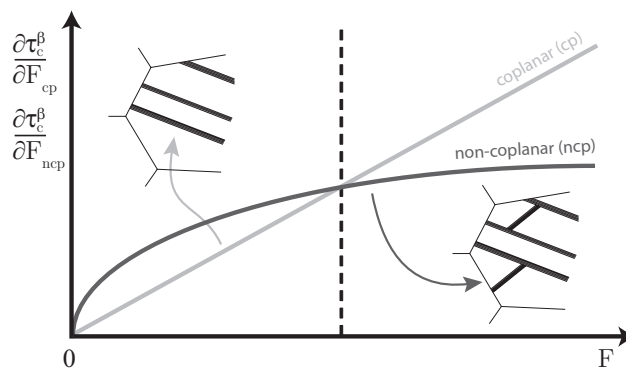

Figure 6.10 Sequential activation of twin systems and its phenomenological treatment for fcc structures. At small cumulative twin volume fractions *F*, newly forming twins harden noncoplanar twin systems more strongly than coplanar ones. Beyond a critical point (dashed line) the situation is reversed, such that coplanar systems experience a stronger hardening, which in turn favors activity of noncoplanar twins. Critical twin shear stress is denoted by τ_c^β.

2005). The second idea refers to a kind of "twin–twin" hardening behavior of the material and originates from the sequential activation of twin variants during deformation. It was often observed that in fcc metals only coplanar twins form at first in a grain. Upon a strain threshold, deformation twins that are noncoplanar with the first ones form and result in a ladderlike microstructure. This sequential activation is phenomenologically translated in terms of two power functions depending on either strain rate (Salem, Kalidindi, and Semiatin, 2005) or twin volume fraction rates (Kalidindi, 2001). The two functions cross at a given point. Below that point, newly formed twins preferentially harden noncoplanar twin systems. Beyond that point, they preferentially harden coplanar twin systems. This model approach is easy to handle and has been successfully applied to α-brass (Kalidindi, 2001), α-Ti (Salem, Kalidindi, and Semiatin, 2005), and TiAl (Schlögl and Fischer, 1997).

6.2.4

Guidelines for Implementing Displacive Transformations in CPFE Constitutive Models

This section discusses the basic constitutive and kinematic ingredients for implementing displacive shear mechanisms as additional carriers of crystallographic plastic deformation in CPFE frameworks. The challenges of rendering such models physically sound and at the same time numerically tractable seem to lie in two areas. The first one is the appropriate formulation of nucleation and growth models. The second one is the identification of appropriate homogenization methods. The first point means that nucleation and growth models should be designed in a way to capture the basic dependence of displacive transformations on thermodynamic and microstructural parameters such as temperature, grain size, strain rate, and stacking fault energy. The second point refers to the desired level of discretization. This means that in some cases multiple and repeated transformations may occur at the same integration point. This requires defining an adequate approach for tracking and homogenizing the volume portions and interaction mechanisms for different twin or martensite lamellae or corresponding higher-order transformations (e.g. twinning of twins), see Figure 5.3b.

**6.3
Damage**

6.3.1
Introduction

Computational plasticity seeks to predict the deformation processes that occur during forming materials or components used in larger assemblies, and to identify locations where damage is likely to develop during either fabrication or service; hence, methods to identify damage locations are a major goal of practical computations. A number of approaches are available to identify such locations, from simple to sophisticated. For example, loading a component will identify locations where stresses are large, and this information can be used to alter the geometry to reduce the magnitude of te stress. However, once the geometry has been established, there will still be locations that are more susceptible to damage than others, and the problem remains as to how damage develops in these regions, especially if there is no damage present in the first place. For damage that has been introduced, the evolution of its growth and its influence on unstable deformation in the neighborhood have been explored with many approaches. However, identifying criteria for damage nucleation and methods to introduce it into an undamaged computational material is an important but often elusive goal of computational plasticity.

6.3.2

Continuum Approaches to Modeling Damage

Continuum damage and fracture mechanics has provided a wealth of methods for modeling the evolution of pre-existing damage, but these methods all depend on knowing where the damage nucleated; hence, a pre-existing void or crack is normally introduced. Though this offers no cognizance of microscopic-scale processes, it has been effective in modeling stochastic aspects of damage multiplication for problems involving multiple phases or pre-existing scattered damage sites. This process is based upon damage sites being isotropically distributed in the continuum material. In these problems, once a localized region develops damage faster than a neighboring region, the degradation of properties allows prediction of locations where macroscopic failure occurs. This well-developed approach has been incorporated into the material constitutive models in finite element method computations without modeling damage sites explicitly. This homogenized damage is based upon the observation that damage reduces the bulk elastic modulus (Lemaitre and Chaboche, 1998), so damage is introduced into the elastic part of the problem,

$$\boldsymbol{\sigma} = (1 - D)\mathbb{C}\boldsymbol{\epsilon}_{\mathrm{e}} \,, \tag{6.69}$$

where the elastic stress $\boldsymbol{\sigma}$ evaluated from the elastic strain $\boldsymbol{\epsilon}_{\mathrm{e}}$ and stiffness $\mathbb{C}$ is reduced by a factor $(1 - D)$. The plastic response to this damage effect follows indirectly from the degraded elastic load carrying capability. For isotropic damage generation, D is a scalar quantity. Many have recognized that damage represented by D is not isotropic, and have introduced vectorial and tensorial modifications to this idea to simulate failure processes associated with crystallographic planes, intergranular fracture, or growth and distortion of voids (Brunig and Ricci, 2005; Luccioni and Oller, 2003; Menzel *et al.*, 2005; Voyiadjis and Dorgan, 2007). However, because these more sophisticated damage shape functions ultimately depend on microstructural heterogeneities such as grain or phase boundaries and the directionality of slip systems, these sophisticated descriptions of D should be informed by the known slip system, crystal orientation, and microstructural characteristics of the material.

Other approaches examine the effect of specific damage sites in a finite element method model. For example, the effects of clustering of hard phases in metal matrix composites, and deformation of porous materials have been modeled using Eshelby inclusions (Wilkinson, Pompe, and Oeschner, 2001). A more common approach is to introduce pores into a mesh because damage sites often result in formation of a pore; for example, when a microcrack exists in a hard particle and the crack grows into the ductile surrounding matrix, but blunted by plastic deformation processes. Such sites can be modeled as pores distributed in a continuum, and then a homogeneous damage evolution process as described above is used to model the degradation of load carrying capability in regions between defect sites. This approach allows the study of microscopic-scale processes of damage or void coalescence, for example, holes close together and aligned with directions of maximum
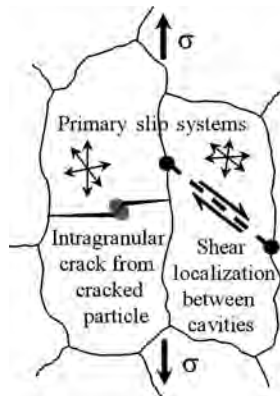
Figure 6.11 Influence of crystal orientation on grain or phase boundary damage nucleation. The grain on the right has two widely spaced damage sites that are favorably oriented for shear localization between them. In contrast, the grain on the left has two closely spaced damage sites that are not favorably oriented for shear localization, but an intragranular crack can develop from the cracked particle.

shear stresses coalesced by shear localization at small strains (see Figure 6.11) subsequently developing into a crack path. For voids or hard particles located in random positions, several researchers (Becker *et al.*, 1989; Horstemeyer, Ramaswamy, and Negrete, 2003; Nicolaou and Semiatin, 2000, 2003; Pardoen *et al.*, 2003; Radhakrishnan and Sarma, 2004) investigated the effects of initial damage location on the development of shear localization that precedes propagation of a macroscopic-scale crack.

Although shear localization can be simulated in continuum models, it is also important to identify the locations of damage nucleation with respect to microstructural features and operative slip systems (e.g., Figure 6.11). In Figure 6.11, plastic deformation processes may not facilitate shear localization between the cracked particle in the interior of the grain on the left and the pore in the grain boundary between the two grains, because no slip system facilitates localized shear. In contrast, two pores that are farther apart on opposite sides of the right grain could be oriented so that shear deformation between them would be favored, and hence damage may develop where it would not be predicted in a continuum model.

As continuum approaches are valuable for design and modeling at the component scale, it is desirable to develop a method by which the continuum anisotropic damage formulations can be informed by physically modeled plastic deformation processes. Thus, if models of microstructures using CPFE methods can identify dislocation-based deformation processes that cause damage nucleation and evolution, existing expressions of damage may be useful in continuum-scale models (such as a tensorial expression of D in Eq. (6.69)).

6.3.3
Microstructurally Induced Damage

Micromechanics studies show that shear localization at the microscale occurs as a result of heterogeneous microstructure and grain orientation features such as inclusion morphology and distribution, grain boundary character, texture, grain shape, and the operation of slip systems coupled with damage site locations, that is,

78 | *6 Constitutive Models*

features illustrated in Figure 6.11. Hence, shear localization, and hence the toughness, will depend upon anisotropic microstructural details. This anisotropic effect is observed at the macroscale by 25 percent variations in K_{Ic} with respect to the direction in rolled sheet material (Barlat *et al.*, 2002). However, there has been limited study of how crystallographic processes lead to failure mechanisms that depend on local grain and grain boundary orientations, making damage modeling using CPFE approaches an important area for future study. In particular, CPFE allows the direct modeling of experimentally characterized microstructures where damage has been observed, to assess physically based theories of damage nucleation and early growth.

Grain or phase boundaries are often sources of critical damage nucleation, even when pre-existing cracks may be present within a grain. In aluminum alloys, the primary mechanisms for grain boundary crack nucleation are void coalescence between grain boundary precipitates (de Koning *et al.*, 2003; Werner and Prantl, 1990). In fatigue conditions, subcritical short cracks either pre-exist owing to cracked inclusions (such as constituent particles, see Figure 6.11) or arise from crack formation in the early stage of fatigue cycling, but do not propagate past a limiting grain boundary or triple line (Gibson and Forwood, 2002; Luster and Morris, 1995). When these short cracks are able to penetrate a grain boundary, they make the transition to longer cracks that may then be adequately modeled with established continuum fracture mechanics. This penetration event often takes place late in the cycling process, indicating that the short crack penetration of the grain boundary may control fatigue life.

6.3.4
Heterogeneous Plastic Deformation

Both experimental and computational studies suggest that damage nucleation occurs in locations of large strain concentrations, which develop in locations of substantial heterogeneous deformation near microstructural features such as grain or phase boundaries. However, if a large local strain is effective in accommodating a required local geometry change (due to *local* boundary conditions imposed by differential strains in the local neighborhood), a locally large strain may prevent damage nucleation. In contrast, damage may nucleate where an insufficient amount of strain occurs to accommodate a locally required shape change, such that opening a free surface may require less energy than further deformation in the local neighborhood. As there are many more large strain sites than damaged sites, large strain sites are not necessarily damage sites. Furthermore, damage could develop at modest strains where localized strain incompatibilities develop.

The effects of heterogeneous deformation due to different crystal orientations across a grain boundary can be more easily illustrated using the hexagonal rather than cubic crystal structure, because there is less symmetry and a smaller number of slip systems. Figure 6.12a and b illustrates how two slip systems, basal and prism, operate with the same Burgers vector on different planes. Yet, neither slip system will allow a dimension change in the *c* direction. Hence, $\langle c + a \rangle$ slip or
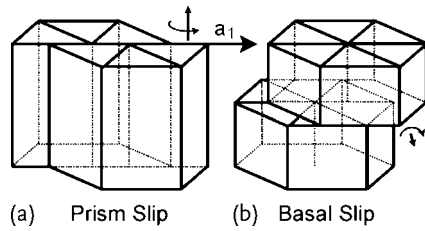
Figure 6.12 Prism (a) and basal (b) slip systems sharing the same slip direction but operating on different planes.
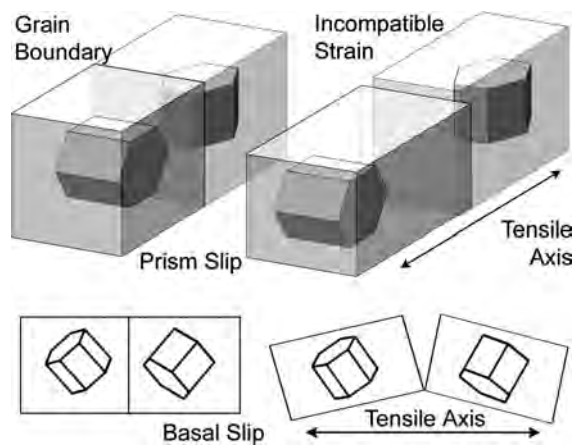

Figure 6.13 Close to 90° misorientation between two grains (regardless of orientation of the *c*-axis) leads to incompatible strains.

twinning is required to change the dimension of a grain in the *c* direction, and these deformation systems are known to be more difficult to operate. Thus, the two thought experiments in Figure 6.13 illustrate how very heterogeneous deformation conditions can arise when the *c*-axes of two grains are misoriented by 90° (Bieler, Goetz, and Semiatin, 2005b). When prism slip is favored, two grain orientations for which basal slip is not favored can deform by extension and elongate similarly in the tensile direction. However, these two grains contract in perpendicular directions, leading to a plastic strain incompatibility at the grain boundary, where either additional slip systems must be activated or voids must develop. For basal slip, both grains shear similarly, but in opposite directions, leading to a mode I opening force along the boundary. Similar issues occur in cubic materials, but in a less dramatic manner, and this may account for the generally higher ductility of cubic metals and alloys.

Hence, it is clear that strain varies from grain to grain, and even within a given grain owing to the effects of differing deformation processes in neighboring grains (effectively illustrated in Figure 6.14 (Delaire, Raphanel, and Rey, 2000)). The spread of deformation within a grain does not only depend on the orientations
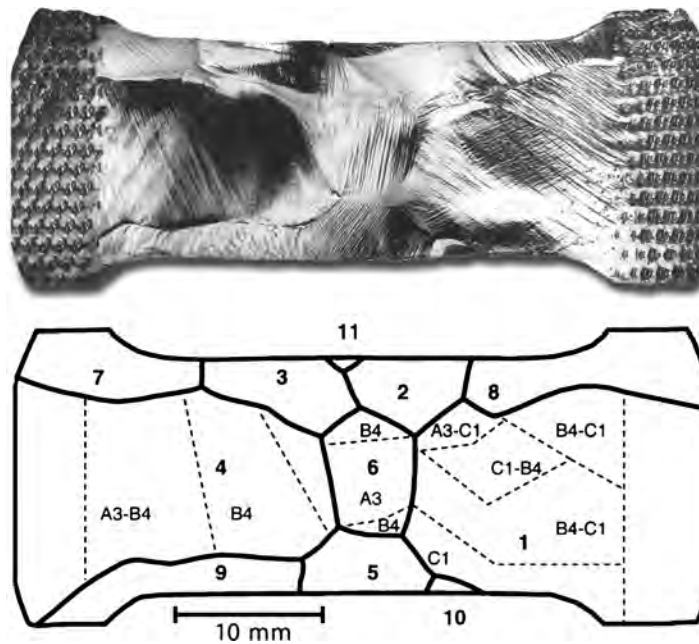
80 | *6 Constitutive Models*

Figure 6.14 Example of heterogeneous strain in a copper oligocrystal deformed to strain of 0.075 (Delaire, Raphanel, and Rey, 2000). Grains 1, 4, and 6 (bold numbers) show differ-ent combinations of activated slip systems (in Schmid and Boas notation), depending on the strain occurring in neighboring grains.

of the neighboring grains, but also on the constraints provided by neighboring grains (which diminish, but are still significant several grains away (Becker, 1991; Dunne, Walker, and Rugg, 2007a; Dunne, Wilkinson, and Allen, 2007b)). Within a given grain, slip traces of deformation systems with high Schmid factors often extend all the way across a grain, whereas planes with moderate Schmid factors may reveal slip traces that extend part way from a boundary into the grain interior. Experimentally measured surface strain maps on high-purity copper polycrystals also show that heterogeneous strains extend 20–100 microns into the grain interior (Clayton and McDowell, 2004; Delaire, Raphanel, and Rey, 2000; Thorning, Somers, and Wert, 2005; Yao and Wagoner, 1993). Local lattice rotations have been measured using orientation imaging microscopy, which has allowed direct comparisons between experiment and CPFE models (Bhattacharyya *et al.*, 2001; Cheong and Busso, 2004; Prasannavenkatesan *et al.*, 2005; Raabe *et al.*, 2001; Sachtleber, Zhao, and Raabe, 2002; Tatschl and Kolednik, 2003). Local rotations measured using high-resolution strain mapping and local strain accumulation effects at the grain scale were simulated more effectively when a *local* microme-chanical Taylor factor was used to identify the activated slip systems (Raabe *et al.*, 2001).

Because damage originates from strain incompatibilities in specific sites, it is most appropriate to investigate conditions that lead to damage nucleation using

CPFE methods that model experimentally realistic microstructures (e.g., Bhattacharyya *et al.* (2001); Cheong and Busso (2004); Clayton and McDowell (2004); Dawson, Mika, and Barton (2002); Hao *et al.* (2004, 2003); Kalidindi and Anand (1993); Ma and Roters (2004); Ma, Roters, and Raabe (2006a,b); Raabe *et al.* (2001); Zaafarani *et al.* (2006)). As damage events reflect interactions between the microstructural scale and the atomic scale, they are intrinsically nanoscopic. Thus, multiscale modeling approaches that include atomistic-scale computations are under development in a number of groups (Buchheit, Wellman, and Battaile, 2005; Clayton and Chung, 2006; Dewald and Curtin, 2007; Hao *et al.*, 2003; Liu *et al.*, 2004; McDowell, 2008; Voyiadjis, Abu Al-Rub, and Palazotto, 2004).

6.3.5
Interfaces

Interfaces represent a profound challenge to modeling heterogeneous deformation and damage nucleation. The cohesive strength of the boundary in real polycrystals varies according to the atomic-scale arrangement; some boundaries have more disorder than others (Watanabe, 1984), leading to lower interfacial cohesive strength. Many studies have correlated properties of boundaries with their interfacial structure through coincident site lattice (or low-Σ) boundaries. Because low-Σ boundaries have less free volume owing to better packing efficiency, these boundaries are assumed to be strong. Materials with large numbers of low-Σ boundaries (Kim and Oh, 2003; Palumbo, Lehockey, and Lin, 1998; Randle, 2004; Watanabe and Tsurekawa, 2004) that are well connected as networks (Schuh, Kumar, and King, 2003) exhibit higher flow stress and ductility than materials with few low-Σ boundaries (a weak boundary percolation can occur if there are less than 78 percent low-Σ boundaries (McGarrity, Duxbury, and Holm, 2005)). Because low-Σ boundaries are less able to absorb lattice dislocations than random boundaries (Kokawa, Watanabe, and Karashima, 1981), many researchers have attributed material strength and ductility (resistance to damage nucleation) to the presence of low-Σ boundaries (Tsurekawa, Kokubun, and Watanabe, 1999; Watanabe, 1984; Watanabe and Tsurekawa, 2004, 2005). This characterization of the boundary state is useful in computational modeling, as the grain boundary energy used in a Griffith criterion provides a criterion for nucleating a crack.

Another class of boundaries referred to as special boundaries have interfaces with low-energy surfaces and repeating polyhedral structural units (generally a subset of low-Σ boundaries). Of the five parameters that geometrically describe a boundary, three for the misorientation and two for the boundary normal, low-Σ boundaries only specify the misorientation, for example, an incoherent $\Sigma 3$ twin boundary (whereas a coherent $\Sigma 3$ boundary is special). Many studies show that the lowest-energy configurations result when the boundary normal is a low-index crystal plane, or has a common crystal direction about which there is a specified tilt or twist (Rohrer *et al.*, 2006, 2004; Tschopp, Spearot, and McDowell, 2007; Wolf, 1990). Hence, low-angle boundaries (referred to as $\Sigma 1$) are special. In analysis of beneficial grain boundary character, the most beneficial boundaries are found to

be those with low surface energy, which also have structural repeating polyhedral units in the boundary plane (Davies and Randle, 2001; Rohrer *et al.*, 2006).

Whereas the coincident site lattice approach considers how well the lattices on either side of a boundary are aligned, another approach for assessing grain boundary character is based upon understanding the geometry of GBDs (Brandon, 1966; Frary and Schuh, 2003). Bollmann (1982) developed the O-lattice approach to identify GBDs, which has been used to explain diffraction contrast features in grain boundaries, for example, Solenthaler and Bollmann (1986). GBD Burgers vectors may or may not reside in the boundary plane, making them mobile or sessile, respectively. Even if boundary dislocations are mobile, they will face barriers at triple lines (where three boundaries meet), where they may or may not be able to continue to propagate, depending on whether the triple line is hard or soft (Fedorov, Gutkin, and Ovid'ko, 2003). Triple lines are often described as I- or U-lines (Bollmann, 1984, 1988, 1991), where I-lines are typically intersections of Σ boundaries. I-lines do not have dislocations entering the boundary from adjacent grains, whereas U-lines do, resulting in disclinations, where crystal dislocations terminate along the triple lines. Dislocation transmission is possible through I-lines without development of dislocation debris, so they allow slip transfer. From this paradigm, triple line characteristics affect properties (Bollmann, 1991; Randle, 1995), including the likelihood of triple-junction cracking (Wu, 1997; Wu and He, 1999). U-lines have higher energy (due to unbalanced dislocation content), providing sources or sinks for lattice dislocations during deformation, and are more susceptible to cavitation damage than I-lines.

There is a possible conceptual disconnect between the slip transparency of I-lines (junctions of low-Σ boundaries) and the sense of boundaries being strengthening elements that resist dislocation motion (Kobayashi, Tsurekawa, and Watanabe, 2005; Lim and Raj, 1985; Tsurekawa, Kokubun, and Watanabe, 1999). Clearly, the influence of low-Σ or special boundaries and associated I-lines on damage nucleation mechanisms is only partially understood. More importantly, the random boundaries that are more likely to develop damage nucleation need focused and systematic attention to identify how damage develops, because there will normally be a significant number of random boundaries in polycrystals.

6.3.6
Cohesive Zone Boundary Modeling

The energy-based definition of the grain boundary character has been modeled in CPFE modeling using the cohesive force model first presented by Needleman (1987) and Xu and Needleman (1994), who described the cohesive energy as an empirical scalar function that relates displacement to normal and shear traction evolution in the boundary plane (Figure 6.15a and b). Such formulations have been adopted in damage nucleation models (Arata *et al.*, 2002; Clayton and McDowell, 2004; Hao *et al.*, 2004, 2003). Clayton and McDowell (2004) used nonlocal models to more accurately predict local stress–strain history, and hence, tractions on the boundary. From this analysis, they identified a parameter which could be used
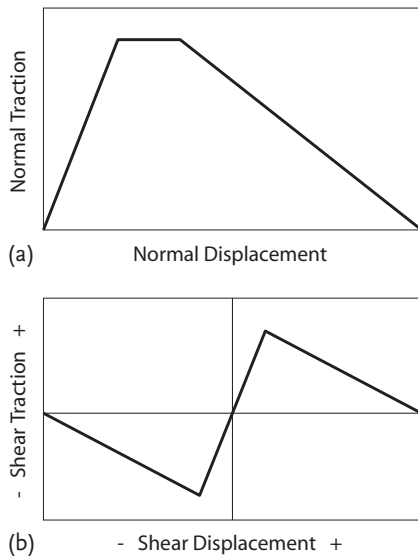
Figure 6.15 (a, b) Cohesive zone interfacial strength models typical of those used in crystal plasticity finite element (CPFE) modeling: the vertical axis represents tensile or shear strength, and the horizontal axis represents displacement.

to predict damage nucleation locations, based upon how much accommodation by void damage is required by the material to deform to a given strain level. This model assumed isotropic interfacial energy for all boundaries. Such models have been evaluated to identify how nucleation and growth of voids affects subsequent deformation processes (e.g., Figure 6.16a and b). However, these models cannot simulate how a high dislocation density near a boundary can facilitate void nucleation (Wilshire and Willis, 2004). Although cohesive zone energy models can be made more physically accurate by using atomistic simulations of particular boundaries (Spearot, Jacob, and McDowell, 2004), the fact that different boundary structures and misorientations have different energies is not usually incorporated. Cohesive zone boundaries are appealing in that they are two-dimensional, but they do not use the available information regarding operating slip systems to examine or analyze damage evolution.

Low-Σ boundary attributes are not a sufficient definition of a strong or weak boundary. First, the beneficial effect of low-Σ boundaries cannot be exclusively ascribed to lower solute content, because solute atoms can also strengthen grain boundaries, for example boron doping in aluminides. Second, even though the benefit of low-Σ boundaries is statistically convincing, some low-Σ boundaries do develop damage, whereas many more random boundaries do not, for example, Lehockey and Palumbo (1997) and Boehlert, Longanbach, and Bieler (2008) (Figure 6.17) suggest that additional criteria for identifying strong and weak boundaries exist, such as the influence of active deformation systems. There has been little study of the effects of deformation systems on boundary character (Davies
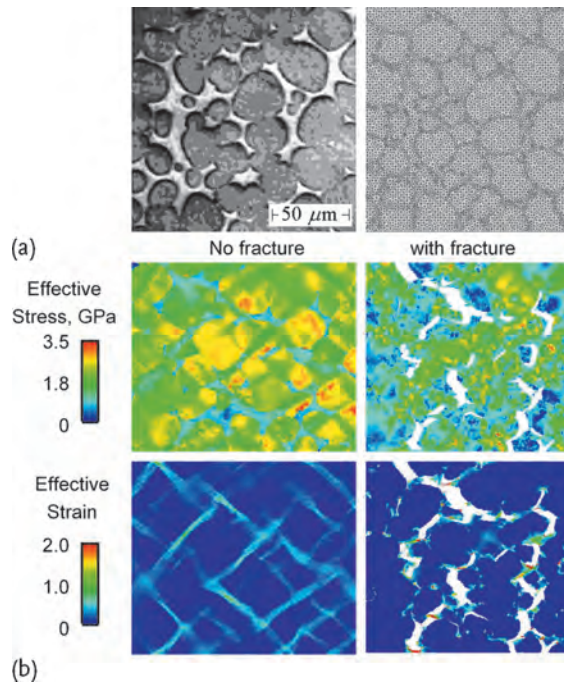
Figure 6.16 Influence of cohesive zone interfacial strength models coupled with nonlocal CPFE microstructure models on plastic strain development with and without use of boundary strength models; representative two-dimensional plane strain microstructure and mesh for a two-phase W–(Ni,Fe) alloy (a), and effects of fracture criteria on stress and strain (b) (Clayton, 2005).
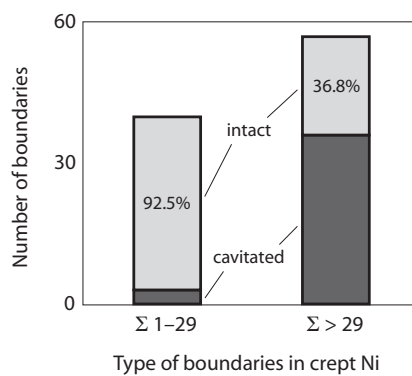

Figure 6.17 The fraction of intact boundaries in crept nickel is very high in the low-Σ boundaries, but many higher-Σ boundaries are also intact (Lehockey and Palumbo, 1997).

and Randle, 2001); only a few special cases have been examined, for example, Pyo and Kim (2005); Su, Demura, and Hirano (2003). Third, some general boundaries have special properties based upon the rotation axis (Lejcek and Paidar, 2005), or

"plane-matching boundaries," which are statistically more common than low-Σ boundaries (Kawahara *et al.*, 2005). Fourth, the benefit of low-Σ boundaries has rarely been examined in noncubic materials, even though the structure of low-Σ boundaries is known (see, e.g., Wu, Nazarov, and Zhou (2004) for hexagonal-close-packed structure and Singh and King (1993) for $L1_0$ structure). Finally, GBDs are also important, as they are interrelated with the structure of the boundary, and they affect how slip can be transferred across a boundary, as discussed in the next section. Most of the grain boundary engineering literature is more focused on creating networks of low-angle boundaries with heat treatments than on examining why they are effective.

6.3.7
Grain Boundary Slip Transfer

The analysis of heterogeneous strain near boundaries was initiated by Livingston and Chalmers (1957), who observed that more slip systems are active near bicrystal grain boundaries than in the grain interiors. However, bicrystals with arbitrarily oriented grains generally activate only one slip system in the grain interior (unless orientations are chosen that have the same Schmid factor for multiple slip systems). In contrast, polycrystals generally require activation of two or more slip systems owing to compatibility constraints. Although bicrystal deformation provides insights into mechanisms of deformation transfer, the results cannot be directly transferred to general grain boundaries in polycrystals.

Studies of deformation transfer have led to identification of some rules by which a dislocation in one grain can penetrate into a neighboring grain (Clark *et al.*, 1992; Werner and Prantl, 1990). These rules have been confirmed with atomistic-scale simulations by de Koning *et al.* (2003, 2002), and, more recently, criteria based upon the need for step removal, nucleation of GBDs, and grain boundary normal stress and shear stress on dislocation pileups have been proposed (Dewald and Curtin, 2007). The slip transmission process often leaves residual dislocations in the boundary and requires a change in direction of the Burgers vector along with a change in the plane orientation, resulting in two intersecting lines in the grain boundary plane. This geometry is illustrated in Figure 6.18. The three original rules and three recently proposed rules based upon simulations (Dewald and Curtin, 2007) for slip transmission are:

- the angle θ between the lines of intersection between the grain boundary and each slip system must be a minimum;
- the magnitude of the Burgers vector of the dislocation left in the grain boundary (correlated to the magnitude of κ) must be a minimum;
- the resolved shear stress on the outgoing slip system must be a maximum;
- the normal compressive stress on the boundary should be small (for GBD nucleation);
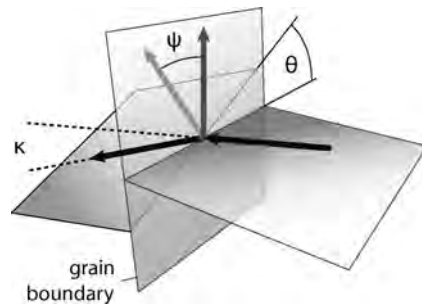- the step associated with the residual defect at the boundary should be small;

Figure 6.18 Angles and vectors used to evaluate the geometrical efficiency of strain transfer at a grain boundary (Bieler *et al.*, 2009).

- if a lagging lattice Shockley partial remains near the intersection but has not been absorbed, the resolved shear stress acting on the leading pileup dislocation should be high.

Semiquantitative geometrical expressions describing the likelihood of a slip transmission event have been developed. Luster and Morris (1995) noted that large values of $\cos\psi\cos\kappa$ were correlated with observed instances of slip transmission. Slip transmission criteria depend strongly on the degree of *coplanarity* of slip systems engaged in deformation transfer (θ will be small if ψ is small). Other studies of deformation transfer have focused more on the misalignment of the Burgers vector *colinearity* ($\cos\kappa$ in Figure 6.18), such as Gibson and Forwood (2002), who found that twin impingement at boundaries in TiAl is accommodated by $a/2\langle110]$ ordinary dislocation slip on a variety of planes on both sides of the boundary, with residual dislocations left in the boundary.

The process of slip transfer is also dependent on GBDs (Bollmann, 1982; Brandon, 1966; Frary and Schuh, 2003). GBD Burgers vectors may or may not reside in the boundary plane, making them mobile or sessile, respectively. Even if boundary dislocations are mobile, they face barriers at triple lines, where they may or may not be able to continue to propagate. Triple lines are often described as I- or U-lines (Fedorov, Gutkin, and Ovid'ko, 2003), where I-lines are typically intersections of low-Σ boundaries. Dislocation transmission without development of dislocation debris is possible through I-lines, so they permit slip transfer, whereas U-lines provide sources or sinks for lattice dislocations during deformation. Thus, triple-line characteristics affect properties (Bollmann, 1991; Randle, 1995), for example, cavitation and cracking are more likely at U-lines (Wu, 1997; Wu and He, 1999).

Consideration of the geometry of slip transfer suggests that there are three classes of boundaries with respect to their mechanical behavior:

- the grain boundary acts as an impenetrable interface that forces operation of additional intragranular (self-accommodating) slip systems that generate localized strain and rotations (Zaefferer *et al.*, 2003) to maintain boundary continuity;

- the boundary is not impenetrable, and slip in one grain can progress into the next grain with some degree of continuity (leaving residual boundary dislocations, and perhaps only partial ability to accommodate a shape change);
- the boundary is transparent to dislocations, and (near) perfect transmission can occur (e.g., low-Σ boundaries related to I-lines (Lim and Raj, 1985), or low-angle boundaries (Kobayashi, Tsurekawa, and Watanabe, 2005; Zaefferer *et al.*, 2003); this type of boundary is most naturally modeled with CPFE methods).

Further complications are suggested from experimental observations. From nanoindentation experiments it is known that grain boundaries impose a threshold stress effect, such that strain bursts through a boundary occur with increasing stress/strain owing to the achievement of a stress sufficient to activate a grain boundary source (Kobayashi, Tsurekawa, and Watanabe, 2005; Wang and Ngan, 2004). The misorientations of boundaries, and hence their properties, change with strain (Sun, Adams, and King, 2000). For example, a change in boundary character that affects dislocation absorption or emission from the boundary will affect the localized rotation gradients arising from GNDs.

Recent computational studies (Tschopp, Spearot, and McDowell, 2008, 2007) have shown that dislocation emission is correlated with the presence of particular kinds of polyhedral structural units. However, boundaries with twist character do not provide the polyhedral units that facilitate atomistic simulations (McDowell, 2008), so random boundaries and curved dislocations are more difficult to simulate. Simulations of this scale of defect and boundary structure require large numbers of atoms and are limited to nanocrystals; recently, a dislocation loop expansion into a grain boundary was modeled, and local stress states resulting from dislocation absorption into the boundary were identified (Bitzek *et al.*, 2009). Atomistic studies are valuable for studying particular cases, and have been effective in identifying or confirming trends and rules that can used at larger scales.

This discussion clearly shows that before damage nucleation can be predicted, deformation transfer mechanisms must be modeled in a reasonable manner (as a catalog of all possible boundaries with different boundary conditions is not easily achieved using atomistic models). Further, if a relationship between deformation transfer characteristics and damage nucleation could be developed, this would provide an effective bridge between atomistic- and continuum-scale models.

To make computational modeling of damage nucleation possible in the CPFE paradigm, grain boundary elements that allow physically realistic deformation transfer are necessary. Two approaches of modeling grain boundary deformation have been proposed, by Ma, Roters, and Raabe (2006b) and Ashmawi and Zikry (2003). In both cases, grain boundary elements with finite thickness were used. Ashmawi and Zikry (2003) used the grain boundary element to track the evolution of dislocation density in elements in an envelope fanning into the grain interior on either side of the boundary. The most active slip system in this envelope was evaluated, and then this density was tracked with each time step. Grain boundary elements accumulated the impinging dislocation density as a damage factor in a continuum element similar to D in Eq. (6.69); this is interpreted as a

pileup that causes cavitation to develop, and hence the reduction in stress carrying capability. Slip transfer was permitted in proportion to the geometrical factor $\cos\theta\cos\kappa$ to reduce the accumulated dislocation density in the grains on either side, that is, if $\theta < 15°$ and $\kappa < 35°$ in Figure 6.18 (based upon experimental observations of Werner and Prantl (1990)). This formulation used arbitrary square crystal plasticity elements in square grains with thinner grain boundary elements having the continuum-based damage nucleation model, so it was not examined using realistic microstructures.

In contrast, Ma, Roters, and Raabe (2006b) developed a grain boundary element with crystal plasticity components with an increased resistance to flow stress based upon the fractional dislocation debris left in a boundary when slip transfer occurs (see the details in Section 6.1.3.3). This increase in flow resistance is expressed as an increase in the activation energy barrier for dislocation slip within the grain boundary element, and hence the deformation process in the boundary is kept crystallographic. However, in both cases, the process of what happens to dislocations that retain some sense of their identity as they penetrate into the neighboring grain is neglected for simplicity in the interest of capturing at least some of the physics of the process. There is clearly opportunity for further insightful development of a practical grain boundary element that can capture both the dislocation slip transfer and the damage nucleation processes in practical and realistic ways.

6.3.8
Experimental Studies of Fracture-Initiation Criteria

Although much research in CPFE modeling has focused on ductile cubic metals, damage nucleation is much more critical in low ductility metals and intermetallics, at both low-temperature and high-temperature conditions. Owing to more limited slip, it is easier to experimentally identify relationships between slip, twinning, and damage nucleation in slip-limited materials. After making unsuccessful attempts to correlate damage with slip transfer in TiAl using only geometrical parameters, Simkin, Crimp, and Bieler (2003) developed a fracture-initiation parameter (termed *fip*) that is based upon the activity of slip and twinning systems in adjacent grains during deformation. The fip is analogous to a probability statement about how likely it is for a given grain boundary to crack when subjected to a stress field. A fip consists of several physical/geometrical factors that could enhance crack nucleation owing to localized shear strain concentrated at the boundary. Variations of this idea are presented in equations as F_i, where i is a label (Bieler *et al.*, 2005a, 2009; Boehlert, Longanbach, and Bieler, 2008; Fallahi *et al.*, 2006; Kumar *et al.*, 2008). For example, the fip parameter F_1 is the product of three terms:

$$F_1 = m_{\mathrm{tw}}|\hat{\mathbf{b}}_{\mathrm{tw}}\cdot\hat{\mathbf{t}}|\sum_{\mathrm{ord}}|\hat{\mathbf{b}}_{\mathrm{tw}}\cdot\hat{\mathbf{b}}_{\mathrm{ord}}|\,. \tag{6.70}$$

The unit vectors used in the fip expression above are illustrated in Figure 6.19. The first term is the Schmid factor of the most highly stressed twinning system in a grain pair, m_{tw}, which identifies twins that cause the largest shear discontinuity at a grain boundary. The second term is the scalar product of the unit vector of this
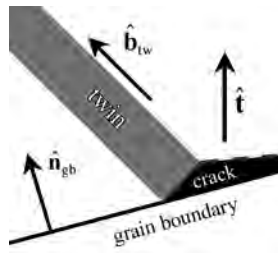
Figure 6.19 Nucleation of a grain boundary crack due to mode I opening strain at a grain boundary due to highly localized twin shear.

twin's Burgers vector direction, $\hat{\mathbf{b}}_{tw}$, and the unit vector pointing in the direction of the maximum tensile stress $\hat{\mathbf{t}}$, that is, $\hat{\mathbf{b}}_{tw} \cdot \hat{\mathbf{t}}$, which identifies the strength of a mode I opening component at the boundary. This term is the part of the Schmid factor related to the slip direction. The third term, $\sum_{ord} |\hat{\mathbf{b}}_{tw} \cdot \hat{\mathbf{b}}_{ord}|$, is the sum of scalar products between the Burgers vector of a highly stressed twin system in the initiating grain (with Schmid factor m_{tw} and the Burgers vector of available ordinary slip systems in either the same grain or the neighboring (responding) grain. This term describes how well the local shear direction at the boundary can be accommodated by dislocation activity in the neighboring or initiating grain, that is, the scalar product defined by the angle κ in Figure 6.18. This quantitatively expresses one of the three requirements identified by Clark *et al.* (1992) for slip transfer. The sum term is maximized when two or more slip systems have a modest value of κ, because when the scalar product is near 1 for one slip system, the scalar product is much smaller for the rest. Thus, the sum is large when the opportunity for imperfect slip transfer is large.

From experimental measurements, the fip is larger for cracked boundaries than intact boundaries, implying that imperfect slip transfer (which leaves residual dislocation content in the boundary) is strongly correlated with crack nucleation. This approach has been shown to be statistically significant in two studies of duplex TiAl alloy, one with deformation of a smooth four-point bend specimen (Kumar *et al.*, 2008; Simkin, Crimp, and Bieler, 2003), and in four-point bending of a notched specimen, where the crack path was successfully predicted using this fip (Ng *et al.*, 2005). A modified version of the fip was used successfully in high-stress creep of a cobalt-based superalloy (Boehlert, Longanbach, and Bieler, 2008), where slip transfer rather than twin-strain transfer was used to evaluate the fip. Although this suggests that the fip concept may be a robust predictor of damage nucleation, further examination of this concept in other material systems is needed.

6.3.9
Strain Energy as a Criterion for Damage

Strain energy is a commonly used criterion for damage. A recent example that illustrates this approach in crystal plasticity studies is in the work of Dunne, Wilkinson, and Allen (2007b), who used cumulative plastic slip as a means to predict damage sites in CPFE studies of nickel and titanium alloys in low cycle fatigue studies.

In the maximum stress region of a continuum model of a three-point bend specimen, they inserted a crystal plasticity section with the same grain configuration as in a carefully analyzed experiment. Planes with highly active slip corresponded to planes with high Schmid factors and observed slip bands in the experiment. With a one-dimensional damage model similar to Eq. (6.69), they were able to simulate the locations of persistent shear bands and crack positions in a three-point fatigue bending specimen. However, the details of the crack nucleation differed between the experiment and the simulation. This was in part due to simplifying assumptions regarding the stress state. This work showed that shear bands and cracks are very sensitive to the actual local geometry of grains.

The importance of local geometry was further emphasized in a systematic computational study of fatigue facet (crack) formation in hard orientations of titanium in polycrystals (Dunne, Walker, and Rugg, 2007a). Particular orientations of adjacent crystals and particular grain boundary inclinations were found to be most likely to generate slip penetration from the adjacent soft grain into the hard grain such that tensile stresses developed normal to basal planes. Such conditions facilitate formation of facets that develop into fatigue cracks. This computational study was consistent with features in deeply characterized experiments of Sinha *et al.* (2006) and Bieler, Goetz, and Semiatin (2005b); Bieler, Nicolaou, and Semiatin (2005c).

CPFE is particularly valuable for identifying microstructural conditions where strain incompatibility develops (this is exaggerated in slip-limited materials). These incompatibilities develop owing to activation of slip systems that cause shears in very different directions in adjacent grains, leading to significant local triaxial stress states and load shedding to harder orientations. Self-consistent modeling of generic microstructural characteristics have been used to estimate plausible stress states, for example, Bieler, Nicolaou, and Semiatin (2005c), but, as the prior examples show, the actual grain geometry leads to very significant variations around such estimates. It is clear that strain energy is an important metric for predicting locations where damage is possible, but clearly there are additional criteria that must be considered (and identified) to account for the fact that not all sites with potentially dangerous characteristics actually develop damage.

6.3.10
Assessment of Current Knowledge about Damage Nucleation

CPFE modeling is an enabling tool for examining conditions that lead to damage nucleation. However, the physical understanding that is needed to develop computationally efficient and robust criteria is relatively undeveloped. Rather than stating what only may be true on the basis of recent studies, we can provide relationships between heterogeneous strain and damage nucleation as a list of hypotheses that can be explored in combined experimental and CPFE computational modeling research programs.

- Damage nucleation always occurs at locations of maximum strain energy density (maximum area under the local stress–strain curve).

- Large local strains can provide geometrical accommodation that can prevent damage nucleation.
- Damage nucleation arises from slip interactions resulting from imperfect slip transfer through a boundary, which leaves residual dislocation content in the boundary plane.
- Damage nucleation occurs in particular boundaries where unfavorable slip interactions take place at the boundary to weaken the boundary.
- Slip interactions at the boundary are more (or less?) important than the magnitude of local strain for predicting damage nucleation.
- Damage nucleation occurs in locations where there is maximum geometrical incompatibility arising from highly activated slip systems that cause dominant shears in very different directions, for example, Bieler, Goetz, and Semiatin (2005b).
- Damage nucleation is highly correlated with severe local strain heterogeneity, for example, lattice curvature.
- Dislocation-density-based (non-local) formulations of crystal plasticity models are necessary to adequately predict the local strains, and hence the slip system activity needed to predict damage nucleation.
- Damage nucleation depends upon cohesive strength of the boundary, that is, the energy needed to separate an existing interface–Griffith criterion.
- Damage nucleation probability is proportional to local hydrostatic tensile stress.
- Damage nucleation is more likely at triple lines than along boundaries, especially along U-lines.
- Slip directions have more influence on damage nucleation than slip planes.
- Low-Σ boundaries are less likely to accumulate damage than random boundaries.
- Twin boundaries resist damage because they repel dislocations from the boundary.
- Twin boundaries resist damage because they allow efficient slip transfer.
- Twin boundaries are schizophrenic (sometimes resistant, sometimes susceptible to damage nucleation).
- Fatal flaws are located where there is the highest density of local damage sites.
- Fatal flaws are located where the size of nucleated damage grows the fastest.

Franz~Roters, Philip~Eisenlohr, Thomas~R.~Bieler, and~Dierk~Raabe: Crystal Plasticity Finite Element Methods —
Chap. roters9419c07 — 2010/7/23 — page 93 — le-tex

93

7
Homogenization

7.1
Introduction

In contrast to the direct crystal plasticity method of modeling aggregates of grains one-to-one, finite element analysis is often used to predict the mechanical behavior of engineering structures. This is typically done at the component or design scale using homogenized material properties (indicated by an overbar). At the continuum scale, material points $\bar{\mathbf{x}}$ in the reference configuration $\overline{\mathcal{B}}_0 \subset \mathbb{R}^3$ are projected by the nonlinear deformation map $\bar{\mathbf{y}}(\bar{\mathbf{x}}) : \bar{\mathbf{x}} \in \bar{\mathcal{B}}_0 \to \bar{\mathbf{y}} \in \overline{\mathcal{B}}$ onto points $\bar{\mathbf{y}}$ in the current configuration $\overline{\mathcal{B}} \subset \mathbb{R}^3$. The corresponding tangent map or deformation gradient is then given by $\overline{\mathbf{F}} = \partial \bar{\mathbf{y}}/\partial \bar{\mathbf{x}} = \operatorname{Grad} \bar{\mathbf{y}}$. To derive the work-conjugate stress $\overline{\mathbf{P}}$ (first Piola–Kirchhoff stress) and solve the equilibrium conditions within the finite element analysis, a constitutive law which connects $\overline{\mathbf{P}}$ to $\overline{\mathbf{F}}$ is required. However, a direct formulation of $\overline{\mathbf{P}}(\overline{\mathbf{F}})$ and its tangent $\partial \overline{\mathbf{P}}/\partial \overline{\mathbf{F}}$ is in general difficult to impossible, since the mechanical response of (metallic) materials is determined by their underlying microstructure.

This microstructure cannot be regarded as a homogeneous continuum; it typically contains grains with differing properties. As a rule, in engineering parts and exemplarily visualized in Figure 7.1, the grain scale is orders of magnitude smaller than the component scale, thus ruling out the possibility to include all degrees of freedom presented by a huge grain aggregate. Therefore, the two-level approach illustrated in Figure 7.1 is pertinent: Each material point $\bar{\mathbf{x}}$ at the component scale is linked to a (sub)domain $\mathcal{B}_0 \subset \mathbb{R}^3$ containing a finite number of microstructure constituents, for example, grains, for which the individual constitutive behavior can be modeled, that is, the constitutive relation between $\mathbf{P}$ and $\mathbf{F}$ is known at this scale. This constitutive relation is – in general – dependent on the state of the material, most notably on its thermomechanical history. Since the macroscopic quantities $\overline{\mathbf{F}}$ and $\overline{\mathbf{P}}$ are related via the volume averages

$$\overline{\mathbf{F}} = \frac{1}{V_0} \int_{\mathcal{B}_0} \mathbf{F} \, dV_0 \,, \tag{7.1}$$

$$\overline{\mathbf{P}} = \frac{1}{V_0} \int_{\mathcal{B}_0} \mathbf{P} \, dV_0 \,, \tag{7.2}$$
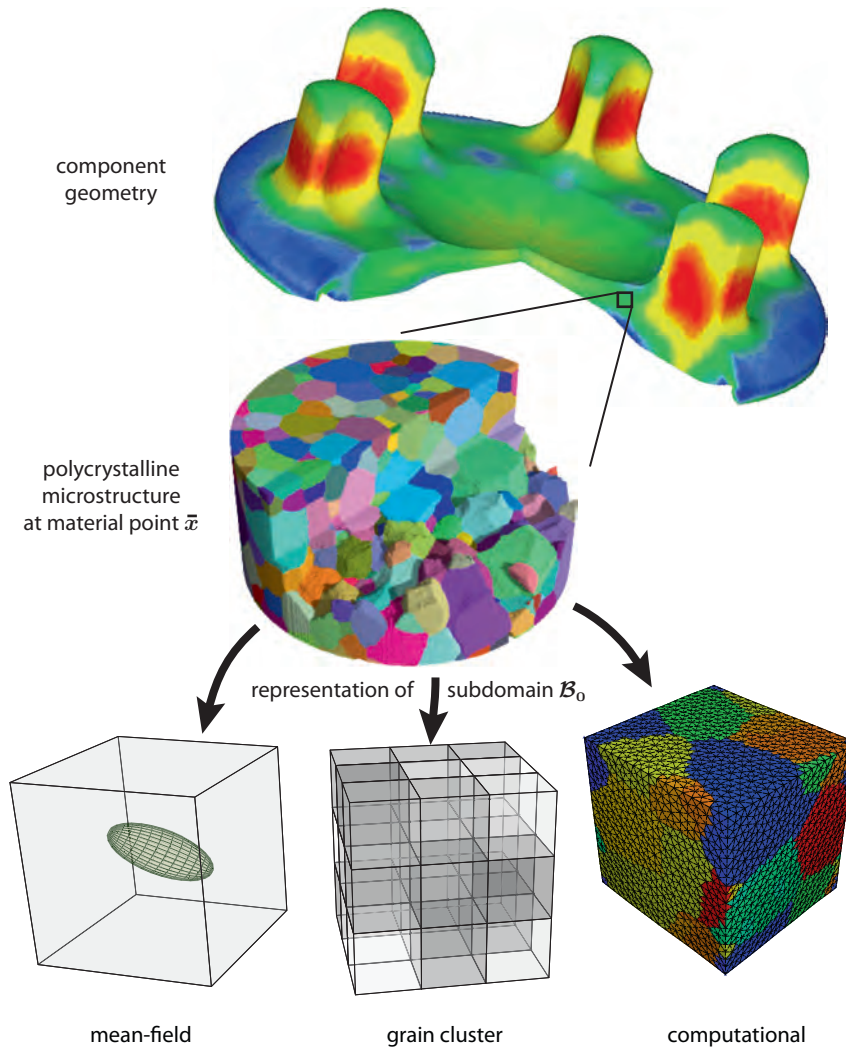
Figure 7.1 Concept of a two-level homogenization strategy. Typically, the constitutive response of material points $\bar{x}$ required in the component-scale calculation (top) is unknown owing to the complicated and evolving microstructure present at those material "points" (center). Therefore, a simpler representation of this microstructure within a (representative) subdomain $\mathcal{B}_0$ is sought (bottom). For that representation the overall response to the boundary conditions of the macroscale material point can be derived from the known constitutive behavior of individual components (grains) making up the representative structure. Material point representations of increasing complexity are illustrated at the bottom from left to right. The component-scale image is a DEFORM result taken from the IMU forming benchmark, the central three-dimensional grain structure is adopted from Ludwig *et al.* (2009), and the finite element mesh at the lower right is from Melchior (2009).

with $\quad V_0 = \displaystyle\int_{\mathcal{B}_0} \mathrm{d}V_0$,

to the corresponding microscopic quantities $\mathbf{F}$ and $\mathbf{P}$ inside $\mathcal{B}_0$, this "numerical zoom" shifts the constitutive assumptions between $\overline{\mathbf{F}}$ and $\overline{\mathbf{P}}$ from the macroscale to the microscale.

The term "homogenization" now refers to the transition between the microscale and the macroscale defined in a general fashion by Eqs. (7.1) and (7.2). In physics, such procedures are also referred to as *coarse graining*. In the next section we first review methods for how to select grain aggregates in each domain $\mathcal{B}_0$ such as to ensure that they reflect the overall crystallographic texture of the material in question in a statistically representative way. After this, the following sections outline three routes which are mainly followed when it comes to the homogenization of polycrystalline materials in the framework of component-scale finite element analysis.

7.2
Statistical Representation of Crystallographic Texture

Crystallographic texture can, for instance, be quantified by the crystallite orientation distribution function (CODF). This distribution function specifies the probability density $f(\mathbf{Q})$ in orientation space by which the volume fraction, $\mathrm{d}V/V$, that is taken up by crystallites falling into an infinitesimal neighborhood around the orientation $\mathbf{Q}$ is determined:

$$v \equiv \frac{\mathrm{d}V}{V} = f(\mathbf{Q})\,\mathrm{d}Q \ . \tag{7.3}$$

The crystal orientation is described by a proper orthogonal matrix $\mathbf{Q} = \mathbf{g} \otimes \mathbf{e} \in SO(3)$ which maps the reference basis $\mathbf{e}$ onto the crystal basis $\mathbf{g}$. Using the notation introduced by Bunge (1982), that is, parameterizing $\mathbf{Q}$ by Euler angles $\{\varphi_1, \phi, \varphi_2\}$, the infinitesimal volume, $\mathrm{d}Q$, of orientation space follows as

$$\mathrm{d}Q = \frac{1}{8\pi^2}\,\mathrm{d}\varphi_1\,\mathrm{d}\varphi_2\,\mathrm{d}\cos\phi = \frac{\sin\phi}{8\pi^2}\,\mathrm{d}\varphi_1\,\mathrm{d}\varphi_2\,\mathrm{d}\phi \ . \tag{7.4}$$

The normalization factor of $1/8\pi^2$ arises owing to the requirement that $\oint \mathrm{d}V/V \equiv 1$. (Note that $f(\mathbf{Q}) \equiv 1$ for a random texture.)

The orientation distribution reflects any symmetry present in the crystal lattice and/or the sample geometry. This implies the following symmetry relations:

$$f(\mathbf{Q}) = f(\mathbf{Q}\mathbf{H}_\mathrm{L}) \quad \forall \mathbf{H}_\mathrm{L} \in \mathbf{S}_\mathrm{L} \subseteq SO(3) \ , \tag{7.5}$$

$$f(\mathbf{Q}) = f(\mathbf{H}_\mathrm{S}\mathbf{Q}) \quad \forall \mathbf{H}_\mathrm{S} \in \mathbf{S}_\mathrm{S} \subseteq SO(3) \ , \tag{7.6}$$

with $\mathbf{S}_\mathrm{L}$ and $\mathbf{S}_\mathrm{S}$ being the symmetry group of the lattice and sample, respectively. Therefore, the CODF is fully determined from $f(\mathbf{Q})$ within any one of the indepen-

dent regions of Euler space (also addressed as fundamental zones) resulting from Eqs. (7.5) and (7.6).

For practical reasons, the CODF is frequently stored in a discrete fashion by subdividing the fundamental zone Z of Euler space into N boxes of equal angular extension – typically $5 \times 5 \times 5$ cubic degrees – and recording discrete values, f^i, for each box. Ideally,

$$f^i = \int\limits_{\text{box}^i} f(\mathbf{Q}) \, dQ \Big/ \int\limits_{\text{box}^i} dQ = v^i \Big/ \int\limits_{\text{box}^i} dQ \,, \tag{7.7}$$

that is, the f^i values are the CODF average within the ith box corresponding to an average volume fraction v^i of crystallites having their orientation falling into this box.

The task now consists in selecting a finite number, N^*, of discrete orientations such that the overall texture is still represented as accurately as possible by the limited set. Depending on the requirements of the intended simulation, the individual volume fractions assigned to each selected orientation may either be equal or differ from one another.

With respect to the first option, Eisenlohr and Roters (2008) recently combined a deterministic scheme with a probabilistic scheme to sample a given number of equally-weighted orientations from a discrete CODF. While the probabilistic scheme accepts a randomly chosen orientation in proportion to the respective value of v^i, the deterministic part is based on the integer

$$n^i = \text{round}\left(C v^i\right), \tag{7.8}$$

which gives the number of times the orientation i should be selected into the representative set. To yield an overall set of N^* samples, the constant C has to be iteratively adjusted to fulfill

$$\sum_{i=1}^{N} n^i \overset{!}{=} N^* \,. \tag{7.9}$$

This iterative procedure is easily solved, for instance, with a binary search algorithm in a matter of split seconds on a standard single-CPU computer. Regarding reconstruction quality, it could be demonstrated that for $N^* > N$ the set resulting from Eqs. (7.8) and (7.9) is much closer to the original CODF than probabilistic sets using v^i as a probability to include orientation i (see Eq. (7.7)). However, for $N^* < N$ a systematic overweighting of orientations with large original v^i, and thus pronounced sharpening of the reconstructed texture, is observed. To overcome this inherent problem, the deterministic method is modified as follows: if the requested number, N^*, of sampled orientations is less than the number of boxes in the (fundamental zone of the) original CODF, that is, if $N^* < N$, one nevertheless generates a population of N discrete orientations according to Eqs. (7.8) and (7.9) but then selects a random subset containing only the requested $N^* < N$ orienta-

tions from the population of N orientations. By this modification, the reconstruction quality achieved is always at least as good as that with probabilistic sampling but it becomes clearly superior with increasing N^*/N.

Melchior and Delannay (2006) tackled the problem of assigning orientations to an aggregate of N^* differently sized grains which constitute a representative volume element. They started from a large set of probabilistically selected, equally-weighted orientations (Tóth and Van Houtte, 1992) and introduced an algorithm to divide this set into N^* collections of mutually similar orientations. Each collection represents a single grain (of average orientation) and comprises as many orientations as are required to match the respective volume fraction of this grain. By allowing this additional degree of freedom in the relative weight of assigned (average) orientations, one can dramatically increase the reconstruction quality resulting from a fixed number of orientations in comparison with equal-weight probabilistic sampling.

Böhlke, Haus, and Schulze (2006) presented a possible solution to the problem of approximating the CODF by a random background plus a small and fixed number of texture components of variable weight. First, a grid of equal angular extension in $\{\varphi_1, \phi, \varphi_2\}$ is constructed within the fundamental zone. An approximation then results from superposition of (at most) N^* von Mises–Fisher distributions, $g(\mathbf{Q}, \mathbf{Q}^\alpha, w)$, each centered on a distinct grid point $\mathbf{Q}^\alpha$ with fixed half-width w:

$$\bar{f}(\mathbf{Q}) = \sum_{\alpha=1}^{N^*} \nu^\alpha g(\mathbf{Q}, \mathbf{Q}^\alpha, w) \,. \tag{7.10}$$

The difficulty arises from selecting appropriate $\mathbf{Q}^\alpha$ out of the available grid points and assigning respective variable weights ν^α such that the distance

$$D = \int_Z (f(\mathbf{Q}) - \bar{f}(\mathbf{Q}))^2 \, \mathrm{d}Q \tag{7.11}$$

between the original CODF and its approximation is minimized. This corresponds to a mixed integer quadratic programming problem, for which robust solvers exists.

7.3
Computational Homogenization

We recall that within each subregion $\mathcal{B}_0$ containing a microstructure attached to a certain (macroscale) material point $\bar{\mathbf{x}}$, one defines the deformation map $\mathbf{y}(\mathbf{x}) : \mathbf{x} \in \mathcal{B}_0 \to \mathbf{y} \in \mathcal{B}$ which translates the reference configuration $\mathcal{B}_0$ of that microstructure to its current configuration $\mathcal{B}$. The associated deformation gradient is given by $\mathbf{F} = \partial\mathbf{y}/\partial\mathbf{x} = \mathrm{Grad}\,\mathbf{y}$. The deformation map can then be expressed as the sum of a homogeneous deformation $\bar{\mathbf{F}}\mathbf{x}$, inherited from the material point, and a superimposed fluctuation field $\tilde{\mathbf{w}}$:

$$\mathbf{y} = \bar{\mathbf{F}}\mathbf{x} + \tilde{\mathbf{w}} \,. \tag{7.12}$$
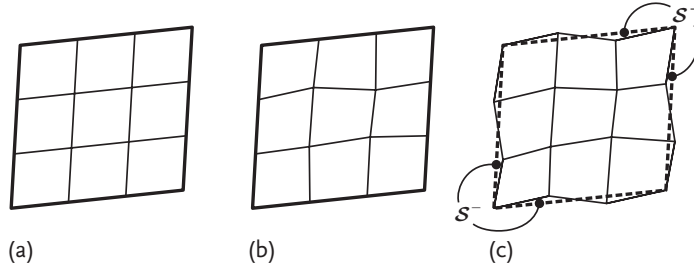
Figure 7.2 (a) Rigid (displacement fluctuation field $\tilde{\mathbf{w}} = \mathbf{0}$ everywhere), (b) homogeneous boundary conditions ($\tilde{\mathbf{w}} = \mathbf{0}$ on the surface), and (c) periodic boundary conditions ($\tilde{\mathbf{w}}^- = \tilde{\mathbf{w}}^+$ on corresponding surfaces $\mathcal{S}^+$ and $\mathcal{S}^-$).

Thus, the microscopic and macroscopic deformation gradients are related by

$$\mathbf{F} = \bar{\mathbf{F}} + \tilde{\mathbf{F}} \quad \text{with} \quad \tilde{\mathbf{F}} = \frac{\partial \tilde{\mathbf{w}}}{\partial \mathbf{x}} = \text{Grad}\, \tilde{\mathbf{w}} \,. \tag{7.13}$$

Combining Eqs. (7.13) and (7.1) results in the constraint that the deformation gradient of the fluctuation field vanishes on average:

$$\int_{\mathcal{B}_0} \tilde{\mathbf{F}} \, dV_0 = \int_{\mathcal{S}_0} \tilde{\mathbf{w}} \otimes d\mathbf{n}_0 = \int_{\mathcal{S}_0^-} \tilde{\mathbf{w}}^- \otimes d\mathbf{n}_0^- + \int_{\mathcal{S}_0^+} \tilde{\mathbf{w}}^+ \otimes d\mathbf{n}_0^+ = \mathbf{0} \,. \tag{7.14}$$

The three equivalent integral terms in Eq. (7.14) indicate the three possible boundary conditions of different rigorousness as shown in Figure 7.2a–c. One might rule out any fluctuations at all (condition 1), that is, $\tilde{\mathbf{w}} = \mathbf{0}$ in $\mathcal{B}_0$. However, homogeneous boundary conditions (condition 2), that is, $\tilde{\mathbf{w}} = \mathbf{0}$ on the surface $\mathcal{S}_0$, also satisfy Eq. (7.14). Still more relaxed (periodic) boundary conditions (condition 3) are possible if the surface is decomposed into two opposite parts $\mathcal{S}_0 = \mathcal{S}_0^- \cup \mathcal{S}_0^+$ with $\mathcal{S}_0^- \cap \mathcal{S}_0^+ = \emptyset$. Periodicity of the domain $\mathcal{B}_0$ is then ensured by requiring for each point $\mathbf{x}^+ \in \mathcal{S}_0^+$ that the associated point $\mathbf{x}^- \in \mathcal{S}_0^-$ has an opposite normal $\mathbf{n}_0^+ = -\mathbf{n}_0^-$ and equal values of the fluctuation field $\tilde{\mathbf{w}}^- = \tilde{\mathbf{w}}^+$. Thus, the degree of freedom offered to the microstructure inside $\mathcal{B}_0$, and hence its compliance, increases from condition 1 to condition 3. For the microcontinuum a static equilibrium is assumed, which, in the absence of body forces, is governed by the field equation

$$\text{Div}\, \mathbf{P} = \mathbf{0} \quad \text{in} \quad \mathcal{B}_0 \,. \tag{7.15}$$

Computational homogenization now refers to the numerical solution of the boundary value problem in $\tilde{\mathbf{w}}$ posed by Eqs. (7.13) and (7.15) in connection with a constitutive relationship $\mathbf{P}(\mathbf{F})$ per individual phase. For this solution, in general, a number of techniques can be employed. The majority of recent contributions discretized the boundary value problem by means of the finite element method, see bottom right of Figure 7.1 and, for instance, Feyel and Chaboche (2000); Kouznetsova, Brekelmans, and Baaijens (2001); Miehe, Schotte, and Lambrecht (2002); Miehe, Schröder, and Schotte (1999); Smit, Brekelmans, and Meijer

(1998), or using a Fourier series approach on a regular grid (Lebensohn, 2001; Moulinec and Suquet, 1998). In addition, the boundary element method or meshless schemes are equally applicable to the task.

7.4
Mean-Field Homogenization

Within the mean-field approach, the microstructure present in domain $\mathcal{B}_0$ is considered as a system of inclusion(s) in a matrix (bottom left in Figure 7.1). Here, the boundary value problem outlined in the preceding section is not solved rigorously, but only in a volume-averaged sense. This means that the spatial variation in $\mathbf{P}$ and $\mathbf{F}$ is not resolved anymore; thus only spatially averaged quantities per phase α are considered and are denoted by $\langle \cdot \rangle^\alpha$. Hence, macroscopic quantities valid for the material point equal the volume-weighted sum of the respective quantities taken over all microstructural constituents. The mean-field counterparts of Eqs. (7.1) and (7.2) then read

$$\overline{\mathbf{F}} = \frac{1}{V_0} \sum_\alpha^N \int_{\mathcal{B}_0^\alpha} \mathbf{F} \, dV_0 = \frac{1}{V_0} \sum_\alpha^N V_0^\alpha \langle \mathbf{F} \rangle^\alpha \, , \qquad (7.16)$$

$$\overline{\mathbf{P}} = \frac{1}{V_0} \sum_\alpha^N \int_{\mathcal{B}_0^\alpha} \mathbf{P} \, dV_0 = \frac{1}{V_0} \sum_\alpha^N V_0^\alpha \langle \mathbf{P} \rangle^\alpha \, , \qquad (7.17)$$

with $\quad V_0^\alpha = \int_{\mathcal{B}_0^\alpha} dV_0 \, .$

Regarding the partitioning of stress or strain, the most basic assumptions would be either equal stress $\langle \mathbf{P} \rangle^\alpha = \overline{\mathbf{P}}$ or equal deformation gradient $\langle \mathbf{F} \rangle^\alpha = \overline{\mathbf{F}}$ among all phases/grains $\alpha = 1, \ldots, N$ present in the microstructure. These extremal cases were introduced by Reuss (1929) and Voigt (1889) for elasticity and by Taylor (1938) assuming uniform plastic strain. Both assumptions disregard the shape and local neighborhood of the inclusions and generally violate compatibility and equilibrium, respectively. More sophisticated assumptions make use of the solution to the problem of an elastic ellipsoidal inclusion in an infinite elastic matrix given by Eshelby (1957). A recent review of the by now well-established laws which govern the strain partitioning in a linear elastic composite has been given by Nemat-Nasser and Hori (1999). Of those, the most frequently employed are the self-consistent approach originally suggested by Kröner (1958a) and the scheme introduced by Mori and Tanaka (1973) (see also Benveniste (1987)). In the former, each inclusion is treated like an isolated one within a matrix having the (unknown) overall stiffness of the composite. The latter embeds each inclusion into the original matrix but considers the average matrix strain to act as far-field strain on the overall composite.

However, extension of such homogenization schemes from the linear to the nonlinear case is facing difficulties, most importantly since the stiffness, that is,

strain(rate) sensitivity of stress, is typically inhomogeneous for a given phase owing to its heterogeneous strain. The stiffnesses are usually homogenized by using the average strain per phase as a reference input into the respective constitutive law. To establish a link between stress and strain per phase, secant (connecting total stress to total strain) and tangent (connecting stress increments to strain increments) formulations for the moduli are employed. The latter has some advantages since it is not restricted to monotonic loading and generally performs better for anisotropic material behavior. Hill (1965) originally introduced this incremental scheme together with a self-consistent approach. Lebensohn and Tomé (1993) later proposed a self-consistent integral formalism which links total stress to strain rate. Further self-consistent schemes are, for example, due to Berveiller and Zaoui (1978), who employed a secant modulus tensor, whereas Masson *et al.* (2000) proposed an affine formulation. Recent developments in the incremental tangent formalism can be found, for instance, in Doghri and Ouaar (2003) and Delannay, Doghri, and Pierard (2007). For a fairly recent review of the use of mean-field methods for elastoplastic composites, we refer to Ponte Castaneda and Suquet (1998).

7.5
Grain-Cluster Methods

Grain-cluster models are an intermediate approach between the mean-field schemes and spatially resolved solutions of a representative volume element outlined above. They reduce the high computational cost of the latter by restricting the discretization to account only for a small number of domains with (typically) homogeneous strain inside each of them. These domains are identified with grains (or parts of grains), thus extending the mean-field approaches by taking into account direct neighbor–neighbor interactions among the constituents of a (multiphase) polycrystal. The introduction of grain aggregates now allows for the relaxation of the (Taylor) assumption of homogeneous strain in each constituent – this assumption generally leads to an overestimation of the polycrystalline strength and rate of texture evolution – by enforcing compatibility only in an average sense for the aggregate as a whole. The basic concept of a partial relaxation of the Taylor hypothesis has been presented in the works of Van Houtte (1982, 1988), Honneff and Mecking (1978), and Kocks and Chandra (1982).

Van Houtte (1982, 1988) considers in his LAMEL model a stack of two grains. Both share a common interface with normal **n**. The stacking direction (and thus the interface normal) corresponds to the smallest dimension of the grains, that is, two flat grains lie on top of each other. The stack is subjected to an imposed overall velocity gradient $\mathbf{L} = \operatorname{grad} \dot{\mathbf{y}}$ (cf. Eq. (3.21)); however, in both grains the local velocity gradients are allowed to deviate from **L** by the two *shear relaxation modes* illustrated in Figure 7.3, which correspond to a movement of the shared interface within its plane. For the particular case of interface orientation shown in Figure 7.3, such
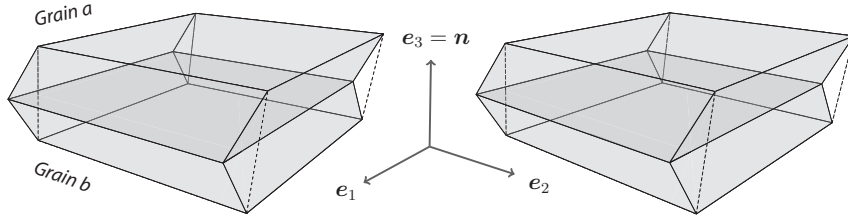
Figure 7.3 Relaxation of an imposed deformation (dotted outline) within a stack of two (flat) grains as assumed by the LAMEL model of Van Houtte (1982, 1988). Both grains share a common interface normal to e_3 and experience equal but opposite shear relaxations normal to e_3, thus moving the shared interface in its plane. The image is a stereo pair.

deviation is given by

$$
\Delta \mathbf{L} = \sum_{r=1}^{2} \dot{\gamma}_{\text{rlx}}^{r} \mathbf{K}_{\text{rlx}}^{r} = \dot{\gamma}_{\text{rlx}}^{1} \begin{pmatrix} 0 & 0 & 1 \\ 0 & 0 & 0 \\ 0 & 0 & 0 \end{pmatrix} + \dot{\gamma}_{\text{rlx}}^{2} \begin{pmatrix} 0 & 0 & 0 \\ 0 & 0 & 1 \\ 0 & 0 & 0 \end{pmatrix}
$$
$$
= \begin{pmatrix} 0 & 0 & \dot{\gamma}_{\text{rlx}}^{1} \\ 0 & 0 & \dot{\gamma}_{\text{rlx}}^{2} \\ 0 & 0 & 0 \end{pmatrix} .
\tag{7.18}
$$

In the special case of both grains having equal volume, the symmetric distribution of the relaxation $\Delta \mathbf{L}$ among them, that is,

$$
\mathbf{L}^{a} = \mathbf{L} + \Delta \mathbf{L} = \mathbf{W}^{a} + \sum_{\alpha=1}^{N^{a}} \dot{\gamma}^{\alpha} (\mathbf{m}^{\alpha} \otimes \mathbf{n}^{\alpha})_{\text{sym}} ,
\tag{7.19a}
$$

$$
\mathbf{L}^{b} = \mathbf{L} - \Delta \mathbf{L} = \mathbf{W}^{b} + \sum_{\beta=1}^{N^{b}} \dot{\gamma}^{\beta} (\mathbf{m}^{\beta} \otimes \mathbf{n}^{\beta})_{\text{sym}} ,
\tag{7.19b}
$$

ensures that the stack fulfills the imposed overall boundary condition. Since grains a and b may deform differently owing to a nonzero relaxation, also different slip systems α and β will become active and result in unequal lattice rotation rates $\mathbf{W}^{a}$ and $\mathbf{W}^{b}$.

To identify the active slip systems together with the amount of relaxation within the stack, the system of Eqs. (7.19) has to be supplemented by an energetic assumption, which is that of minimum plastic dissipation rate:

$$
\mathcal{P} = \sum_{\alpha=1}^{N^{a}} \tau^{\alpha} \dot{\gamma}^{\alpha} + \sum_{\beta=1}^{N^{b}} \tau^{\beta} \dot{\gamma}^{\beta} + \sum_{r=1} \tau_{\text{rlx}}^{r} \left| \dot{\gamma}_{\text{rlx}}^{r} \right| = \min .
\tag{7.20}
$$

In Eq. (7.20) $\tau^{\alpha,\beta}$ denotes the resolved shear stress on the respective slip system (see Eq. (6.5)) and τ_{rlx}^{r} are suitably chosen penalty stresses for the corresponding relaxation shears. Frequently, the penalty stress is ignored and set to zero.

A certain drawback of the original LAMEL model consists in its restriction to deformation modes which are compatible with the presumed grain aspect ratio, for example, pancake-like grains in rolling. This restriction is overcome by two recent

models (Evers *et al.*, 2002; Van Houtte *et al.*, 2005) which focus on the boundary layer between neighboring grains. Both models consider multiple relaxation sites per grain. The relaxation is then applied along the grain perimeter with regard to the *local* grain boundary with normal **n**.

The first one, called the ALAMEL model and introduced by Van Houtte *et al.* (2005), symmetrically relaxes two local velocity gradient components across the interface of the central grain and each of its neighboring grains such that $\sum_r \mathbf{K}_{\mathrm{rlx}}^r = \mathbf{a} \otimes \mathbf{n}$, with $\mathbf{a} \perp \mathbf{n}$. Each individual grain pair is thus relaxed identically to the LAMEL case of pancake grains discussed above. As a result, stress equilibrium at the boundary is maintained except for the normal component (Van Houtte *et al.*, 2005).

The relaxation proposed by Evers *et al.* (2002) is slightly different, as they, firstly, symmetrically relax the *deformation* gradient on both grains by $\Delta \mathbf{F} = \pm \mathbf{a} \otimes \mathbf{n}$, and, secondly, determine the components of **a** by prescribing full stress equilibrium at the grain boundary, which is in fact equivalent to a minimization of deformation energy. A real grain structure can then be mimicked by enclosing each grain with bicrystalline contacts toward its neighbors (as in the ALAMEL case). The distribution of interface orientations reflects the initial grain morphology and evolves with it, thus separating preconditions on initial grain shape from the deformation mode under consideration.

An extension of the monodirectional, thus anisotropic, two-grain stack considered in the above-mentioned LAMEL model to a tridirectional cluster of $2 \times 2 \times 2$ hexahedral grains is due to Crumbach *et al.* (2001), based on former work by Wagner (1994). In this scheme, termed grain interaction (GIA) model, relaxation of strain components $\epsilon_{ij'}(i = 1, 2, 3$ and j' the shortest cluster dimension) and $\epsilon_{ij''}(i \neq j'$ and j'' the second-shortest cluster dimension) is performed in the spirit of the LAMEL model, that is, via mutually compensating shear contributions of two stacked grains, such that each two-grain stack fulfills the external boundary conditions – and in consequence also the cluster as a whole. To maintain intergrain compatibility – possibly violated by different relaxations in neighboring stacks – a density of geometrically necessary dislocations is introduced, which forms the basis for the evaluation of the last contribution (mismatch penalty energy) in Eq. (7.20). The profound progress of the GIA approach is that it connects the intergrain misfit penalty measure to material quantities such as the Burgers vector, shear modulus, work-hardening behavior, and grain size. Owing to its tridirectional setup, the GIA model formulation is compatible with arbitrary deformation modes and is, hence, not necessarily confined to plane strain.

A recent generalization of the tridirectional grain cluster concept was suggested by Eisenlohr *et al.* (2009); Tjahjanto, Eisenlohr, and Roters (2009, 2010) and termed *relaxed grain cluster (RGC)*. This generalization of the original GIA concept comprises mainly two aspects:

- Deformation kinematics are formulated within a finite deformation framework as compared with the framework of (symmetric) infinitesimal strain employed (and violated by nonsymmetric relaxations) in the GIA model. Extension from
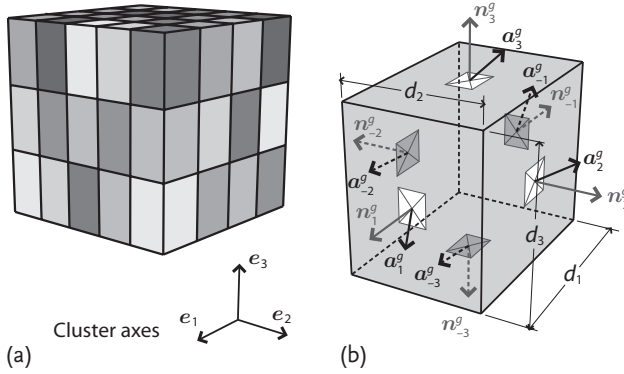
Figure 7.4 Material point representation in the relaxed grain cluster scheme. (a) Cluster of $p \times q \times r$ hexahedral grains at macroscale material point. (b) Hexahedral grain g of di- mensions d_1, d_2, d_3. Interfaces are charac- terized by outward normals $\mathbf{n}_\alpha^g$, which are aligned with the cluster axes. Each interface α carries an attached relaxation vector $\mathbf{a}_\alpha^g$.

the infinitesimal strain formulation to the finite deformation framework ade- quately captures the large strains as well as rigid-body rotations which grains may experience in, for instance, forming operations. Furthermore, mismatch due to elastic deformations and rigid-body rotations are accounted for in this formalism.

- The local constitutive model at the grain level is separated from the macroscale homogenization formulation. This allows the RGC scheme to be implemented in conjunction with various microscale constitutive models, whereas the orig- inal GIA formulation is limited to a single-crystal viscoplastic constitutive law, that is, excluding all elastic effects.

The RGC scheme simplifies the situation at a macroscale material point by approx- imating it as a cluster containing $N = p \times q \times r$ hexahedral (and homogeneously deforming) grains as shown in Figure 7.4a. Grain dimensions along the cluster ref- erence frame $\mathbf{e}_1, \mathbf{e}_2, \mathbf{e}_3$ are denoted by d_1, d_2, d_3, respectively, and are identical for all grains. The interfaces α of each grain g are characterized by their outward-pointing normals $\mathbf{n}_\alpha^g$ and follow the convention illustrated in Figure 7.4b with respect to the cluster frame.

For each individual grain to be able to deviate from the average cluster deforma- tion gradient, $\overline{\mathbf{F}}$, so-called *relaxation vectors* $\mathbf{a}_\alpha^g$ are attached to all interfaces of all grains (see Figure 7.4b). They quantify the displacement of the corresponding in- terface α relative to the overall deformation $\overline{\mathbf{F}}$, such that the individual deformation gradient, $\mathbf{F}^g$, experienced by a particular grain follows as

$$\mathbf{F}^g = \overline{\mathbf{F}} + \sum_{\pm\alpha=1}^{3} \frac{1}{d_\alpha} \left(\mathbf{a}_\alpha^g \otimes \mathbf{n}_\alpha^g \right) , \tag{7.21}$$

that is, all six interface displacements contribute to the deviation of the local defor- mation gradient from the macroscale one.
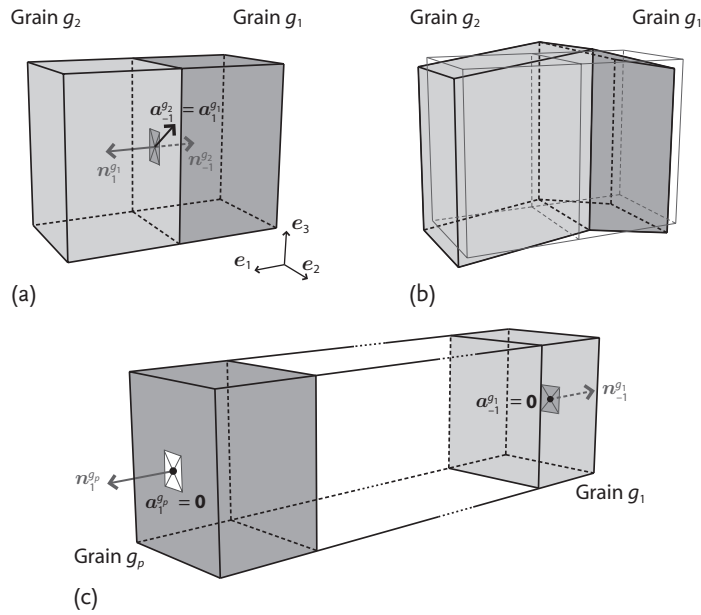
Figure 7.5 Relaxation vectors on interior and exterior interfaces of the grain cluster. (a) Exemplary pair of grains g_1 and g_2, which are neighbors along $\mathbf{e}_1$ and share a common interface. Since the same interface is targeted, the two respective relaxation vectors are set equal $\mathbf{a}_1^{g_1} = \mathbf{a}_{-1}^{g_2}$ for both grains. (b) Combined relaxation of grains g_1 and g_2 due to the relaxation vector shown in (a). (c) Periodic boundary conditions require equal relaxation vectors at opposite exterior interfaces. A vanishing relaxation vector for exterior interfaces is most convenient and does not alter the overall relaxation due to displacements of all same-oriented interior interfaces between them.

The relaxation vectors are subject to two constraints. First, for any two grains g_1 and g_2 the relaxation vectors assigned by either of them to their shared interface α are set to be identical,

$$\mathbf{a}_\alpha^{g_1} = \mathbf{a}_{-\alpha}^{g_2} \;,\tag{7.22}$$

as shown in Figure 7.5a for an exemplary grain pair with an interface normal along $\mathbf{e}_1$. The contribution of such an individual relaxation vector to the grain deformation gradient (given by Eq. (7.21)) is illustrated in Figure 7.5b for the same grain pair. Second, since the overall relaxation behavior is not altered by a constant offset in all those relaxation vectors which belong to a row of interfaces that is aligned with one of the crystal axes, we can (most conveniently) ensure periodic boundary conditions by setting the relaxation vectors on all exterior interfaces to zero as shown in Figure 7.5c. With the above conditions in place, the deformation state of the cluster is determined once all independent[11] relaxation vectors are known.

11) A cluster of size $p \times q \times r$ has in total $(p-1)qr + p(q-1)r + pq(r-1)$ interior interfaces at which independent grain deformation relaxation can occur.
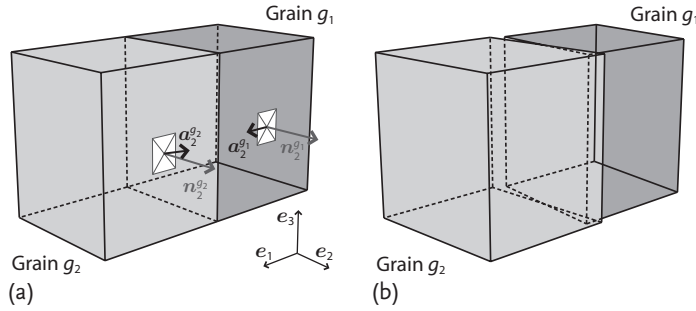
Figure 7.6 Source of mismatch within the grain cluster. Nonequal relaxation vectors on neighboring and same-oriented interfaces result in overlaps and gaps across perpendicular interfaces sharing a trace with the former two. (a) Grain pair exhibiting nonmatching relaxation vectors ($\mathbf{a}_2^{g_2} \neq \mathbf{a}_2^{g_1}$) on neighboring interfaces having a common orientation ($\mathbf{n}_2$). (b) Discontinuity in the gradients of displacement and deformation across the shared interface of the grain pair resulting from the nonmatching relaxation shown in (a).

From Figure 7.5b we observe that the relaxation resulting from a relative displacement of an interface maintains the tight connection between the two neighboring grains. A different picture emerges when we consider the effect of two neighboring interfaces of the same orientation on which the respective relaxation vectors *differ*. This is shown in Figure 7.6 and results in a discontinuity in the gradients of displacement as well as deformation across the interface shared by both grains. To quantify the magnitude of such overlaps and gaps, a measure, which is similar to the surface dislocation tensor of Bilby (1955), is used:

$$\mathbf{M}_\alpha^g = -\frac{1}{2}\left(\mathbf{n}_\alpha^g \times \Delta\mathbf{F}_\alpha^{g\,\mathrm{T}}\right)^{\mathrm{T}} \quad \text{or}$$

$$\text{in index notation} \quad \left[M_\alpha^g\right]_{ij} = -\frac{1}{2}\left[n_\alpha^g\right]_k \left[\Delta F_\alpha^g\right]_{il}\epsilon_{jkl}, \tag{7.23}$$

in which $\Delta\mathbf{F}_\alpha^g$ denotes the jump in deformation gradient between grain g and the neighboring grain sharing interface α.

On the basis of the mismatch measure, a (penalty) energy density, $\mathcal{R}_\alpha^g$, associated with interface α of grain g is introduced. An expression for the penalty energy is rationalized by considering the density of dislocations which could accommodate such deformation mismatch. According to Nye (1953) and Bilby (1955), the presence of a dislocation network can be *uniquely* translated into a tensorial representation of deformation mismatch in the case of three-dimensional and two-dimensional dislocation networks, respectively; however, the inverse is not true. If the mismatch is known, then only a minimum content of geometrically necessary dislocation density can be derived using various optimization procedures (see, e.g., Arsenlis and Parks (1999)). In general, the larger the mismatch the more dislocations are required to accommodate it. This would imply a linear relation between mismatch and penalty energy; the latter could be identified with the line energy of the dislocations in the accommodating network. However, since the accommodation by dislocations is unlikely to be perfect, there will additionally be redundant

(statistically stored) dislocations present. Assuming that the number of these statistically stored dislocations grows increasingly more rapidly with mismatch than the geometrically necessary dislocation content suggests an *overproportional* growth of penalty energy with increasing mismatch. To phenomenologically capture such an overproportionality, a hyperbolic sine function is employed as the relation between the magnitude,

$$\|\mathbf{M}_\alpha^g\| = \left(\mathbf{M}_\alpha^g \cdot \mathbf{M}_\alpha^g\right)^{\frac{1}{2}} , \tag{7.24}$$

of mismatch and the penalty energy density,

$$\mathcal{R}_\alpha^g = \frac{\mu^g}{c_\alpha \xi_\alpha} \sinh\left(c_\alpha \|\mathbf{M}_\alpha^g\|\right) , \tag{7.25}$$

where μ^g denotes the equivalent shear modulus of grain g. The parameter c_α determines the overproportionality of the penalty energy density with respect to the magnitude of mismatch, that is, the larger c_α, the more expensive additional mismatch becomes. An interpretation of the parameter ξ_α can be based on the simplification of the accommodation dislocation network as individual (straight) dislocations and utilizing the textbook (Hull and Bacon, 2001) expression of their line energy. Then, ξ_α turns out to be proportional to the grain dimension d_α in the direction normal to interface α and normalized by the length of Burgers vector b. Despite such simplifications introduced to quantify the accommodating dislocation content and its energy contribution, the value of ξ_α is believed to reflect about the order of magnitude of d_α/b.

The effective penalty energy density $\overline{\mathcal{R}}$ associated with all interfacial incompatibilities within the cluster is finally computed as the volumetric average over the whole domain:

$$\overline{\mathcal{R}} = \frac{1}{\overline{V}_0} \sum_{g=1}^N \sum_{\pm\alpha=1}^3 V_0^g \mathcal{R}_\alpha^g . \tag{7.26}$$

A second contribution to the cluster energy results from the work dissipated in its deformation (see Eq. (3.38)). Let $\mathbf{P}^g$ be the first Piola–Kirchhoff stress tensor of grain g, which is a function of the local deformation gradient $\mathbf{F}^g$ through the local constitutive model, $\mathbf{P}^g = \tilde{\mathbf{P}}^g(\mathbf{F}^g)$. The resulting effective first Piola–Kirchhoff stress tensor, denoted as $\overline{\mathbf{P}}$, is then again computed as the volumetric average of the local stresses $\mathbf{P}^g$ as

$$\overline{\mathbf{P}} = \frac{1}{\overline{V}_0} \sum_{g=1}^N V_0^g \mathbf{P}^g . \tag{7.27}$$

The constitutive energy (or work) density of grain g per unit volume in the reference configuration at time t, denoted by $\mathcal{W}^g$, is given by

$$\mathcal{W}^g = \int_0^t \mathbf{P}^g(\tau) \cdot \dot{\mathbf{F}}^g(\tau)\, d\tau , \tag{7.28}$$

where $\dot{\mathbf{F}}^g$ is the rate of change of the deformation gradient of grain g. It is assumed that the total work density of the cluster, $\overline{\mathcal{W}}$, can be obtained as the volumetric

average of the work density of all grains as

$$\overline{\mathcal{W}} = \frac{1}{\overline{V}_0} \sum_{g=1}^{N} V_0^g \mathcal{W}^g \ . \tag{7.29}$$

The RGC model now postulates that the relaxation behavior of the overall cluster – determined by the set of all relaxation vectors $\mathbf{a} = \{\mathbf{a}_\alpha^g\}$ – is such that for a given $\overline{\mathbf{F}}$ the total energy $\overline{\mathcal{W}} + \overline{\mathcal{R}}$ is a minimum, that is,

$$\hat{\mathbf{a}} = \min \left\{ \overline{\mathcal{W}}(\mathbf{a}) + \overline{\mathcal{R}}(\mathbf{a}) \right\} \ . \tag{7.30}$$

It has to be noted that $\overline{\mathcal{W}}$ is, in general, a nonconvex function of the $\mathbf{F}^g$, which might lead to multiple local minima, prompting algorithmic difficulties in finding the global minimum, and nonunique global minima. The convexity of the overall energy density can, however, be enforced by the introduction of the penalty term $\overline{\mathcal{R}}$. Thus, relying on a convex overall energy density, the solution of the energy minimization problem in Eq. (7.30) corresponds to the stationary point

$$\left. \frac{\partial \left(\overline{\mathcal{W}} + \overline{\mathcal{R}} \right)}{\partial \mathbf{a}} \right|_{\hat{\mathbf{a}}} = \mathbf{0} \ . \tag{7.31}$$

Equation (7.31) has to hold individually for each relaxation vector attached to an (interior) interface out of the set $\hat{\mathbf{a}}$. Selecting an arbitrary interface, which is shared between grains g_1 and g_2 and has a normal $\mathbf{n}_\alpha^{g_1}$ and $\mathbf{n}_{-\alpha}^{g_2}$ when referred to from the two grains respectively, we find that Eq. (7.31) is equivalent to an equation of force equilibrium (or balance of traction) at the shared interface:

$$\frac{\partial \left(\overline{\mathcal{W}} + \overline{\mathcal{R}} \right)}{\partial \mathbf{F}^{g_1}} \frac{\partial \mathbf{F}^{g_1}}{\partial \mathbf{a}_\alpha^{g_1}} + \frac{\partial \left(\overline{\mathcal{W}} + \overline{\mathcal{R}} \right)}{\partial \mathbf{F}^{g_2}} \frac{\partial \mathbf{F}^{g_2}}{\partial \mathbf{a}_{-\alpha}^{g_2}} =$$
$$(\mathbf{P}^{g_1} + \mathbf{R}^{g_1}) \frac{\mathbf{n}_\alpha^{g_1}}{d_\alpha} + (\mathbf{P}^{g_2} + \mathbf{R}^{g_2}) \frac{\mathbf{n}_{-\alpha}^{g_2}}{d_\alpha} = \mathbf{0} \ . \tag{7.32}$$

In Eq. (7.32) the terms $\mathbf{R}^g$ are shorthand for the derivative of the overall penalty energy density $\overline{\mathcal{R}}$ with respect to the grain deformation gradient $\mathbf{F}^g$. It is a stresslike penalty associated with the mismatch at all interfaces of grain g and can be obtained as

$$\mathbf{R}^g = \frac{\partial \overline{\mathcal{R}}}{\partial \mathbf{F}^g} = \sum_{\pm\beta=1}^{3} \frac{\mu^g + \mu^{g\beta}}{\xi_\beta} \left(\frac{\mathbf{M}_\beta^{g\,\mathrm{T}}}{\|\mathbf{M}_\beta^g\|} \times \mathbf{n}_\beta^g \right)^{\mathrm{T}} \cosh \left(c_\beta \|\mathbf{M}_\beta^g\| \right), \tag{7.33}$$

or in components

$$[R^g]_{ij} = \sum_{\pm\beta=1}^{3} \frac{\mu^g + \mu^{g\beta}}{\xi_\beta} \cosh \left(c_\beta \|\mathbf{M}_\beta^g\| \right) \frac{1}{\|\mathbf{M}_\beta^g\|} \left[M_\beta^g \right]_{ik} \left[n_\beta^g \right]_l \epsilon_{klj} \ , \tag{7.34}$$

with g_β being the grain that shares interface β with grain g.

In summary, the minimization of the total cluster energy $\overline{\mathcal{W}} + \overline{\mathcal{R}}$, which is equivalent to establishing balance of traction (see Eq. (7.32)) at each interior interface, yields all relaxation vectors. From those the partitioning of the overall deformation $\overline{\mathbf{F}}$ into individual grain deformations $\mathbf{F}^g$ is determined by Eq. (7.21). The local stress responses $\mathbf{P}^g$, given by the corresponding (but independent) constitutive laws $\tilde{\mathbf{P}}^g(\mathbf{F}^g)$, are averaged according to Eq. (7.27) and compose the overall stress of the cluster $\overline{\mathbf{P}}(\overline{\mathbf{F}})$.

8
Numerical Aspects
of Crystal Plasticity Finite Element Method Implementations

8.1
General Remarks

As far as the finite element method is concerned, crystal plasticity finite element
(CPFE) approaches can be regarded as a class of constitutive material models;
therefore, they can be implemented directly into an finite element code when it
is available in source form. In the case of commercial finite element codes, CPFE
constitutive laws are implemented in the form of a user subroutine, for example,
HYPELA2 in MSC.Marc (Mar, 2007) or UMAT/VUMAT in Abaqus (Aba, 2007). De-
pending on whether the finite element code is implicit or explicit, the purpose of
a material model is onefold or twofold: (1) calculate the stress $\boldsymbol{\sigma}$ required to reach
the final deformation gradient (implicit and explicit); (2) calculate the Jacobi matrix
$\mathbf{J} = \partial\boldsymbol{\sigma}/\partial\mathbf{E}$ (implicit only, $\mathbf{E}$ is the symmetric strain tensor).

The stress calculation is usually implemented using a predictor–corrector
scheme. Figure 8.1 visualizes the setup of the clockwise loop of calculations to
be performed. In principle, one could start predicting any of the quantities in-
volved, follow the loop, and compare the resulting quantity with the predicted
one. Subsequently, the prediction would be updated using, for instance, a Newton–
Raphson scheme. Various implementations were suggested using the elastic defor-
mation gradient $\mathbf{F}_e$ (Sarma and Zacharia, 1999), the plastic deformation gradient
$\mathbf{F}_p$ (Maniatty, Dawson, and Lee, 1992), the second Piola–Kirchhoff stress $\mathbf{S}$ (Ka-
lidindi, Bronkhorst, and Anand, 1992), or the shear rates $\dot{\gamma}^{\alpha}$ (Peirce, Asaro, and
Needleman, 1983) as a starting point. Although they certainly all should lead to the
same results, there are two numerical aspects to consider: first, the inversion of the
Jacobi matrix occurring in the Newton–Raphson algorithm; second, the character
of the equations to be evaluated.

Regarding the first point, one has to realize that the dimension of the Jacobi ma-
trix is equal to the number of independent variables of the quantity that is used as
a predictor. These are nine variables for $\mathbf{F}_e$, eight for $\mathbf{F}_p$ (owing to volume conserva-
tion), and six for $\mathbf{S}$ (owing to the symmetry of the stress tensor). However, if the $\dot{\gamma}^{\alpha}$
are chosen, there are at least 12 variables (number of slip systems in face-centered
cubic crystals), but up to 48 (number of slip systems in body-centered cubic crys-
tals), or even more in the case of additional twinning. Inverting such large matrices
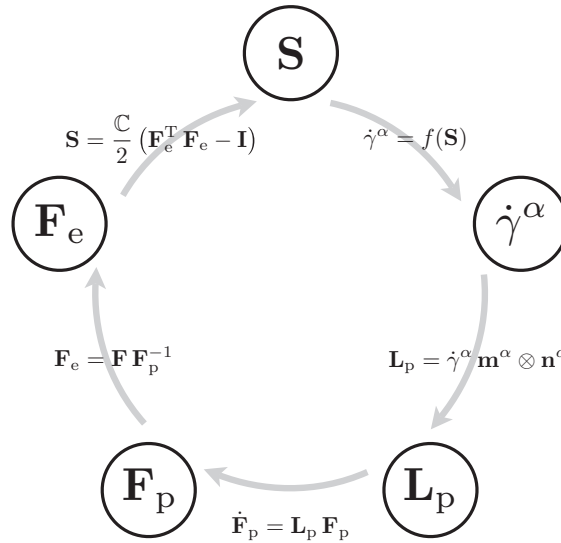
Figure 8.1 Clockwise loop of calculations during stress determination (**S** second Pio-la–Kirchhoff stress, $\dot{\gamma}^{\alpha}$ shear rate, $\mathbf{L}_{\mathrm{p}}$ plastic velocity gradient, $\mathbf{m}^{\alpha}$ slip direction, $\mathbf{n}^{\alpha}$ slip plane normal, $\mathbf{F}_{\mathrm{p}}$ plastic deformation gradient, $\mathbf{F}_{\mathrm{e}}$ elastic deformation gradient, $\mathbb{C}$ elasticity tensor, $\mathbf{I}$ identity matrix).

(i. e., 48×48) is computationally quite demanding, which is the reason why such implementations spend effort on tracking the number of currently active slip systems (Cuitino and Ortiz, 1992).

The second point concerns the numerical convergence behavior of the overall system. When an iteration is started from any quantity other than $\dot{\gamma}^{\alpha}$, the procedure involves calculating the slip rates from the stress. This is usually done using a power law or an exponential law. The slope of these highly nonlinear functions is rapidly increasing, that is, small variations in stress lead to increasingly larger deviations in the strain rate. Therefore, for large deformations, where convergence becomes a main issue, the iteration behavior of the stress loop becomes worse. However, when starting from $\dot{\gamma}^{\alpha}$, the inverse tendency applies, that is, stress variations with varying shear rates get smaller and smaller. This is why the second approach promises a better numerical stability at large strains, however at the cost of dealing with a large Jacobi matrix.

Calculating the Jacobi matrix for implicit finite element codes in the case of a crystal plasticity constitutive model has generally to be done numerically by perturbing **E** (Kalidindi, Bronkhorst, and Anand, 1992), as a closed analytical form exists only in special cases. This numerical evaluation includes six stress evaluations, which makes it computationally expensive.

8.2
Explicit Versus Implicit Integration Methods

When discussing explicit versus implicit integration schemes, one has to distinguish between two aspects. Firstly, the finite element solver can follow an explicit or implicit approach and, secondly, the material model can be iterated using explicit or implicit integration schemes. Concerning the first point, Harewood and McHugh (2007) recently compared the efficiency of both methods when applying crystal plasticity models to forming problems. As could be expected, to some extent the outcome of this comparison is problem-dependent. As a rule, the explicit scheme generally seemed favorable when contact is involved. This is, however, not special for the CPFE method but applies to any finite element method simulation including contact.

Regarding the material model itself, that is, the material subroutine in the case of commercial finite element solvers, anything from explicit to fully implicit integration methods is possible. The task of the material model is twofold. Firstly, the stress necessary to achieve the prescribed deformation has to be determined. Secondly, the material state has to be updated. In most codes, first the stress is determined implicitly for a fixed state of the material and in a subsequent step the material state is updated. In the case of a fully implicit implementation, the stress has to be determined again until convergence is achieved, whereas in a semi-implicit code the calculation is stopped after the state was updated. An advantage of the fully implicit scheme is that it truly converges to the correct solution (if it converges at all), whereas the explicit solution converges generally but not necessarily to the correct solution. Since explicit schemes typically use very small time steps, semi-implicit integration schemes should generally work satisfactorily with respect to precision in that case, whereas they are at the same time faster than a fully implicit scheme.

8.3
Element Types

CPFE constitutive models as introduced in Chapter 6 are formulated in a tensorial way to account for material anisotropy; therefore, they are based on a three-dimensional stress tensor. In terms of finite element design this means that crystal plasticity works best for three-dimensional models and, when used for two-dimensional models it is restricted to plane strain boundary conditions and does not work for plane stress boundary conditions.

Most CPFE simulations use linear elements, that is, elements using linear interpolation functions for the displacements. Therefore, these elements cannot describe strain gradients within one element. When the resolution of the finite element mesh is reasonably fine, this can be tolerated for single-phase materials. However, when strong strain gradients occur, either owing to boundary conditions or owing to the presence of multiple phases, linear elements are usually not suf-

ficient to correctly capture these strong gradients. In such cases higher-order elements should be used.

In cases with advanced CPFE material models, such as introduced in Section 6.1.3.2, that include strain gradients, the situation becomes more complicated. The standard element formulations are only continuous in the displacements (C_0-continuous). This implies that strains can be calculated as displacement gradients, but strain gradients might be undefined. To overcome this problem one has to use enhanced element formulations as done by Evers, Brekelmans, and Geers (2004a) and Arsenlis *et al.* (2004). However, the definition of boundary conditions becomes rather complicated in the case of complex loadings for such element formulations. Therefore, many authors still use standard elements for such simulations and derive the necessary gradients from multielement patches as described, for example, in Han *et al.* (2007).

Part Three   Application

9

Microscopic and Mesoscopic Examples

9.1
Introduction to the Field of Crystal Plasticity Finite Element Experimental Validation

Crystal plasticity finite element (CPFE) simulations can be validated by experiments in a detailed manner, with respect to both mechanical and microstructural observable quantities, Figure 9.1. Measures of the former group can be monitored in terms of forces, elastic stiffness (including springback effects), stresses, mechanical size effects, mechanical anisotropy, shape changes, hardness, strain paths, strain rates, and strains including local strain maps obtained by digital image correlation or speckle methods.

Quantities based upon microstructure observations can be mapped in terms of crystallographic texture, grain shapes, dislocation substructures and densities, internal stresses, and surface roughness. Many such comparisons can be conducted one-to-one and at different scales, Table 5.1. In addition to these well-established methods, novel tomographic experiments allow one to compare CPFE predictions
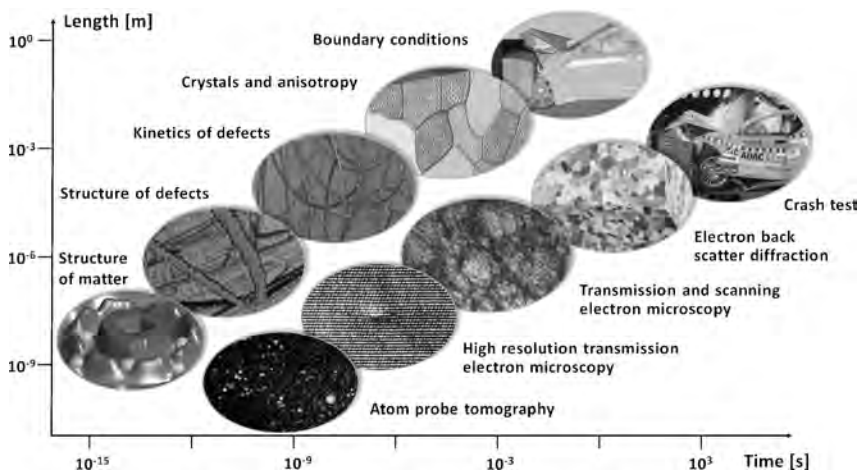
Figure 9.1 The various theoretical approaches and microstructural observables in the field of crystal plasticity modeling encountered at various scales.

with real microstructures also in three dimensions, for instance, by synchrotron orientation tomography (Larson *et al.*, 2002; Nielsen *et al.*, 2001) and electron backscatter diffraction (EBSD) tomography (three-dimensional EBSD) (Bastos, Zaefferer, and Raabe, 2008; Demir *et al.*, 2009; Konrad, Zaefferer, and Raabe, 2006; Zaafarani *et al.*, 2008, 2006; Zaefferer, Wright, and Raabe, 2008). Other new techniques to validate CPFE predictions are microscopic mechanical tests conducted on micrometer- or nanometer-sized samples prepared by electrochemical or focused ion beam (FIB) methods (Dimiduk, Uchic, and Parthasarathy, 2005; Greer, Oliver, and Nix, 2005; Kiener *et al.*, 2006; Uchic *et al.*, 2004). In this section we review a selection of some literature examples which document applications of the CPFE method from microscopic to macroscopic scales.

9.2
Stability and Grain Fragmentation in Aluminum under Plane Strain Deformation

It has been frequently observed that during plastic deformation initially uniformly oriented grains can gradually build up large in-grain orientation scatter under gradient-free boundary conditions (Beaudoin, Mecking, and Kocks, 1996). In this section this phenomenon is investigated with the aim to understand how this phenomenon depends on the crystal orientation, on neighbor grains, and on the external boundary conditions (e.g., friction) (Raabe *et al.*, 2002c; Raabe, Zhao, and Roters, 2002d, 2004b; Zhao, Mao, and Raabe, 2002).

It was found that the orientation stability (under plane strain loading) in aluminum (as an example of a face-centered cubic material with high stacking fault energy) can fall into one of three basic categories. This can be demonstrated by CPFE simulations and by classical homogenization theory. Basically, the tendency for orientation stability can be expressed in terms of the divergence behavior of the reorientation field (which is sometimes also referred to as flow field) for an orientation under a given load. The first group of orientations is stable and does not build up substantial in-grain orientation scatter even for minor variations in the initial orientation spread or in the boundary conditions (e.g., change in the friction coefficient). Typically, such orientations show a very symmetric arrangement of the active slip systems. Their reorientation behavior is characterized by negative divergence of their reorientation field (for a given load tensor). They are stable and not prone to build up internal orientation scatter. The second group is extremely unstable and builds up strong in-grain orientation scatter. These orientations show positive divergence of the reorientation field. Crystals that fall into the third category reveal very small divergence of their reorientation field, which means that they have the same tendency for orientation changes as their neighborhood. A first-order classification for orientation stability, therefore, can be simply expressed in terms of the reorientation divergence for a given orientation.

Substantial dependence of the formation of in-grain orientation scatter on the neighbor grains or on details of the boundary conditions exists mainly for the orientations of the second and third categories, Figures 9.2 and 9.3a–c.

initial orientation:
45° rotated cube orientation
($\varphi_1=45°$, $\phi=0°$, $\varphi_3=0°$), fcc

initial orientation:
Brass orientation
($\varphi_1=35°$, $\phi=45°$, $\varphi_3=0°$), fcc

initial orientation:
S orientation
($\varphi_1=60°$, $\phi=32°$, $\varphi_3=65°$), fcc
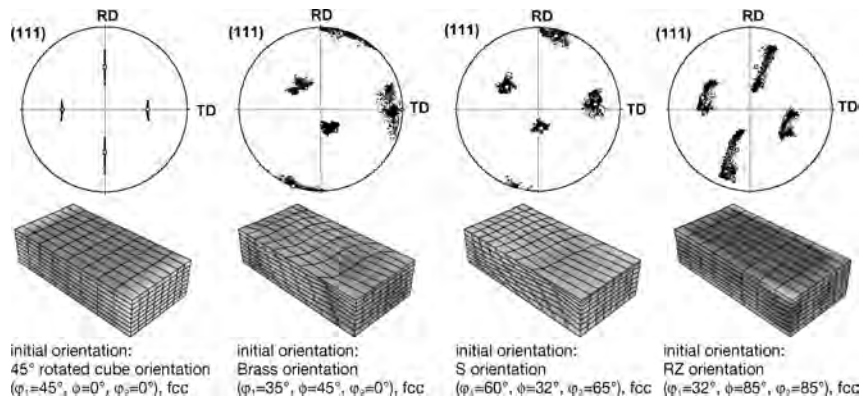
initial orientation:
RZ orientation
($\varphi_1=32°$, $\phi=85°$, $\varphi_3=85°$), fcc

Figure 9.2 Accumulated misorientations in gray-scale coding (light values indicate large misorientations) for aluminum grains together with {111} pole figures after 50% plane strain deformation for different orientations. The simulations used 12 slip systems. The

open squares in the pole figures show the initial orientation (which was the same at all integration points) and the black dots show the orientations scatter after the deformation.
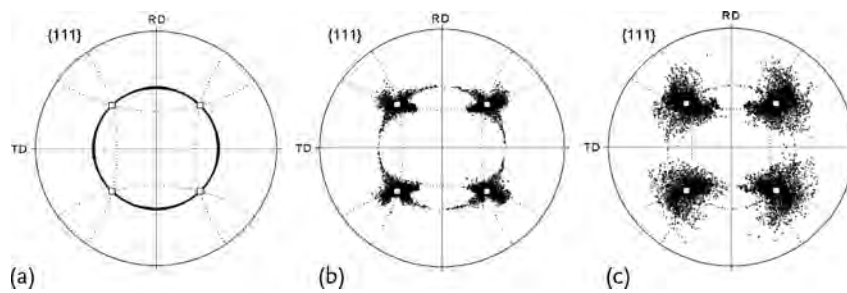
Figure 9.3 Orientation stability of the cube orientation after 50% plane strain compression for different internal and external boundary conditions. (a) Starting condition: exact cube orientation without initial orientation scatter, Coulomb friction coefficient 0.1.

(b) Starting condition: cube orientation with 2.5° initial orientation scatter, Coulomb friction coefficient 0.1. (c) Starting condition: initial cube orientation with 2.5° initial orientation scatter, Coulomb friction coefficient 0.3.

9.3
Texture and Dislocation Density Evolution in a Bent Single-Crystalline Copper Nanowire

This section presents an investigation of a bending test using experiments and CPFE simulations. A 2-μm-long single-crystalline copper nanowire was produced by FIB fabrication (Weber *et al.*, 2008). The average cross section of the specimen was 750 nm × 750 nm. The nanowire was bent *in situ* using a micromanipulator. Characterization was done using scanning electron microscopy (SEM) and EBSD. The experiment was compared with simulations conducted by a CPFE
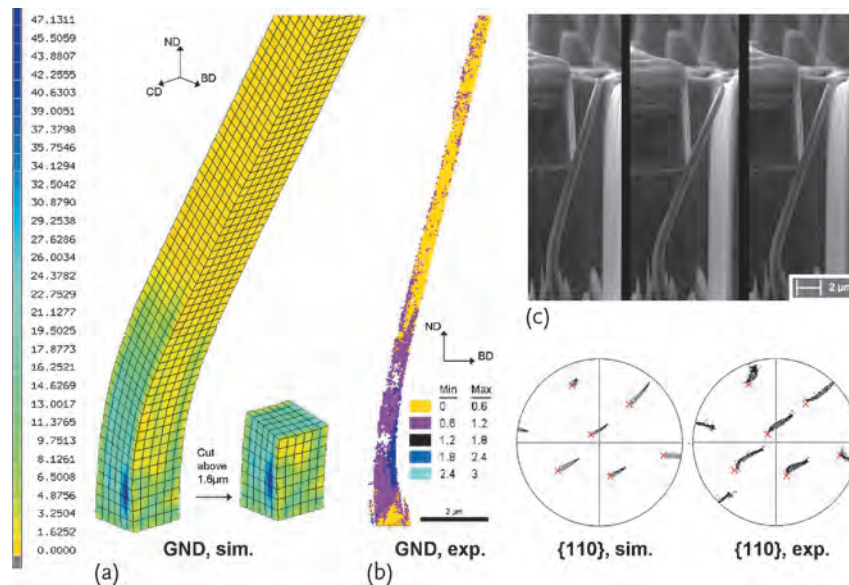
Figure 9.4 (a) Predicted density of the geometrically necessary dislocations during nanowire bending in units of per square micrometer. (b) Experimentally determined geometrically necessary dislocation density, quantified in terms of the average local orientation gradient determined via high-resolution electron backscatter diffraction. (c) Subsequent scenes taken during bending. (d) Pole figures of the bent nanowire obtained from experiment and simulation. The predictions were used to determine the exact boundary conditions that occurred during testing. The crosses indicate the initial orientation. CD: cross direction; BD: bending direction; ND normal direction; GND: geometrically necessary dislocation. Bending took place in the negative *Y*-direction; ND normal direction.

analysis using a dislocation-density-based constitutive hardening law (Ma and Roters, 2004; Ma, Roters, and Raabe, 2006a; Zaafarani *et al.*, 2008). The simulations were required to study the influence of the boundary conditions on the results since the boundary conditions can have a substantial influence on the evolution of the texture during bending. The simulations and the experimental results revealed good agreement in terms of texture evolution and elastic springback as long as the boundary conditions were reflected accurately. The model provides information about the microstructure evolution in terms of particular material parameters such as the evolution of the dislocation density, Figure 9.4a–d. Similar CPFE simulations on the deformation of pillars by microscale compression tests were presented by Raabe, Ma, and Roters (2007a). The motivation for selecting this example is to document the capability of the CPFE approach to yield good texture predictions even at small scales where the constitutive law, which is built on a statistical dislocation model (Ma and Roters, 2004; Ma, Roters, and Raabe, 2006a, 2007), reaches its limits owing to the small size of the elements.

9.4
Texture and Microstructure Underneath a Nanoindent in a Copper Single Crystal

This example is about the origin of deformation-induced orientation patterns below nanoindents in a {111}-oriented copper single crystal. The experiments and the simulations were conducted using a conical indenter with a spherical tip (Wang *et al.*, 2004; Zaafarani *et al.*, 2006). The patterns were characterized by neighboring crystalline zones with opposite rotation rates. The approach to analyze and understand the phenomenon was as follows: First, the deformation-induced orientation patterns were investigated in three dimensions using a high-resolution tomographic EBSD technique (Demir *et al.*, 2009; Zaafarani *et al.*, 2008). This method works by a fully automated alternating serial sectioning and EBSD mapping procedure in a SEM-FIB setup (three-dimensional EBSD) (Bastos, Zaefferer, and Raabe, 2008; Konrad, Zaefferer, and Raabe, 2006; Zaefferer, Wright, and Raabe, 2008). Second, the problem was modeled using a CPFE method which is based on a constitutive model that uses dislocation densities as state variables (Ma and Roters, 2004; Roters, Raabe, and Gottstein, 2000). It was found that the rotation patterns induced

(a) Measured lattice rotation about [11-2]   (b) Simulated lattice rotation about [11-2]
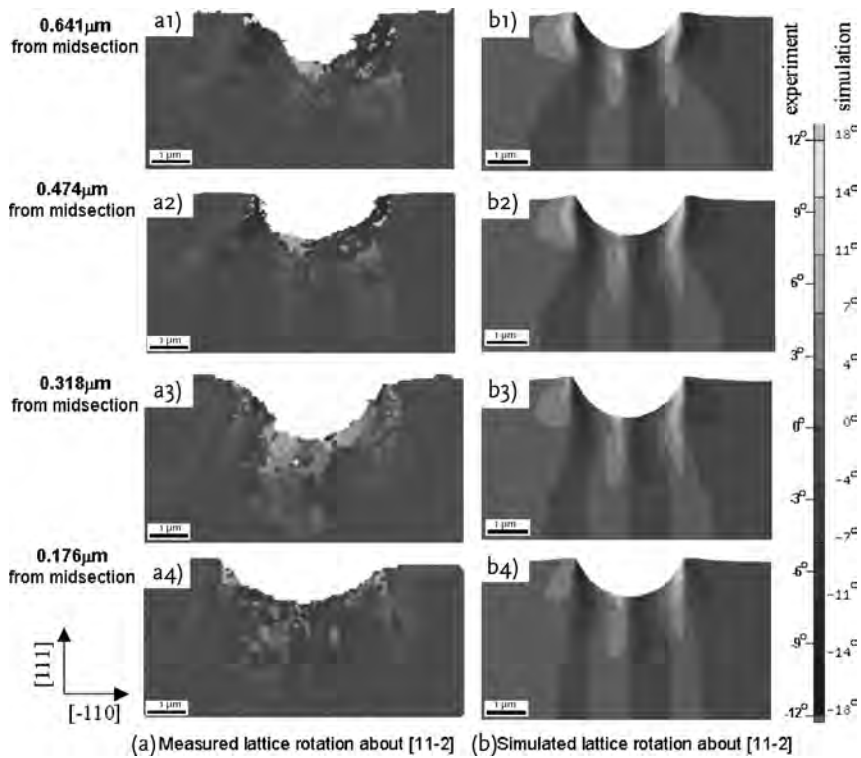
Figure 9.5 Comparison of crystal rotation about the direction $[11\bar{2}]$ in the sample reference system underneath the indent at different sections between experiment and simulation (positive values mean counterclockwise rotation) (Demir *et al.*, 2009; Zaafarani *et al.*, 2008, 2006).

during indentation were well predicted by the CPFE model. The change of the crystal rotation directions could be explained by the different slip system combinations that were activated owing to the geometry of the indenter causing a gradual change in the loading axis that evolved differently at different locations during indentation, Figure 9.5.

9.5
Application of a Nonlocal Dislocation Model Including Geometrically Necessary Dislocations to Simple Shear Tests of Aluminum Single Crystals

9.5.1
Comparisons of von Mises Strain Distributions

In this section experimental results are compared with simulations achieved using a phenomenological viscoplastic local model as presented in Section 6.1.2 and the nonlocal model presented in Section 6.1.3 in Figure 9.6. In the experiments the maximum deformation is found in the lower-left corner of the single crystal and extends diagonally across the crystal surface. Although this behavior is correctly reproduced by the nonlocal model, the phenomenological viscoplastic model predicts the highest strains in the higher-left corner of the specimen. One can assume that the better prediction yielded by the nonlocal model is mainly a consequence of the physically based latent hardening law and the introduction of the geometrically necessary dislocations (GNDs). This assumption is supported by the data presented in Figure 9.7b, which reveals that substantial densities of GNDs are generated near sample borders. For better comparisons of the relative contributions of the two types of dislocations, Figure 9.7b and c shows both the statistically stored dislocation (SSD) and the GND distributions on the normal direction surface.

9.5.2
Size Dependence of the Nonlocal Model

The introduction of the GNDs renders the nonlocal model size-sensitive; therefore, the shear simulation is repeated for a set of three virtual specimens of different height-to-length ratios. For this purpose the height of the sheared sample is changed to one half and one tenth of the original height, respectively. The resulting shear stress–shear strain curves are shown in Figure 9.8.

Equations (6.33a), (6.33b), (6.18), and (6.19) reveal that the GNDs contribute to the passing stress and to the multiplication term of the immobile dislocations. For this reason one would expect higher predicted stresses for the thinnest sample owing to the relative increase of zones which are mechanically affected by the presence of interfaces. This is indeed confirmed by Figure 9.8. From the middle row in Figure 9.7 it becomes obvious how the relative size of the zone influenced by the GND increases with the decreasing sample height. This increased GND entails also an increase of the SSD as expected and shown in the bottom row in Figure 9.7.
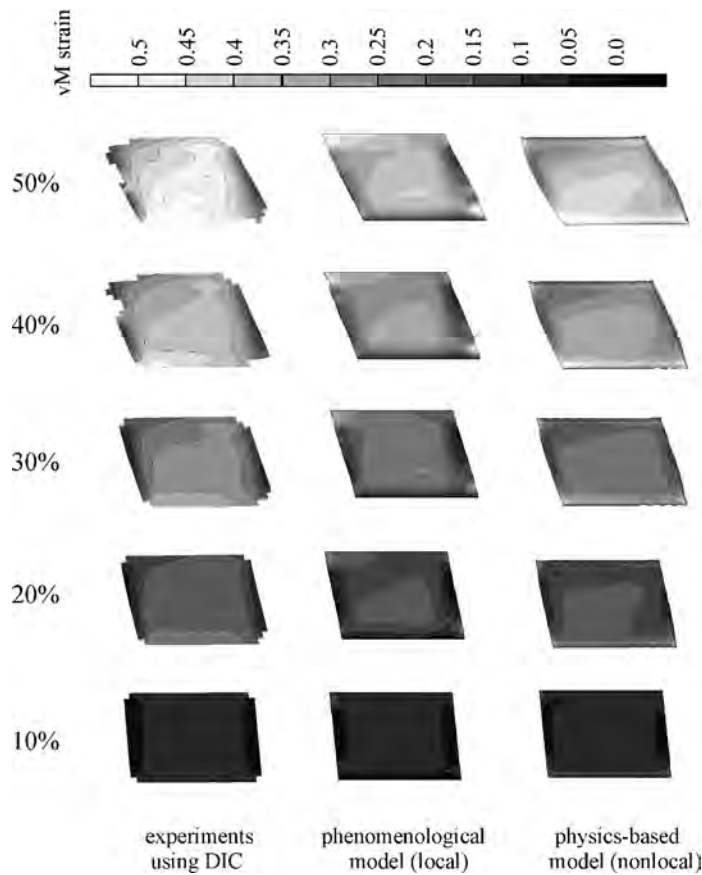
Figure 9.6 Comparison of the von Mises equivalent strain on the surface of an aluminum single crystal (3.1 mm long, 2.0 mm thick, and 2.2 mm high) for a simple shear test. The left column shows experimental results obtained by strain measurements via digital image correlation (DIC). The central column shows results obtained by using a conventional viscoplastic formulation. The right column shows results obtained by using an enhanced nonlocal model (see Section 6.1.3) which considers geometrically necessary dislocations.

Additionally, the top row in Figure 9.7 also shows that the texture evolution of the crystal is changed. This results in an intersection of the stress–strain curves for $H = H_0$ and $H = H_0/2$ in Figure 9.8.

The strong influence of incorporating GNDs into the CPFE framework on the predicted reorientation rates is due to the penalty function they impose. This means that each reorientation step which introduces an orientation divergence with respect to the neighborhood (Raabe, Zhao, and Mao, 2002b) is impeded owing to the corresponding introduction of GNDs.

Figure 9.9 shows profiles of the two immobile dislocation densities (SSDs and GNDs) across the specimen near the sample center for a shear deformation of
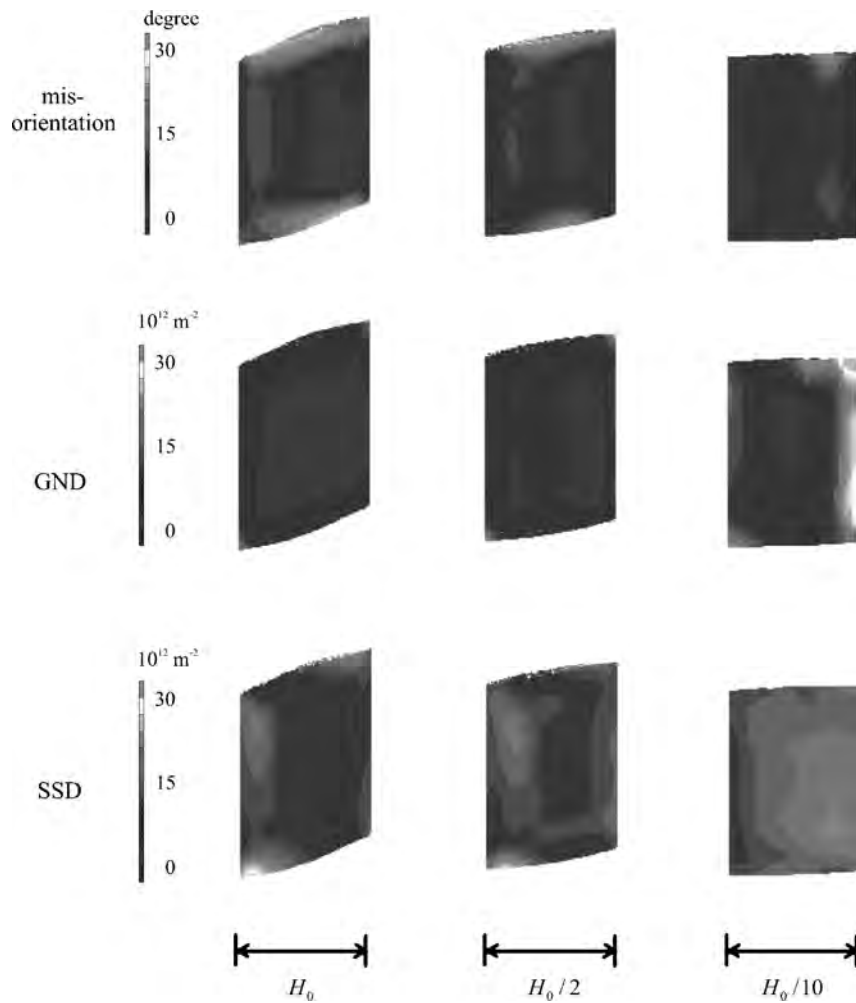
Figure 9.7 Comparisons of dislocation densities and misorientation for different samples after a 30% shear deformation. The heights of the samples are $H = H_0$, $H = H_0/2$, and $H = H_0/10$ (all plots are scaled to the same height for a better comparison), respectively. GND: geometrically necessary dislocation density, SSD: statistically stored dislocation density.

about 30%. Although both dislocation densities are always of the same order of magnitude, their ratio is clearly influenced by the relative sample height. For $H = H_0$ the SSD density is always higher than the GND density; however, this situation is gradually changed with decreasing relative sample height. Finally, for $H = H_0/10$ the GND density surpasses the SSD density near the edges of the heavily sheared zone of the sample.
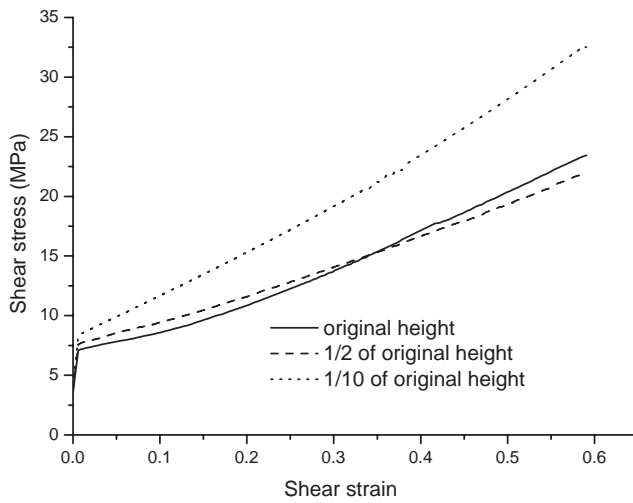
Figure 9.8 Simulated shear stress–shear strain curves for samples with different height-to-length ratios demonstrating the size sensitivity of the nonlocal dislocation model.
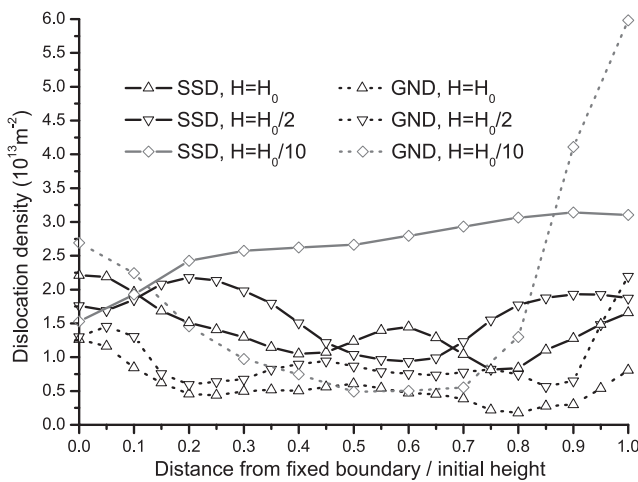
Figure 9.9 Comparison of statistically stored dislocation density (SSD) and the geometrically necessary dislocation density (GND) for simulated shear tests of samples with different heights after a 30% shear deformation (line scan near the sample center).

9.5.3
Conclusions

A simple shear experiment of an aluminum single crystal was used to validate the nonlocal dislocation model. The predicted distribution of the local deformation was found to be in better accordance with the experiment than for a conventional viscoplastic phenomenological model. One can assume that the better prediction

yielded by the new model is mainly a consequence of the introduction of the GNDs and the physically based latent hardening law into the framework.

The size sensitivity of the model has been clearly demonstrated numerically for samples of different heights. Besides the Hall–Petch hardening effect, also the texture evolution is found be be size-sensitive.

9.6
Application of a Grain Boundary Constitutive Model to Simple Shear Tests of Aluminum Bicrystals with Different Misorientation

This example is about the use of the dislocation-based constitutive model to incorporate the mechanical interaction between mobile dislocations and grain boundaries into the CPFE framework. The grain boundary model which was presented in detail in Section 6.1.3.3 was implemented in the commercial solver MSC.Marc200x using the subroutine HYPELA2 (Mar, 2007). Details of the experimental setup, finite element mesh, and boundary conditions are presented in Ma, Roters, and Raabe (2006a,b). The new model is applied to the case of 50% (frictionless) simple shear deformation of three aluminum bicrystals with a low-, intermediate-, and high-angle grain boundary, respectively, parallel to the shear plane. The simulations are compared with the findings of experiments with respect to the von Mises equivalent strain distributions and the crystallographic orientation distributions (textures). Some of the constitutive parameters required in the dislocation model (which contains also nonlocal gradient terms) are fitted by using the stress–strain response of the single-crystal simple shear test presented in the previous section.

Figures 9.10–9.12 show the comparison of the von Mises strain patterns obtained from the experiment (left column), from the simulation with a conventional viscoplastic constitutive law without an interface model (center column), and from the simulation series which is based on the new set of constitutive laws as introduced in Section 6.1.3.3 (right column). The figures show the von Mises equivalent strain distributions for five subsequent stages of shear with a constant increase of 10% per load step.

The experimental data clearly reveal for all three bicrystals the strong micromechanical effect imposed by the presence of the respective grain boundary. Even for the low-angle grain boundary (7.4°) the shear experiment clearly shows an effect of strain partitioning among the two crystals. With increasing grain boundary misorientation, the heterogeneous partitioning of the von Mises strain between the two grains becomes even more pronounced.

Concerning the corresponding simulation results it is essential to note that the use of the empirical viscoplastic (local) law (second rows in Figures 9.10–9.12) does not adequately reproduce the influence of the grain boundaries on the distribution of the accumulated von Mises strain. This applies, in particular, for the two bicrystals which have a low- and intermediate-angle grain boundary, respectively. For the bicrystal with the high-angle grain boundary, Figure 9.12, the empirical (local)
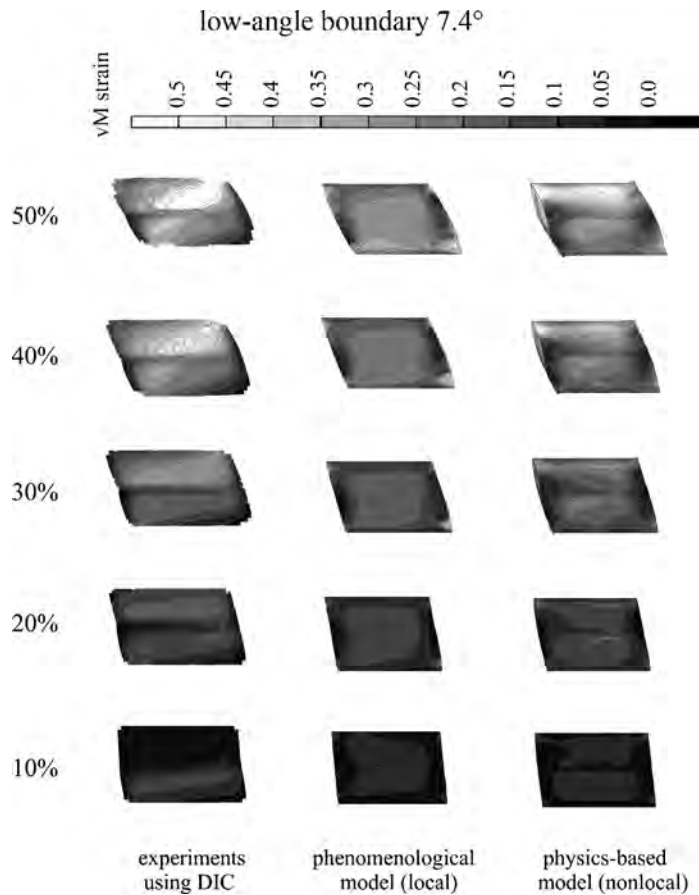
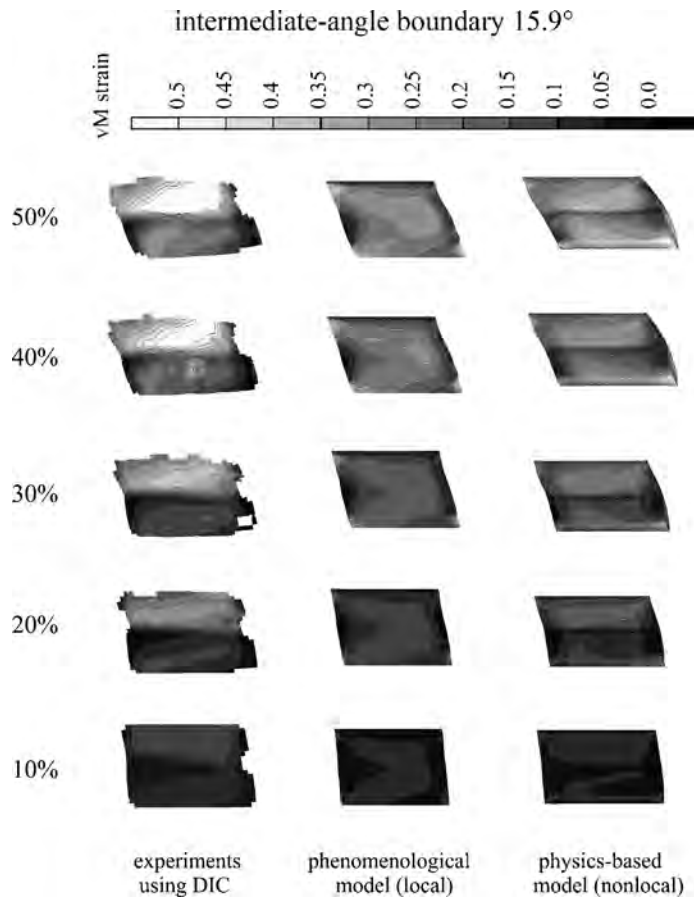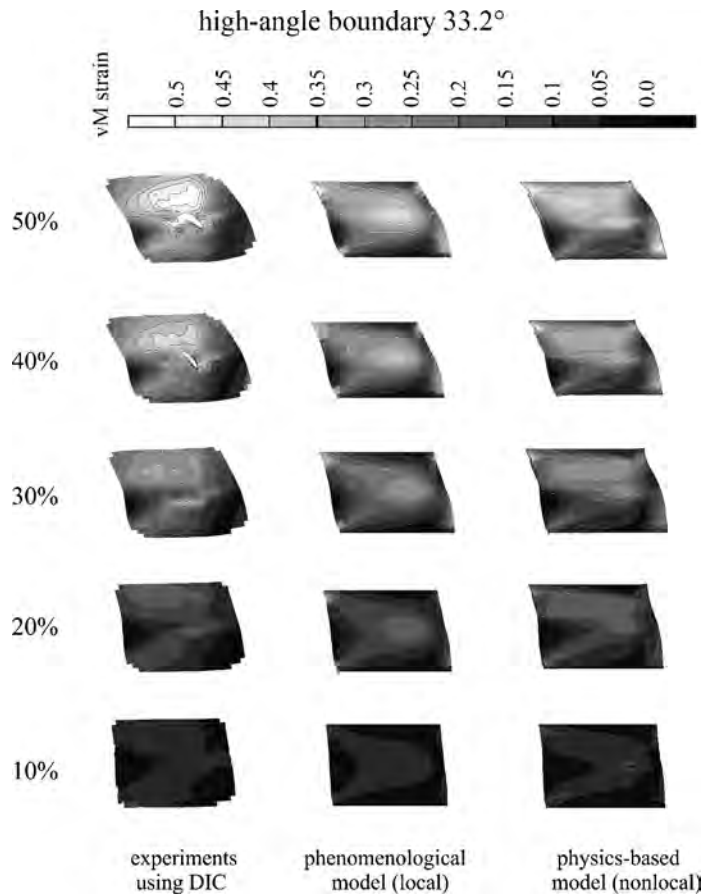**Figure 9.10** Simple shear test of a bicrystal (3.1 mm long, 2.0 mm thick, and 2.2 mm high) with a low-angle grain boundary (7.4°). Comparison of the von Mises strain patterns of the experiment obtained by digital image correlation (DIC, left column), from the simulation with a conventional viscoplastic constitutive law (center column), and from the simulation which uses the new set of constitutive laws (right column).

model is capable of predicting some – although not all – characteristics of the strain partitioning between the two crystals. The partial success of the simulation with the empirical viscoplastic hardening law in the case of the high-angle grain boundary is attributed to the strong effect of the change in the Schmid factor across the interface. This means that the kinematic effect which arises from distinct differences in the slip system selection on either side of a grain boundary plays an essential role in this case. We refer to this effect as *kinematic hardening* imposed by grain boundaries.

Figure 9.13 shows the {111} pole figures for the three bicrystals as obtained from the experiments and simulations using both a conventional local model and the new nonlocal model (50% shear deformation). The experimental pole figures show

Figure 9.11 Simple shear test of a bicrystal (3.1 mm long, 2.0 mm thick, and 2.2 mm high) with an intermediate-angle grain boundary (15.9°). Comparison of the von Mises strain patterns of the experiment obtained by digital image correlation (DIC, left column), from the simulation with a conventional viscoplastic constitutive law (center column), and from the simulation which uses the new set of constitutive laws (right column).

reorientation zones with a strong *Z*-rotation (around normal direction) which is common to both crystals for all three bicrystal specimens. The scatter of the texture in all samples is rather weak, that is, the reorientation took place rather homogeneously throughout the crystal when considering that the two original orientations were not stable in all three cases under the load imposed. The scatter is due to minor differences in the reorientation rates (similar rotation direction) which originate from local differences in the accumulated strain as is evident from the von Mises strain diagrams shown before. The texture predictions which were obtained by using the local viscoplastic constitutive model (Figure 9.13, pole figures d–f) show a rather large orientation scatter in all three cases. The texture spread substantially exceeds the scatter observed in the experiments. The texture evolution

Figure 9.12 Simple shear test of a bicrystal (3.1 mm long, 2.0 mm thick, and 2.2 mm high) with a high-angle grain boundary (33.2°). Comparison of the von Mises strain patterns of the experiment obtained by digital image correlation (DIC, left column), from the simulation with a conventional viscoplastic constitutive law (center column), and from the simulation which uses the new set of constitutive laws (right column).

in the two abutting crystals is similar, that is, the bicrystal character of the pole figures is lost. This observation matches the strain distributions predicted by the viscoplastic constitutive model. The viscoplastic simulations do not show any influence of the grain boundary on the micromechanical behavior except for the case of the high-angle grain boundary with 33.2° misorientation where the kinematics of the interface prevailed in terms of the change in the Schmid factor across the boundary.

The texture predictions obtained by the use of the coupled nonlocal dislocation and grain boundary constitutive model (Figure 9.13, pole figures g–i) reveal much smaller orientation scatter and smaller reorientation rates when compared with the simulations obtained by the local phenomenological model (Figure 9.13, pole fig-

experimental
results

(a)   (b)   (c)

phenomenological
model (local)

(d)   (e)   (f)

physics based
model (non-local)

(g)   (h)   (i)

7.4° bicrystal   15.9° bicrystal   33.2° bicrystal
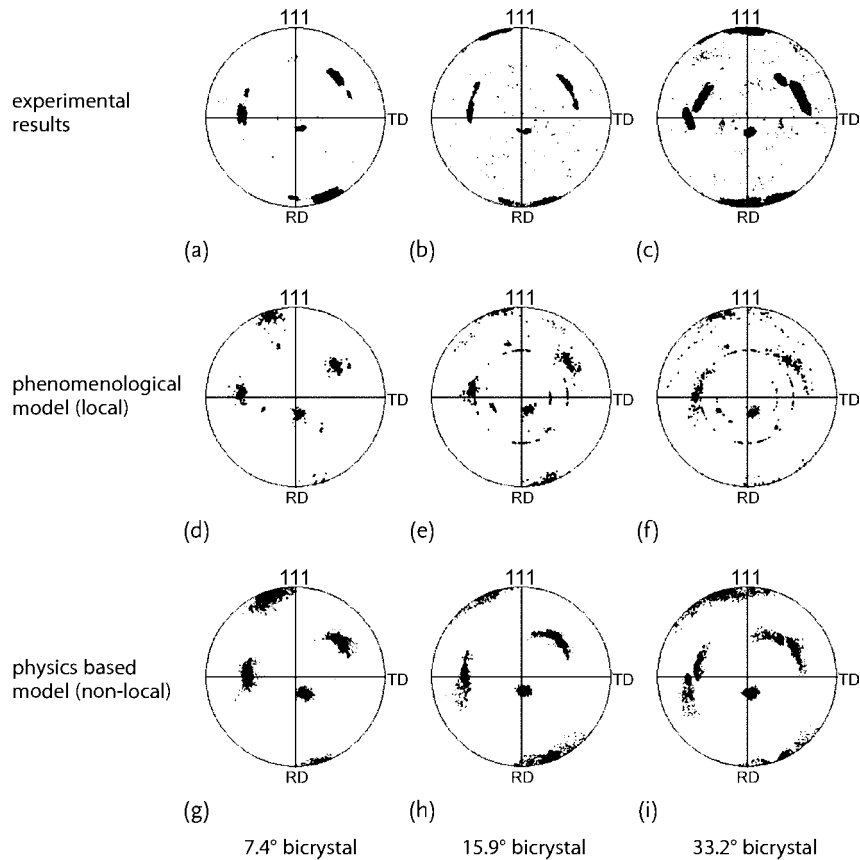
Figure 9.13 Texture comparison for the simple shear tests conducted with three bicrystals: (a, b, c) experimental textures; (d, e, f) phenomenological local model; (g, h, i) dislocation and grain boundary nonlocal model; (a, d, g) bicrystal with low-angle grain boundary (7.4°); (b, e, h) bicrystal with intermediate-angle grain boundary (15.9°); (c, f, i) bicrystal with high-angle grain boundary (33.2°).

ures d–f). The simulated textures are in excellent agreement with the experimental pole figures. We explain this *smoothing* effect on the texture evolution mainly in terms of the influence of the GNDs which act twofold. First, their accumulation in conjunction with the generation of orientation gradients introduces a direct mechanical resistance to the further deformation of the material points affected by such gradients in terms of the increase in the overall local dislocation density. The second aspect (coupled to the first one) is the resulting constitutive tendency of the nonlocal model to reduce the difference in lattice rotation between neighboring material points. This means that the implicit introduction of the GNDs imposes a strong penalty or respectively drag force against lateral gradients in the reorientation rates. The {111} pole figures (c and i) shown in Figure 9.13 reveal that the projected orientation points cluster in the form of two groups, whereas in pole

figure 9.13f this effect is less pronounced. This is attributed to the influence of the grain boundary on the texture evolution, in particular to the *anisotropy* of the modeled resistance of the grain boundaries for different slip systems. The influence of the nonlocal and of the grain boundary model on the overall reduction in the rate at which the deformation textures evolve is a long-standing problem in texture research, because many classical texture models (including the CPFE approach) suffer from the drawback that the predicted textures are often too sharp and the predicted evolution rates are often too high when compared with experimental findings.

The simulations and experiments show that the classical kinematic treatment of grain boundaries which is automatically included in all CPFE models owing to the change in the Schmid factor across the interfaces is not sufficient to adequately reproduce the micromechanics associated with the presence of grain boundaries.

9.7
Evolution of Dislocation Density in a Crystal Plasticity Model

Arsenlis and Parks (2002) were among the first groups to account for the evolution of the defect density in a crystal plasticity implementation. Their approach to
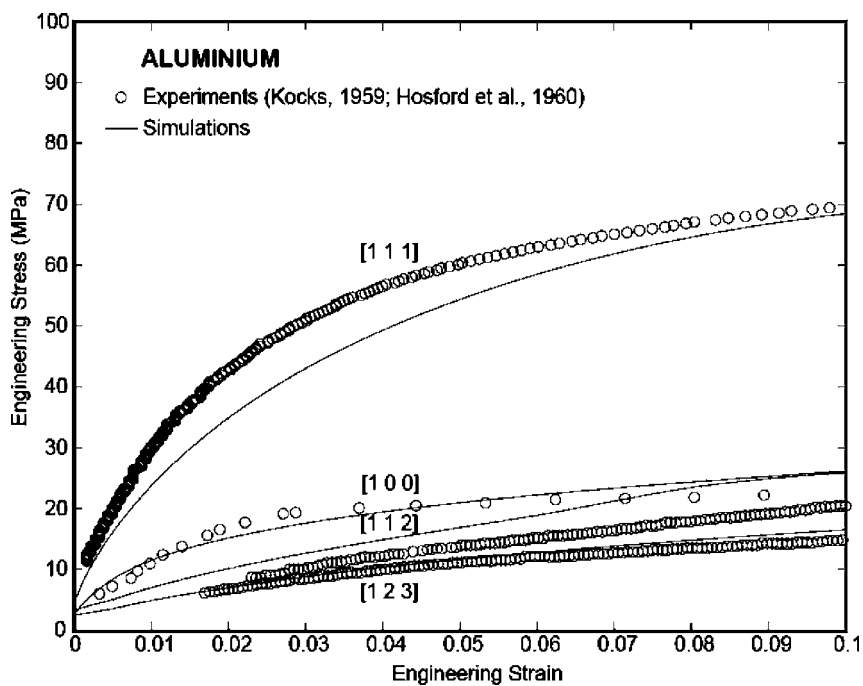
Figure 9.14 Crystal plasticity finite element (CPFE) simulated and experimentally observed orientation dependence of the stress–strain profile of aluminum single crystals during tensile loading (Arsenlis and Parks, 2002).

implement dislocation-based constitutive laws into a CPFE framework marked an essential advance. The basics and further developments along these lines were published in a sequence of works where the recent emphasis is placed on extracting constitutive information, for instance, on strain hardening, from discrete dislocation modeling (Arsenlis and Parks, 1999, 2002; Arsenlis *et al.*, 2004; Arsenlis and Tang, 2003). They suggested a constitutive formulation where dislocation density variables gradually evolve from initial conditions according to a set of structure evolution laws considering basic dislocation mechanics such as the continuity of dislocation lines and Burgers vector conservation in a set of generic multiplication and annihilation processes (Arsenlis and Parks, 2002). The density evolution equations use three classes of internal variables, namely, the average dislocation mobility, the average segment length, and the capture radii. The model is based on a set of 18 discrete dislocation densities comprising 12 edge and six screw components.

The model was implemented in a CPFE framework to study the multislip behavior of aluminum single crystals of different initial crystallographic orientation under tensile loading, Figure 9.14. The results did not only yield reasonable mechanical stress–strain response for the differently oriented crystals, but also provided insight into the development of the dislocation structure responsible for the respective plastic behavior observed. A similar approach in which conventional viscoplastic hardening rules were replaced by dislocation density evolution laws including also GNDs was suggested by Ma and Roters (2004) and Ma, Roters, and Raabe (2006a,b, 2007) (see also Section 6.1.3.2).

9.8
Three-Dimensional Aspects of Oligocrystal Plasticity

Zhao *et al.* (2008) conducted a study of plastic strain localization and deformation-induced surface roughening in an aluminum polycrystal consisting of a small set of coarse grains (oligocrystal). A dog-bone specimen was plastically deformed under uniaxial tensile loading. During deformation, the history of strain localization, surface roughening, microstructure, and in-grain fragmentation was recorded. Using a CPFE model, they conducted corresponding one-to-one high-resolution simulations, Figure 9.15. The study reveals that the grain topology and microtexture have a significant influence on the origin of strain heterogeneity. Moreover, it suggests that the final surface roughening profiles are related both to the macro strain localization and to the intragrain interaction. Finally, slip lines observed on the surface of the samples were used to probe the activation of slip systems in detail.

Particular attention in the analysis is placed on the ability of the CPFE model to capture the fine details of the surface roughening effects, orientation-dependent strain localization, and the pattern of activation of slip systems in the grains. It was observed that the grain stretching over the whole width of the dog-bone specimen was remarkably soft. The absence of dislocation barriers provided by grain boundaries promotes strain localization owing to a single isolated soft grain. Owing to
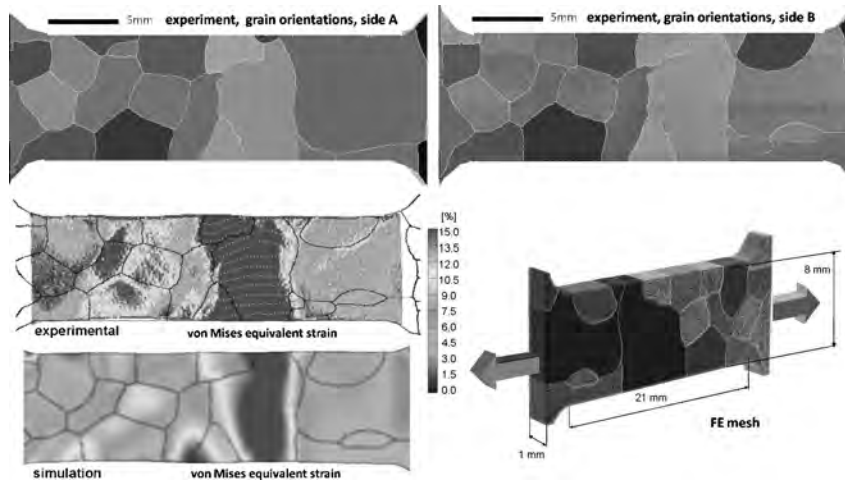
Figure 9.15 Study by Zhao *et al.* (2008) on plastic strain localization and deformation-induced surface roughening in a three-dimensional aluminum polycrystal consisting of a small assembly of coarse grains (oligocrystal).
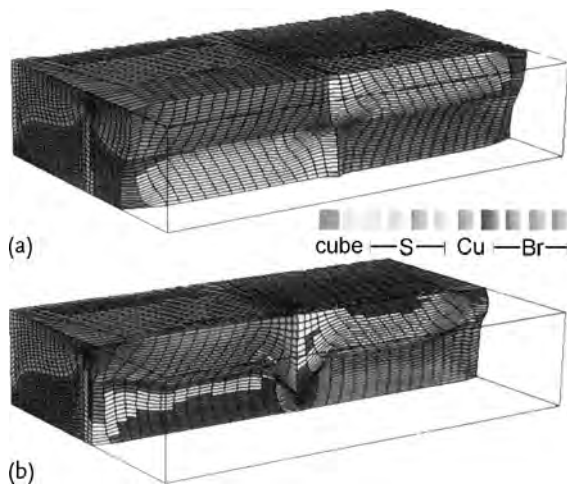

Figure 9.16 Simulation by Beaudoin, Mecking, and Kocks (1996) of a cluster, which initially consisted of eight S-oriented grains (face-centered cubic). The results shown are after a thickness reduction of 85%: (a) section with stable S orientations; (b) section with cube bands. The images are stretched by a factor of ten in thickness (vertical) direction.

the significant thickness reduction, a severe surface roughening was particularly observed in the soft region of the sample.

Similar studies on the mechanical heterogeneity and the texture evolution in coarse-grained samples were presented by Beaudoin, Mecking, and Kocks (1996) and Sachtleber, Zhao, and Raabe (2002). Common to these works is that they show, depending on grain orientation, substantial in-grain orientation fragmentation and

strain localization. Beaudoin, Mecking, and Kocks (1996) idealized in their study a simple polycrystal as a three-dimensional arrangement of eight grains, each consisting of many finite elements per crystal. Nonuniform deformation within individual grains led to the development of domains that are separated by boundaries of high misorientation. Also, localized shearing was seen to occur at the microscopic grain scale. The authors also discussed the importance of such plastic and orientation localization phenomena for recrystallization nucleation (see also the next section). Particularly, the landmark paper of Beaudoin, Mecking, and Kocks (1996) motivated further investigations on in-grain orientation scatter (grain fragmentation) and corresponding approaches to classify grains according to their kinematic stability upon loading. The aim of these works was to systematically investigate which types of grains (texture components) tend to build up large orientation gradients under certain loading states (Raabe, Zhao, and Mao, 2002b; Raabe *et al.*, 2002c), Figure 9.16.

9.9
Simulation of Recrystallization Using Micromechanical Results of CPFE Simulations

CPFE models can be also used for the prediction of recrystallization phenomena. More specifically, this section presents methods for simulating primary static recrystallization and related grain coarsening phenomena by combining CPFE simulations with Monte Carlo, cellular automaton, or network models (Bate, 1999; Loge *et al.*, 2008; Raabe, 1999, 2002, 2007; Raabe and Becker, 2000; Zambaldi *et al.*, 2007). Such combined methods can predict microstructures and texture evolution during thermomechanical treatment. The advantage of these approaches is that they consider the material heterogeneity of the deformation microstructure and recrystallization phenomena as opposed to classical statistical approaches which are based on the assumption of material homogeneity.

Bate (1999) assumed that the von Mises stress obtained from a CPFE bicrystal model is linearly related to the substructure density in deformed metals that undergo extensive dynamic recovery. From the CPFE results, he constructed a cell structure and used it as input to a two-dimensional network model for recrystallization simulation. Cell centers were included at random coordinates, with specific exclusion rules to ensure that the cell size was inversely proportional to the local von Mises stress. Cell orientations were interpolated from the CPFE results and the initial network was set up via Dirichlet tessellation. Figure 9.17a and b shows two stages in the simulation. At an early stage of annealing, the essential features of the deformed structure remain apparent. The crystallite size is larger, and more high-angle grain boundaries emerge near the original grain boundary. There are some high-angle boundaries associated with the deformation inhomogeneity in the upper grain. At the later stage, considerable strain-induced boundary migration has occurred. Some of the new grains have orientations corresponding to a cube texture rotated by 15° about the extension direction (circled points in Figure 9.17).
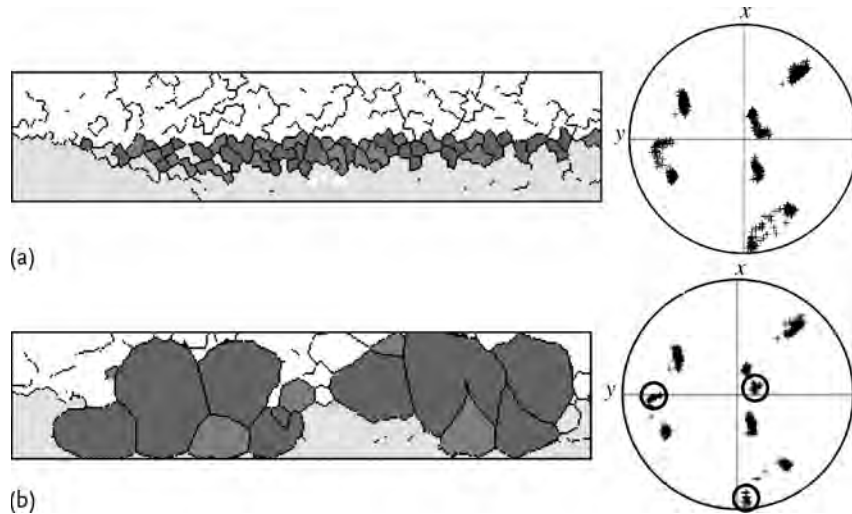
(a)

(b)

Figure 9.17 (a) Results of Bate (1999) from a two-dimensional network annealing model with the initial representation of microstructure derived from a CPFE simulation. The initial number of crystallites was 900. Only grain boundaries with misorientations above 3° are shown. Darker grains are near the cube orientation. A snapshot at 400 remaining crystallites is shown in (b). The resulting grain orientations are given in the {001} pole figure.

Raabe (2001); Raabe and Becker (2000) used a method where the results of a CPFE simulation served as a starting microstructure for a subsequent discrete cellular automaton recrystallization simulation. The CPFE model simulated plane strain compression of aluminum with a coarse columnar grain structure to a total logarithmic strain of 0.434. The values of the state variables (dislocation density, crystal orientation) given at the integration points of the finite element mesh were mapped on the cellular automaton lattice. The original size of the specimen which provided the input microstructure to the CPFE simulation gave a lattice point spacing of 61.9 µm. The maximum driving force in the region arising from the stored dislocation density was about 1 MPa. The annealing temperature was 800 K. High-angle grain boundaries were characterized by an activation energy for the mobility of 1.3 eV. Low-angle grain boundaries were assumed to be immobile.

The nucleation process during primary static recrystallization has been explained for pure aluminum in terms of discontinuous subgrain growth. According to this model, nucleation takes place in areas which reveal high misorientations among neighboring subgrains and a high local driving force for curvature-driven discontinuous subgrain coarsening. The present simulation approach works above the subgrain scale, that is, it does not explicitly describe cell walls and subgrain coarsening phenomena such as the approach of Bate (1999). Instead, it incorporates nucleation on a more phenomenological basis using the kinetic and thermodynamic instability criteria known from classical recrystallization theory. Kinetic instability means that nucleation leads to the formation of a mobile high-angle grain boundary which can sweep the deformed matrix. Thermodynamic instability means that
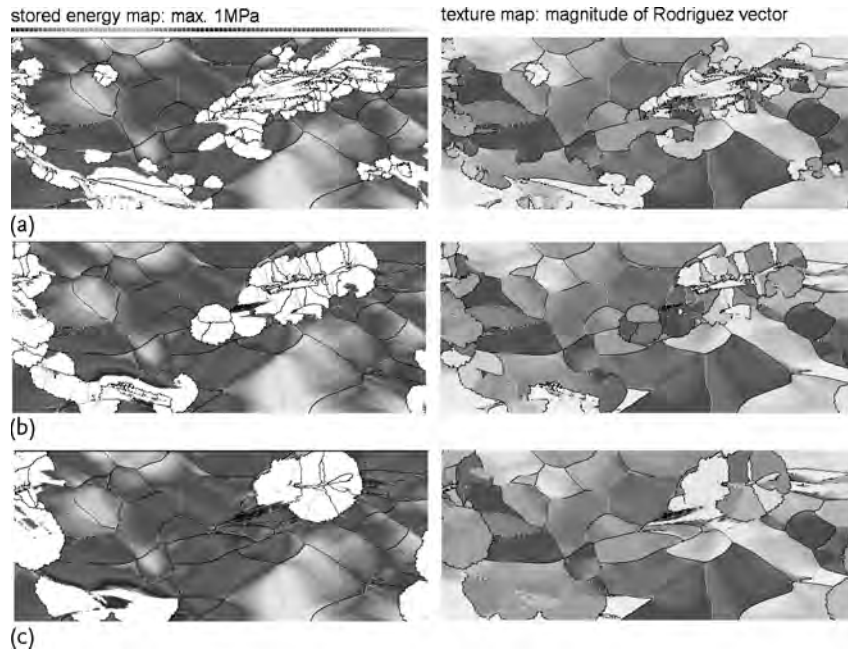
stored energy map: max. 1MPa

texture map: magnitude of Rodriguez vector

(a)

(b)

(c)

Figure 9.18 Two-dimensional simulation of recrystallization in deformed aluminum on the basis of CPFE data. Dislocation density in terms of the driving force (left) and microtexture (right) at an intermediate recrystallization step for different nucleation conditions. The texture is given in terms of the magnitude of the Rodriguez vector. The bright regions on the left indicate recrystallization. The maximum-occurring driving force is 1 MPa. Black lines indicate grain boundaries above 15°. Thinner gray indicate misorientations between 5 and 15°. The simulation parameters are 217 600 automaton cells and 800 K. THe thermodynamic instability criterion is site-saturated spontaneous nucleation in automaton cells with at least 50% (a), 60% (b), and 70% (c), respectively, of the maximum-occurring dislocation density (threshold value).

the stored energy changes across the new high-angle grain boundary, which gives a net driving force. Nucleation in this simulation is performed in accord with these two criteria (Raabe, 2001), Figure 9.18. A similar approach of applying a cellular automaton model to CPFE simulation data of a deformed superalloy for the prediction of local recrystallization phenomena was used by Zambaldi *et al.* (2007), Figure 9.19.

9.10
Simulations of Multiphase Transformation-Induced-Plasticity Steels

The mechanical behavior of a transformation-induced-plasticity (TRIP)-assisted steel is simulated for a uniaxially loaded sample composed of a single austenitic grain surrounded by a matrix of ferritic grains. The purpose of the present simulation is to study the TRIP effect as a function of crystallographic orientations, that
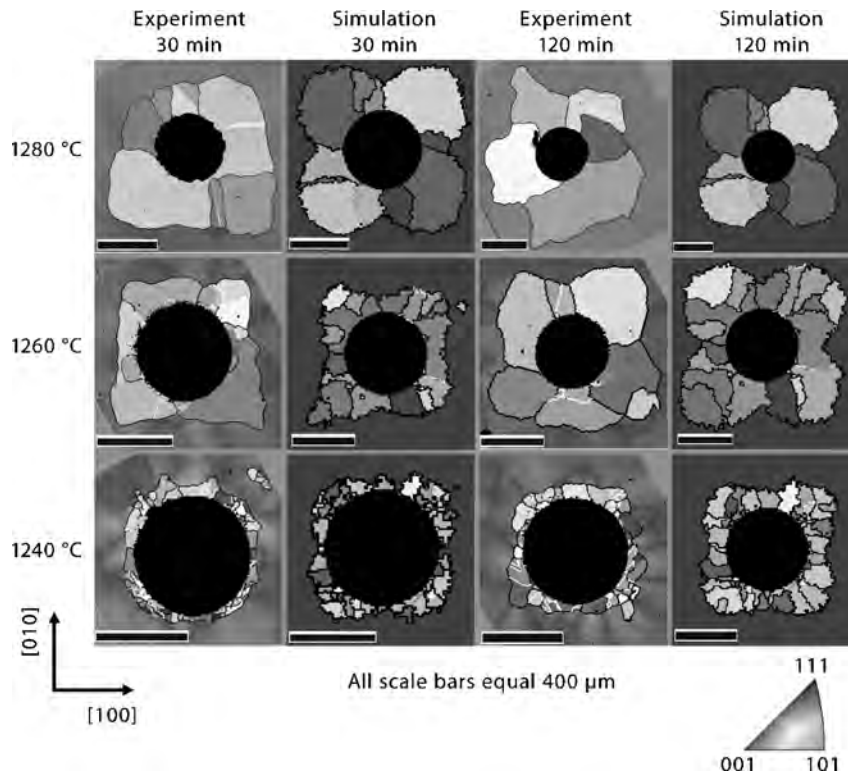
Figure 9.19 Comparison of evolving recrystallization microstructures around an indent in a nickel-based superalloy measured by electron backscatter diffraction and simulated with a cellular automaton. The Miller indices parallel to ND are shown using an inverse pole figure color scheme. The coordinate system indicates the orientation of the parent single crystal. White lines in the experimental results correspond to first-order annealing twins; black lines coincide with high-angle grain boundaries above 15°.

is, the orientation of the austenitic and ferritic grains with respect to the applied load as well as the orientation mismatch between neighboring grains.

In the present analysis, a cubic sample of size a^3 (see Figure 9.20) that represents a single grain of austenite surrounded by a matrix of ferrite is considered. In the undeformed state, the polyhedral austenitic grain occupies approximately 13% of the total volume of the sample. The sample is initially stress-free and is subsequently subjected to a uniaxial tensile loading, which is prescribed through the following boundary conditions: (1) the normal displacement and the tangential traction on external faces 2, 3 and 5 are set to zero; (2) the normal displacement on external face 1 is $u_1 = 1 \times 10^{-4} a t$, with time interval $0 < t \leq 2000$ s, and the tangential traction is set to zero; (3) the remaining faces (4 and 6) are traction-free. The boundary conditions applied correspond to an axial straining rate of 1×10^{-4} s^{-1}. The simulation is performed at a constant temperature of 300 K. Model parameters for ferrite and austenite are taken
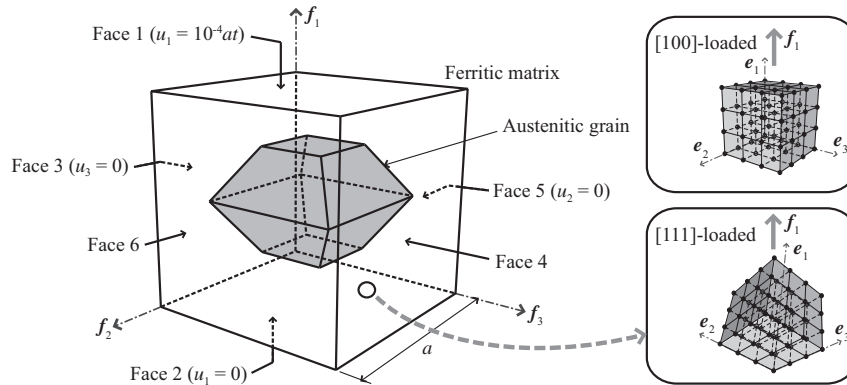
Figure 9.20 A cubic sample representing a transformation-induced-plasticity (TRIP) steel microstructure that consists of one grain of austenite in a ferritic matrix under uniaxial tensile loading.

from Tjahjanto, Turteltaub, and Suiker (2008). They are representative of a ferrite-based matrix in typical multiphase TRIP steels and are calibrated from a TRIP steel with an austenite carbon concentration of 1.4 wt%. In the simulations, four TRIP steel microstructures with different austenitic and ferritic crystallographic orientations (textures) are considered, namely, the directions $[100]_A$-$[100]_F$ (1), $[100]_A$-$[111]_F$ (2), $[111]_A$-$[100]_F$ (3), and $[111]_A$-$[111]_F$ (4) being parallel to the loading direction.

Figure 9.21 illustrates the effective stress–strain response (Figure 9.21a) and the evolution of the austenitic volume fraction (Figure 9.21b) of TRIP steel samples 1–4. In general, samples 2 and 4 (with a $[111]_F$-loaded ferritic matrix) show a higher axial stress response than samples 1 and 3 (with a $[100]_F$-loaded ferritic matrix), which indicates that ferrite loaded in the $[111]_F$ direction is stronger than that loaded in the $[100]_F$ direction (an analysis of the Schmid stress suggests that $[111]_F$-loaded ferrite gives the highest stress response under uniaxial tensile loading). Furthermore, samples containing a $[111]_A$-loaded austenitic grain give a relatively high initial yield stress in comparison with the corresponding samples with a $[100]_A$-loaded austenitic grain. As reported in Tjahjanto, Turteltaub, and Suiker (2008) and Turteltaub and Suiker (2005, 2006c), $[100]_A$-loaded austenite is in a more favorable orientation for transformation. In other words, $[100]_A$-loaded austenite transforms at a low stress level, whereas transformation of the $[111]_A$-loaded austenite occurs at a relatively high stress level. This is in agreement with experimental observations for TRIP steels (see, e.g., Kruijver *et al.* (2003); Oliver *et al.* (2002)). In addition, the $[100]_A$-loaded austenitic grain (in samples 1 and 2) transforms at a higher rate than the austenitic grain loaded in the $[111]_A$ direction (samples 3 and 4), as depicted in Figure 9.21b. At about 0.08 axial strain, the austenitic grain in samples 1 and 2 has been (almost) fully transformed into the harder martensitic phase. Consequently, the axial stress response of samples 1 and 2 increases rapidly after about 0.08 axial strain. Furthermore, Figure 9.21b shows that transformation behavior in
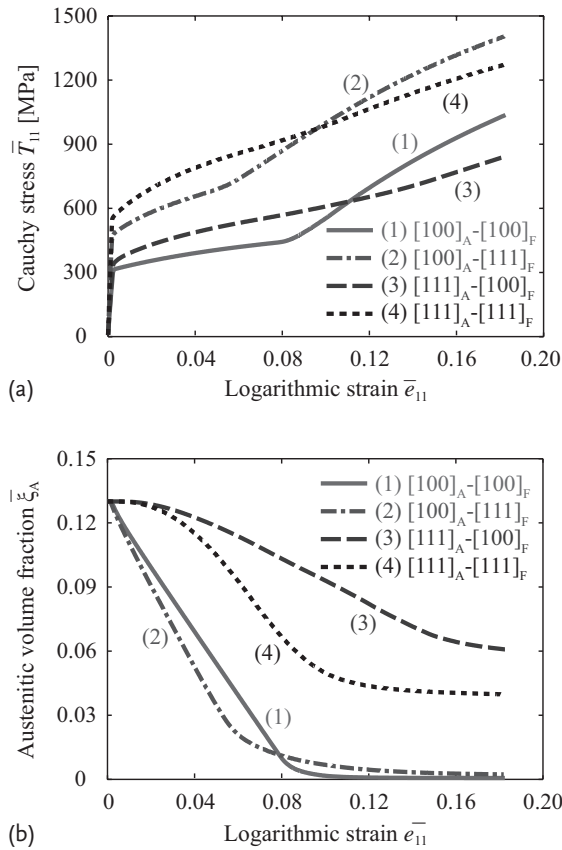
Figure 9.21 Axial stress response (a) and the evolution of austenitic volume fraction (b) as a function of the axial logarithmic strain of TRIP steel samples consisting of an austenitic grain embedded in a ferritic matrix.

the austenitic grain is dependent not only on the orientation of the austenitic grain itself but also on the orientation of the surrounding ferritic matrix. The effect of the mismatch between the orientation of the transforming austenitic grain and the surrounding matrix can be quite significant (compare, e.g., samples 3 and 4).

9.11
Damage Nucleation Example

9.11.1
Introduction

Although the number of computational studies of microscale heterogeneous deformation is increasing each year, the fraction of these that attempt to study damage

nucleation using a CPFE foundation is still small. Clayton (2005) and Ashmawi and Zikry (2003) sought ways to predict damage nucleation, but neither were correlated directly with experimental measurements (a more recent work (Vogler and Clayton, 2008) indicates only vague agreement with modeled experiments). Ashmawi and Zikry (2003) examined an unrealistic microstructure with cubic grains and thick grain boundary elements used to evaluate slip transfer based upon $\cos\theta\cos\kappa$ illustrated in Figure 6.18, which was used as a criterion for damage nucleation. Clayton (2005) examined how a two-dimensional material model with cohesive zone boundary elements fractured. In contrast, a recent study by Kumar *et al.* (2008) and Bieler *et al.* (2009) examined the three-dimensional heterogeneous deformation that occurred in a patch of microstructure where well-characterized damage nucleation events were observed in an experimental study from which the fracture-initiation parameter *fip* was developed (Simkin, Crimp, and Bieler, 2003). The fip (described in Section 6.3.8) can be conveniently evaluated using information available in CPFE models, and this example is used to illustrate the potential for the use of the CPFE method for tracking the geometrical conditions that can identify high-probability sites for crack nucleation.

An important experimental observation was that no obvious correlation was found between microcrack nucleation sites and boundaries having high or low values of geometrical slip transfer parameters (Figure 6.18). However, in determining the maximum or minimum value of the slip transfer parameters, one should pay attention to the activity of the respective slip/twin systems, which is linked to their resolved shear stress. Thus, boundaries with particularly low (or high) values of a slip transfer parameter given by $m' = \cos\psi\cos\kappa$, which indicates the degree of coplanarity and collinearity of slip planes and directions, respectively, may not be relevant if the respective slip systems are not activated. As an improvement, the fip includes components of the stress and the likelihood of activation of specific slip systems, as well as a slip transfer term containing only $\cos\kappa$, the term that assesses the collinearity of slip directions. Remarkably, evaluation of fip variants using the slip plane coplanarity $\cos\psi$ or plane matching conditions at the boundary $\cos\theta$ were unable to predict vulnerable boundaries (Kumar *et al.*, 2008), which was the criterion used by Ashmawi and Zikry (2003). The significance for slip collinearity was also observed in a recent study of fatigued copper bicrystals, where the slip direction of dislocation pileups (which depend on the slip system with the highest Schmid factor) was identified to be more significant than slip planes, boundary plane normals, or boundary character in nucleating fatigue cracks (Zhang and Wang, 2003). This corroboration suggests that a slip-vector-based (rather than slip-plane-based) metric may provide a robust method to predict damage nucleation.

9.11.2
Assessing Strains Related to a Fip

In the experimental work, the fip was evaluated with the *global* stress state, so the effects of heterogeneous deformation on the local stress state were not considered

Franz~Roters, Philip~Eisenlohr, Thomas~R.~Bieler, and~Dierk~Raabe: Crystal Plasticity Finite Element Methods —
Chap. roters9419c09 — 2010/7/23 — page 139 — le-tex

9.11 Damage Nucleation Example | **139**

when evaluating the fip. Even with this crude approximation, the fip has statistical significance based upon appropriate statistical tools for small populations (Kumar *et al.,* 2008). CPFE modeling provides an estimate of local stress and strain states at boundaries that can be used effectively to determine if the ability of the fip to identify vulnerable boundaries can be sharpened.

Microcrack nucleation in TiAl is highly correlated with concentrated shear activity at or near grain boundaries resulting from mechanical twinning (Simkin *et al.,* 2007), which has a large intrinsic shear of 0.7 in this crystal structure (TiAl is face-centered tetragonal with a c/a ratio of 1.02, which makes it close to face-centered cubic in some respects). The specimen investigated was deformed in four-point bending, to cause a relatively uniform uniaxial tension stress state in the middle part of the specimen. In about 6 mm^2, 11 microcracked boundaries were identified at gamma–gamma grain boundaries, and analyzed carefully to obtain crystal orientations and observations of slip and mechanical twinning activity. Ten of the 11 microstructural patches showed that the microcracks resulted from the most highly stressed twin system that caused highly concentrated shear displacements in the boundary, Figure 6.19. The microstructure patch shown in Figure 9.22 (Bieler *et al.,* 2009; Kumar *et al.,* 2008) shows microcracks in the one outlier patch from the trend where the third most highly stressed twin system in grain 14 caused the microcracks (based upon the global stress state). The CPFE analysis was conducted to determine if the information provided by CPFE models could provide additional mechanistic or physical insight.

9.11.3
CPFE Model of TiAl Patch with Active Mechanical Twins

This patch was two-dimensionally meshed with common nodes along the boundary (simulating type III transparent boundaries described above) to determine if the local stress tensors were significantly different from the global stress state, or if the grain geometry led to nonobvious deformation effects. The model was made three-dimensional by expanding it into a five-element-thick stack with about 8000 elements, such that the grain boundaries were all perpendicular to the surface. (A more accurate three-dimensional model was also built that included proper grain boundary and annealing twin inclinations obtained from serial sectioning, and it gave similar results to the projected two-dimensional model shown, but it was less numerically stable and did not permit strains as large as in the experiment.) The modeled microstructure was surrounded by a rim of elements to provide a constraint that represents the surrounding microstructure. Boundary conditions were imposed with zero vertical displacement on the bottom edge and a tensile face load on the top edge, with the front and back surfaces being unconstrained (see Figure 9.22). While developing the mesh, computations were also made where the z-displacement beneath the surface was constrained, and the patterns of deformation were similar, but led to a lesser strain with the same loading history. In the physical experiment the microstructure probably deformed with displacements be-
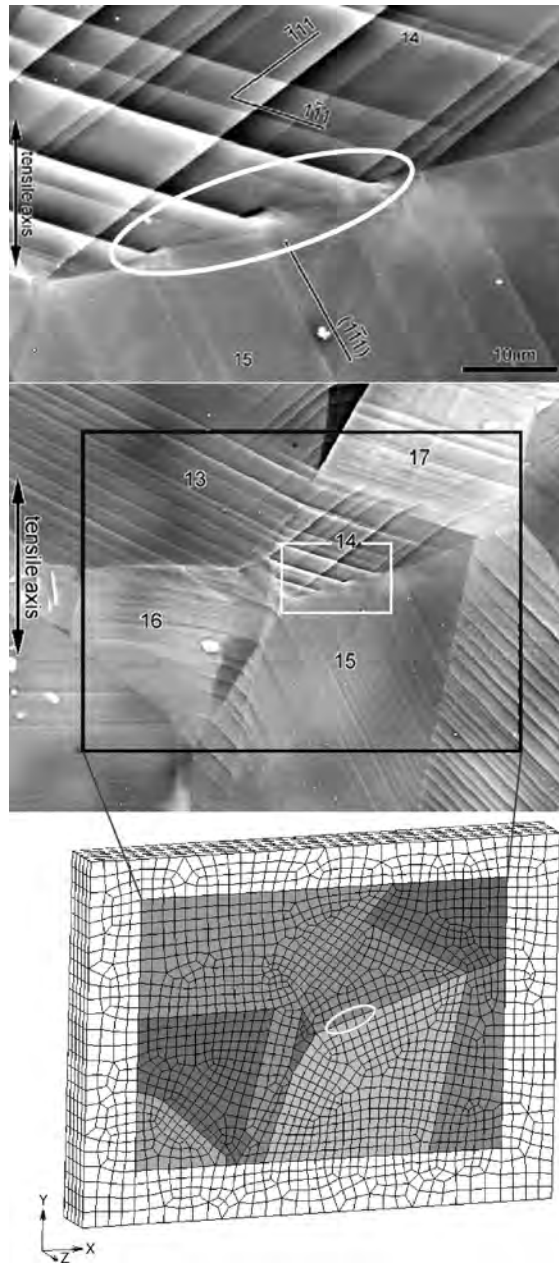
Figure 9.22 Nucleation of a grain boundary crack due to mode I opening strain at the grain boundary owing to highly localized twin shear and the local microstructural patch that was modeled to assess the local stress and strain states.

neath the surface that were between these two convenient computational boundary conditions.

The constitutive description of the material is based on a crystal plasticity formulation using the multiplicative decomposition of the total deformation gradient that takes the anisotropic elastic constants into account (Kalidindi and Anand, 1993; Kalidindi, Bronkhorst, and Anand, 1992; Raabe *et al.*, 2001; Sachtleber, Zhao, and Raabe, 2002). A phenomenological flow stress for each slip system was identified from tensile test experiments and adjusted for the plastic anisotropy of the tetragonal $L1_0$ crystal structure of TiAl (Bieler *et al.*, 2009). Dislocation slip and mechanical twinning were incorporated as bidirectional and unidirectional slip systems, respectively. Hence, mechanical twinning operated in a diffuse manner, rather than as discretely spaced planes of intense shear that are apparent in the micrographs in Figure 9.22 (Simkin *et al.*, 2007). This material model was implemented as a user material of type HYPELA2 into the commercial finite element method package MSC.Marc.

Figure 9.23a shows the von Mises stress and the equivalent total strain after simulated loading to a strain of about 1.8×10^{-2}. Most of the grain boundaries (identified with white lines) developed large stresses owing to the elastic anisotropy and differential strain conditions from neighboring grains. The strains are more evenly spread than the stresses, and the locations of high and low total strain are not directly related to the stress, indicating that complex relationships exist between local
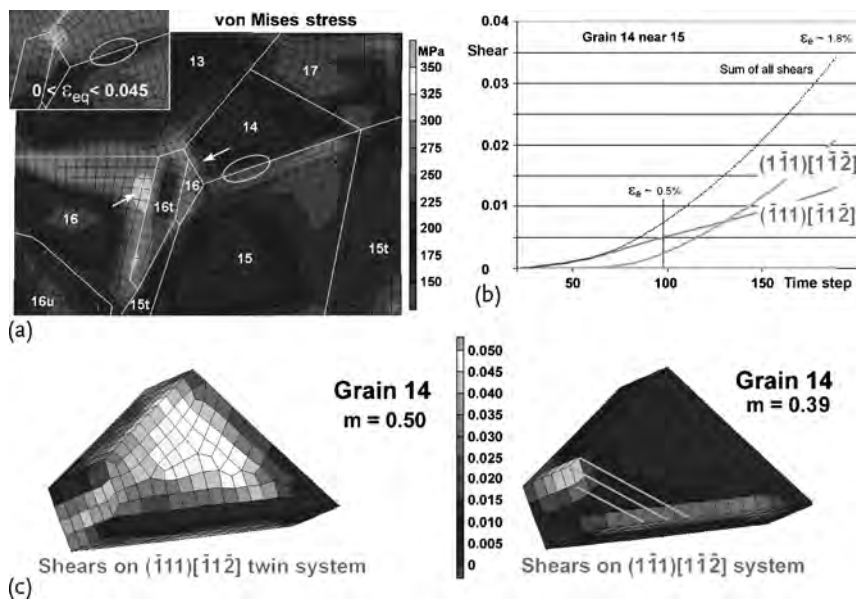
Figure 9.23 Distribution of equivalent stress and strain (a), evolution of shears on two twin systems active where microcracks were observed (b), and the three-dimensional spatial distribution of shears on these two twin systems at a strain of about 1.8×10^{-2} on the interfaces and surfaces of grain 14 (c).
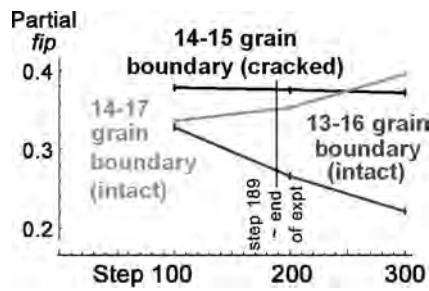
Figure 9.24 Using data extracted from the CPFE simulation illustrated in Figure 9.23, the first two terms in the fracture-initiation parameter (fip) for three grain boundaries having a high normal tensile stress component evolve; the fip of the boundary between grains 14 and 15 was the highest among the three boundaries at the end of the physical experiment.

stresses, strains, and grain geometry. Surprisingly, in the region where the microcrack nucleation was observed (indicated by ovals), the strains and stresses are in the middle of the range of stress and strain that occurred throughout the modeled region. This lack of correlation between local strain energy and damage nucleation suggests that the fip analysis described above provides information about crack vulnerability that cannot be inferred from a simple maximum stress, strain, or strain energy criterion.

In Figure 9.23b, the amount of shear on the most active slip systems in grain 14 near the microcracks is plotted as a function of loading step, and the spatial variation of shear on the two most active twin deformation systems is illustrated in the three-dimensional extractions of grain 14 in Figure 9.23c. Up to a strain of about 5×10^{-3} engineering strain, a greater shear occurred on the twin system with the larger global Schmid factor. After a strain of about 5×10^{-3}, the shear on the twin system with a lower global Schmid factor accelerated considerably, presumably owing to the need to maintain compatibility, eventually contributing more shear to the total strain than the system with the higher Schmid factor, but only in the region where cracks nucleated; that is, the secondary twin system became the primary one *locally*, where microcracks were observed. This result is consistent with the the ideas behind the fip, where the most active slip system *at* the boundary is the one that should be used to evaluate the fip. Hence, the CPFE simulation revealed local deformation activity consistent with the implications arising from the rest of the experimental observations.

This computation shows that the fip must evolve as a result of changes in the relative activation of slip systems, and hence in local strain history. This implies that a dynamic fip could be developed. Figure 9.24 shows how the first two terms in the fip evolve, using data extracted from the CPFE run, indicating that the fip of the boundary between grains 14 and 15 was initially high, and remained high, whereas the other two boundaries with a high normal tensile stress had lower fip values. However, this calculation lacks the sum term, which should also evolve according to the strain history. The formulation of a tensorial evolutionary fip is under development.

9.11.4
Issues Regarding Modeling Mechanical Twins in CPFE Models

At this point in time, CPFE approaches are not able to model the extremely planar shear processes on discrete planes that develop with mechanical twinning. Nevertheless, the diffuse twin activation regions deform in a manner that is consistent with the experimental observations, if the regions of high twin shear activity are connected by planes aligned with crystallographic planes, such as that suggested in Figure 9.23.

Clearly, the intense mechanical twin shears that occur in TiAl cause very sharp shear displacements at grain boundaries (Figure 6.19). Other kinds of twins in other alloys have much smaller shear associated with them, such as the $\{10\bar{1}2\}\langle\bar{1}011\rangle$ twin system in titanium alloys, which have a shear strain of 0.17. Figure 9.25 illustrates a less common $\{11\bar{2}1\}\langle\bar{1}\bar{1}26\rangle$ twin that was activated in the midst of many of the more common twins, where a microcrack developed at a global strain of only about 0.02. Modeling this kind of damage nucleation is more challenging owing to the activation of several kinds of twins, and innovative methods to incorporate changes in the volume fractions taken up by particular orientations will need to be developed, perhaps following the lead of methods to reorient the grain used in statistical modeling approaches such as those of Karaman *et al.* (2000a); Proust, Tome, and Kaschner (2007). It remains to be seen if the simpler diffuse twin modeling approach will be sufficient to identify boundaries that are vulnerable to cracking.
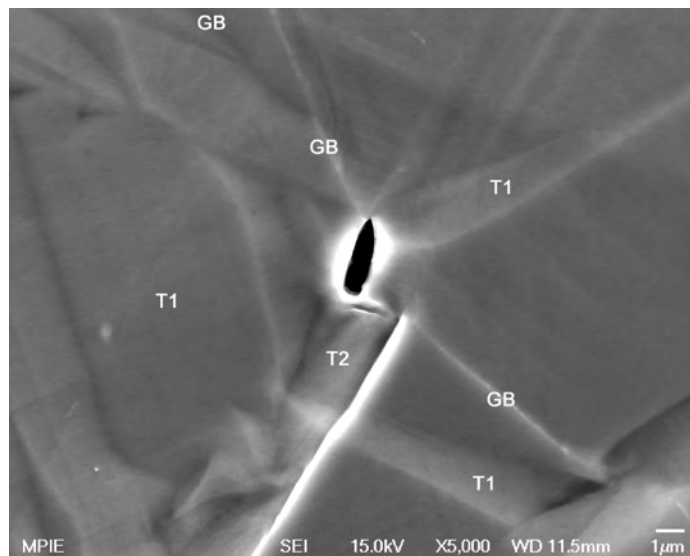
Figure 9.25 Two types of twins were activated at a grain boundary (GB) location where a microcrack was observed after a global strain of about 0.02. The less common $\{11\bar{2}1\}\langle\bar{1}\bar{1}26\rangle$ twin associated with the crack (marked T2) has a large shear of 0.629, whereas the more common $\{10\bar{1}2\}\langle\bar{1}011\rangle$ T1 twins have a shear of 0.171.

This preliminary assessment of the effectiveness of the fip in relation to the CPFE approach shows that the combined use of experimental analysis coupled with CPFE modeling provides synergistic opportunities to explore and sharpen our understanding of damage nucleation. Given that encouraging results were obtained using a moderately accurate two-dimensional representation of the microstructure (two-dimensional mesh extended into the third dimension), extending this approach to accurate three-dimensional analysis will lead to a profoundly useful tool for examining the development of heterogeneous strains that cause nanoscale

(a)

(b)
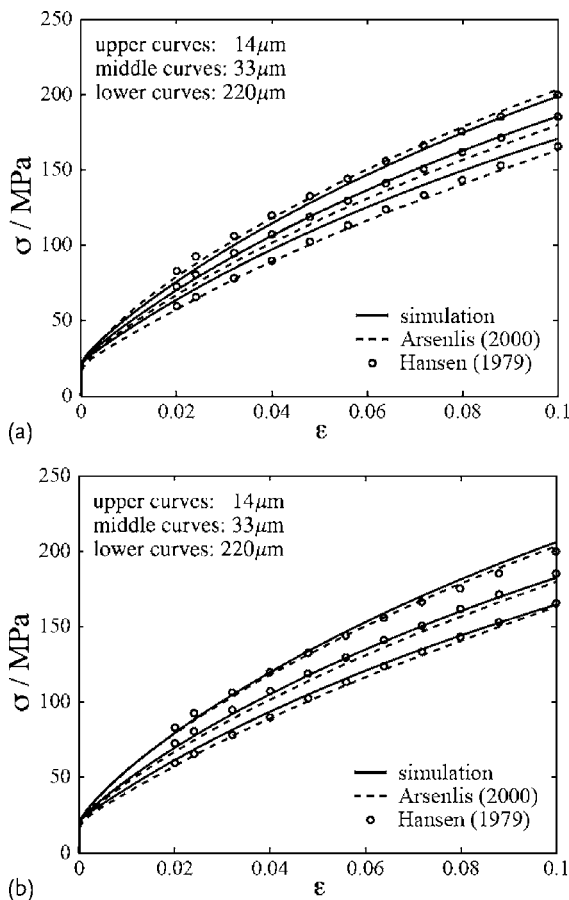
Figure 9.26 Stress–strain curves for polycrystals with different average grain diameters of 14, 33, and 220 μm. Open circles indicate experimental data of Hansen (1979). Dashed lines result from earlier finite element calculations of Arsenlis and Parks (2000, unpublished). Solid lines correspond to results of Evers *et al.* (2002), showing a closer agreement with experimental data for the case which adds statistically stored dislocation and geometrically necessary dislocation densities (b) to model the flow stress. (a) Flow stress model adds individual strength contributions from statistically stored dislocation and geometrically necessary dislocation content. (b) Flow stress model is based on addition of statistically stored dislocation density and geometrically necessary dislocation density.

damage nucleation that can be directly introduced into mesoscale microstructural models, and thus efficiently bridge over a level of scale that has been difficult to overcome (Hao *et al.*, 2004).

9.12
The Grain Size Dependence in Polycrystal Models

Evers, Brekelmans, and Geers studied approaches to include the size-dependent effects associated with interfaces and GNDs in CPFE and Taylor-type homogenization frameworks (Evers, Brekelmans, and Geers, 2004a,b; Evers *et al.*, 2002; Geers and Kouznetsova, 2007). For instance in Evers *et al.* (2002), a local plastic strain gradient-dependent crystal plasticity model was suggested which is capable of describing the grain-size-dependent mechanical response of polycrystals.

This approach consists in assigning GND populations to intragranular incompatible deformations that arise as a result of the existence of grain boundaries between abutting crystals. The polycrystal appears in this model as a statistical set of bicrystal aggregates which altogether provide an orientation-dependent density of misfit dislocations, which in turn provide extra hardening to the system. As the intragranular heterogeneous deformation is related to the grain size, the amount of GND-enhanced hardening grows as the crystal size drops, Figure 9.26a and b.

The conventional slip system hardening through SSDs is described by a system of phenomenological equations that capture the influence of self-hardening and latent hardening. The model provides a crystallographically and physically motivated hardening dependence in polycrystals based on their grain size. The morphological texture can be incorporated through the inclination and crystallographic distribution of the grain boundaries and their mutual weights.

147

10
Macroscopic Examples

10.1
Using Elastic Constants from ab initio Simulations for Predicting Textures and Texture-Dependent Elastic Properties of β-Titanium

This section presents applications of multiscale crystal plasticity finite element (CPFE) simulations where the elastic constants are obtained by ab initio simulations (density-functional theory) (Bockstedte *et al.*, 1997) for the prediction of textures and texture-dependent elastic properties. We apply this approach to Ti–Nb binary biomaterial alloys that can be used for human implants. The two models we combine (ab initio, CPFE) work at very different length and time scales. The strength of this combination for predicting certain polycrystal properties lies in the fact that continuum-based theoretical models such as CPFE rely on a number of ground-state properties (e.g., elastic tensor). The use of texture data is in such cases (elasticity) is sufficient to predict realistic data also for complex polycrystalline aggregates irrespective of their thermomechanical process history. A particular advantage of using finite-element-based methods rather than an analytical or semi-analytical approach for obtaining the polycrystal stiffness from corresponding ab initio single-crystal data is that it allows one to consider any kind of crystallographic texture, including also intragrain or in-grain interactions. Most homogenization methods for obtaining the elastic modulus of a polycrystal, such as the Voigt (1889), Reuss (1929), Hill (1952), and Hershey (1954) models, usually either neglect texture or assume highly simplified boundary conditions. A further important aspect of using ab initio elastic results in conjunction with crystal mechanical simulations is the fact that for the elastic constants of single crystals (which are a necessary input to CPFE simulations) experimental data are often lacking (Counts *et al.*, 2008b; Ma *et al.*, 2008). Details about the ab initio calculations used in this section are given in Raabe *et al.* (2007b).

The goal of the first example is to investigate the dependence of the rolling texture evolution of two β-Ti–Nb binary alloys on the elastic properties. For this purpose we used different elastic constants in terms of the magnitude of the tensor components and the elastic anisotropy. These elastic constants, which were obtained from ab initio electronic structure calculations (Raabe *et al.*, 2007b), served
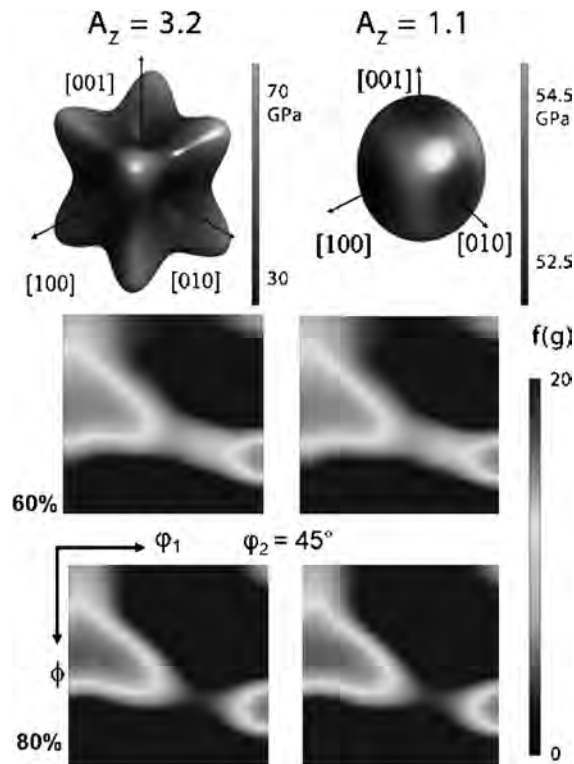
Figure 10.1 $\varphi_2 = 45°$ sections of the orientation distribution functions obtained for deformation texture simulations of two β-Ti–Nb binary alloys at engineering thickness reductions of 60 and 80% using two different sets of elastic constants. Top row: Young's modulus surface diagram of Ti–19 atom%Nb (left) and Ti–31 atom%Nb (right). The Zener ratio is defined as $A_Z = 2C_{44}/(C_{11} - C_{12})$.

as constitutive input variables in a CPFE simulation in conjunction with a viscoplastic hardening law (Ma *et al.*, 2008).

β-Ti alloys have a body-centered cubic crystal lattice structure. At room temperature the structure can be stabilized by the addition of niobium or molybdenum. As slip systems we used {110}, {112}, and {123} slip planes and $\langle 111 \rangle /2$ Burgers vectors (Raabe, 1995a,b). Two alloys were investigated, namely, Ti–19 atom%Nb and Ti–31 atom%Nb. The elastic constants for Ti–19 atom%Nb as calculated by the ab initio method were $C_{11} = 131.2$ GPa, $C_{12} = 114.5$ GPa, and $C_{44} = 26.8$ GPa. The Zener anisotropy ratio, which is defined as $A_Z = 2C_{44}/(C_{11} - C_{12})$, amounts to 3.2. The predicted elastic constants for Ti–31 atom%Nb were $C_{11} = 154.8$ GPa, $C_{12} = 118.5$ GPa, and $C_{44} = 19.2$ GPa, giving a Zener ratio of 1.1. The rolling texture simulation was conducted using plane strain compression boundary conditions and random initial texture. Figure 10.1 shows the predicted crystallographic textures in terms of a set of $\varphi_2 = 45°$ sections through Euler space for the two cas-
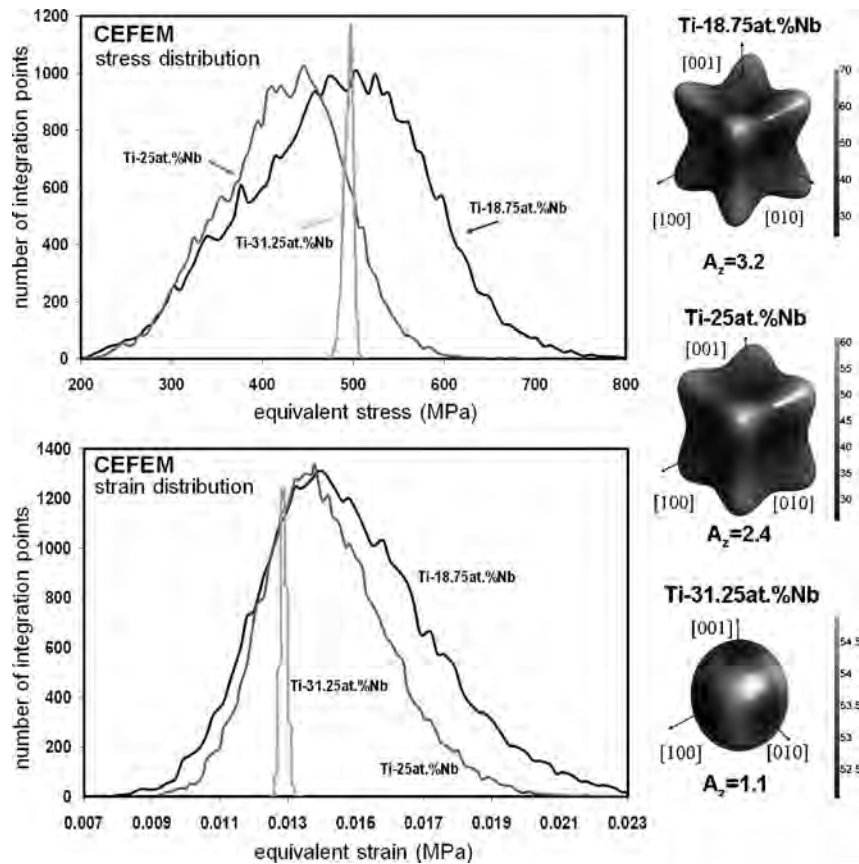
Figure 10.2 Crystal elasticity finite element method (CEFEM) predictions of the distribution of elastic equivalent stress and strain values in three randomly textured polycrystalline β-Ti alloy aggregates each consisting of 200 grains and $32 \times 32 \times 32$ finite elements. Each polycrystalline aggregate is characterized by a specific elastic tensor which was calculated using ab initio methods. The (nearly) isotropic case yields a very narrow distribution of stresses and strains, whereas the most anisotropic case leads to pronounced local stress–strain fluctuations (and thus concentrations). The samples were subjected to (purely elastic) tensile loading.

es. The results show that there is no pronounced relationship between slip system selection and the magnitude and anisotropy of the elastic constants.

A second (elastic) example of using ab initio elastic stiffness constants in a CPFE framework is shown in Figure 10.2. The two diagrams present the distribution of the equivalent elastic stress and strain values in a randomly textured polycrystalline aggregate consisting of 200 grains and $32 \times 32 \times 32$ elements for three different elastic tensors (magnitude, anisotropy) of three β-Ti alloys. The specimens were subjected to a purely elastic unidirectional tensile load. The data show that an increase in the elastic anisotropy (quantified here in terms of the Zener ratio A_Z) leads to a remarkable increase in the width of the distribution of both stress and

strain. This means that local elastic loads (hot spots) among neighboring grains become more frequent as the elastic anisotropy increases. This effect may play a role in such diverse fields as internal stress evolution and stress corrosion cracking.

10.2
Simulation of Earing during Cup Drawing of Steel and Aluminum

Cup drawing is a standard material test for the characterization of material anisotropy. In this section three application examples of the CPFE method to deep drawing are presented. The first example is an AA3104 hot band with a pronounced cube texture. In this, the through-thickness variation of texture is ignored, that is, the same texture is used over the whole sheet. In contrast, the second example shows how through-thickness texture gradients can be taken into account using a ferritic 17 wt%Cr (X6Cr17, AISI 430) stainless steel as an example. Finally, the third example demonstrates how CPFE simulations can be used to optimize the earing behavior during cup drawing.

10.2.1
Earing Behavior of AA3104 Hot Band

The cup drawing simulation shown in this section is for AA3104 hot band. Figure 10.3a shows the experimental {111} pole figure of the material. It shows a cube texture typical for hot-rolled aluminum alloys. Figure 10.3b shows the pole figure recalculated from the texture component fit (Helming, 1996; Helming *et al.*, 1994; Raabe and Roters, 2004). Besides the random portion of the texture, only one spherical component was used to fit this rather pronounced cube texture (Table 10.1). Owing to the orthorhombic sample symmetry, the single orientation has
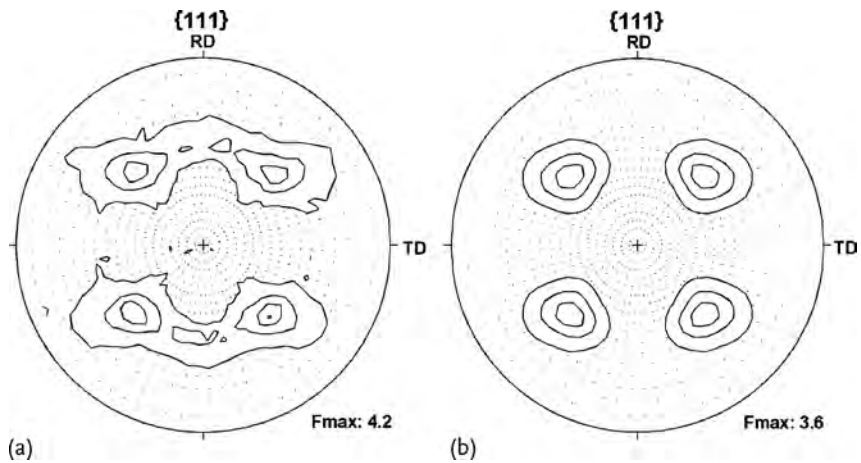

Figure 10.3 Experimental (a) and recalculated (b) {111} pole figure of the AA3104 hot band.

Table 10.1 Texture components used for fitting the texture of the AA3104 hot band (Helming, 1996; Helming *et al.*, 1994; Raabe and Roters, 2004).

Euler angles (°)			Scatter (°)	Intensity
φ_1	ϕ	φ_2	b^c	I^c
197.9	6.5	245.0	15.2	0.29
	random		–	0.71
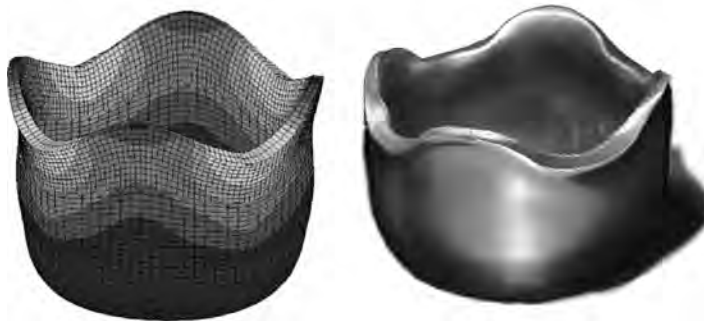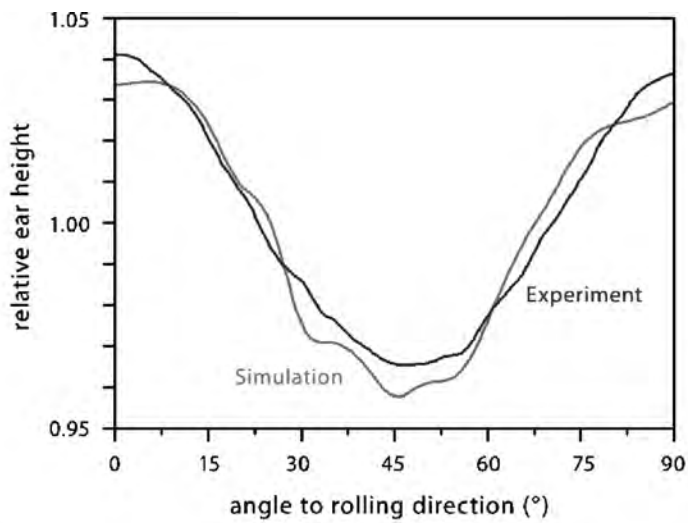
Figure 10.4 Simulated and experimental earing profiles for the AA3104 hot band.

to be balanced by three additional symmetrically equivalent orientations to correctly reproduce the response of the material in the CPFE calculations. The resulting earing profile is shown in Figure 10.4 together with the experimentally measured earing profile. There is a very good agreement between simulation and experiment. Figure 10.5 shows the relative wall thickness distribution for the drawn cup (only
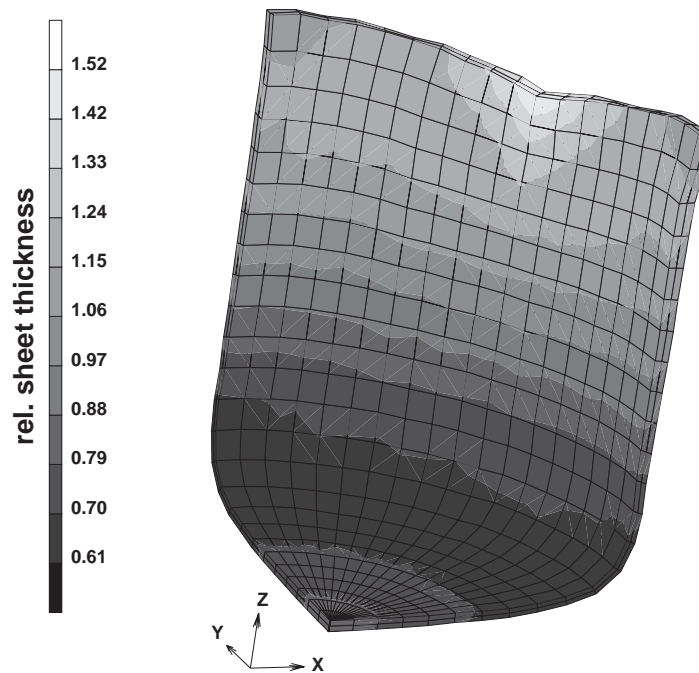
Figure 10.5 Relative wall thickness of the drawn cup (brighter is thicker).

one quarter has been simulated owing to sample symmetry). It can be seen that the bottom of the cup is thinner, whereas the upper part of its side is thicker than the original sheet. The thickening is most pronounced in the valley of the earing profile (i. e., at the 45° position).

10.2.2
Effect of Texture Gradients on Earing Behavior of X6Cr17

The deep-drawing simulation in this section includes the through-thickness texture gradient of the starting hot band of a ferritic 17 wt%Cr (X6Cr17, AISI 430) stainless steel (Fedosseev and Raabe, 1994; Raabe and Lücke, 1993). In the simulation this is achieved by using three finite elements to mesh the blank thickness. To take the texture gradient into account, the center element layer is assigned different texture components compared with the outer element layers (Figure 10.6). For simulations without a through-thickness gradient the same set of components is assigned to all three element layers. Table 10.2 shows the two sets of texture components for the center layer ($s = 0$) and the subsurface layer ($s = 0.8$). The simulation considers {110}⟨111⟩, {112}⟨111⟩, and {123}⟨111⟩ slip systems (Raabe, 1995b). The results are compared with another finite element simulation based on a Hill48 yield surface (Hill, 1948) calibrated using experimental r-values ($r_0 = 1.387$, $r_{45} = 0.817$, $r_{90} = 0.92$) and with experimental data.

Table 10.2 Texture components used for fitting the texture of ferritic 17 wt%Cr (X6Cr17, AISI 430) stainless steel (Helming, 1996; Helming *et al.*, 1994; Raabe and Roters, 2004).

position	Euler angles (°)			Scatter (°) b^c	Intensity I^c
	φ_1	ϕ	φ_2		
Center, $s=0$					
	257.6	119.9	122.9	16.8	0.1684
	238.9	83.1	81.6	20.1	0.1436
	47.4	133.1	52.9	19.1	0.1176
	137.0	62.0	32.6	15.3	0.0996
	209.7	72.7	68.7	11.4	0.0420
	125.5	57.2	44.0	16.5	0.0100
	random			–	0.4188
Subsurface, $s=0.8$					
	262.3	96.9	20.6	20.9	0.2452
	251.0	59.0	42.1	21.7	0.2224
	121.7	84.6	6.2	16.0	0.1136
	218.1	113.9	28.0	13.5	0.0820
	155.1	45.5	42.3	13.0	0.0736
	231.0	55.6	51.4	7.2	0.0104
	random			–	0.2528
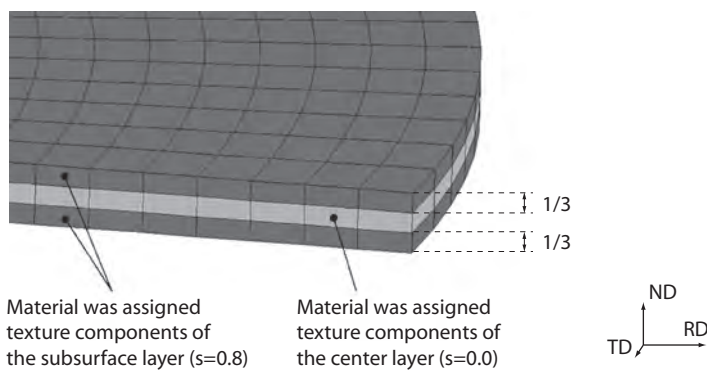
Figure 10.6 Mapping of the through-thickness texture gradient in the finite element mesh of the blank.

Figure 10.7 shows the predicted and the measured earing profiles in terms of the relative ear height (normalized by the average height). The ear profile predicted by the simulation with the texture components of only the center layer ($s = 0.0$) reveals a shape with a broad *maximum* around 45°. On the other hand, the profile simulated with the texture of only the subsurface layer ($s = 0.8$) is characterized by a broad *minimum* in the same region (45°). The reason for this difference is
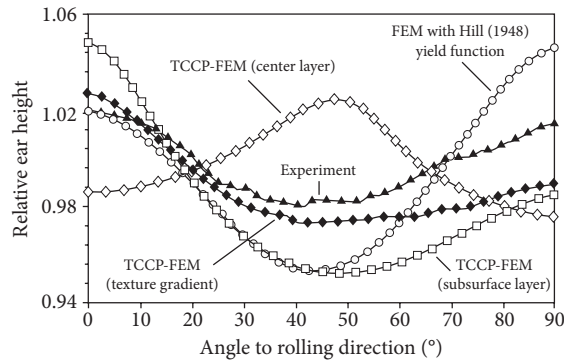
Figure 10.7 Experimental and simulated earing profiles for ferritic 17 wt%Cr (X6Cr17, AISI 430) stainless steel.

that the texture components fitted from each respective layer of the material reproduced different initial textures and, consequently, different anisotropy. The course of the ear profile calculated by using only the texture components of the subsurface layer, $s = 0.8$, can be presumably explained by the influence of the relatively weak intensity of the $\{111\}\langle 112\rangle$ component of the starting texture in this layer. The high orientation density of the $\{111\}\langle 112\rangle$ texture component in the initial texture of the center layer ($s = 0.0$) is responsible for the ear shape with the strong peak at 45° observed for the simulation that was performed by using the texture components of this layer. The results also show that the texture component CPFE simulation which used the gradient texture (1/3 of the through-thickness volume occupied by the center layer texture ($s = 0.0$) and 2/3 of the volume occupied by the sub-surface layer texture ($s = 0.8$) where 1/3 accounts for the bottom and 1/3 for the top surface region, respectively) fits the experimental data better than that obtained from the Hill48 yield surface prediction.

10.3
Simulation of Lankford Values

The Lankford value (also referred to as *r* value), that is, the ratio of lateral strains ϵ_{22} and ϵ_{33} for a tensile test in the 1-direction, is an important measure for the in-plane anisotropy of sheet materials. It is also required for the calibration of anisotropic yield models, for example, the frequently used Hill48 model (Hill, 1948). Experimentally, the *r* value is usually measured for three directions only, namely, for 0°, 45°, and 90° with respect to the rolling direction. Starting with an experimentally measured texture, the CPFE approach can be used to predict *r* values for any sheet orientation by simply rotating the initial texture by the respective angle. As the material orientation is specified by Euler angles, the angle between the rolling direction and the tensile direction can be easily adopted by modifying the angle φ_1. Moreover, such predictions do not only provide the *r* value(s) for a given strain
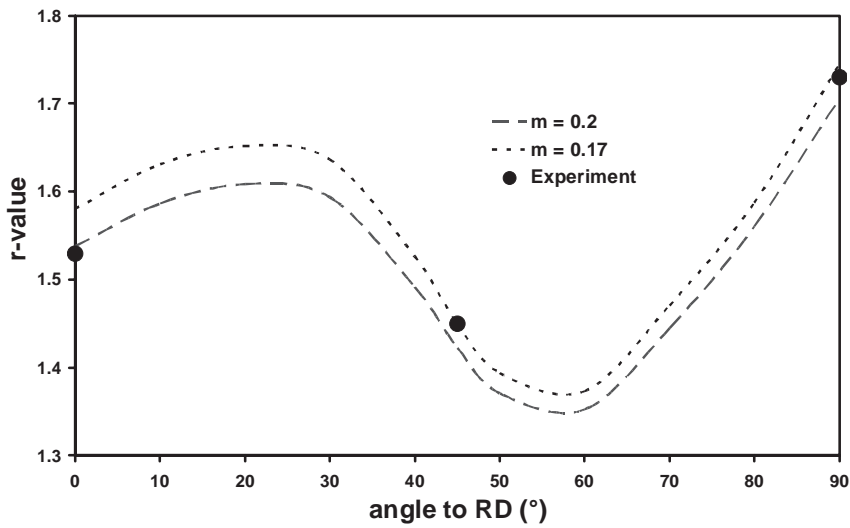
Figure 10.8 Comparison of simulated (lines) and experimental (symbols) values of the Lankford value (or *r* value) for a DC04 deep-drawing steel at 20% strain. The two curves show the results for different values of the strain rate sensitivity (see Eq. (6.8)).

(in engineering applications the *r* value is measured at 20% strain), but also yield information on the development of the *r* value as a function of strain.

In the simulation the *r* value is then determined as $\epsilon_{22}/\epsilon_{33}$ for the center node of the mesh. Figure 10.8 shows a comparison of simulated and experimental values of the *r* value for a low-carbon automotive deep-drawing steel (DC04). Although only three experimental points are available, the *r* value was calculated at steps of 5°. It should be mentioned that the magnitude of the orientation-dependent *r* value can be systematically shifted with the choice of the strain rate sensitivity assigned to individual slip systems. Since the slip system rate sensitivity need not necessarily coincide with the macroscopic rate sensitivity of the sheet material, a fitting of the strain rate sensitivity of the slip mechanism, which is difficult to determine directly in an experiment, is conceivable from measured *r* values.

10.4
Virtual Material Testing for Sheet Stamping Simulations

10.4.1
Introduction

Predicting springback of complex industrial parts after stamping and (particularly) trimming still lacks accuracy. The direct use of constitutive models involving crystallographic slip for industrial forming simulations at the component scale is currently not realistic, owing to the high computational costs. Nevertheless, these

Table 10.3 Hardening parameters derived from calibration of the virtual specimen.

Parameter	DC04	H320LA
h_0	1293	5569
τ_s	48	101
a	7	3.5

complex models, which incorporate microstructure information such as slip systems and orientation distribution, can be incorporated at the lower scale in a two-scale computational homogenization as outlined in Section 7.3.

In this section the calibration of empirical constitutive models (yield locus) used at the component scale on the basis of virtual deformation tests of a representative volume element (RVE) is demonstrated. The constitutive response of the RVE is modeled with the CFFE method and calibrated against a standard tensile test. Owing to the large flexibility in boundary conditions applied to the RVE, it then becomes possible to mimic more complex strain paths, such as biaxial tensile, compressive or shear tests, to extract the required parameters of the analytical material description. This procedure is frequently termed *virtual material testing* and, provided the virtual specimen is sufficiently reliable, allows for testing along strain paths that would be very expensive or even impossible to perform in reality. The application of the CPFE method for the virtual testing is demonstrated for two ferritic steel grades (DC04 and H320LA). The Vegter yield locus (Vegter *et al.*, 2003) is used as the analytical material model allowing for the simulation of a typical industrial part in PAM-STAMP 2G.

10.4.2
Virtual Specimen

The virtual specimen employed in the present work consists of $10 \times 10 \times 10$ differently oriented grains, each discretized by one finite element. This grain aggregate is considered representative of the microstructure and associated texture, hence serves as a RVE. The initial texture was discretized using the texture component method (Raabe and Roters, 2004). The phenomenological model described in Section 6.1.2 served as the constitutive law in which the hardening behavior of the 48 slip systems is assumed identical.

The virtual specimen was calibrated by determining the slip system hardening parameters on the basis of uniaxial tensile test data along the rolling direction ($0°$ see Figures 10.9a and 10.10a). This leads to the hardening parameters given in Table 10.3. The quality of the model prediction was evaluated by comparing the remaining experimental data (stress–strain response and *r* value of tensile tests in different directions and tension–compression tests) with corresponding simulations.
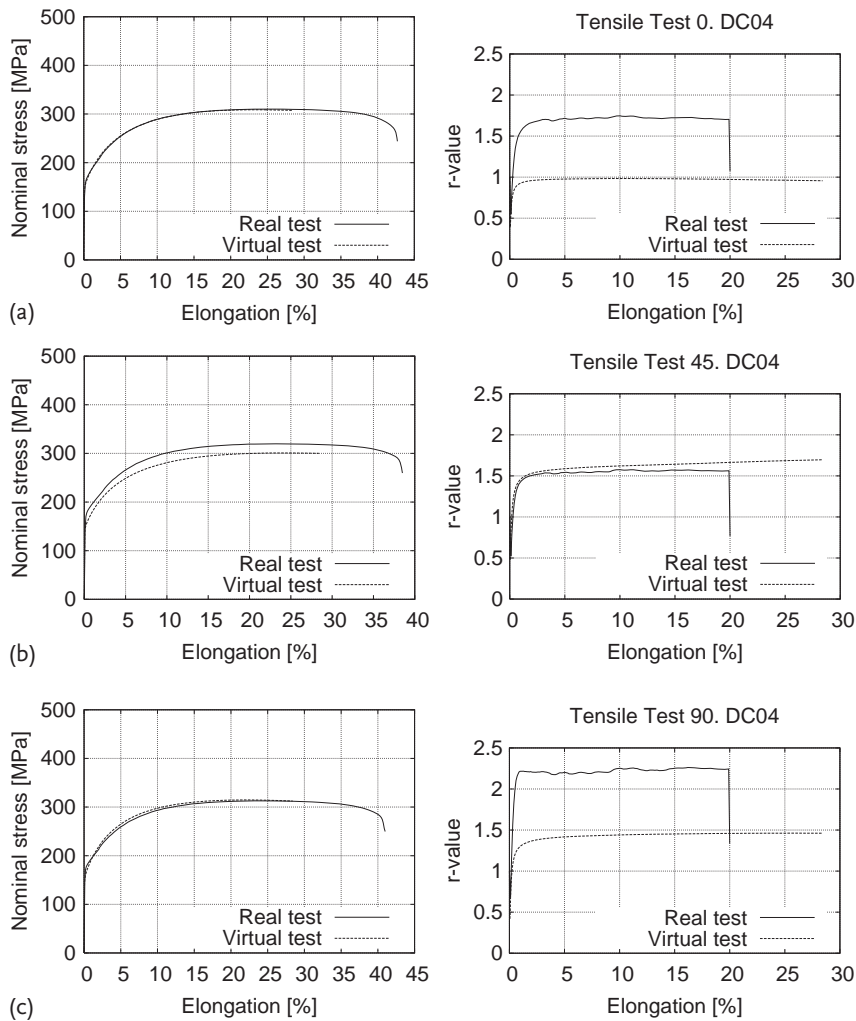
Figure 10.9 Calibration basis and resulting predictions of uniaxial stress–strain response and strain evolution of the Lankford value for DC04 steel. (a) Calibration data on nominal stress (left) for uniaxial tension along 0°. The Lankford value (right) has no direct influence on the calibration. (b) Prediction of nominal stress and *r* value for uniaxial tension along 45°. (c) Prediction of nominal stress and *r* value for uniaxial tension along 90°.

Generally, predicted stress–strain responses for tensile loading under 45° and 90° agree well with the corresponding experiments (see Figures 10.9b and c and 10.10b and c), with the exception of a slight underestimation (deviating less than 10%) in the case of DC04 under 45° (Figure 10.9b). However, the prediction for *r* values is far from perfect. In particular, for the cold rolling steel DC04, the simulated *r* values for 0° and 90° are strongly underestimated (Figure 10.9a and
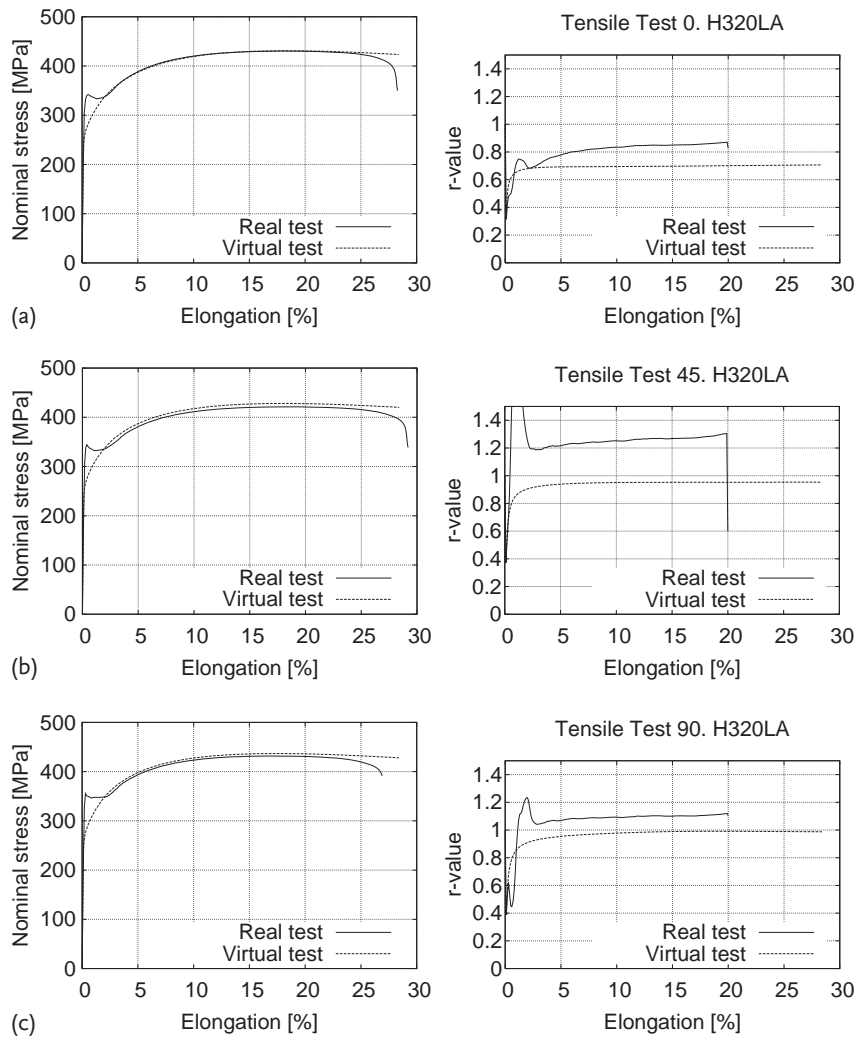
Figure 10.10 Calibration basis and resulting predictions of uniaxial stress–strain response and strain evolution of the Lankford value for H320LA steel. (a) Calibration data on nominal stress (left) for uniaxial tension along 0°. The Lankford value (right) has no direct influence on the calibration. (b) Prediction of nominal stress and *r* value for uniaxial tension along 45°. (c) Prediction of nominal stress and *r* value for uniaxial tension along 90°.

b). in the case of H320LA steel, the discrepancies are less severe as can be seen in Figure 10.10.

A further validation of the calibration was done against a more complicated test involving load reversal, that is, tension–compression. Figure 10.11a and b compares experiment and simulation of unidirectional tension and reverse loading into compression after about 0.08 strain. The predicted equivalent stress agrees quite
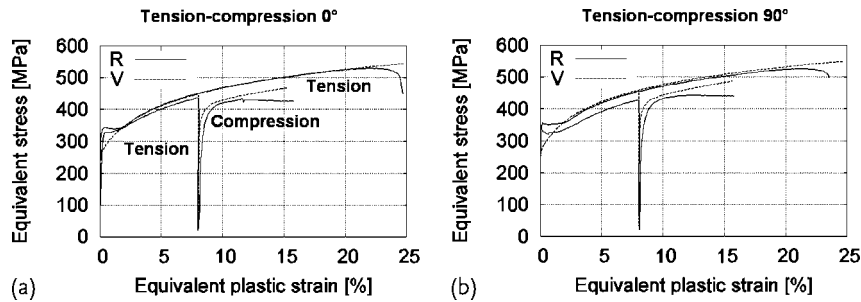
Figure 10.11 (a, b) The reversal of the loading direction from tension to compression results in a lower equivalent stress compared with the level observed under continued tensile load-ing (Bauschinger effect). This effect is found in real tension–compression tests (R) and is well reproduced by the virtual specimen (V).

well and the observed Bauschinger effect (lower flow stress after change of loading direction) is nicely reproduced. Compared with the simulation, the curve measured after load reversal exhibits less strain hardening (even softening) after compressive strains of about 0.05. This softening is caused by buckling of the specimen in compression. An important point to notice is that the virtual specimen exhibits a Bauschinger effect, even without kinematic hardening being explicitly incorporated into the constitutive law.

10.4.2.1 Influence of Finite Element Type

As discussed in Chapter 8, the approximation of displacement field gradients depends on the polynomial degree of the finite element shape function (as well as the integration scheme used). Therefore, simulations with four different element types (linear and quadratic shape functions, reduced and full integration scheme) were compared. The resulting stress–strain response, evolution of the *r* value, and exemplary displacement fields are shown in Figure 10.12.

In view of the accuracy with respect to experimental results, the deviation between the four different element types regarding the stress–strain response as well as the *r*-value evolution is minor. It can be noted that elements with a full integration scheme lead to a slightly higher tensile strength than those with reduced integration. The RVE discretized by finite elements using reduced integration and linear shape functions (Abaqus notation "C3D8R," eight nodes) exhibits the largest fluctuation in displacements. Although quadratic elements (and full integration) can reproduce inhomogeneous deformation more accurately, the significant reduction in computation time with only small differences in the calculated tensile strength justifies the use of "C3D8R" elements in all subsequently presented simulations.
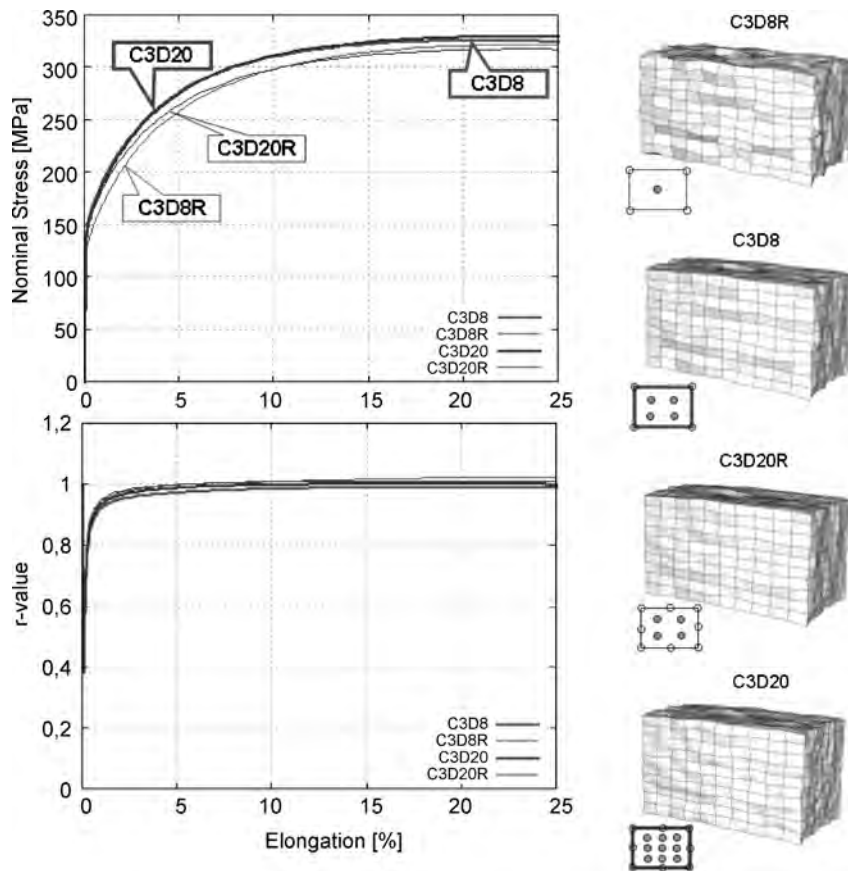
Figure 10.12 Stress–strain response and *r* values for different element types.

10.4.3
Stamping and Trimming Simulation

The material model as proposed by Vegter *et al.* (2003) and implemented in PAM-STAMP 2G (PAM, 2004) is, essentially, a very flexible description of the yield locus based on interpolation of experimental data by means of a cubic Bezier spline (Figure 10.13). The interpolation requires at least the following deformation tests:

- A stack compression test with measurement of ovalization.
- Three uniaxial tensile tests (0°, 45°, 90°) with lateral strain measurement.
- Three tensile tests with constrained lateral strain (plane strain, 0°, 45°, 90°). In contrast to real tests, the lateral stress can be identified in virtual tests.
- Three shear tests, providing yield locus data in the lower-right quadrant for different principal stress directions with respect to the rolling direction.
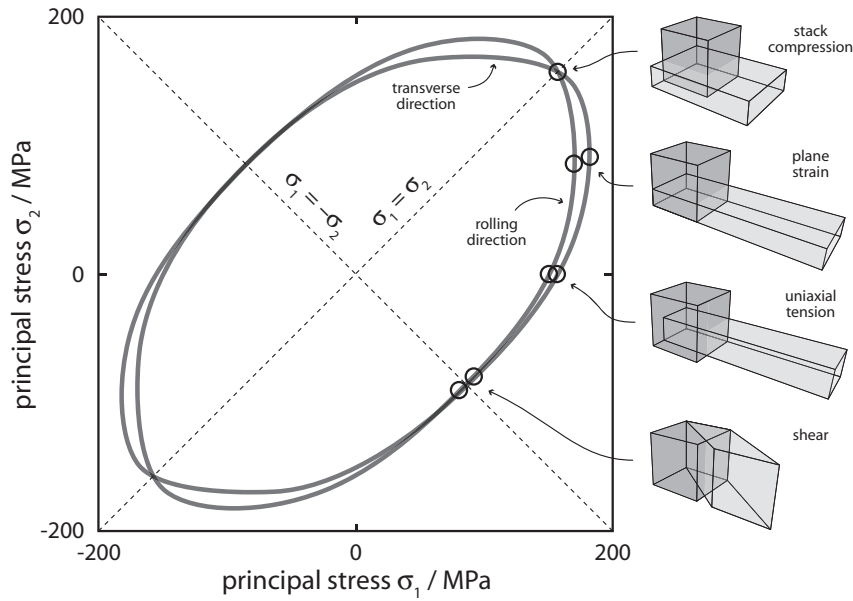
Figure 10.13 The Vegter yield locus (Vegter *et al.*, 2003) derived from virtual test data. Corresponding individual deformation tests are depicted on the right.

Table 10.4 Parameters for the Vegter yield locus (PAM-STAMP 2G (PAM, 2004)) obtained from virtual deformation tests on H320LA.

Parameter	Angle to rolling direction (°)		
	0	**45**	**90**
σ uniaxial	1	1.01	1.029
r uniaxial	0.624	0.798	0.950
σ-plane strain	1.1	1.14	1.16
α-plane strain	0.5	0.5	0.5
σ-pure shear	0.5615	0.5743	0.603
r biaxial	0.75	–	–
σ biaxial	1.004	–	–

All the parameters required (see Table 10.4) are determined from virtual deformation experiments at 1% accumulated shear deformation on the slip systems, which corresponds to approximately 0.4% plastic strain.

With the above yield locus parameterization, stamping, trimming, and springback of a car boot made of H320LA are simulated (Figure 10.14). For comparison, two additional simulations were carried out: one using a simple yield locus (Hill48 (Hill, 1948)) fitted to tensile data from experiments and another in which

Figure 10.14 Stamping part of a car boot. Photographs and visualized measured data. After stamping and after trimming.

yield criteria	test data	r0	r45	r90	max. difference [mm]	7.0 5.6 4.2 2.8 1.4 0.0 mm
Hill 48	real correspond to DIN	0.815	1.245	1.087	5.7	
Vegter	virtual, 0.4% plastic strain	0.624	0.798	0.950	6.9	
Vegter	virtual and real (r-values)	0.815	1.245	1.087	5.6	

Figure 10.15 Shape deviation between measured and simulated geometry for different material models and different types of test data for parameter fitting.

the Vegter parameterization relied on experimentally determined *r* values instead of those resulting from the virtual deformation tests.

The differences between optically scanned and simulated geometries are illustrated in Figure 10.15. The maximum deviation of the simulation using purely virtual test data (center row) is larger than that of the simple yield locus. If the *r* values of the virtually fitted Vegter model are replaced by measured ones, the discrepancy is reduced. However, the remaining disagreement is only marginally less than that resulting from the Hill48 yield locus.

10.4.4
Conclusions

Springback simulation and compensation generate an increasing demand for precise material models. Microstructural approaches such as texture-based crystal plasticity, however, still require too many resources in terms of memory and computational power for a direct simulation of industrial sheet metal forming; therefore, more sophisticated empirical models are likely to emerge. The resulting increased flexibility (and accuracy) of those models entails a higher experimental effort for parameter identification. In this context, virtual specimens with mi-

crostructure-based constitutive laws may be used to move the effort from real-world mechanical testing to computer simulation.

In this chapter a virtual specimen was used to demonstrate the process from model calibration over virtual deformation tests to simulation of a real part. The particular setting of the constitutive model and RVE setup still lacks the important capability to predict the *r* values correctly. On the other hand, the satisfactory prediction of the Bauschinger effect encourages further work. Shortcomings of the presented virtual specimen could be addressed by

- improving the texture sampling for better reproduction of the measured pole figures by discrete grain orientations,
- accounting for anisotropy of the grain shape, that is, use more than one element per grain,
- improving the calibration procedure, which should include the latent hardening matrix.

Even with the given restrictions, it was shown that material parameters obtained from texture data and tensile tests using the virtual test program can compete in simulation quality with the full parameter set obtained experimentally.

11
Outlook and Conclusions

The crystal plasticity finite element (CPFE) method is a powerful and comprehensive theoretical approach for the inclusion of micromechanical models and concepts in a unified theory of crystal plasticity including proper boundary condition treatment capable of treating a wide range of mechanical problems in materials science and engineering. The dyadic formulation of the constitutive laws within the CPFE approach allows the user to map such different deformation mechanisms as dislocation slip, martensite formation, twinning, grain boundary shear, and deformation via shear banding (in glass) and, in part, also their interactions, rendering the method a multimechanism and multiphysics approach. Its greatest potential lies, therefore, in the mesoscopic (intergrain scale, grain-cluster scale) and the microscopic (grain scale, intragrain scale) regime. It was further shown that the CPFE method, when formulated in conjunction with an appropriate homogenization scheme, is also suited to predict macroscopic mechanical behavior in metal forming, tool design, and process engineering. The particular strength of the finite element method lies in studying the influence of boundary conditions on mechanical or microstructural predictions. This advantage renders the CPFE method an ideal companion for the synergistic analysis of complex mechanical tests where a detailed sensitivity check is of relevance for a proper interpretation of the experimental observations. Another more practical advantage of the method is that it can be used in conjunction with commercial or academic finite element solvers in the form of user-defined material subroutines (the software of the authors is available as freeware for noncommercial use upon request).

Besides these profound achievements of the CPFE approach, there are also some critical gaps in the framework and in the experimental information that is required to support further development. The open questions can be grouped into issues of microstructure patterning, homogenization, physics and statistics behind constitutive models, damage mechanics, multiscale approaches, numerical stability, coupling to experiments, and alternative solution methods for crystal plasticity constitutive models.

The first category (microstructure patterning) refers to the fact that during deformation defects in crystals tend to self-organize into patterns which often reveal hierarchical structure. Different types of lattice defects reveal, in part, different deformation-induced pattern characteristics which often change in character and

size scale as deformation proceeds (dislocation cells, subgrains, microbands, shear bands, martensite lamellae, twin packages, faceting, rafting). Presently, there is no adequate description of these processes within CPFE models linking the properties and dynamics of individual defects to a quantitative description of patterns in a form suitable for inclusion in nonlocal continuum theories, although promising energy minimization approaches have been discussed by Müller (1996), Ortiz and Repetto (1999), Bhattacharya (2003), Aubry and Ortiz (2003), Conti, Hauret, and Ortiz (2007), and Dmitrieva *et al.* (2009).

The second category (homogenization) refers to the process by which the properties of a certain aggregate volume are derived from the local properties of its constituents by averaging over space and/or time. Homogenization is a most critical aspect for successful applications of the CPFE method at the mesoscopic scale and for macroscopic forming applications. It is clear that the microstructure and crystallographic texture of large parts cannot be represented via grain-by-grain maps (e.g., transferred from electron backscatter diffraction data onto a finite element mesh). Instead, homogenized averages, which are formulated as separate submodels, must provide the mechanical response of a representative volume element (Böhlke, Risy, and Bertram, 2005; Raabe *et al.*, 2002a; Raabe and Roters, 2004; Zhao *et al.*, 2001). These submodels deal with complex deformation mechanisms concerning the details of the interaction among competing deformation carriers, grains, and phases at a simplified level. Typical approaches in this domain follow Taylor–Bishop–Hill or self-consistent model assumptions. Recent developments toward a more realistic treatment of local interactions in the field of multicrystal homogenization are advanced grain-interaction Taylor–Bishop–Hill-type model variants as introduced by the groups of Gottstein (Crumbach *et al.*, 2001), Van Houtte (Van Houtte, Delannay, and Samajdar, 1999), and Eisenlohr (Eisenlohr *et al.*, 2009). Alternatively, homogenization can also be conducted in two subsequent steps in the form of a hybrid approach. The first one consists of the assembly of virtual polycrystalline (and, if required, multiphase) specimens and the subsequent simulation of their integral response under load. The second step consists in feeding these results into simpler constitutive laws (for instance, as fitting constants into a yield surface polynomial) which do not require a CPFE model framework. These techniques are, for instance, currently under development for engineering applications in the automotive industry (Kraska *et al.*, 2009) (see also Section 10.4).

The third category (physics and statistics) refers to open questions behind constitutive CPFE model formulations. Some issues in this context involve the treatment of nucleation and growth phenomena of twins and martensite lamellae. In this field even some of the fundamental metallurgical mechanisms are not yet fully understood. Examples are nucleation models for deformation twins which are based on cooperatively acting configurations of partial dislocations or the nucleation of martensite plates at shear bands or existing interfaces. Also the degree of plastic deformation of martensite in an austenitic environment is not yet well understood. Methods need to be developed to efficiently model the formation of ultrathin twins, twin packages, and repeated twinning (higher-order deformation twins). Another issue is the constitutive formulation of misfit stresses around martensite lamellae.

A further challenge associated with the consideration of multiple crystallographic deformation mechanisms within the same volume element lies in the degree of local homogenization that is required to tackle their interactions. This means that for some cases only one type of deformation mechanism (e.g., dislocation slip) may prevail, whereas in others a mix (e.g., dislocation slip and deformation twinning) must be considered at the same integration point. The latter situation requires definition of a submodel (homogenization model) that describes the interaction of coexisting deformation mechanisms at the same field point. In addition to developing better modeling approaches for mechanistic details, modeling approaches for alloy element effects will also be a strategic area of further research. Future efforts in this direction must aim at capturing elementary chemical details in constitutive laws. Most CPFE simulations which are compared with experimental data have, for good reasons, been conducted on (commercially) pure metals or certain well-characterized simple alloys. Future formulations should consider changes caused by solid solution effects and coherent or incoherent precipitations (Zambaldi *et al.*, 2007) on a sound physical and systematic basis so that variations in the mechanical response among similar alloys can be investigated. Incorporation strategies that transfer the results of phase field modeling are promising to connect alloying and microstructure evolution to assess mechanical response. Other open questions in this field refer to the statistical limits of constitutive laws that typically anticipate some average density of defects but not their discrete arrangement. For dislocation-based constitutive formulations it may be important to consider in more detail mechanical effects that possibly start to dominate at small scales such as slip localization and slip burst events, dislocation source depletion, geometrically necessary dislocations, surface source/sink effects, and grain boundary nucleation of dislocations (Dmitrieva *et al.*, 2009; Huang and Van Swygenhoven, 2009). Suitable dislocation-based frameworks which could be modified to capture at least certain aspects of these mechanisms were suggested by various groups, for example, Arsenlis and Parks (1999, 2002); Cheong and Busso (2004); Evers, Brekelmans, and Geers (2004a,b); Evers *et al.* (2002); Li *et al.* (2009); Ma and Roters (2004); Ma, Roters, and Raabe (2006a,b). Similar questions exist for the effect of the grain boundary structure on the mechanical response (Clark *et al.*, 1992; Evers, Brekelmans, and Geers, 2004b; Ma, Roters, and Raabe, 2006b,c; Shen, Wagoner, and Clark, 1986; Wei and Anand, 2004; Wei, Su, and Anand, 2006; Zaefferer *et al.*, 2003). The role of diffusion in accommodating local strain concentrations particularly in the context of creep and grain boundary sliding has only recently been attempted, but only in two dimensions (Agarwal *et al.*, 2007; Bower and Wininger, 2004). Finally, it must be discussed how small the density of lattice defects may become within a certain element without violating the statistics behind a constitutive law. The latter questions are particularly relevant when applying the CPFE method to ultrafine structures (small samples, small grain size, lamellar structures, wire drawn microstructures).

The fourth category (damage mechanics) deals with the overlap between crystal plasticity and fracture phenomena. The CPFE method is well suited for the identification of critical local parameters which may lead to damage initiation. This advantage is obviously due to its ability to map realistic grain assemblies so that the

effects of certain critical ingredients or configurations of such a given microstructure can be properly taken into account in a simulation. The main open question in this field is the identification of the mechanical and microstructure criteria that are responsible for local damage initiation. In some cases, such as in the presence of weak second phase interfaces or brittle inclusions, the location of damage nucleation is rather trivial, but in other cases where damage occurs in otherwise homogeneous single-phase polycrystals, more complex rules are required. Possible criteria that are currently being investigated by CPFE simulations are critical local values for the accumulated amount of shear, deformation energy density, and stress. Besides the comparison of corresponding simulations with experiments, it would also make sense to derive adequate damage criteria, such as modified Griffith models, which can help to establish a quantitative link between mechanical quantities that the CPFE method provides and damage nucleation. Promising approaches along these lines were recently investigated by the group of Bieler (Bieler *et al.*, 2005a, 2009; Kumar *et al.*, 2008) (see also Section 6.3).

The fifth main aspect comprises multiscale models in conjunction with the CPFE method. Obviously, this is a broad term which needs to be refined. The term multiscale modeling refers to the integration of constitutive model ingredients which stem from different time and/or length scales and, as a rule, from different submodels. In the case of the CPFE method, a most obvious need for multiscale approaches exists for those topics where current constitutive models have reached their limits. A prominent example is the integration of dislocation interactions which have been obtained from discrete dislocation dynamic codes into statistical dislocation density-based laws used in CPFE models. This approach is currently being pursued by Arsenlis and Tang (2003). The direct use of results obtained from atomic-scale simulations is still a great challenge since a huge discrepancy in space and particularly in time scale exists between the atomistic and the crystal plasticity scale. Recent progress along these lines has been reported in the field of damage initiation where interactions between the microstructure scale and the atomic scale play a dominant role (Buchheit, Wellman, and Battaile, 2005; Clayton and McDowell, 2004; Curtin and Miller, 2003; Hao *et al.*, 2003; Liu *et al.*, 2004; Voyiadjis, Abu Al-Rub, and Palazotto, 2004). For conventional dislocation motion it must be considered though that plasticity investigations via molecular dynamics simulations usually describe high-rate loading situations owing to the tiny integration steps required by the method. The deformation rates in such cases are typically orders of magnitude above realistic scales, so the transfer of such information must be done with great care since the results cannot in all cases be used for low-rate deformation constitutive models that typically prevail in CPFE simulations. Therefore, it may be more pertinent for molecular dynamics simulations of plasticity to provide certain constants or mechanisms for improved formulations of dislocation core structures, mobility, non-Schmid behavior, dislocation reactions, damage initiation, and hardening mechanisms. Other combinations are conceivable where a continuum-scale finite element method is used for a proper boundary condition treatment around a simulation regime that is treated by an atomistic method. Much progress may be expected from including thermodynamic and kinetic quantities that are derived by
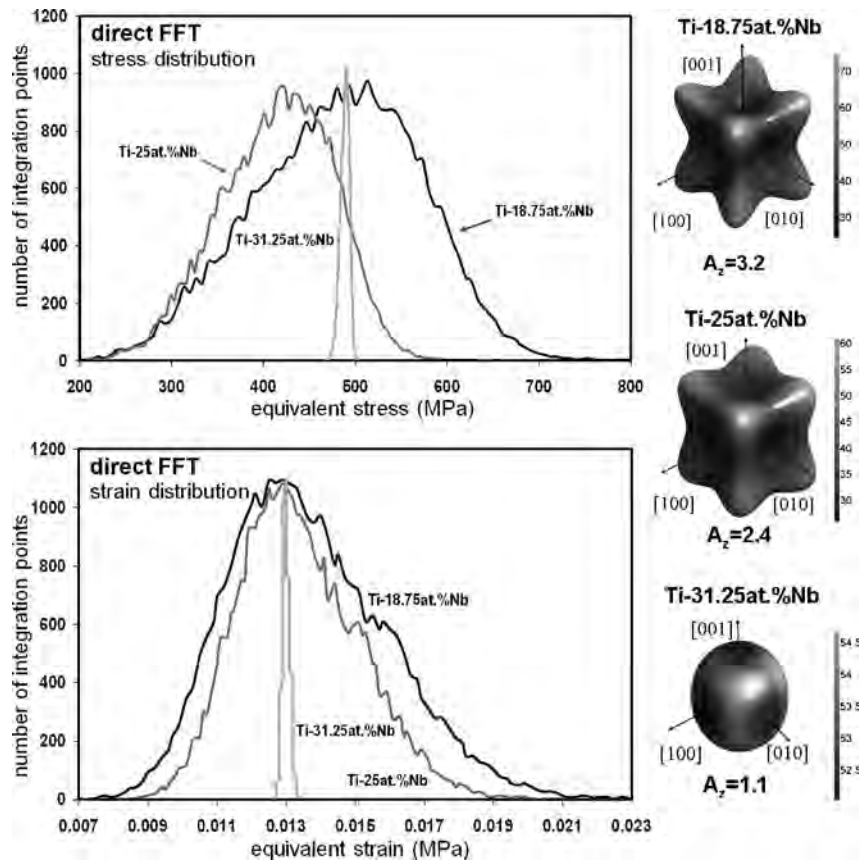
Figure 11.1 Direct fast Fourier predictions of an elastic problem based on the approach of Lebensohn (2001); Lebensohn *et al.* (2008). The results show the distribution of elastic equivalent stress and strain in three randomly textured polycrystalline β-titanium alloy aggregates each consisting of 200 grains and $32 \times 32 \times 32$ Fourier points. Each polycrystalline aggregate is characterized by a specific elastic tensor which was calculated using ab initio methods. The (nearly) isotropic case yields practically no internal mechanical spread, whereas the most anisotropic case leads to pronounced local stress–strain concentrations. The samples were subjected to tensile loading. The results are similar to the corresponding finite element predictions presented in Figure 10.2. The differences between the direct fast Fourier and the finite element results are attributed to the fact that the direct fast Fourier predictions used periodic boundary conditions, whereas the finite element approach used a free surface.

ab initio simulations (Bockstedte *et al.*, 1997; Counts *et al.*, 2008b, 2009; Ma *et al.*, 2008; Raabe *et al.*, 2007b). These quantities can be fractions of coexisting phases, elastic constants (Counts *et al.*, 2008b; Friak *et al.*, 2008; Ma *et al.*, 2008), or the dependence of certain metallurgical properties on the chemical composition (Raabe *et al.*, 2007b). Although ab initio methods work at the electronic scale, that is, at smaller integration steps than molecular dynamics simulations, many predictions

obtained by them, such as thermodynamic quantities, can be directly linked to mesoscopic CPFE constitutive laws. We expect that results from parameter-free ab initio simulations obtained by using electron density functional approaches will particularly provide basic insight and constants for constitutive problems which are not accessible otherwise. Concerning the combination of the CPFE method with macroscopic mechanical simulation approaches, a most promising development might be the introduction of virtual laboratories, where expensive mechanical tests can be replaced by mesoscopic CPFE simulations. A typical example is the replacement of biaxial polycrystal tests as required for fitting yield surface formulations by CPFE predictions (Kraska *et al.*, 2009).

Numerical and software aspects associated with the CPFE method are the sixth category of challenges. In this area the main issues are improved convergence behavior of the CPFE constitutive equations as well as a robust, modular, and parallelized code architecture. A more practical advantage of the CPFE method in that context is that it can be used in conjunction with commercial or academic finite element solvers in the form of easy-to-use user-defined material subroutines. Various groups (including the current authors) make their software available as freeware for noncommercial use upon request.

The seventh category concerns the requirement of a more detailed comparison between crystal plasticity predictions and the findings of corresponding experiments. Modern characterization tools allow a detailed mechanical, metallurgical, and crystallographic description of materials. The advantage of CPFE models is that they predict not only one internal variable, but a set of variables that can be effectively compared with the findings of corresponding experiments. Typical examples are crystallographic orientations, crack analysis, surface roughness, stress, and strain, as well as gradient, patterning, and localization effects associated with them (Table 5.1).

The last category concerns alternatives to the finite element method for solving crystal elasticity or crystal plasticity constitutive models. Some classical approaches were discussed in Chapter 7. For instance self-consistent and Taylor-based models, including in part also higher-order grain interaction terms, can serve for solving polycrystal mechanical problems without using finite elements, at least under simplified boundary conditions (Berveiller and Zaoui, 1978; Crumbach *et al.*, 2001; Lebensohn and Tomé, 1993; Molinari, Canova, and Ahzi, 1987; Van Houtte, Delannay, and Samajdar, 1999; Van Houtte *et al.*, 2005). Direct fast Fourier methods (Lebensohn, 2001) and Fourier-based spectral approaches (Kalidindi *et al.*, 2006a; Kalidindi, Duvvuru, and Knezevic, 2006b) are another important development for integrating crystal elasticity and plasticity constitutive models. They solve the equilibrium and compatibility constraints for anisotropic elastic or elastic–plastic polycrystal and polyphase problems using fast Fourier transforms (Kalidindi *et al.*, 2006a; Kalidindi, Duvvuru, and Knezevic, 2006b; Lebensohn, 2001; Lebensohn *et al.*, 2008; Michel, Moulinec, and Suquet, 1999; Wu *et al.*, 2007). The discrete Fourier approach renders the governing set of differential equations into a discrete algebraic problem which can be solved more quickly than the conventional weak-form variational approach used by the finite element method. To use

discrete series expansions, such spectral methods have to use a fixed grid and a representative cell arrangement of the microstructure considered. Discrete Fourier formulations imply periodicity of the modeled aggregate. Since the displacements lead to state values between the fixed coordinates of the discrete Fourier setup, interpolation functions must be used.

A purely elastic example of using different stiffness tensors in the direct fast Fourier method of Lebensohn (2001); Lebensohn *et al.* (2008) is shown in Figure 11.1. The two graphs present the distribution of the equivalent elastic stress and strain values in a randomly textured polycrystalline aggregate consisting of 200 grains and $32 \times 32 \times 32$ Fourier points for three different elastic tensors (magnitude, anisotropy) under a unidirectional tensile load. The entire aggregate remained in the elastic regime during loading. The results are very similar to the corresponding finite element predictions presented in Figure 10.2. The differences are attributed to the fact that the direct fast Fourier predictions used periodic boundary conditions, whereas the finite element approach used a free surface.

Franz~Roters, Philip~Eisenlohr, Thomas~R.~Bieler, and~Dierk~Raabe: Crystal Plasticity Finite Element Methods —
Chap. roters9419b01 — 2010/7/23 — page 173 — le-tex

173

References

Aba(2007) *Abaqus User Subroutines Reference Manual Version 6.7*, Dassault Systèmes.

Acharya, A. and Beaudoin, A.J. (2000) Grain-size effect in viscoplastic polycrystals at moderate strains. *J. Mech. Phys. Solids*, **48**, 2213–2230.

Agarwal, S., Briant, C.L., Krajewski, P.E., Bower, A.F., Taleff, E.M. (2007) Experimental Validation of Two-dimensional Finite Element Method for Simulating Constitutive Response of Polycrystals During High Temperature Plastic Deformation. *J. Mat. Eng. Perf.*, **16**, 170–178.

Alcala, J., Casals, O., and Ocenasek, J. (2008) Micromechanics of pyramidal indentation in fcc metals: Single crystal plasticity finite element analysis. *J. Mech. Phys. Solids*, **56**, 3277–3303.

Amirkhizi, A.V. and Nemat-Nasser, S. (2007) A framework for numerical integration of crystal elasto-plastic constitutive equations compatible with explicit finite element codes. *Int. J. Plasticity*, **23**, 1918–1937.

Anand, L. (2004) Single-crystal elasto-viscoplasticity: application to texture evolution in polycrystalline metals at large strains. *Comput. Methods Appl. Mech. Eng.*, **193**, 5359–5383.

Anand, L. and Gurtin, M.E. (2003) Thermal effects in the superelasticity of crystalline shape-memory materials. *J. Mech. Phys. Solids*, **51**, 1015–1058.

Anand, L. and Sun, C. (2007) A constitutive theory for metallic glasses at high homologous temperatures. *Acta Mater.*, **55**, 3755–3747.

Anand, L. and Sun, C. (2005) A theory for amorphous viscoplastic materials undergoing finite deformations, with application to metallic glasses. *J. Mech. Phys. Solids*, **53**, 1362–1396.

Arata, J.J.M., Kumar, K.S., Curtin, W.A., Needleman, A. (2002) Crack growth across colony boundaries in binary lamellar TiAl. *Mat. Sci. Eng. A*, **329**, 532–537.

Armstrong, R. and Worthington, P.J. (1973) *Metallurgical Effects at High Strain Rates*, eds Rohde, R. W., Butcher, B. M., Holland, J. R. and Karnes, C. H., Plenum Press, New York.

Arsenlis, A. and Parks, D.M. (1999) Crystallographic aspects of geometrically-necessary and statistically-stored dislocation density. *Acta Mater.*, **47** (5), 1597–1611.

Arsenlis, A. and Parks, D.M. (2002) Modeling the evolution of crystallographic dislocation density in crystal plasticity. *J. Mech. Phys. Solids*, **50** (9), 1979–2009.

Arsenlis, A., Parks, D., Becker, R., Bulatov, V. (2004) On the evolution of crystallographic dislocation density in non-homogeneously deforming crystals. *J. Mech. Phys. Solids*, **52** (6), 1213–1246.

Arsenlis, A. and Tang, M. (2003) Simulations on the growth of dislocation density during Stage 0 deformation in BCC metals. *Modelling Simul. Mater. Sci. Eng.*, **11**, 251–264.

Asaro, R.J. and Needleman, A. (1985) Texture development and strain hardening in rate dependent polycrystals. *Acta Metall.*, **33**, 923–953.

Asaro, R.J. and Rice, J.R. (1977) Strain localization in ductile single crystals. *J. Mech. Phys. Solids*, **25**, 309–338.

Ashby, M.F. (1970) The deformation of plastically non-homogeneous materials. *Philos. Mag.*, **21**, 399–424.

174 *References*

Ashmawi, W.M. and Zikry, M.A. (2003) Grain boundary effects and void porosity evolution. *Mech. Mater.*, **35**, 537.

Aubry, S. and Ortiz, M. (2003) The mechanics of deformation-induced subgrain-dislocation structures in metallic crystals at large strains. *Proc. Roy. Soc. London A*, **459**, 3131–3158.

Bachu, V. and Kalidindi, S.R. (1998) On the accuracy of the predictions of texture evolution by the finite element technique for fcc polycrystals. *Mat. Sci. Eng. A*, **257**, 108–117.

Balasubramanian, S. and Anand, L. (2002) Plasticity of initially textured hexagonal polycrystals at high homologous temperatures: application to titanium. *Acta Mater.*, **50**, 133–148.

Ball, J.M. and James, R.D. (1987) Fine phase mixtures as minimizers of energy. *Arch. Ration. Mech. An.*, **100** (1), 13–52.

Banerjee, P.K. (1994) *The Boundary Element Methods in Engineering*, McGraw-Hill College.

Barbe, F., Decker, L., Jeulin, D., Cailletaud, G. (2001) Intergranular and intragranular behavior of polycrystalline aggregates. Part 1: F.E. model. *Int. J. Plasticity*, **17**, 513–536.

Barlat, F., Brem, J.C., Yoon, J.W., Chung, K., Dick, R.E., Lege, D.J., Pourboghrat, F., Choi, S.H., Chu, E. (2002) Plane stress yield function for aluminum alloy sheets-Part I: Theory. *Int. J. Plasticity*, **19**, 1297–1319.

Barton, N.R., Knap, J., Arsenlis, A., Becker, R., Hornung, R.D., Jefferson, D.R. (2008) Embedded polycrystal plasticity and adaptive sampling. *Int. J. Plasticity*, **24**, 242–266.

Bassani, J.L., Ito, K., and Vitek, V. (2001) Complex macroscopic plastic flow arising from non-planar dislocation core structures. *Mat. Sci. Eng. A*, **319–321**, 97–101.

Bastos, A., Zaefferer, S., and Raabe, D. (2008) 3-dimensional EBSD study on the relationship between triple junctions and columnar grains in electrodeposited CoNi films. *J. Microscopy*, **230**, 487–498.

Bate, P. (1999) Modelling deformation microstructure with the crystal plasticity finite-element method. *Philos. T. Roy. Soc. London A*, **357**, 1589–1601.

Bate, P.S. and Hutchinson, W.B. (2005) Grain boundary area and deformation. *Scripta Mater.*, **52**, 199–203.

Bate, P. and An, Y. (2004) Plastic anisotropy in AA5005 Al-1Mg: predictions using crystal plasticity finite element analysis. *Scripta Mater.*, **51**, 973–977.

Bayley, C.J., Brekelmans, W.A.M., and Geers, M.G.D. (2006) A comparison of dislocation induced back stress formulations in strain gradient crystal plasticity. *Int. J. Solids Struct.*, **43** (24), 7268–7286.

Beaudoin, A.J., Dawson, P.R., Mathur, K.K., Kocks, U.F. (1995) A hybrid finite element formulation for polycrystal plasticity with consideration of macrostructural and microstructural linking. *Int. J. Plasticity*, **11**, 501–521.

Beaudoin, A.J., Dawson, P.R., Mathur, K.K., Kocks, U.F., Korzekwa, D.A. (1994) Application of polycrystal plasticity to sheet forming. *Comput. Methods Appl. Mech. Eng.*, **117**, 49–70.

Beaudoin, A.J., Mathur, K.K., Dawson, P.R., Johnson, G.C. (1993) Three-dimensional deformation process simulation with explicit use of polycrystal plasticity models. *Int. J. Plasticity*, **9**, 833–860.

Beaudoin, A.J., Mecking, H., and Kocks, U.F. (1996) Development of localized orientation gradients in fcc polycrystals. *Philos. Mag. A*, **73**, 1503–1517.

Becker, R. (1991) Analysis of texture evolution in channel die compression – I. Effects of grain interaction. *Acta Metall. Mater.*, **39**, 1211–1230.

Becker, R. (1998) Effects of strain localization on surface roughening during sheet forming. *Acta Mater.*, **46**, 1385–1401.

Becker, R., Butler, J.F., Hu, H., Lalli, L.A. (1991) Analysis of an aluminum single crystal with unstable initial orientation (001) [111] in channel die compression. *Metall. Trans. A*, **22**, 45–58.

Becker, R., Needleman, A., Suresh, S., Tvergaard, V., Vasudevan, A.K. (1989) An analysis of ductile fracture by grain boundary void growth. *Acta Metall.*, **37**, 99–120.

Becker, R. and Panchanadeeswaran, S. (1995) Effects of grain interactions on deformation and local texture in polycrystals. *Acta Mater.*, **43**, 2701–2719.

Benveniste, Y. (1987) A new approach to the application of Mori-Tanaka's theory in composite materials. *Mech. Mater.*, **6** (2), 147–157.

Bertram, A., Böhlke, T., and Kraska, M. (1997) Numerical simulation of deformation induced anisotropy of polycrystals. *Comp. Mater. Sci.*, **9**, 158–167.

Berveiller, M. and Zaoui, A. (1978) An extension of the self-consistent scheme to plastically-flowing polycrystals. *J. Mech. Phys. Solids*, **26** (5–6), 325–344.

Betten, J. (1993) *Kontinuumsmechanik*, Springer Verlag, Berlin, Heidelberg, New York.

Bhattacharya, K. (2003) *Microstructure of Martensite*, Oxford University Press, Oxford.

Bhattacharyya, A., El-Danaf, E., Kalidindi, S.R., Doherty, R.D. (2001) Evolution of grain-scale microstructure during large strain simple compression of polycrystalline aluminum with quasi-columnar grains: OIM measurements and numerical simulations. *Int. J. Plasticity*, **17**, 861–883.

Bhattacharyya, A. and Weng, G.J. (1994) An energy criterion for the stress-induced martensitic transformation in a ductile system. *J. Mech. Phys. Solids*, **42**, 1699–1724.

Bieler, T.R., Fallahi, A., Ng, B.C., Kumar, D., Crimp, M.A., Simkin, B.A., Zamiri, A., Pourboghrat, F., Mason, D.E. (2005a) Fracture Initiation/Propagation Parameters for Duplex TiAl Grain Boundaries Based on Twinning, Slip, Crystal Orientation, and Boundary Misorientation. *Intermetallics*, **13**, 979–984.

Bieler, T.R., Goetz, R.L., and Semiatin, S.L. (2005b) Anisotropic plasticity and cavity growth during upset forging of Ti-6Al-4V. *Mat. Sci. Eng. A*, **405**, 201–213.

Bieler, T.R., Nicolaou, P.D., and Semiatin, S.L. (2005c) An experimental and theoretical investigation of the effect of local colony orientations and misorientation on cavitation during hot working of Ti-6Al-4V. *Metall. Mater. Trans. A*, **36**, 129–140.

Bieler, T., Eisenlohr, P., Roters, F., Kumar, D., Mason, D., Crimp, M., Raabe, D. (2009) The role of heterogeneous deformation on damage nucleation at grain boundaries in single phase metals. *Int. J. Plasticity*, **25** (9), 1655–1683.

Bilby, B.A. (1955) Types of dislocation source, in *Report of the Conference on Defects in Crystalline Solids (Bristol, 1954)*, 124–133, The Physical Society, London, UK.

Bishop, J.F.W. and Hill, R. (1951a) A theoretical derivation of the plastic properties of a polycrystalline face centered metal. *Philos. Mag.*, **42**, 1298–1307.

Bishop, J.F.W. and Hill, R. (1951b) A theory of the plastic distortion of a polycrystalline aggregate under combined stresses. *Philos. Mag.*, **42**, 414–427.

Bitzek, E., Brandl, C., Weygand, D., Derlet, P.M., Van Swygenhoven, H. (2009) Atomistic simulation of a dislocation shear loop interacting with grain boundaries in nanocrystalline aluminium. *Modelling Simul. Mater. Sci. Eng.*, **17**, 055 008 (8 pp).

Bitzek, E., Derlet, P., Anderson, P., Van Swygenhoven, H. (2008) The stress-strain response of nanocrystalline metals: A statistical analysis of atomistic simulations. *Acta Mater.*, **56**, 4846–4857.

Bockstedte, M., Kley, A., Neugebauer, J., Scheffler, M. (1997) Density-functional theory calculations for poly-atomic systems: electronic structure, static and elastic properties and ab initio molecular dynamics. *Comput. Phys. Commun.*, **107**, 187–222.

Boehlert, C.J., Longanbach, S.C., and Bieler, T.R. (2008) The effect of thermomechanical processing on the creep behavior of Udimet Alloy 188. *Philos. Mag. A*, **88**, 641–664.

Böhlke, T., Haus, U.U., and Schulze, V. (2006) Crystallographic texture approximation by quadratic programming. *Acta Mater.*, **54**, 1359–1368.

Böhlke, T., Risy, G., and Bertram, A. (2005) A texture component model for anisotropic polycrystal plasticity. *Comp. Mater. Sci.*, **32**, 284–293.

Bolling, G.F. and Richman, R.H. (1965) Continual mechanical twinning: Part I: Formal description. *Acta Metall.*, **13**, 709–745.

Bollmann, W. (1982) *Crystal Lattices, Interfaces, Matrices*, Bollmann, Geneva.

Bollmann, W. (1984) Triple lines in polycrystalline aggregates as disclinations. *Philos. Mag. A*, **49**, 73–79.

Bollmann, W. (1988) Triple-line disclinations representations, continuity and reactions. *Philos. Mag. A*, **57**, 637–649.

Bollmann, W. (1991) The stress-field of a model triple-line disclination. *Mat. Sci. Eng.*, **136**, 1–7.

176 | *References*

Boole, G. (1872) *A Treatise On The Calculus of Finite Differences*, 2nd edn, Macmillan and Company, London.

Borg, U., Niordson, C.F., and Kysar, J.W. (2008) Size effects on void growth in single crystals with distributed voids. *Int. J. Plasticity*, **24**, 688–701.

Bower, A.F. and Wininger, E. (2004) A two-dimensional finite element method for simulating the constitutive response and microstructure of polycrystals during high temperature plastic deformation. *J. Mech. Phys. Solids*, **52**, 1289–1317.

Bower, A. (2010) *Applied Mechanics of Solids*, Taylor & Francis, Boca Raton.

Brandon, D. (1966) Structure of high-angle grain boundaries. *Acta Metall.*, **14**, 1479–1484.

Bronkhorst, C.A., Kalidindi, S.R., and Anand, L. (1992) Polycrystalline plasticity and the evolution of crystallographic texture in FCC metals. *Philos. T. Roy. Soc. London A*, **341** (1662), 443–477.

Brunig, M. and Ricci, S. (2005) Nonlocal continuum theory of anisotropically damaged metals. *Int. J. Plasticity*, **21**, 1346–1382.

Bruzzi, M.S., McHugh, P.E., O'Rourke, F., Linder, T. (2001) Micromechanical modelling of the static and cyclic loading of an Al 2124-SiC MMC. *Int. J. Plasticity*, **17**, 565–599.

Buchheit, T.E., Wellman, G.W., and Battaile, C.C. (2005) Investigating the limits of polycrystal plasticity modeling. *Int. J. Plasticity*, **21**, 221–249.

Bunge, H.J. (1982) *Texture Analysis in Materials Science*, Butterworths, London.

Casals, O., Ocenasek, J., and Alcala, J. (2007) Crystal plasticity finite element simulations of pyramidal indentation in copper single crystals. *Acta Mater.*, **55**, 55–68.

Chadwick, P. (1999) *Continuum Mechanics Concise Theory and Problems*, 2nd edn, Dover Publications, Inc., Mineola, NY.

Chen, Y.P., Lee, W.B., and To, S. (2007) Influence of initial texture on formability of aluminum sheet metal by crystal plasticity FE simulation. *J. Mater. Process. Tech.*, **192–193**, 397–403.

Cheong, K.S. and Busso, E.P. (2004) Discrete dislocation density modelling of single phase FCC polycrystal aggregates. *Acta Mater.*, **52**, 5665–5675.

Cheong, K.S., Smillie, M.J., and Knowles, D.M. (2007) Predicting fatigue crack initiation through image-based micromechanical modeling. *Acta Mater.*, **55**, 1757–1768.

Cherkaoui, M., Berveiller, M., and Lemoine, X. (2000) Coupling between plasticity and martensitic phase transformation: Overall behavior of polycrystalline TRIP steels. *Int. J. Plasticity*, **16**, 1215–1241.

Cherkaoui, M., Berveiller, M., and Sabar, H. (1998) Micromechanical modeling of martensitic transformation-induced plasticity (TRIP) in austenitic single crystals. *Int. J. Plasticity*, **14**, 597–626.

Choi, S.H. (2003) Simulation of stored energy and orientation gradients in cold-rolled interstitial free steels. *Acta Mater.*, **51**, 1775–1788.

Christian, J.W. and Mahajan, S. (1995) Deformation twinning. *Prog. Mater. Sci.*, **39** (1–2), 1–157.

Clark, W.A.T., Wagoner, R.H., Shen, Z.Y., Lee, T.C., Robertson, I.M., Birnbaum, H.K. (1992) On the criteria for slip transmission across interfaces in polycrystals. *Scripta Metall. Mater.*, **26** (2), 203–206.

Clarke, A.P., Humphreys, F.J., and Bate, P.S. (2003) Lattice rotations at large second-phase particles in polycrystalline aluminum. *Mat. Sci. Forum*, **426**, 399–404.

Clayton, J.D. (2005) Dynamic plasticity and fracture in high density polycrystals: constitutive modeling and numerical simulation. *J. Mech. Phys. Solids*, **53**, 261–301.

Clayton, J.D. and Chung, P.W. (2006) An atomistic-to-continuum framework for nonlinear crystal mechanics based on asymptotic homogenization. *J. Mech. Phys. Solids*, **54**, 1604–1639.

Clayton, J.D. and McDowell, D.L. (2004) Homogenized finite elastoplasticity and damage: theory and computations. *Mech. Mater.*, **36**, 825–847.

Conti, S., Hauret, P., and Ortiz, M. (2007) Concurrent multiscale computing of deformation microstructure by relaxation and local enrichment with application to single-crystal plasticity. *Multiscale Modeling and Simulation*, **6**, 135–157.

Counts, W.A., Braginsky, M.V., Battaile, C.C., Holm, E.A. (2008a) Predicting the Hall–Petch effect in fcc metals using non-local

crystal plasticity. *Int. J. Plasticity*, **24**, 1243–1263.

Counts, W.A., Friak, M., Battaile, C.C., Raabe, D., Neugebauer, J. (2008b) A comparison of polycrystalline elastic constants computed by analytic homogenization schemes and FEM. *Phys. Status Solidi B*, **245**, 2644–2649.

Counts, W.A., Friak, M., Raabe, D., Neugebauer, J. (2009) Using ab initio calculations in designing bcc Mg-Li alloys for ultra light-weight applications. *Acta Mater.*, **57**, 69–76.

Courant, R. (1943) Variational methods for the solution of problems of equilibrium and vibrations. *B. Am. Math. Soc.*, **49**, 1–23.

Crumbach, M., Pomana, G., Wagner, P., Gottstein, G. (2001) A Taylor Type Deformation Texture Model Considering Grain Interaction and Material Properties. Part I – Fundamentals, in *Recrystallisation and Grain Growth*, Proc. First Joint Conference, Springer, Berlin, pp. 1053–1060, eds. G. Gottstein and D. A. Molodov.

Cuitiño, A.M. and Ortiz, M. (1992) Computational modelling of single crystals. *Modelling Simul. Mater. Sci. Eng.*, **1**, 225–263.

Curtin, W.A. and Miller, R.E. (2003) Atomistic/continuum coupling in computational materials science. *Modelling Simul. Mater. Sci. Eng.*, **11**, R33–R68.

daFonseca, J.Q., Oliver, E.C., Bate, P.S., Withers, P.J. (2006) Evolution of intergranular stresses during in situ straining of IF steel with different grain sizes. *Mat. Sci. Eng. A*, **437**, 26–32.

Davies, P. and Randle, V. (2001) Grain boundary engineering and the role of the interfacial plane. *Mat. Sci. Tech.*, **17**, 615–626.

Dawson, P.R., Mika, D.P., and Barton, N.R. (2002) Finite element modeling of lattice misorientations in aluminum polycrystals. *Scripta Mater.*, **47**, 713–717.

de Koning, M., Kurtz, R.J., Bulatov, V.V., Henager, C.H., Hoagland, R.G., Cai, W., Nomura, M. (2003) Modeling of dislocation-grain boundary interactions in FCC metals. *J. Nucl. Mater.*, **323**, 281–289.

de Koning, M., Miller, R., Bulatov, V.V., Abraham, F.F. (2002) Modelling grain-boundary resistance in intergranular dislocation slip

transmission. *Philos. Mag. A*, **82**, 2511–2527.

Deka, D., Joseph, D.S., Ghosh, S., Mills, M.J. (2006) Crystal plasticity modeling of deformation and creep in polycrystalline Ti-6242. *Metall. Mater. Trans. A*, **37**, 1371–1388.

Delaire, F., Raphanel, J.L., and Rey, C. (2000) Plastic heterogeneities of a copper multicrystal deformed in uniaxial tension: Experimental study and finite element simulations. *Acta Mater.*, **48**, 1075–1087.

Delannay, L., Beringhier, M., Chastel, Y., Loge, R.E. (2005) Simulation of cup-drawing based on crystal plasticity applied to reduced grain samplings. *Mat. Sci. Forum*, **495–497**, 1639–1644.

Delannay, L., Doghri, I., and Pierard, O. (2007) Prediction of tension-compression cycles in multiphase steel using a modified incremental mean-field model. *Int. J. Solids Struct.*, **44** (22–23), 7291–7306.

Delannay, L., Jacques, P., and Kalidindi, S. (2006) Finite element modeling of crystal plasticity with grains shaped as truncated octahedrons. *Int. J. Plasticity*, **22**, 1879–1898.

Delannay, L., Kalidindi, S.R., and Van Houtte, P. (2002) Quantitative prediction of textures in aluminium cold rolled to moderate strains. *Mat. Sci. Eng. A*, **336**, 233–244.

Delannay, L., Melchior, M., Signorelli, J., Remacle, J., Kuwabara, T. (2009) Influence of grain shape on the planar anisotropy of rolled steel sheets – evaluation of three models. *Comp. Mater. Sci.*, **45**, 739–743.

Demir, E., Raabe, D., Zaafarani, N., Zaefferer, S. (2009) Experimental investigation of geometrically necessary dislocations beneath small indents of different depths using EBSD tomography. *Acta Mater.*, **57**, 559–569.

Dewald, M.P. and Curtin, W.A. (2007) Multiscale modelling of dislocation/grain-boundary interactions: I. Edge dislocations impinging on Sigma 11 (1 1 3) tilt boundary in Al. *Modelling Simul. Mater. Sci. Eng.*, **15**, S193–S215.

Diani, J.M. and Parks, D.M. (1998) Effects of strain state on the kinetics of strain-induced martensite in steels. *J. Mech. Phys. Solids*, **46** (9), 1613–1635.

Diani, J.M., Sabar, H., and Berveiller, M. (1995) Micromechanical modelling of the

178 | *References*

transformation induced plasticity (TRIP) phenomenon in steels. *Int. J. Eng. Sci.*, **33**, 1921–1934.

Diard, O., Leclercq, S., Rousselier, G., Cailletaud, G. (2005) Evaluation of finite element based analysis of 3D multicrystalline aggregates plasticity: Application to crystal plasticity model identification and the study of stress and strain fields near grain boundaries. *Int. J. Plasticity*, **21**, 691–722.

Dick, T. and Cailletaud, G. (2006) Fretting modelling with a crystal plasticity model of Ti6Al4V. *Comp. Mater. Sci.*, **38**, 113–125.

Dimiduk, D.M., Uchic, M.D., and Parthasarathy, T.A. (2005) Size affected single slip behavior of pure Ni microcrystals. *Acta Mater.*, **53**, 4065–4077.

Dmitrieva, O., Dondl, P.W., Müller, S., Raabe, D. (2009) Lamination microstructure in shear deformed copper single crystals. *Acta Mater.*, **57**, 3439–3449.

Doghri, I. and Ouaar, A. (2003) Homogenization of two-phase elasto-plastic composite materials and structures: Study of tangent operators, cyclic plasticity and numerical algorithms. *Int. J. Solids Struct.*, **40** (7), 1681–1712.

Doquet, V. (1993) Twinning and multiaxial cyclic plasticity of a low stacking-fault-energy f.c.c alloy. *Acta Metall. Mater.*, **41**, 2451–2459.

Duesbery, M.S. and Vitek, V. (1998) Plastic anisotropy in BCC transition metals. *Acta Mater.*, **46** (5), 1481–1492.

Dunne, F.P.E., Walker, A., and Rugg, D. (2007a) A systematic study of hcp crystal orientation and morphology effects in polycrystal deformation and fatigue. *Proc. Roy. Soc. London A*, **463**, 1467–1489.

Dunne, F.P.E., Wilkinson, A.J., and Allen, R. (2007b) Experimental and computational studies of low cycle fatigue crack nucleation in a polycrystal. *Int. J. Plasticity*, **23**, 273–295.

Eisenlohr, P. and Roters, F. (2008) Selecting a set of discrete orientations for accurate texture reconstruction. *Comp. Mater. Sci.*, **42**, 670–678.

Eisenlohr, P., Tjahjanto, D., Hochrainer, T., Roters, F., Raabe, D. (2009) Comparison of texture evolution in fcc metals predicted by various grain cluster homogenization schemes. *Int. J. Mat. Res.*, **100**, 500–509.

El-Dana, E., Kalidindi, S.R., and Doherty, R.D. (1998) Influence of grain size and stacking fault energy on deformation twinning in FCC metals. *Metall. Mater. Trans. A*, **30**, 1223.

Erieau, P. and Rey, C. (2004) Modeling of deformation and rotation bands and of deformation induced grain boundaries in IF steel aggregate during large plane strain compression. *Int. J. Plasticity*, **20**, 1763–1788.

Eshelby, J.D. (1957) The determination of the elastic field of an ellipsoidal inclusion, and related problems. *Proc. Roy. Soc. London A*, **241**, 376–396.

Evers, L.P., Brekelmans, W.A.M., and Geers, M.G.D. (2004a) Non-local crystal plasticity model with intrinsic SSD and GND effects. *J. Mech. Phys. Solids*, **52** (10), 2379–2401.

Evers, L.P., Brekelmans, W.A.M., and Geers, M.G.D. (2004b) Scale dependent crystal plasticity framework with dislocation density and grain boundary effects. *Int. J. Solids Struct.*, **41** (18–19), 5209–5230.

Evers, L.P., Parks, D.M., Brekelmans, W.A.M., Geers, M.G.D. (2002) Crystal plasticity model with enhanced hardening by geometrically necessary dislocation accumulation. *J. Mech. Phys. Solids*, **50** (11), 2403–2424.

Fallahi, A., Kumar, D., Bieler, T.R., Crimp, M.A., Mason, D.E. (2006) The effect of grain boundary normal on predicting microcrack nucleation using fracture initiation parameters in duplex TiAl. *Mat. Sci. Eng. A*, **432**, 281–291.

Fedorov, A.A., Gutkin, M.Y., and Ovid'ko, I.A. (2003) Transformations of grain boundary dislocation pile-ups in nano- and polycrystalline materials. *Acta Mater.*, **51** (4), 887–898.

Fedosseev, A. and Raabe, D. (1994) Application of the method of superposition of harmonic currents for the simulation of inhomogeneous deformation during hot rolling of FeCr. *Scripta Metall.*, **30**, 1–6.

Feyel, F. and Chaboche, J.L. (2000) FE² multiscale approach for modelling the elasto-viscoplastic behaviour of long fibre SiC/Ti composite materials. *Comput. Methods Appl. Mech. Eng.*, **183** (3–4), 309–330.

Fischer, F.D., Reisner, G., Werner, E.A., Tanaka, K., Cailletaud, G., Antretter, T. (2000)

A new view on transformation-induced plasticity (TRIP). *Int. J. Plasticity*, **16**, 723–748.

Forest, S. (1998) Modeling slip, kink and shear banding in classical and generalized single crystal plasticity. *Acta Mater.*, **46**, 3265–3281.

Forest, S., Barbe, F., and Cailletaud, G. (2000) Cosserat modelling of size effects in the mechanical behaviour of polycrystals and multi-phase materials. *Int. J. Solids Struct.*, **37** (46–47), 7105–7126.

Frary, A. and Schuh, C.A. (2003) Combination rule for deviant CSL grain boundaries at triple junctions. *Acta Mater.*, **51**, 3731–3743.

Friak, M., Counts, W.A., Raabe, D., Neugebauer, J. (2008) Error-propagation in multiscale approaches to the elasticity of polycrystals. *Phys. Status Solidi B*, **245**, 2636–2641.

Fu, H.H., Benson, D.J., and Meyers, M.A. (2004) Computational description of nanocrystalline deformation based on crystal plasticity. *Acta Mater.*, **52**, 4413–4425.

Gao, H. and Huang, Y. (2003) Geometrically necessary dislocation and size-dependent plasticity. *Scripta Mater.*, **48** (2), 113–118.

Geers, M.G.D. and Kouznetsova, V.G. (2007) Modeling the interaction between plasticity and the austenite-martensite transformation. *Int. J. Multiscale Com.*, **5**, 129–140.

Gerken, J.M. and Dawson, P.R. (2008a) A crystal plasticity model that incorporates stresses and strains due to slip gradients. *J. Mech. Phys. Solids*, **56**, 1651–1672.

Gerken, J.M. and Dawson, P.R. (2008b) A finite element formulation to solve a nonlocal constitutive model with stresses and strains due to slip gradients. *Comput. Method. Appl. M.*, **197**, 1343–1361.

Gibson, M.A. and Forwood, C.T. (2002) Slip transfer of deformation twins in duplex gamma-based Ti-Al alloys. III. Transfer across general large-angle gamma-gamma grain boundaries. *Philos. Mag. A*, **82**, 1381.

Goh, C.H., Neu, R.W., and McDowell, D.L. (2003) Crystallographic plasticity in fretting of Ti-6AL-4V. *Int. J. Plasticity*, **19**, 1627–1650.

Govindjee, S. and Miehe, C. (2001) A multivariant martensitic phase transformation model: Formulation and numerical implementation. *Comput. Method. Appl. M.*, **191**, 215–238.

Greenwood, G.W. and Johnson, R.H. (1965) The deformation of metals under small stresses during phase transformation. *Proc. Roy. Soc. London A*, **283**, 403.

Greer, J.R., Oliver, W.C., and Nix, W.D. (2005) Size dependence of mechanical properties of gold at the microscale in the absence of strain gradients. *Acta Mater.*, **53**, 1821–1830.

Gross, D. and Seelig, T. (2001) *Bruchmechanik mit einer Einführung in die Mikromechanik*, Springer Verlag, Berlin, Heidelberg, New York.

Gurtin, M. (2002) A gradient theory of single-crystal viscoplasticity that accounts for geometrically necessary dislocations. *J. Mech. Phys. Solids*, **50** (1), 5–23.

Gurtin, M.E. (2008) A finite-deformation, gradient theory of single-crystal plasticity with free energy dependent on densities of geometrically necessary dislocations. *Int. J. Plasticity*, **24** (4), 702–725.

Gurtin, M.E., Anand, L., and Lele, S.P. (2007) Gradient single-crystal plasticity with free energy dependent on dislocation densities. *J. Mech. Phys. Solids*, **55** (9), 1853–1878.

Hall, E.O. (1951) The deformation and ageing of mild steel: III discussion of results. *Proc. Phys. Soc. B*, **64**, 747.

Han, C.S., Gao, H., Huang, Y., Nix, W. (2005) Mechanism-based strain gradient crystal plasticity – I. Theory. *J. Mech. Phys. Solids*, **53**, 1188–1203.

Han, C.S., Ma, A., Roters, F., Raabe, D. (2007) A Finite Element approach with patch projection for strain gradient plasticity formulations. *Int. J. Plasticity*, **23**, 690–710.

Han, T.S. and Dawson, P.R. (2007) A two-scale deformation model for polycrystalline solids using a strongly-coupled finite element methodology. *Comput. Method. Appl. M.*, **196**, 2029–2043.

Hansen, N. (1979) *The effect of grain size and strain on the tensile flow stress of copper at room temperature.* Proceedings of ICSMA 2 (Haasen, P., Gerold, V., Kostorz, G.), pp. 849–854, Pergamon Press, Oxford.

Hao, S., Liu, W.K., Moran, B., Vernerey, F., Olson, G.B. (2004) Multi-scale constitutive model and computational framework for the design of ultra-high strength, high

180 *References*

toughness steels. *Comput. Method. Appl. M.*, **193**, 1865–1908.

Hao, S., Moran, B., Liu, W.K., Olson, G.B. (2003) A hierarchical multi-physics model for design of high toughness steels. *J. Computer-Aided Materials Design*, **10**, 99–142.

Harding, J. (1967) The yield and fracture behaviour of high-purity iron single crystals at high rates crystals at high rates of strain. *Proc. Roy. Soc. London A*, **299**, 464–490.

Harding, J. (1968) Yield and fracture of high-purity iron single crystals under repeated tensile impact loading. *Mem. Sci. Rev. Met.*, **65**, 245.

Harewood, F.J. and McHugh, P.E. (2006) Investigation of finite element mesh independence in rate dependent materials. *Comp. Mater. Sci.*, **37**, 442–453.

Harewood, F.J. and McHugh, P.E. (2007) Comparison of the implicit and explicit finite element methods using crystal plasticity. *Comp. Mater. Sci.*, **39**, 481–494.

Hartig, C. and Mecking, H. (2005) Finite element modelling of two phase FeCu polycrystals. *Comp. Mater. Sci.*, **32**, 370–377.

Hasija, V., Ghosh, S., Mills, M.J., Joseph, D.S. (2003) Deformation and creep modeling in polycrystalline Ti-6Al alloys. *Acta Mater.*, **51**, 4533–4549.

Helming, K. (1996) *Texturapproximation durch Modellkomponenten*, Cuvillier Verlag, Göttingen.

Helming, K., Schwarzer, R.A., Rauschenbach, B., Geier, S., Leiss, B., Wenk, H., Ullemeier, K., Heinitz, J. (1994) Texture estimates by means of components. *Z. Metallkd.*, **85**, 545–553.

Hershey, A.V. (1954) The elasticity of an isotropic aggregate of anisotropic cubic crystals. *J. Appl. Mech. ASME*, **21**, 236–240.

Hill, R. (1948) A theory of the yielding and plastic flow of anisotropic metals. *Proc. Roy. Soc. London A*, **193**, 281–297.

Hill, R. (1952) The elastic behavior of a crystalline aggregate. *Proc. Roy. Soc. London A*, **65**, 349–354.

Hill, R. (1965) Continuum micro-mechanics of elastoplastic polycrystals. *J. Mech. Phys. Solids*, **13** (2), 89–101.

Hirth, J.P. and Lothe, J. (1982) *Theory of Dislocations*, 2nd edn., Krieger Publishing

Company – John Wiley & Sons, Ltd., New York

Hokka, M., Kuokkala, V.T., Curtze, S., Vuoristo, T., Apostol, M. (2006) Characterization of strain rate and temperature dependent mechanical behavior of TWIP steels. *J. Phys. IV*, **134**, 1301–1306.

Honneff, H. and Mecking, H. (1978) *A method for the determination of the active slip systems and orientation changes during single crystal deformation*, Proceedings of the 5th International Conference on Texture of Materials (ICOTOM-5) (G. Gottstein, K. Lücke), 265, Springer, Berlin.

Hoover, W.G. (2006) *Smooth Particle Applied Mechanics: The State of the Art*, World Scientific, Singapore..

Horstemeyer, M., Ramaswamy, S., and Negrete, M. (2003) Using a micromechanical finite element parametric study to motivate a phenomenological macroscale model for void/crack nucleation in aluminum with a hard second phase. *Mech. Mater.*, **35**, 675–687.

Huang, H.C. and Van Swygenhoven, H. (2009) Atomistic simulations of mechanics of nanostructures. *MRS Bull.*, **34**, 160–162.

Hull, D. and Bacon, D.J. (2001) *Introduction to Dislocations*, 4th edn, Butterworth-Heinmann, Oxford.

Hutchinson, J.W. (1976) Bounds and self-consistent estimates for creep of polycrystalline materials. *Proc. Roy. Soc. London A*, **348**, 1001–127.

Inal, K., Simha, H.M., and Mishra, R.K. (2008) Numerical modeling of second-phase particle effects on localized deformation. *J. Eng. Mater. Tech.*, **130**, 021 003.

Jacques, J.P., Ladrière, J., and Delannay, F. (2001) On the influence of interactions between phases on the mechanical stability of retained austenite in transformation-induced plasticity multiphase steels. *Metall. Mater. Trans. A*, **32**, 2759–2768.

Jirásek, M. and Bažant, Z.P. (2002) *Inelastic Analysis of Structures*, John Wiley & Sons, Ltd, Chichester.

Kalidindi, S.R. (1998) Incorporation of deformation twinning in crystal plasticity models. *J. Mech. Phys. Solids*, **46**, 267–290.

Kalidindi, S.R. (2001) Modeling anisotropic strain hardening and deformation textures

in low stacking fault energy fcc metals. *Int. J. Plasticity*, **17**, 837–860.

Kalidindi, S.R. (2004) *Continuum Scale Simulation of Engineering Materials*, in A Crystal plasticity Framework for Deformation Twinning, Wiley-VCH Verlag-GmbH, pp. 543–560.

Kalidindi, S.R. and Anand, L. (1993) Large deformation simple compression of a copper single crystal. *Metall. Trans. A*, **24**, 989–992.

Kalidindi, S.R., Binci, M., Fullwood, D., Adams, B.L. (2006a) Elastic properties closures using second-order homogenization theories: Case studies in composites of two isotropic constituents. *Acta Mater.*, **54**, 3117–3126.

Kalidindi, S.R., Bronkhorst, C.A., and Anand, L. (1992) Crystallographic texture evolution in bulk deformation processing of fcc metals. *J. Mech. Phys. Solids*, **40**, 537–569.

Kalidindi, S.R., Duvvuru, H.K., and Knezevic, M. (2006b) Spectral calibration of crystal plasticity models. *Acta Mater.*, **54**, 1795–1804.

Kalidindi, S.R. and Schoenfeld, S.E. (2000) On the prediction of yield surfaces by the crystal plasticity models for fcc polycrystals. *Mat. Sci. Eng. A*, **293**, 120–129.

Karaman, I., Sehitoglu, H., Beaudoin, A.J., Chumlyakov, Y.I., Maier, H.J., Tome, C. (2000a) Modeling the deformation behavior of Hadfield steel single and polycrystals due to twinning and slip. *Acta Mater.*, **48**, 2031–2047.

Karaman, I., Sehitoglu, H., Gall, K., Chumlyakov, Y.I., Maier, H.J. (2000b) Deformation of a single crystal Hadfield steel by twinning and slip. *Acta Mater.*, **48**, 1345–1359.

Karaman, I., Sehitoglu, H., Gall, K., Chumlyakov, Y.I. (1998) On the deformation mechanisms in single crystal hadfield manganese steels. *Scripta Mater.*, **38**, 1009–1015.

Kawahara, K., Ibaraki, K., Tsurekawa, S., Watanabe, T. (2005) Distribution of plane matching boundaries for different types and sharpness of textures. *Mat. Sci. Forum*, **475–479**, 3871–3874.

Kiener, D., Pippan, R., Motz, C., Kreuzer, H. (2006) Microstructural evolution of the deformed volume beneath microindents

in tungsten and copper. *Acta Mater.*, **54**, 2801–2811.

Kim, H.K. and Oh, S.I. (2003) Finite element analysis of grain-by-grain deformation by crystal plasticity with couple stress. *Int. J. Plasticity*, **19**, 1245–1270.

Kim, K.H., Kim, H.K., and Oh, S.I. (2006) Deformation behavior of pure aluminum specimen composed of a few grains during simple compression. *J. Mater. Process. Tech.*, **171**, 205–213.

Kobayashi, S., Tsurekawa, S., and Watanabe, T. (2005) Grain boundary hardening and triple junction hardening in polycrystalline molybdenum. *Acta Mater.*, **53**, 1051–1057.

Kocks, U.F. (1966) A statistical theory of flow stress and work-hardening. *Philos. Mag.*, **13**, 541.

Kocks, U.F. (1976) Laws of work-hardening and low temperature creep. *J. Eng. Mater. Tech.*, **98**, 76–83.

Kocks, U.F. and Chandra, H. (1982) Slip geometry in partially constrained deformation. *Acta Metall.*, **30**, 695–709.

Kokawa, H., Watanabe, T., and Karashima, S. (1981) Sliding behavior and dislocation-structures in aluminum grain-boundaries. *Philos. Mag. A*, **44**, 1239.

Konrad, J., Zaefferer, S., and Raabe, D. (2006) Investigation of orientation gradients around a hard Laves particle in a warm rolled Fe3Al-based alloy by a 3D EBSD-FIB technique. *Acta Mater.*, **54**, 1369–1380.

Köster, W. and Speidel, M.O. (1965) Der Einfluss der Temperatur und der Korngröße auf die ausgeprägte Streckgrenze von Kupferlegierungen. *Z. Metallkd.*, **9**, 1050.

Kouznetsova, V., Brekelmans, W.A.M., and Baaijens, F.P.T. (2001) An approach to micro-macro modeling of heterogeneous materials. *Comput. Mech.*, **27** (1), 37–48.

Kraska, M., Doig, M., Tikhomirov, D., Raabe, D., Roters, F. (2009) Virtual material testing for stamping simulations based on polycrystal plasticity. *Comp. Mater. Sci.*, **46**, 383–392.

Kröner, E. (1958a) Berechnung der elastischen Konstanten des Vielkristalls aus den Konstanten des Einkristalls. *Z. Phys.*, **151**, 504–518.

182 | *References*

Kröner, E. (1958b) *Kontinuumstheorie der Versetzungen und Eigenspannungen (in German)*, Springer, Berlin.

Kröner, E. (1960) Allgemeine Kontinuumstheorie der Versetzungen und Eigenspannungen. *Arch. Rational Mech. Anal.*, **4**, 275–334.

Kröner, E. (1961) On the plastic deformation of polycrystals. *Acta Metall.*, **9**, 155–161.

Kröner, E. (1981) *Physics of defects*, Continuum theory of defects, 217, North-Holland Publishing Company, Amsterdam, Netherlands.

Kruijver, S.O., Zhao, L., Sietsma, J., Offerman, S.E., van Dijk, N.H., Lauridsen, E.M., Margulies, L., Grigull, S., Poulsen, H.F., van der Zwaag, S. (2003) In situ observation on the mechanical stability of austenite in TRIP-steel. *J. Phys. IV*, **104**, 499–502.

Kuchnicki, S.N., Cuitiño, A.M., and Radovitzky, R.A. (2006) Efficient and robust constitutive integrators for single-crystal plasticity modeling. *Int. J. Plasticity*, **22**, 1988–2011.

Kumar, D., Bieler, T.R., Eisenlohr, P., Mason, D.E., Crimp, M.A., Roters, F., Raabe, D. (2008) On predicting nucleation of microcracks due to slip-twin interactions at grain boundaries in duplex γ-TiAl. *J. Eng. Mater. Tech.*, **130**, 021 012–1–021 012–12.

Kuo, J.C., Zaefferer, S., Zhao, Z., Winning, M., Raabe, D. (2003) Deformation behaviour of aluminium-bicrystals. *Adv. Eng. Mater.*, **5**, 563–566.

Kurdjumov, G. and Sachs, G. (1930) Über den Mechanismus der Stahlhärtung. *Z. Physik*, **64**, 325–343.

Kuroda, M. and Tvergaard, V. (2008a) On the formulations of higher-order strain gradient crystal plasticity models. *J. Mech. Phys. Solids*, **56**, 1591–1608.

Kuroda, M. and Tvergaard, V. (2006) Studies of scale dependent crystal viscoplasticity models. *J. Mech. Phys. Solids*, **54** (9), 1789–1810.

Kuroda, M. and Tvergaard, V. (2008b) A finite deformation theory of higher-order gradient crystal plasticity. *J. Mech. Phys. Solids*, **56** (8), 2573–2584.

Kysar, J.W., Gan, Y.X., and Mendez-Arzuza, G. (2005) Cylindrical void in a rigid-ideally plastic single crystal. Part I: Anisotropic slip line theory solution for face-centered cubic crystals. *Int. J. Plasticity*, **21**, 1481–1520.

Lan, Y.J., Xiao, N.M., Li, D.Z., Li, Y.Y. (2005) Mesoscale simulation of deformed austenite decomposition into ferrite by coupling a cellular automaton method with a crystal plasticity finite element model. *Acta Mater.*, **53**, 991–1003.

Larson, B.C., Yang, W., Ice, G.E., Swadener, J.G., Budai, J.D., Tischler, J.Z. (2002) Three-dimensional X-ray structural microscopy with submicrometre resolution. *Nature*, **415**, 887–890.

Lebensohn, R.A. (2001) N-site modeling of a 3D viscoplastic polycrystal using fast fourier transform. *Acta Mater.*, **49** (14), 2723–2737.

Lebensohn, R.A., Brenner, R., Castelnau, O., Rollett, A.D. (2008) Orientation image-based micromechanical modelling of sub-grain texture evolution in polycrystalline copper. *Acta Mater.*, **56**, 3914–3926.

Lebensohn, R.A. and Tomé, C.N. (1993) A self-consistent anisotropic approach for the simulation of plastic deformation and texture development of polycrystals: Application to zirconium alloys. *Acta Metall. Mater.*, **41** (9), 2611–2624.

Leblond, J.B., Mottet, G., and Devaux, J.C. (1986a) A theoretical and numerical approach to the plastic behaviour of steels during phase-transformation – I. Derivation of general relations. *J. Mech. Phys. Solids*, **34**, 395–409.

Leblond, J.B., Mottet, G., and Devaux, J.C. (1986b) A theoretical and numerical approach to the plastic behaviour of steels during phase-transformation – II. Study of classical plasticity for ideal-plastic phases. *J. Mech. Phys. Solids*, **34**, 411–432.

Lee, E.H. (1969) Elastic-plastic deformation at finite strains. *J. Appl. Mech. ASME*, **36**, 1–6.

Lee, E.H. and Liu, D.T. (1967) Finite-strain elastic-plastic theory with application to plane-wave analysis. *J. Appl. Phys.*, **38**, 19–27.

Lee, M.G., Wang, J., and Anderson, P.M. (2007) Texture evolution maps for upset deformation of body-centered cubic metals. *Mat. Sci. Eng. A*, **463**, 263–270.

Lehockey, E.M. and Palumbo, G. (1997) On the creep behaviour of grain boundary

engineered nickel. *Mat. Sci. Eng. A*, **237**, 168–172.

Lejcek, P. and Paidar, V. (2005) Challenges of interfacial classification for grain boundary engineering. *Mat. Sci. Tech.*, **21**, 393–398.

Lemaitre, J. and Chaboche, J.L. (1998) *Mechanics of Solid Materials*, 2nd edn, Cambridge University Press, Cambridge.

Levitas, V.I., Idesman, A.V., and Olson, G.B. (1999a) Continuum modeling of strain-induced martensitic transformation at shear-band intersections. *Acta Mater.*, **47** (1), 219–233.

Levitas, V.I., Idesman, A.V., and Stein, E. (1999b) Shape memory alloys: Micromechanical modeling and numerical analysis of structures. *J. Intel. Mat. Syst. Str.*, **10**, 983–996.

Levkovitch, V. and Svendsen, B. (2006) On the large-deformation- and continuum-based formulation of models for extended crystal plasticity. *Int. J. Solids Struct.*, **43** (24), 7246–7267.

Li, H.W., Yang, H., and Sun, Z.C. (2008a) A robust integration algorithm for implementing rate dependent crystal plasticity into explicit finite element method. *Int. J. Plasticity*, **24**, 267–288.

Li, H., Jiang, Z., Han, J., Wei, D., Pi, H., Tieu, A. (2008b) Crystal plasticity finite element modeling of necking of pure aluminium during uniaxial tensile deformation. *Steel Res.*, **2**, 655–662.

Li, L., Anderson, P.M., Lee, M.G., Bitzek, E., Derlet, P., Van Swygenhoven, H. (2009) The stress-strain response of nanocrystalline metals: A quantized crystal plasticity approach. *Acta Mater.*, **57**, 812–822.

Li, S., Donohue, B.R., and Kalidindi, S.R. (2008c) A crystal plasticity finite element analysis of cross-grain deformation heterogeneity in equal channel angular extrusion and its implications for texture evolution. *Mat. Sci. Eng. A*, **480**, 17–23.

Li, S., Kalidindi, S.R., and Beyerlein, I.J. (2005) A crystal plasticity finite element analysis of texture evolution in equal channel angular extrusion. *Mat. Sci. Eng. A*, **410–411**, 207–212.

Li, S.Y., Van Houtte, P., and Kalidindi, S.R. (2004) A quantitative evaluation of the deformation texture predictions for aluminium alloys from crystal plasticity finite element method. *Modelling Simul. Mater. Sci. Eng.*, **12**, 845–870.

Lim, L.C. and Raj, R. (1985) Continuity of slip screw and mixed-crystal dislocations across bicrystals of nickel at 573-K. *Acta Metall.*, **33**, 1577.

Liu, W.H., Zhang, X.M., Tang, J.G., Du, Y. (2007) Simulation of void growth and coalescence behavior with 3D crystal plasticity theory. *Comp. Mater. Sci.*, **40**, 130–139.

Liu, W.K., Karpov, E.G., Zhang, S., Park, H.S. (2004) An introduction to computational nanomechanics and materials. *Comput. Method. Appl. M.*, **193**, 529–1578.

Livingston, J. and Chalmers, B. (1957) Multiple slip in bicrystal deformation. *Acta Metall.*, **5**, 322.

Loge, R., Bernacki, M., Resk, H., Delannay, L., Digonnet, H., Chastel, Y., Coupez, T. (2008) Linking plastic deformation to recrystallization in metals using digital microstructures. *Philos. Mag.*, **88**.

Luccioni, B. and Oller, S. (2003) A directional damage model. *Comput. Method. Appl. M.*, **192**, 1119–1145.

Ludwig, W., Reischig, P., King, A., Herbig, M., Lauridsen, E.M., Johnson, G., Marrow, T.J., Buffiere, J.Y. (2009) Three-dimensional grain mapping by x-ray diffraction contrast tomography and the use of Friedel pairs in diffraction data analysis. *Rev. Sci. Instrum.*, **80** (3), 033 905.

Luster, J. and Morris, M.A. (1995) Compatibility of deformation in two-phase Ti-Al alloys: Dependence on microstructure and orientation relationships. *Metall. Mater. Trans. A*, **26**, 1745.

Ma, A. and Roters, F. (2004) A constitutive model for fcc single crystals based on dislocation densities and its application to uniaxial compression of aluminium single crystals. *Acta Mater.*, **52** (12), 3603–3612.

Ma, A., Roters, F., and Raabe, D. (2006a) A dislocation density based constitutive model for crystal plasticity FEM including geometrically necessary dislocations. *Acta Mater.*, **54**, 2169–2179.

Ma, A., Roters, F., and Raabe, D. (2006b) On the consideration of interactions between dislocations and grain boundaries in crystal plasticity finite element modeling – theory, experiments, and simulations. *Acta Mater.*, **54**, 2181–2194.

184 | *References*

Ma, A., Roters, F., and Raabe, D. (2006c) Studying the effect of grain boundaries in dislocation density based crystal plasticity finite element simulations. *Int. J. Solids Struct.*, **43**, 7287–7303.

Ma, A., Roters, F., and Raabe, D. (2007) A dislocation density based consitutive law for BCC materials in crystal plasticity FEM. *Comp. Mater. Sci.*, **39**, 91–95.

Ma, D., Friak, M., Neugebauer, J., Raabe, D., Roters, F. (2008) Multiscale simulation of polycrystal mechanics of textured β-Ti alloys using ab initio and crystal-based finite element methods. *Phys. Status Solidi B*, **245**, 2642–2648.

Mahajan, S. and Williams, D.F. (1973) Deformation twinning in metals and alloys. *Int. Metal. Rev.*, **18**, 43.

Maniatty, A.M., Dawson, P.R., and Lee, Y.S. (1992) A time integration algorithm for elasto-viscoplastic cubic crystals applied to modelling polycrystalline deformation. *Int. J. Numer. Meth. Eng.*, **35**, 1565–1588.

Mar(2007) *MSC.Marc user's manual 2007, User Subroutines and Special Routines, Volume D*, MSC.

Marketz, F. and Fischer, F.D. (1994) Micromechanical modelling of stress-assisted martensitic transformation. *Modelling Simul. Mater. Sci. Eng.*, **2**, 1017–1046.

Marketz, F. and Fischer, F.D. (1995) A mesoscale study on the thermodynamic effect of stress on martensitic transformation. *Metall. Mater. Trans. A*, **26**, 267–278.

Marketz, W.T., Fischer, F.D., and Clemens, H. (2003) Deformation mechanisms in TiAl intermetallics – experiments and modeling. *Int. J. Plasticity*, **19**, 281–321.

Marketz, W.T., Fischer, F.D., Kauffmann, F., Dehm, G., Bidlingmaier, T., Wanner, A., Clemens, H. (2002) On the role of twinning during room temperature deformation of TiAl based alloys. *Mat. Sci. Eng. A*, **329–331**, 177–183.

Masson, R., Bornert, M., Suquet, P., Zaoui, A. (2000) An affine formulation for the prediction of the effective properties of nonlinear composites and polycrystals. *J. Mech. Phys. Solids*, **48** (6–7), 1203–1227.

Mayama, T., Sasaki, K., and Kuroda, M. (2008) Quantitative evaluations for strain amplitude dependent organization of dislocation structures due to cyclic plasticity in austenitic stainless steel 316L. *Acta Mater.*, **56**, 2735–2743.

Mayeur, J.R., McDowell, D.L., and Neu, R.W. (2008) Crystal plasticity simulations of fretting of Ti-6Al-4V in partial slip regime considering effects of texture. *Comp. Mater. Sci.*, **41**, 356–365.

McDowell, D.L. (2008) Viscoplasticity of heterogeneous metallic materials. *Mat. Sci. Eng. R*, **62**, 67–123.

McGarrity, E.S., Duxbury, P.M., and Holm, E.A. (2005) Statistical physics of grain-boundary engineering. *Phys. Rev. E*, **71**, Art. No. 026 102 Part 2.

McGarry, J.P., O'Donnell, B.P., McHugh, P.E., McGarry, J.G. (2004) Analysis of the mechanical performance of a cardiovascular stent design based on micromechanical modelling. *Comp. Mater. Sci.*, **31**, 421–438.

McHugh, P.E. and Mohrmann, R. (1997) Modelling of creep in a Ni base superalloy using a single crystal plasticity model. *Comp. Mater. Sci.*, **9**, 134–140.

Mecking, H., Hartig, C., and Kocks, U.F. (1996) Deformation modes in gamma-TiAl as derived from the single crystal yield surface. *Acta Mater.*, **44**, 1309–1321.

Mecking, H. and Kocks, U.F. (1986) Kinetics of flow and strain hardening. *Acta Metall.*, **29**, 1865–1875.

Meissonnier, F.T., Busso, E.P., and O'Dowd, N.P. (2001) Finite element implementation of a generalised non-local rate-dependent crystallographic formulation for finite strains. *Comp. Mater. Sci.*, **17**, 601–640.

Melchior, M. and Delannay, L. (2006) A texture discretization technique adapted to polycrystalline aggregates with non-uniform grain size. *Comp. Mater. Sci.*, **37** (4), 557–564.

Melchior, M. (2009) *Modelling of texture and hardening of TWIP steel – Advanced finite element representation of polycrystalline aggregates*, Ph. D. thesis, Université catholique de Louvain, Louvain la Neuve.

Meng, L., Yang, P., Xie, Q., Ding, H., Tang, Z. (2007) Dependence of deformation twinning on grain orientation in compressed high manganese steels. *Scripta Mater.*, **56**, 931–934.

Menzel, A., Ekh, M., Runesson, K., Steinmann, P. (2005) A framework for multiplicative elastoplasticity with kinematic

hardening coupled to anisotropic damage. *Int. J. Plasticity*, **21**, 397–434.

Meyers, M.A., Andrade, U.R., and Chokshi, A.H. (1995) Effect of grain size on the high-strain, high-strain-rate behavior of copper. *Metall. Mater. Trans. A*, **26**, 2881–2893.

Michel, J.C., Moulinec, H., and Suquet, P. (1999) Effective properties of composite materials with periodic microstructure: A computational approach. *Comput. Method. Appl. M.*, **172**, 109–143.

Miehe, C. (1996) Exponential map algorithm for stress updates in anisotropic multiplicative elastoplasticity for single crystals. *Int. J. Numer. Meth. Eng.*, **39**, 3367–3390.

Miehe, C., Schotte, J., and Lambrecht, M. (2002) Homogenization of inelastic solid materials at finite strains based on incremental minimization principles. Application to the texture analysis of polycrystals. *J. Mech. Phys. Solids*, **50** (10), 2123–2167.

Miehe, C., Schröder, J., and Schotte, J. (1999) Computational homogenization analysis in finite plasticity simulation of texture development in polycrystalline materials. *Comput. Method. Appl. M.*, **171**, 387–418.

Mika, D.P. and Dawson, P.R. (1998) Effects of grain interaction on deformation in polycrystals. *Mat. Sci. Eng. A*, **257**, 62–76.

Mika, D.P. and Dawson, P.R. (1999) Polycrystal plasticity modeling of intracrystalline boundary textures. *Acta Mater.*, **47**, 1355–1369.

Miller, M.P. and Turner, T.J. (2001) A methodology for measuring and modeling crystallographic texture gradients in processed alloys. *Int. J. Plasticity*, **17**, 783–805.

Molinari, A., Canova, G.R., and Ahzi, S. (1987) A self-consistent approach of the large deformation polycrystal viscoplasticity. *Acta Metall.*, **35** (12), 2983–2994.

Monaghan, J.J. (1988) An introduction to SPH. *Comput. Phys. Commun.*, **48**, 88–96.

Mori, T. and Tanaka, K. (1973) Average stress in matrix and average elastic energy of materials with misfitting inclusions. *Acta Metall.*, **21** (5), 571–574.

Moulinec, H. and Suquet, P. (1998) A numerical method for computing the overall response of nonlinear composites with complex microstructure. *Comput. Method. Appl. M.*, **157** (1–2), 69–94.

Müller, S. (1996) *Variational models for microstructure and phase transitions,* in Lectures at the C.I.M.E. summer school on calculus of variations and geometric evolution problems, *Springer Lecture Notes in Mathematics*, vol. 2 (eds. Hildebrandt, S. ,Struwe, M.), C. I. M. E., Cetraro, Springer, pp. 85–210.

Munjiza, A. (2004) *The Combined Finite-Discrete Element Method*, Wiley, Chinchester.

Murphy, B.P., Cuddy, H., Harewood, F.J., Connolley, T., McHugh, P.E. (2006) The influence of grain size on the ductility of micro-scale stainless steel stent struts. *J. Mat. Sci. – Mat. Med.*, **17**, 1–6.

Musienko, A., Tatschl, A., Schmidegg, K., Kolednik, O., Pippan, R., Cailletaud, G. (2007) Three-dimensional finite element simulation of a polycrystalline copper specimen. *Acta Mater.*, **55**, 4121–4136.

Nakamachi, E., Tam, N.N., and Morimoto, H. (2007) Multi-scale finite element analyses of sheet metals by using SEM-EBSD measured crystallographic RVE models. *Int. J. Plasticity*, **23**, 450–489.

Nakamachi, E., Xie, C.L., and Harimoto, M. (2001) Drawability assessment of BCC steel sheet by using elastic/crystalline viscoplastic finite element analyses. *Int. J. Mech. Sci.*, **43**, 631–652.

Neale, K.W. (1993) Use of crystal plasticity in metal forming simulations. *Int. J. Mech. Sci.*, **35**, 1053–1063.

Needleman, A. (1987) A continuum model for void nucleation by inclusion debonding. *J. Appl. Mech. ASME*, **54**, 525–531.

Nemat-Nasser, S. and Hori, M. (1999) *Micromechanics: Overall Properties of Heterogeneous Materials*, 2nd edn, Elsevier, Amsterdam.

Nemat-Nasser, S., Ni, L., and Okinaka, T. (1998) A constitutive model for fcc crystals with application to polycrystalline OFHC copper. *Mech. Mater.*, **30** (4), 325–341.

Ng, B.C., Bieler, T.R., Crimp, M.A., Mason, D.E. (2005) Prediction of crack paths based upon detailed microstructure characterization in a near-γ TiAl Alloy, *Materials Damage Prognosis*, TMS, Warrendale, PA, pp. 307–314.

Nicolaou, P.D. and Semiatin, S.L. (2000) An analysis of the effect of continuous nucleation and coalescence on cavitation during

186 | *References*

hot tension testing. *Acta Mater.*, **48**, 3441–3450.

Nicolaou, P.D. and Semiatin, S.L. (2003) Hybrid micromechanical – macroscopic model for the analysis of tensile behavior of cavitating materials. *Metall. Mater. Trans. A*, **34**.

Nielsen, S.F., Lauridsen, E.M., Juul Jensen, D., Poulsen, H.F. (2001) A three-dimensional X-ray diffraction microscope for deformation studies of polycrystals. *Mat. Sci. Eng. A*, **319–321**, 179–181.

Nishiyama, Z. (1934) X-ray investigation on the mechanism of the transformation from face-centered cubic lattice to body-centered cubic lattice. *Sci. Rep. Tohoku Imp. Univ. Tokyo*, **23**, 637–664.

Noll, W. (1972) A new mathematical theory of simple materials. *Arch. Ration. Mech. An.*, **48**, 1–50.

Nye, J.F. (1953) Some geometrical relations in dislocated crystals. *Acta Metall.*, **1**, 153–162.

Ocenasek, J., Rodriguez Ripoll, M., Weygand, S.M., Riedel, H. (2007) Multi-grain finite element model for studying the wire drawing process. *Comp. Mater. Sci.*, **39**, 23–28.

Okumura, D., Higashi, Y., Sumida, K., Ohno, N. (2007) A homogenization theory of strain gradient single crystal plasticity and its finite element discretization. *Int. J. Plasticity*, **23**, 1148–1166.

Oliver, E.C., Whithers, P.J., Daymond, M.R., Ueta, S., Mori, T. (2002) Neutron-diffraction study of stress-induced martensitic transformation in TRIP steel. *Appl. Phys. A – Mater. Sci. Proc.*, **74**, S1143–S1145.

Olson, G.B. and Cohen, M. (1975) Kinetics of strain-induced martensitic nucleation. *Metall. Trans. A*, **6** (4), 791–795.

Ortiz, M. and Repetto, E.A. (1999) Non-convex energy minimization and dislocation structures in ductile single crystals. *J. Mech. Phys. Solids*, **47**, 397–462.

Palumbo, G., Lehockey, E.M., and Lin, P. (1998) Applications for grain boundary engineered materials. *JOM*, **50**, 40–43.

PAM(2004) *PAM-STAMP 2G, Version 2004.1 Standard. Stamping solutions manual.*, ESI Group, Paris.

Pardoen, T., Dumont, D., Deschamps, A., Brechet, Y. (2003) Grain Boundary versus transgranular ductile failure. *J. Mech. Phys. Solids*, **51**, 637.

Park, S.J., Han, H.N., Oh, K.H., Raabe, D., Kim, J.K. (2002) Finite element simulation of grain interaction and orientation fragmentation during plastic deformation of BCC metals. *Mat. Sci. Forum*, **408–4**, 371–376.

Patel, J.R. and Cohen, M. (1953) Criterion for the action of applied stress in martensitic transformation. *Acta Metall.*, **1** (5), 531–538.

Patil, S.D., Narasimhan, R., Biswas, P., Mishra, R.K. (2008) Crack tip fields in a single edge notched aluminum single crystal specimen. *J. Eng. Mater. Tech.*, **130**, 021 013.

Peirce, D., Asaro, R.J., and Needleman, A. (1982) An analysis of nonuniform and localized deformation in ductile single crystals. *Acta Metall.*, **30**, 1087–1119.

Peirce, D., Asaro, R.J., and Needleman, A. (1983) Material rate dependence and localized deformation in crystalline solids. *Acta Metall.*, **31**, 1951–1976.

Petch, N.J. (1953) The cleavage strength of polycrystals. *J. Iron Steel Inst.*, 25.

Ponte Castañeda, P. and Suquet, P. (1998) Nonlinear Composites, in *Advances in Applied Mechanics*, vol. 34 (eds Van der Giessen, E., Wu, T.), Academic Press, New York, NY, pp. 171–302.

Potirniche, G.P., Hearndon, J.L., Horstemeyer, M.F., Ling, X.W. (2006) Lattice orientation effects on void growth and coalescence in fcc single crystals. *Int. J. Plasticity*, **22**, 921–942.

Prasannavenkatesan, R., Li, B.Q., Field, D.P., Weiland, H. (2005) A parallel macro/micro elastoplasticity model for aluminum deformation and comparison with experiments. *Metall. Mater. Trans. A*, **36**, 241–256.

Proust, G., Tome, C.N., and Kaschner, G. (2007) Modeling texture, twinning and hardening evolution during deformation of hexagonal materials. *Acta Mater.*, **55**, 2137–2148.

Pyo, S.G. and Kim, N.J. (2005) Role of interface boundaries in the deformation behavior of TiAl polysynthetically twinned crystal, in situ transmission electron microscopy deformation study. *J. Mat. Res.*, **20**, 1888–1901.

Raabe, D. (1995a) Investigation of contribution of 123 slip planes to development of

rolling textures in bcc metals by use of Taylor models. *Mat. Sci. Tech.*, **11**, 455–460.

Raabe, D. (1995b) Simulation of rolling textures of bcc metals under consideration of grain interactions and 110, 112 and 123 slip planes. *Mat. Sci. Eng. A*, **197**, 31–37.

Raabe, D. (1999) Introduction of a scaleable 3D cellular automaton with a probabilistic switching rule for the discrete mesoscale simulation of recrystallization phenomena. *Philos. Mag. A*, **79**, 2339–2358.

Raabe, D. (2000) Yield surface simulation for partially recrystallized aluminum polycrystals on the basis of spatially discrete data. *Comp. Mater. Sci.*, **19**, 13–26.

Raabe, D. (2001) Mesoscale simulation of recrystallization textures and microstructures. *Adv. Eng. Mater.*, **3**, 745–752.

Raabe, D. (2002) Cellular automata in materials science with particular reference to recrystallization simulation. *Annual Review of Materials Research*, **32**, 53–76.

Raabe, D. (2007) Recrystallization models for the prediction of crystallographic textures with respect to process simulation. *J. Strain Anal. Eng. Des.*, **42**, 253–268.

Raabe, D. and Becker, R. (2000) Coupling of a crystal plasticity finite element model with a probabilistic cellular automaton for simulating primary static recrystallization in aluminum. *Modelling Simul. Mater. Sci. Eng.*, **8**, 445–462.

Raabe, D., Klose, P., Engl, B., Imlau, K.P., Friedel, F., Roters, F. (2002a) Concepts for integrating plastic anisotropy into metal forming simulations. *Adv. Eng. Mater.*, **4**, 169–180.

Raabe, D. and Lücke, K. (1993) Textures of ferritic stainless steels. *Mat. Sci. Tech.*, **9**, 302–312.

Raabe, D., Ma, D., and Roters, F. (2007a) Effects of initial orientation, sample geometry and friction on anisotropy and crystallographic orientation changes in single crystal microcompression deformation: A crystal plasticity finite element study. *Acta Mater.*, **55**, 4567–4583.

Raabe, D. and Roters, F. (2004) Using texture components in crystal plasticity finite element simulations. *Int. J. Plasticity*, **20**, 339–361.

Raabe, D., Roters, F., Barlat, F., Chen, L.Q. (eds) (2004a) *Continuum Scale Simulation of Engineering Materials, Fundamentals – Microstructures – Process Applications*, Wiley-VCH Verlag GmbH.

Raabe, D., Sachtleber, M., Weiland, H., Scheele, G., Zhao, Z. (2003) Grain-scale micromechanics of polycrystal surfaces during plastic straining. *Acta Mater.*, **51**, 1539–1560.

Raabe, D., Sachtleber, M., Zhao, Z., Roters, F., Zaefferer, S. (2001) Micromechanical and macromechanical effects in grain scale polycrystal plasticity experimentation and simulation. *Acta Mater.*, **49** (17), 3433–3441.

Raabe, D., Sander, B., Friak, M., Ma, D., Neugebauer, J. (2007b) Theory-guided bottom-up design of beta-titanium alloys as biomaterials based on first principles calculations: theory and experiments. *Acta Mater.*, **55**, 4475–4487.

Raabe, D., Wang, Y., and Roters, F. (2005) Crystal plasticity simulation study on the influence of texture on earing in steel. *Comp. Mater. Sci.*, **34**, 221–234.

Raabe, D., Zhao, Z., and Mao, W. (2002b) On the dependence of in-grain subdivision and deformation texture of aluminum on grain interaction. *Acta Mater.*, **50**, 4379–4394.

Raabe, D., Zhao, Z., Park, S.J., Roters, F. (2002c) Theory of orientation gradients in plastically strained crystals. *Acta Mater.*, **50**, 421–440.

Raabe, D., Zhao, Z., and Roters, F. (2002d) Theory of Orientation Gradients. *Mat. Sci. Forum*, **408–412**, 275–280.

Raabe, D., Zhao, Z., and Roters, F. (2004b) Study on the orientational stability of cube-oriented FCC crystals under plane strain by use of a texture component crystal plasticity finite element method. *Scripta Mater.*, **50**, 1085–1090.

Radhakrishnan, B. and Sarma, G. (2004) The effect of coarse non-deformable particles on the deformation and static recrystallization of aluminium alloys. *Philos. Mag. E*, **84**, 2341–2366.

Radhakrishnan, B., Sarma, G., Weiland, H., Baggethun, P. (2000) Simulations of deformation and recrystallization of single crystals of aluminum containing hard particles. *Modelling Simul. Mater. Sci. Eng.*, **8**, 737–750.

Randle, V. (1995) The influence of grain junctions and boundaries on superplastic

188 | *References*

deformation. *Acta Metall. Mater.*, **43**, 1741–1749.

Randle, V. (2004) Twinning-related grain boundary engineering. *Acta Mater.*, **52**, 4067–4081.

Rémy, L. (1975) *Maclage et transformation martensitique CFC–HC induite par déformation plastique dans les alliages austéniques à basse énergie de défaut d'empilement des sytèmes Co-Ni-Cr-Mo et Fe-Mn-Cr-C*, Ph. D. thesis, ENSMP, Paris.

Reuss, A. (1929) Berechnung der Fließgrenze von Mischkristallen auf Grund der Plastizitätsbeding für Einkristalle. *Z. Angew. Math. Mech.*, **9**, 49–58.

Rice, J.R. (1971) Inelastic constitutive relations for solids: an internal variable theory and its application to metal plasticity. *J. Mech. Phys. Solids*, **19**, 433–455.

Richtmyer, R.D. and Morton, K.W. (1967) *Difference Methods for Initial Value Problems*, 2nd edn, John Wiley & Sons, New York.

Ritz, H. and Dawson, P.R. (2009) Sensitivity to grain discretization of the simulated crystal stress distributions in FCC polycrystals. *Modelling Simul. Mater. Sci. Eng.*, **17**.

Rohrer, G.S., Randle, V., Kim, C.S., Hu, Y. (2006) Changes in the five-parameter grain boundary character distribution in a-brass brought about by iterative thermomechanical processing. *Acta Mater.*, **54**, 4489–4502.

Rohrer, G.S., Saylor, D.M., El-Dasher, B.S., Adams, B.L., Rollett, A.D., Wynblatt, P. (2004) The distribution of internal interfaces in polycrystals. *Z. Metallkd.*, **95**, 197–214.

Roters, F., Eisenlohr, P., Hantcherli, L., Tjahjanto, D.D., Bieler, T.R., Raabe, D. (2010) Overview of constitutive laws, kinematics, homogenization and multiscale methods in crystal plasticity finite-element modeling: Theory, experiments, applications. *Acta Mater.*, **58**, 1152–1211.

Roters, F., Jeon-Haurand, H.S., and Raabe, D. (2005) A texture evolution study using the texture component crystal plasticity FEM. *Mat. Sci. Forum*, **495–497**, 937–944.

Roters, F., Raabe, D., and Gottstein, G. (2000) Work hardening in heterogeneous alloys – a microstructural approach based on three internal state variables. *Acta Mater.*, **48**, 4181–4189.

Roters, F., Wang, Y., Kuo, J.C., Raabe, D. (2004) Comparison of single crystal simple shear deformation experiments with crystal plasticity finite element simulations. *Adv. Eng. Mater.*, **6** (8), 653–656.

Sachs, G. (1928) Zur Ableitung einer Fliessbedingung. *Z. VDI*, **72**, 734–736.

Sachtleber, M., Zhao, Z., and Raabe, D. (2002) Experimental investigation of plastic grain interaction. *Mat. Sci. Eng. A*, **336** (1–2), 81–87.

Salem, A.A., Kalidindi, S.R., Doherty, R.D., Semiatin, S.L. (2006) Strain hardening due to deformation twinning in α-titanium: Mechanics. *Metall. Mater. Trans. A*, **37**, 259–268.

Salem, A.A., Kalidindi, S.R., and Semiatin, S.L. (2005) Strain hardening due to deformation twinning in α-titanium: Constitutive relations and crystal-plasticity modeling. *Acta Mater.*, **53**, 3495–3502.

Sarma, G.B. and Dawson, P.R. (1996a) Effects of interactions among crystals on the inhomogeneous deformations of polycrystals. *Acta Mater.*, **44**, 1937–1953.

Sarma, G.B. and Dawson, P.R. (1996b) Texture predictions using a polycrystal plasticity model incorporating neighbor interactions. *Int. J. Plasticity*, **12** (8), 1023–1054.

Sarma, G.B. and Radhakrishnan, B. (2004) Modeling microstructural effects on the evolution of cube texture during hot deformation of aluminum. *Mat. Sci. Eng. A*, **385**, 91–104.

Sarma, G.B., Radhakrishnan, B., and Zacharia, T. (1998) Finite element simulations of cold deformation at the mesoscale. *Comp. Mater. Sci.*, **12**, 105–123.

Sarma, G.B. and Zacharia, T. (1999) Integration algorithm for modeling the elasto-viscoplastic response of polycrystalline materials. *J. Mech. Phys. Solids*, **47**, 1219–1238.

Schlögl, S.M. and Fischer, F.D. (1997) The role of slip and twinning in the deformation behaviour of polysynthetically twinned crystals of TiAl: A micromechanical model. *Philos. Mag. A*, **75**, 621–636.

Schuh, C.A., Kumar, M., and King, W.E. (2003) Analysis of grain boundary networks and their evolution during grain boundary engineering. *Acta Mater.*, **51**, 687–700.

Semiatin, S.L., Weaver, D.S., Goetz, R.L., Thomas, J.P., Turner, T.J. (2007) Deformation and recrystallization during thermomechanical processing of a nickel-base superalloy ingot material. *Mat. Sci. Forum*, **550**, 129–140.

Shen, Z., Wagoner, R.H., and Clark, W.A.T. (1986) Dislocation pile-up and grain boundary interactions in 304 stainless steel. *Scripta Metall.*, **20** (6), 921–926.

Simkin, B.A., Crimp, M.A., and Bieler, T.R. (2003) A factor to predict microcrack nucleation at γ-γ grain boundaries in TiAl. *Scripta Mater.*, **49**, 149–154.

Simkin, B.A., Ng, B.C., Crimp, M.A., Bieler, T.R. (2007) crack opening due to deformation twin shear at grain boundaries in near-gamma TiAl. *Intermetallics*, **15**, 55–60.

Singh, A. and King, A.H. (1993) tables of coincidence orientations for ordered tetragonal l lo alloys for a range of axial ratios. *Acta Cryst. B*, **49**, 266–272.

Sinha, S. and Ghosh, S. (2006) Modeling cyclic ratcheting based fatigue life of HSLA steels using crystal plasticity FEM simulations and experiments. *Int. J. Fatigue*, **28**, 1690–1704.

Sinha, V., Spowart, M.J., Mills, M.J., Williams, J.C. (2006) Observations on the faceted initiation site in the dwell-fatigue tested Ti-6242 alloy: crystallographic orientation and size effects. *Metall. Mater. Trans. A*, **37**, 1507–1518.

Siska, F., Forest, S., and Gumbsch, P. (2007) Simulations of stress strain heterogeneities in copper thin films: Texture and substrate effects. *Comp. Mater. Sci.*, **39**, 137–141.

Smit, R.J.M., Brekelmans, W.A.M., and Meijer, H.E.H. (1998) Prediction of the mechanical behavior of nonlinear heterogeneous systems by multi-level finite element modeling. *Comput. Method. Appl. M.*, **155** (1–2), 181–192.

Solenthaler, C. and Bollmann, W. (1986) Between primary and secondary relaxation in a grain-boundary. *Mat. Sci. Eng. A*, **81**, 35–49.

Song, S.G. and Gray, G.T.I. (1995) Influence of temperature and strain rate on slip and twinning behavior of Zr. *Metall. Mater. Trans. A*, **26**, 2665–2675.

Spearot, D.E., Jacob, K.I., and McDowell, D.L. (2004) Non-local separation constitutive laws for interfaces and their relation to nanoscale simulations. *Mech. Mater.*, **36**, 825–847.

Staroselsky, A. and Anand, L. (1998) Inelastic deformation of polycrystalline face centered cubic materials by slip and twinning. *J. Mech. Phys. Solids*, **46**, 671–696.

Staroselskya, A. and Anand, L. (2003) A constitutive model for hcp materials deforming by slip and twinning: application to magnesium alloy AZ31B. *Int. J. Plasticity*, **19**, 1843–1864.

Stringfellow, R.G., Parks, D.M., and Olson, G.B. (1992) A constitutive model for transformation plasticity accompanying strain-induced martensitic transformations in metastable austenitic steels. *Acta Metall. Mater.*, **40** (7), 1703–1716.

Su, J.Q., Demura, M., and Hirano, T. (2003) Mechanical behaviour of $\Sigma 3$ boundaries in Ni_3Al. *Acta Mater.*, **51**, 2505–2515.

Suiker, A.S.J. and Turteltaub, S. (2005) Computational modelling of plasticity induced by martensitic phase transformations. *Int. J. Numer. Meth. Eng.*, **63**, 1655–1693.

Sun, S., Adams, B.L., and King, W.E. (2000) Observations of lattice curvature near the interface of a deformed aluminium bicrystal. *Philos. Mag. A*, **80**, 9–25.

Takaki, T., Yamanaka, Y., Higa, Y., Tomita, Y. (2007) Phase-field model during static recrystallization based on crystal-plasticity theory. *J. Computer-Aided Mater. Des.*, **14**, 75–84.

Tang, J.G., Zhang, X.M., Chen, Z.Y., Deng, Y.L. (2006) Simulation of rolling deformation texture of fcc metals with crystal plasticity finite element model. *Mat. Sci. Tech.*, **22**, 1171–1176.

Tatschl, A. and Kolednik, O. (2003) On the experimental characterization of crystal plasticity in polycrystals. *Mat. Sci. Eng. A*, **342**, 152.

Taylor, G.I. (1938) Plastic strain in metals. *J. Inst. Metals*, **62**, 307–324.

Thamburaja, P. (2005) Constitutive equations for martensitic reorientation and detwinning in shape-memory alloys. *J. Mech. Phys. Solids*, **53**, 825–856.

Thamburaja, P. and Anand, L. (2001) Polycrystalline shape-memory materials: effect of crystallographic texture. *J. Mech. Phys. Solids*, **49**, 709–737.

190 | *References*

Thorning, C., Somers, M.A.J., and Wert, J.A. (2005) Grain interaction effects in polycrystalline Cu. *Mat. Sci. Eng. A*, **397**, 215–228.

Tikhovskiy, I., Raabe, D., and Roters, F. (2006) Simulation of the deformation texture of a 17 component crystal plasticity FE method considering texture gradients. *Scripta Mater.*, **54**, 1537–1542.

Tikhovskiy, I., Raabe, D., and Roters, F. (2007) Simulation of earing during deep drawing of an Al-3 component crystal plasticity FEM. *J. Mater. Process. Tech.*, **183**, 169–175.

Tjahjanto, D.D. (2007) *Micromechanical modeling and simulations of transformation-induced plasticity in multiphase carbon steels*, Delft University of Technology, Delft.

Tjahjanto, D.D., Roters, F., and Eisenlohr, P. (2007) Iso-work-rate weighted-Taylor homogenization scheme for multiphase steels assisted by transformation-induced plasticity effect. *Steel Res. Int.*, **78** (10–11), 777–783.

Tjahjanto, D.D., Turteltaub, S., and Suiker, A.S.J. (2008) Crystallographically-based model for transformation-induced plasticity in multiphase carbon steels. *Continuum Mech. Therm.*, **19**, 399–422.

Tjahjanto, D., Eisenlohr, P., and Roters, F. (2009) *Relaxed Grain Cluster (RGC) Homogenization Scheme*, Proc. 12th International ESAFORM Conference on Material Forming (eds van den Boogaard, T., Akkerman, R.), Enschede.

Tjahjanto, D., Eisenlohr, P., and Roters, F. (2010) A novel grain cluster-based homogenization scheme. *Modelling Simul. Mater. Sci. Eng.*, **18**, 015 006.

Tomita, Y. and Iwamoto, T. (1995) Constitutive modeling of TRIP steel and its application to the improvement of the mechanical properties. *Int. J. Mech. Sci.*, **37**, 1295–1305.

Tomita, Y. and Iwamoto, T. (2001) Computational prediction of deformation behavior of TRIP steels under cyclic loading. *Int. J. Mech. Sci.*, **43**, 2017–2034.

Tóth, L.S. and Van Houtte, P. (1992) Discretization techniques for orientation distribution functions. *Texture Microstruct.*, **19**, 229–244.

Tschopp, M.A., Spearot, D.E., and McDowell, D.L. (2008) Dislocation nucleation in Sigma 3 asymmetric tilt grain boundaries. *Int. J. Plasticity*, **24**, 191–217.

Tschopp, M.A., Spearot, D.E., and McDowell, D.L. (2007) Atomistic simulations of homogeneous dislocation nucleation in single crystal copper. *Modelling Simul. Mater. Sci. Eng.*, **15**, 693–709.

Tsurekawa, S., Kokubun, S., and Watanabe, T. (1999) Effect of grain boundary microstructures of brittle fracture in polycrystalline molybdenum. *Mat. Sci. Forum*, **304–3**, 687–692.

Tugcu, P., Neale, K.W., Wu, P.D., Inal, K. (2004) Crystal plasticity simulation of the hydrostatic bulge test. *Texture Microstruct.*, **20**, 1603–1653.

Turkmen, H.S., Dawson, P.R., and Miller, M.P. (2002) The evolution of crystalline stresses of a polycrystalline metal during cyclic loading. *Int. J. Plasticity*, **18**, 941–969.

Turkmen, H.S., Loge, R.E., Dawson, P.R., Miller, M.P. (2003) On the mechanical behavior of AA 7075-t6 during cyclic loading. *Int. J. Fatigue*, **25**, 267–281.

Turteltaub, S. and Suiker, A.S.J. (2005) Transformation-induced plasticity in ferrous alloys. *J. Mech. Phys. Solids*, **53**, 1747–1788.

Turteltaub, S. and Suiker, A.S.J. (2006a) A multi-scale thermomechanical model for cubic to tetragonal martensitic phase transformations. *Int. J. Solids Struct.*, **43**, 4509–4545.

Turteltaub, S. and Suiker, A.S.J. (2006b) Grain size effects in multiphase steels assisted by transformation-induced plasticity. *Int. J. Solids Struct.*, **43**, 7322–7336.

Turteltaub, S. and Suiker, A. (2006c) A multiscale thermomechanical model for cubic to tetragonal martensitic phase transformations. *Int. J. Solids Struct.*, **43**, 4509–4545.

Uchic, M.D., Dimiduk, D.M., Florando, J.N., Nix, W.D. (2004) Sample dimensions influence strength and crystal plasticity. *Science*, **305**, 986–989.

Van Houtte, P. (1978) Simulation of the rolling and shear texture of brass by the Taylor theory adapted for mechanical twinning. *Acta Metall.*, **26**, 591–604.

Van Houtte, P. (1982) On the equivalence of the relaxed Taylor theory and the Bishop–Hill theory for partially constrained plastic

deformation of crystals. *Mat. Sci. Eng.*, **55** (1), 69–77.

Van Houtte, P. (1988) A comprehensive mathematical formulation of an extended Taylor–Bishop–Hill model featuring relaxed constraints, the Renouard–Wintenberger theory and a strain rate sensitivity model. *Texture Microstruct.*, **8–9**, 313–350.

Van Houtte, P., Delannay, L., and Kalidindi, S.R. (2002) Comparison of two grain interaction models for polycrystal plasticity and deformation texture prediction. *Int. J. Plasticity*, **18**, 359–377.

Van Houtte, P., Delannay, L., and Samajdar, I. (1999) Quantitative prediction of cold rolling textures in low-carbon steel by means of the LAMEL model. *Texture Microstruct.*, **31**, 109–149.

Van Houtte, P., Kanjarla, A.K., Van Bael, A., Seefeldt, M., Delannay, L. (2006) Multi-scale modelling of the plastic anisotropy and deformation texture of polycrystalline materials. *Eur. J. Mech. A. Solids*, **25**, 634–648.

Van Houtte, P., Li, S., Seefeldt, M., Delannay, L. (2005) Deformation texture prediction: from the Taylor model to the advanced Lamel model. *Int. J. Plasticity*, **21** (3), 589–624.

Van Houtte, P., Van Bael, A., Seefeldt, M., Delannay, L. (2005) The application of multi-scale modelling for the prediction of plastic anisotropy and deformation textures. *Mat. Sci. Forum*, **495–497**, 31–41.

Vegter, H., Horn, C.T., An, Y., Atzema, E., Pijlman, H., Boogaard, A.V.D., Huétink, J. (2003) *Characterisation and modelling of the plastic material behaviour and its application in sheet metal forming simulation.* Proceedings of COMPLAS VII, CIMNE (eds Oñate, E., Owen, D.), Barcelona.

Venables, J.A. (1964) *Deformation Twinning in f.c.c metals* in Deformation Twinning 77–116 (eds Reed-Hill, R. E., Hirth, J. P. and Rogers, H. C.) Gordon & Breach, New York.

Venkataramani, G., Kirane, K., and Ghosh, S. (2008) Microstructural parameters affecting creep induced load shedding in Ti-6242 by a size dependent crystal plasticity FE model. *Int. J. Plasticity*, **24**, 428–454.

Venkatramani, G., Ghosh, S., and Mills, M. (2007) A size-dependent crystal plasticity

finite-element model for creep and load shedding in polycrystalline titanium alloys. *Acta Mater.*, **55**, 3971–3986.

Vitek, V., Mrovec, M., and Bassani, J.L. (2004a) Influence of non-glide stresses on plastic flow: From atomistic to continuum modeling. *Mat. Sci. Eng. A*, **365**, 31–37.

Vitek, V., Mrovec, M., Gröger, R., Bassani, J.L., V. Racherla, Yin, L. (2004b) Effects of non-glide stresses on the plastic flow of single and polycrystals of molybdenum. *Mat. Sci. Eng. A*, **387–389**, 138–142.

Voce, E. (1948) The relationship between stress and strain for homogeneous deformation. *J. Inst. Metals*, **74**, 537–562.

Vogler, T.J. and Clayton, J.D. (2008) Heterogeneous deformation and spall of an extruded tungsten alloy: plate impact experiments and crystal plasticity modeling. *J. Mech. Phys. Solids*, **56**, 297–335.

Vöhringer, O. (1976) Einsatzpannung für mechanishe Zwillingsbildung bei α-Kupferlegierungen. *Z. Metallkd.*, **67**, 518–524.

Voigt, W. (1889) Über die Beziehung zwischen den beiden Elastizitätskonstanten isotroper Körper. *Wied. Ann.*, **38**, 573–587.

Volterra, V. (1907) Sur l'équilibre des corps élastiques multiplement connexes. *Ann. Sci. Ecole Norm. Super.*, **24**, 401–517.

Voyiadjis, G.Z., Abu Al-Rub, R.K., and Palazotto, A.N. (2004) Thermodynamic framework for coupling of non-local viscoplasticity and non-local anisotropic viscodamage for dynamic localization problems using gradient theory. *Int. J. Plasticity*, **20**, 981–1038.

Voyiadjis, G.Z. and Dorgan, R.J. (2007) Framework using functional forms of hardening internal state variables in modeling elasto-plastic-damage behavior. *Int. J. Plasticity*, **23**, 1826–1859.

Wagner, P. (1994) *Zusammenhänge zwischen mikro- und makroskopischen Verformungsinhomogenitäten und der Textur*, Ph. D. thesis, RWTH Aachen.

Wang, M.G. and Ngan, A.H.W. (2004) Indentation strain burst phenomenon induced by grain boundaries in niobium. *J. Mat. Res.*, **19**, 2478–2486.

Wang, Y., Raabe, D., Küber, C., Roters, F. (2004) Orientation dependence of nanoindentation pile-up patterns and of nanoin-

192 *References*

dentation microtextures in copper single crystals. *Acta Mater.*, **52**, 2229–2238.

Wassermann, G. (1935) Ueber den Mechanismus der $\alpha-\gamma$-Umwandlung des Eisens. *Mitt. K.-Wilh.-Inst. Eisenforsch.*, **17**, 149–155.

Watanabe, I., Terada, K., deSouza, E.A., Peric, D. (2008) Characterization of macroscopic tensile strength of polycrystalline metals with two-scale finite element analysis.*J. Mech. Phys. Solids*, **56**, 1105–1125.

Watanabe, T. (1984) An approach to grain-boundary design for strong and ductile polycrystals. *Res Mech.*, **11**, 47–84.

Watanabe, T. and Tsurekawa, S. (2004) Toughening of brittle materials by grain boundary engineering. *Mat. Sci. Eng. A*, **387–389**, 447–455.

Watanabe, T. and Tsurekawa, S. (2005) Prediction and control of grain boundary fracture in brittle materials on the basis of the strongest-link theory. *Mat. Sci. Forum*, **485**, 55–62.

Weber, F., Schestakow, I., Roters, F., Raabe, D. (2008) Texture evolution during bending of a single crystal copper nanowire studied by EBSD and crystal plasticity finite element simulations. *Adv. Eng. Mater.*, **10**, 737–741.

Wechsler, M.S., Lieberman, D.E., and Read, T.A. (1953) On the theory of the formation of martensite. *Appl. Phys. A-Mater.*, **197** (11), 1503–1515.

Wei, Y.J. and Anand, L. (2004) Grain-boundary sliding and separation in polycrystalline metals: application to nanocrystalline fcc metals. *J. Mech. Phys. Solids*, **52**, 2587–2616.

Wei, Y.J., Su, C., and Anand, L. (2006) A computational study on the mechanical behavior of nanocrystalline fcc metals. *Acta Mater.*, **54**, 3177–3190.

Werner, E. and Prantl, W. (1990) Slip transfer across grain and phase boundaries. *Acta Metall. Mater.*, **38**, 3231–3242.

Wilkinson, D.S., Pompe, W., and Oeschner, M. (2001) Modeling the mechanical behavior of heterogeneous multi-phase materials. *Prog. Mater. Sci.*, **46**, 379–405.

Williams, J.R. and Mustoe, G.H.G.G.W. (1985) The Theoretical Basis of the Discrete Element Method, in *NUMETA 1985, Numerical Methods of Engineering, Theory and Applications* (ed Balkema, A.A.), Rotterdam.

Wilshire, B. and Willis, M. (2004) Mechanisms of strain accumulation and damage development during creep of prestrained 316 stainless steels. *Metall. Trans. A*, **35**, 563–571.

Wolf, D. (1990) Correlation between structure, energy, and ideal cleavage fracture for symmetrical grain-boundaries in FCC metals. *J. Mat. Res.*, **5**, 1708–1730.

Wrobel, L.C. and Aliabadi, M.H. (2002) *The Boundary Element Method*, John Wiley & Sons, Chinchester.

Wu, M.S. (1997) Crack nucleation due to dislocation pile-ups at I-, U- and amorphized triple lines. *Mech. Mater.*, **25**, 215–234.

Wu, M.S. and He, M.D. (1999) Prediction of crack statistics in a random polycrystal damaged by the pile-ups of extrinsic grain-boundary dislocations. *Philos. Mag.*, **79**, 271–292.

Wu, M.S., Nazarov, A.A., and Zhou, K. (2004) Misorientation dependence of the energy of [1-100] symmetrical tilt boundaries in hcp metals: prediction by the disclination-structural unit model. *Philos. Mag.*, **84**, 785–806.

Wu, X., Proust, G., Knezevic, M., Kalidindi, S.R. (2007) Elastic-plastic property closures for hexagonal close-packed polycrystalline metals using first-order bounding theories. *Acta Mater.*, **55**, 2729–2737.

Xie, C.L. and Nakamachi, E. (2002) Investigations of the formability of BCC steel sheets by using crystalline plasticity finite element analysis. *Mater Design*, **23**, 59–68.

Xu, B., Yonezu, A., Yue, Z., Chen, X. (2009) Indentation creep surface morphology of nickel-based single crystal superalloys. *Comp. Mater. Sci.*, **46**, 275–285.

Xu, X.P. and Needleman, A. (1994) Numerical simulations of fast crack growth in brittle solids. *J. Mech. Phys. Solids*, **42**, 1397–1434.

Yao, Z. and Wagoner, R.H. (1993) Active slip in aluminum multicrystals. *Acta Metall. Mater.*, **41**, 451–468.

You, X., Connolley, T., McHugh, P.E., Cuddy, H., Motz, C. (2006) A combined experimental and computational study of deformation in grains of biomedical grade 316LVM stainless steel. *Acta Mater.*, **54**, 4825–4840.

Yue, Z.F. (2005) Surface roughness evolution under constant amplitude fatigue loading

using crystal plasticity. *Eng. Fract. Mech.*, **72**, 749–757.

Zaafarani, N., Raabe, D., Roters, F., Zaefferer, S. (2008) On the origin of deformation-induced rotation patterns below nanoindents. *Acta Mater.*, **56**, 31–42.

Zaafarani, N., Raabe, D., Singh, R.N., Roters, F., Zaefferer, S. (2006) Three dimensional investigation of the texture and microstructure below a nanoindent in a Cu single crystal using 3D EBSD and crystal plasticity finite element simulations. *Acta Mater.*, **54**, 1707–1994.

Zaefferer, S., Kuo, J.C., Zhao, Z., Winning, M., Raabe, D. (2003) On the influence of the grain boundary misorientation on the plastic deformation of aluminum bicrystals. *Acta Mater.*, **51** (16), 4719–4735.

Zaefferer, S., Wright, S.I., and Raabe, D. (2008) 3D-orientation microscopy in a FIB SEM: a new dimension of microstructure characterisation. *Metall. Mater. Trans. A*, **39**, 374–389.

Zambaldi, C., Roters, F., Raabe, D., Glatzel, U. (2007) Modeling and experiments on the indentation deformation and recrystallization of a single-crystal nickel-base superalloy. *Mat. Sci. Eng. A*, **454–455**, 433–440.

Zamiri, A., Bieler, T.R., and Pourboghrat, F. (2009) Anisotropic crystal plasticity finite element modeling of the effect of crystal orientation and solder joint geometry on deformation after temperature change. *J. Electron. Mat.*, **38**, 231–240.

Zhang, F., Bower, A.F., Mishra, R.K., Boyle, K.P. (2009) Numerical simulations of necking during tensile deformation of aluminum single crystals. *Int. J. Plasticity*, **25**, 49–69.

Zhang, M., Zhang, J., and McDowell, D.L. (2007) Microstructure-based crystal plasticity modeling of cyclic deformation of Ti-6Al-4V. *Int. J. Plasticity*, **23**, 1328–1348.

Zhang, Z.F. and Wang, Z.G. (2003) Dependence of intergranular fatigue cracking on the interactions of persistent slip bands with grain boundaries. *Acta Mater.*, **51**, 347–364.

Zhao, Z., Kuchnicki, S., Radovitzky, R., Cuitiño, A. (2007) Influence of in-grain mesh resolution on the prediction of deformation textures in fcc polycrystals by crystal plasticity FEM. *Acta Mater.*, **55**, 2361–2373.

Zhao, Z., Mao, W., and Raabe, D. (2002) Influence of grain neighborhood on FCC texture simulation. *Mat. Sci. Forum*, **408–412**, 281–286.

Zhao, Z., Mao, W., Roters, F., Raabe, D. (2001) Introduction of a texture component crystal plasticity finite element method for anisotropy simulations. *Adv. Eng. Mater.*, **3**, 984–990.

Zhao, Z., Mao, W., Roters, F., Raabe, D. (2004a) A texture optimization study for minimum earing in aluminium by use of a texture component crystal plasticity finite element method. *Acta Mater.*, **52**, 1003–1012.

Zhao, Z., Radovitzky, R., and Cuitiño, A. (2004b) A study of surface roughening in fcc metals using direct numerical simulation. *Acta Mater.*, **52** (20), 5791–5804.

Zhao, Z., Ramesh, M., Raabe, D., Cuitiño, A., Radovitzky, R. (2008) Investigation of three-dimensional aspects of grain-scale plastic surface deformation of an aluminum oligocrystal. *Int. J. Plasticity*, **24**, 2278–2297.

Zhuang, W.M., Wang, S., Cao, J., Lin, L., Hart, C. (2008) Hydroforming of micro tubes: crystal plasticity finite element modeling. *Steel Res.*, **spec. issue 1**, 293–300.

Zienkiewicz, O.C. (1967) *The Finite Element Method in Structural and Continuum Mechanics*, 1st edn, McGraw-Hill, New York.

Zienkiewicz, O.C. and Taylor, R.L. (2005) *The Finite Element Method for Solid and Structural Mechanics*, 6th edn, Butterworth-Heinemann, Oxford.

Zienkiewicz, O.C., Taylor, R.L., and Nithiarasu, P. (2005a) *The Finite Element Method for Fluid Dynamics*, 6th edn, Butterworth-Heinemann, Oxford.

Zienkiewicz, O.C., Taylor, R.L., and Zhu, J.Z. (2005b) *The Finite Element Method: Its Basis and Fundamentals*, 6th edn, Butterworth-Heinemann, Oxford.

Index

Franz Roters, Philip Eisenlohr, Thomas R. Bieler, and Dierk Raabe: Crystal Plasticity Finite Element Methods —
2010/7/23 — page 197 — le-tex

Index | **197**